THERESA
Subproject MOLDAU

Coupled Thermal-Hydrological-Mechanical-Chemical Processes in Repository Safety Assessment

Final Report

Joint Project of:

DBE TECHNOLOGY GmbH

IfG Institut für Gebirgsmechanik GmbH
Untersuchung - Prüfung - Beratung - Begutachtung

Gesellschaft für Anlagen- und Reaktorsicherheit (GRS) mbH

GRS - 262

Gesellschaft für Anlagen-
und Reaktorsicherheit
(GRS) mbH

THERESA
Subproject MOLDAU

Coupled Thermal-Hydrological-Mechanical-Chemical Processes in Repository Safety Assessment

Final Report

Klaus Wieczorek
Bernd Förster
Tilmann Rothfuchs
Chung-Liang Zhang
Sebastia Olivella (CIMNE)
Peter Kamlot (IfG)
Ralf-Michael Günther (IfG)
Christian Lerch (DBE TEC)

June 2010

Remark:

This report was prepared under contract No. 02 E 10236 with the German Bundesministerium für Wirtschaft und Technologie (BMWi).

The work was conducted by the DBE TECHNOLOGY GmbH (DBE TEC), the Gesellschaft für Anlagen- und Reaktorsicherheit (GRS) mbH, the Institut für Gebirgsmechanik (IfG) and the Centre Internacional de Mèthodes Numèrics en Enginyeria (CIMNE).

The authors are responsible for the content of the report.

GRS - 262
ISBN 978-3-939355-37-3

Keywords:
Nuclear waste, Disposal, Rock salt, Numerical modelling, THMC, Safety assessment

Preface

The THERESA project ("Coupled thermal-hydrological-mechanical-chemical (THMC) processes for application in repository safety assessment") was performed between January 1, 2007, and December 31, 2009, as a Specific Targeted Research and Training Project (STREP) within the Sixth Framework Programme of the European Community (contract no. FP6-036458).

The overall goal of THERESA was to develop a scientific method for evaluating the capabilities of mathematical models and computer codes used for the design, construction, operation, performance assessment (PA), safety assessment (SA), and post-closure monitoring of geological nuclear waste repositories. The project work consisted of five work packages (WP1-WP5). WP1 was the overall planning package, designed to supervise the implementation of the other four work packages throughout the duration of the project. In WP2, the issue evaluation tables (IETs) were developed with respect to WP3 and WP4. Therefore, the specific issues in PA that are related to THMC modelling in rock salt, buffer, and buffer-rock interfaces were identified and with these results the project was guided in addressing the relevant issues in WP3 and WP4. WP3 and WP4 are the packages addressing numerical modelling of coupled processes, which are THM processes in salt (WP3) and THMC processes in buffer and buffer-rock interfaces (WP4). WP5 was defined to implement a technical auditing (TA) of the models and codes applied in WP3 and WP4, according to specificly developed IETs in WP2.

16 organisations took part in the THERESA project:

- Royal Institute of TECHNOLOGY (KTH), Sweden, as the coordinator of the project
- Swedish Radioactive Safety Authority (SSM) (replacing Swedish Nuclear Power Inspectoratev(SKI), as of July 1, 2008), Sweden
- Swedish Nuclear Fuel and Waste Management Co. (SKB), Sweden
- Federal Institute for Geosciences and Natural Resources (BGR), Germany
- DBE TECHNOLOGY GmbH (DBE TEC), Germany
- Forschungszentrum Karlsruhe GmbH (FZK), Germany
- Gesellschaft für Anlagen- und Reaktorsicherheit GmbH (GRS), Germany

- Institut für Gebirgsmechanik GmbH (IfG), Germany
- Nuclear Research and Consultancy Group (NRG), Netherlands
- Technische Universität Clausthal (TUC), Germany
- Centre International de Métodes Numèrics en Enginyeria (CIMNE), Spain
- Cardiff University (CU), UK
- Posiva Oy (POSIVA), Finland
- Marintel Ky (Marintel), Finland
- Quintessa Limited (Quintessa), UK
- Institut de Radioprotection et de Sûreté Nucléaire (IRSN), France

The organisations involved in the work regarding rock salt (WP3 and the respective IET of WP2) were GRS as the lead contractor, BGR, DBE TEC, FZK, IfG, NRG, TUC, and CIMNE. Of these partners, GRS, DBE TEC, IfG, and CIMNE as contractor of GRS, received a national co-funding via the “Projektträger Karlsruhe“ (PTKA). This report presents the work carried out by these organisations during the THERESA project.

Table of Contents

	Preface	**I**
1	**Introduction**	**1**
2	**Issue evaluation table for rock salt**	**5**
3	**Experimental work**	**7**
3.1	Small-scale tests	7
3.1.1	Testing method	7
3.1.2	Results	10
3.2	Large-scale tests	18
3.2.1	Tested material	19
3.2.2	Test design	19
3.2.3	First large-scale test	23
3.2.4	Second large-scale test	26
3.3	Benchmark tests	32
3.3.1	Testing method	33
3.3.2	TC test 1	35
3.3.3	TC test 2	37
4	**Description of models and improvements**	**43**
4.1	CODE_BRIGHT (CIMNE)	43
4.1.1	Model description	43
4.1.2	Calibration work	50
4.2	FLAC (IfG)	54
4.2.1	Model description	54
4.2.2	Calibration work	57
4.3	$FLAC^{3D}$ (DBE TEC)	65
4.3.1	Model description	65
4.3.2	Calibration work	69
4.4	PFC^{3D} (DBE TEC)	72

4.4.1 Model description 74
4.4.2 Calibration work 79
4.4.3 Conclusions from experience with DEM 82

5 Benchmark simulation 83
5.1 CODE_BRIGHT simulation (CIMNE) 83
5.1.1 Simulation of TC2A and TC2B 83
5.1.2 Simulation of TC2B with alternative parameters 86
5.1.3 Simulation of the large hollow cylinder test 88
5.1.4 Conclusions 89
5.2 FLAC simulation (IfG) 90
5.2.1 Blind prediction of the large hollow cylinder test 90
5.2.2 Blind prediction and interpretation modelling of benchmark test TC2A 94
5.2.3 Interpretation modelling of benchmark test TC2B 99
5.2.4 Conclusions 104
5.3 FLAC^{3D} simulation (DBE TEC) 105
5.3.1 Simulation of TC2A and TC2B 105
5.3.2 Conclusions 114

6 Reference case simulation 117
6.1 Definition of reference case 117
6.2 Process-level modelling of EDZ evolution 119
6.3 Equivalent permeability and porosity as input for TSPA codes 122
6.4 Results of the drift model calculation with LOPOS 127
6.5 Discussion of Reference Case calculation results 131

7 Summary and conclusions 133
7.1 Background and objectives 133
7.2 Work plan and achievements 134
7.3 Conclusions and lessons learned 136

8 References 139

9 List of figures 143

10 List of tables 151

A Appendix: Issue evaluation table for rock salt..... 153

1 Introduction

The aim of THERESA project was to develop a scientific method for evaluating the capabilities of mathematical models and computer codes used in Performance Assessment (PA) - using process level models - or Total System Performance Assessment (TSPA) - mostly using simplified PA models. The project was applied to the design, construction, operation, performance and safety assessment, and post-closure monitoring of geological nuclear waste repositories, based on the scientific principles governing coupled thermo-hydro-mechanical and chemical (THMC) processes in geological systems and geo-materials. The project work concentrated on the most essential issues for PA identified in the Issue Evaluation Tables (IET), with a focus on rock salt, buffer materials, and the buffer-rock interface. Details on the overall contents of the project can be found in the description of work /DOW 06/, annex I to the project contract.

Two different types of host rock were considered within this project, i. e. rock salt, as it is the mostly considered host rock in Germany covered in Work Package 3 (WP3), and hard rock (WP4). With respect to the German point of view, the German participants in THERESA project are cooperated in WP3. WP3 of the project addressed the evaluation and improvement of numerical modelling capabilities for assessing the performance and safety of nuclear waste repositories in rock salt, with particular emphasis on the long-term evolution of the excavation damaged zone (EDZ), which is one of the most important issues identified in the IET for rock salt (see section 2). The focus of the study was placed on

1. calibration of existing constitutive models of rock salt for coupled THM processes using relevant data, either already available or concurrently produced,

2. laboratory benchmark tests (BMT) for the validation of the calibrated constitutive models and computer codes, and

3. application of validated models and codes for the simulation of a representative reference case for the rock salt option, taking into account requirements of long-term performance assessment.

WP3 consisted of the following components:

- WP3.1: Compilation of data and definition of work for model calibration

The existing constitutive models for the thermal-hydraulic-mechanical (THM) behaviour of the excavation damaged zone (EDZ) in rock salt, particularly its long-term behaviour and its self-sealing ability under the conditions that will occur in and near repositories were reviewed, and all relevant results obtained within the scope of earlier projects (e.g., NF-PRO, national programmes) were compiled, evaluated, and discussed with regard to their usability for calibrating the different models (project deliverable D5 /WIE 07/).

- WP3.2: Calibration of models

Based on the data sets previously compiled, the constitutive models for the EDZ behaviour were calibrated as far as possible and/or improved. Test calculations were carried out and the numerical results were compared with experimental results to demonstrate the suitability of the models (Deliverable D6 /WIE 08/).

- WP3.3 Test case

Supporting laboratory tests were performed at GRS' geotechnical laboratory to provide more reliable experimental data for the validation of the models calibrated in work packages WP3.1 and WP3.2. The definition of the test case, the laboratory BMT of WP3, was discussed and agreed upon the WP3 members, and the tests were then conducted. The technical definition of the BMT and its experimental results are descriebed in the Deliverable D7 /ZHA 09/.

The modelling teams performed predictions of the laboratory benchmark tests for checking the capabilities of the models to describe the relevant processes, such as EDZ generation and sealing/healing, using the computer codes involved (Deliverable D8 /WIE 09a/).

- WP3.4 RC calculation (dynamic phase of the repository; 500 to 1000 years) and integration of improved models in PA codes

A repository reference case in rock salt was defined by the three WP3 partners DBE TEC, GRS, and NRG, and its performance was simulated using the participating process level and PA codes. The focus was on predicting the long-term evolution of the EDZ and its impact on the long-term performance of the reference repository.

The work and the results from all of the international project partners regarding WP3 of the THERESA project are summarised in Deliverable D9 /WIE 09b/. The report in hand is the final report of the project MOLDAU which was carried out by DBE TEC, IfG, CIMNE as subcontractor of GRS, and GRS itself. The project MOLDAU provided the national co-funding to the EC project THERESA by the German BMWi under FKZ 02 E 10236, 02 E 10246, and 02 E 10256.

Section 2 contains a short summary of the IET prepared by DBE TEC and GRS is given; the complete IET can be found in the appendix. Section 3 contains the description and results of the experimental work carried out by GRS. In section 4, the models for the simulation of EDZ behaviour and their improvement in the course of THERESA are described. Section 5 presents the results of the benchmark simulations carried out by CIMNE, DBE TEC, and IfG. The simulations for the reference case can be found in section 6, and section 7 gives the conclusions to the project.

2 Issue evaluation table for rock salt

In Work Package 2 of THERESA, issue evaluation tables for the work packages 3 and 4 were created and updated throughout the project. For waste disposal in a rock salt formation, the following structure was chosen:

- The individual processes were grouped by their relevance to repository design, operational phase, closure phase, post-closure phase, and altered repository conditions.
- The relevance as input to PA, the availability of data and their respective reference, and the possible need for improvement and/or experiments were specified for each process.

The most important issues which are not yet sufficiently resolved were found to be

- optimization of sealing concepts with respect to safety assessment regarding the repository design and the closure phase,
- backfill behaviour during the closure and post-closure phases and in altered conditions,
- gas transport and storage during the post-closure phase,
- EDZ evolution and re-compaction during the operational phase, the closure and post-closure phases, and altered conditions, and
- brine transport in altered conditions.

As can be seen, the EDZ plays a major role in all phases of repository evolution. This is the reason why the WP3 work concentrated on the EDZ issue. Only a few aspects pointed out above, the last ones, concern altered repository conditions, most concern the improvement of the quality of the safety assessment, especially with respect to the long-term safety at late times of post-closure phase. Accordingly, the important physical quantities reach low values during this late period compared with values during the preceding phases.

The full tables with their specific references to the data references are given in the annex.

3 Experimental work

The experimental work performed at the GRS laboratory comprises small-scale damage/sealing tests performed to obtain additional data for model calibration (section 3.1) large-scale tests which were originally planned as the benchmark test case (section 3.2), and finally the actual benchmark tests on normal-scale samples which had to be added due to shortcomings of the large-scale tests (section 3.3). This work is also documented in Deliverable D7 “Laboratory Benchmark Tests on Rock Salt” of the THERESA project /ZHA 09/.

3.1 Small-scale tests

3.1.1 Testing method

Combined damage and sealing tests were carried out on three salt samples in a triaxial apparatus with measurement of deformation and gas permeability under various stress conditions. One sample (D = 86.5 mm / L = 175 mm) was taken from the 511-m-level of the Asse mine, while the other two (D = 90 mm / L = 200 mm) are from the 800-m-level. From the pictures in fig. 3.1 one can clearly recognize the grain boundaries (micro-cracks) on the surface of sample 1; some of them were more or less open. They were mainly produced by the coring procedure. In contrast to that, no open grain boundaries can be found in the other two samples. The size of most crystalline grains in the samples varies between 2 to 10 mm. The porosity of sample 1 was determined to ϕ = 0.46 %, whereas samples 2 and 3 have a porosity of ϕ = 0.37 %.

Figure 3.2 illustrates schematically the assembly of a sample in a triaxial cell. The sample was isolated in a jacket and porous discs at top and bottom. The annular gap between sample and jacket was sealed with silicon to avoid leakage. To reduce friction resistance between the sample and the load pistons, a thin sand layer of ~ 1 mm was put between the porous disc and the end face, or thin silicon strips with 0.2 mm thickness and ~ 5 mm width were laid between the piston and the end face.

(a) sample 1 from 511m-level of Asse mine

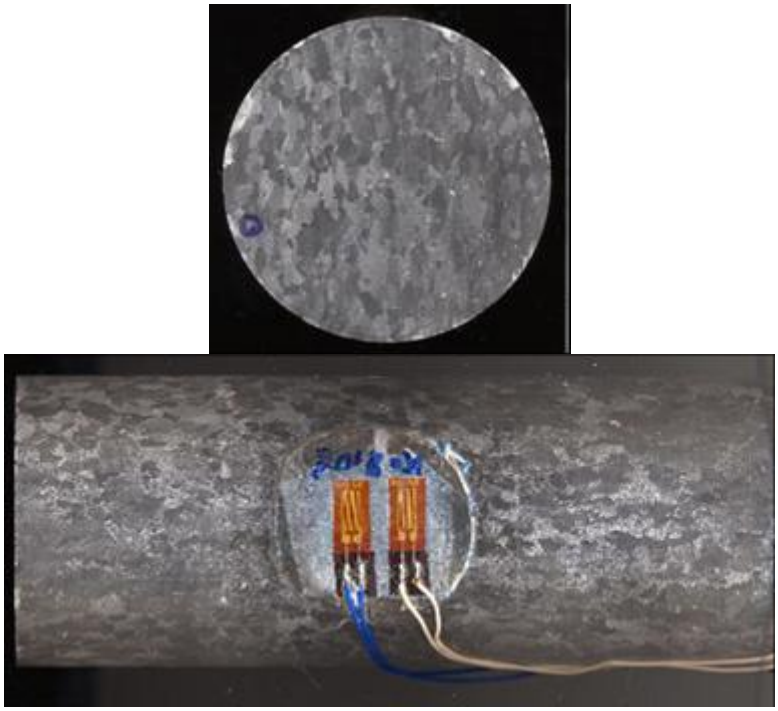

(b) sample 2 from 800m-level of Asse mine

Fig. 3.1 Salt samples with attached strain gauges before testing

The samples were loaded in three phases of isostatic pre-compaction, deviatoric loading, and isostatic re-compaction. The aim of the isostatic pre-compaction was to approach the intact state of the samples with respect to permeability. But it has to be pointed out that no effective healing has to be expected during the pre-compaction phase. This was performed by simultaneously increasing axial and radial stress to $\sigma_a = \sigma_r = 20$ MPa at a loading rate of 1 MPa/min, then keeping stress constant for several days, and unloading to a low stress of $\sigma_a = \sigma_r = 1$ or 2 MPa. The subsequent deviatoric loading to damage of the samples was carried out by increasing axial deformation ε_a at radial stress of $\sigma_r = 1$ or 2 MPa. A low strain rate of $\dot{\varepsilon}_a = 1 \cdot 10^{-7}\ s^{-1}$

was applied. As soon as a significant damage appeared, the samples were unloaded and then isostatically re-compacted step by step to a stress level of 14 MPa.

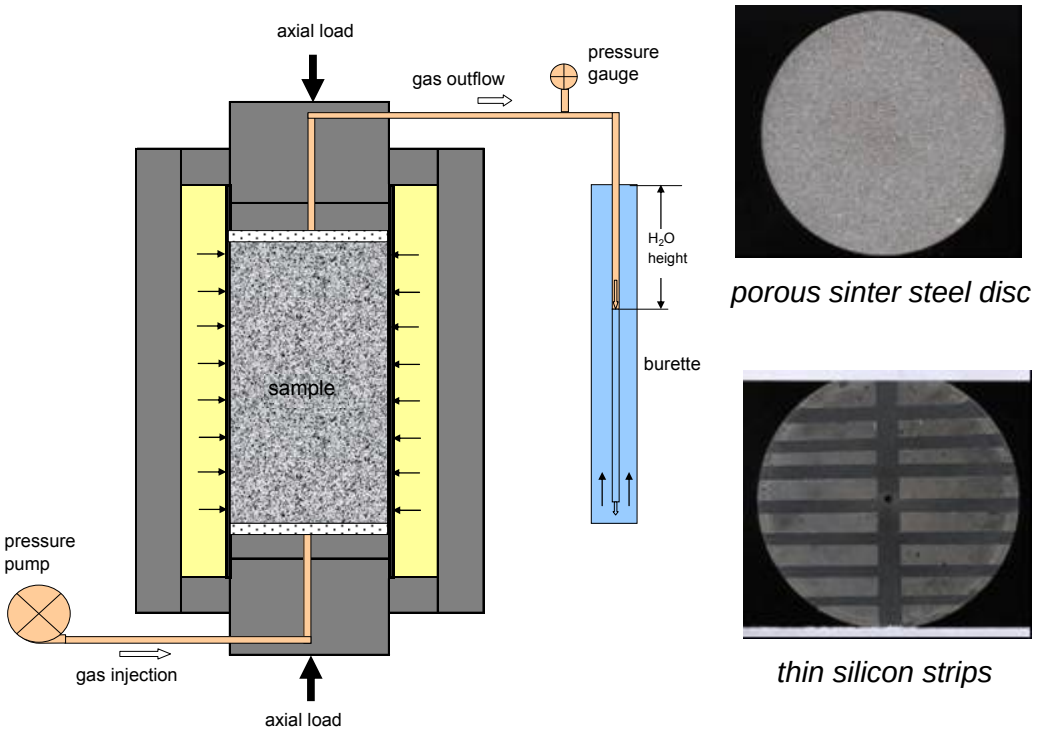

Fig. 3.2 Principle of triaxial compression tests with permeability measurement

During the tests, axial strain was measured by a LVDT-transducer installed outside of the cell, while volumetric strain was determined both directly from the volume change of the confining oil in the cell by using a pressure/volume GDS-controller and indirectly by strain gauges attached on the sample surface at the middle of the length. Permeability changes induced by the mechanical loading were measured along the sample axis by injecting dry nitrogen gas to the bottom at constant pressure of p = 0.5 ~ 1 MPa and recording the outflow at the opposite side. The gas outflow was continuously recorded by using a burette. During steady state gas flow, the permeability is determined according to Darcy's law for compressive media:

$$k = \frac{2 \cdot Q \cdot \mu \cdot L \cdot p_o}{A \cdot (p_g^2 - p_o^2)} \tag{3.1}$$

where k is the intrinsic permeability (m^2), Q is the flow rate of the gas (m^3/s), μ is the gas dynamic viscosity (Pa·s), L is the length of the sample (m), A is the section of the sample (m^2), p_o is the atmospheric pressure (Pa), p_g is the gas injection pressure (Pa).

This measuring system allows a precise determination of low permeability down to ~ 10^{-21} m^2.

3.1.2 Results

3.1.2.1 Pre-compaction

As an example, results of the pre-compaction of sample 1 are presented in fig. 3.3 showing the evolution of volumetric strain and permeability change. The test was started from a confining stress of 2 MPa, at which the initial permeability of the sample was measured to $1 \cdot 10^{-18}$ m^2, indicating the existence of micro-cracks and connected paths as visually identified from the crystalline structure before testing (fig. 3.1). Increasing the load to 6 MPa led to a small volume compaction of $\Delta\varepsilon_v \approx 0.01$ % but a significant decrease in permeability to $3 \cdot 10^{-19}$ m^2. It is interesting that over a 3-days creep phase at 6 MPa, the permeability decreased strongly with time but without a clear volume reduction. Further stress increase to 20 MPa reduced the volume by $\Delta\varepsilon_v \approx 0.04$ % and decreased the permeability to ~ $1 \cdot 10^{-22}$ m^2. This very low permeability value could only roughly be estimated with the employed measuring system. Because of the limited precision of the measuring systems, further small volume and permeability changes could not be detected during the following 4-days creep compaction phase. The subsequent unloading to the initial stress of 2 MPa over 5 days resulted in a full volume recovery but no permeability increase. The reversibility of the volume suggests a completely elastic deformation on one hand, but on the other hand the remaining permeability being four orders of magnitude lower than the initial value indicates a permanent closure of most of the micro-cracks in the sample. The inconsistent conclusions from the measurements of deformation and permeability might be due to the insufficient precision of the detecting methods, particularly for very small changes of the sample volume.

On the other two samples which were even pre-compacted from 1 to 20 MPa, the similar deformation behaviour was observed, as shown in fig. 3.4 illustrating the volumetric strain as a function of the applied stress obtained on sample 2. It seemed that a small amount of plastic compaction remained after unloading. On the other hand, no gas outflow at a pressure of 0.5 MPa could be detected before, during and after the compaction. This suggests a very low permeability of the samples, $k < 10^{-22}$ m^2.

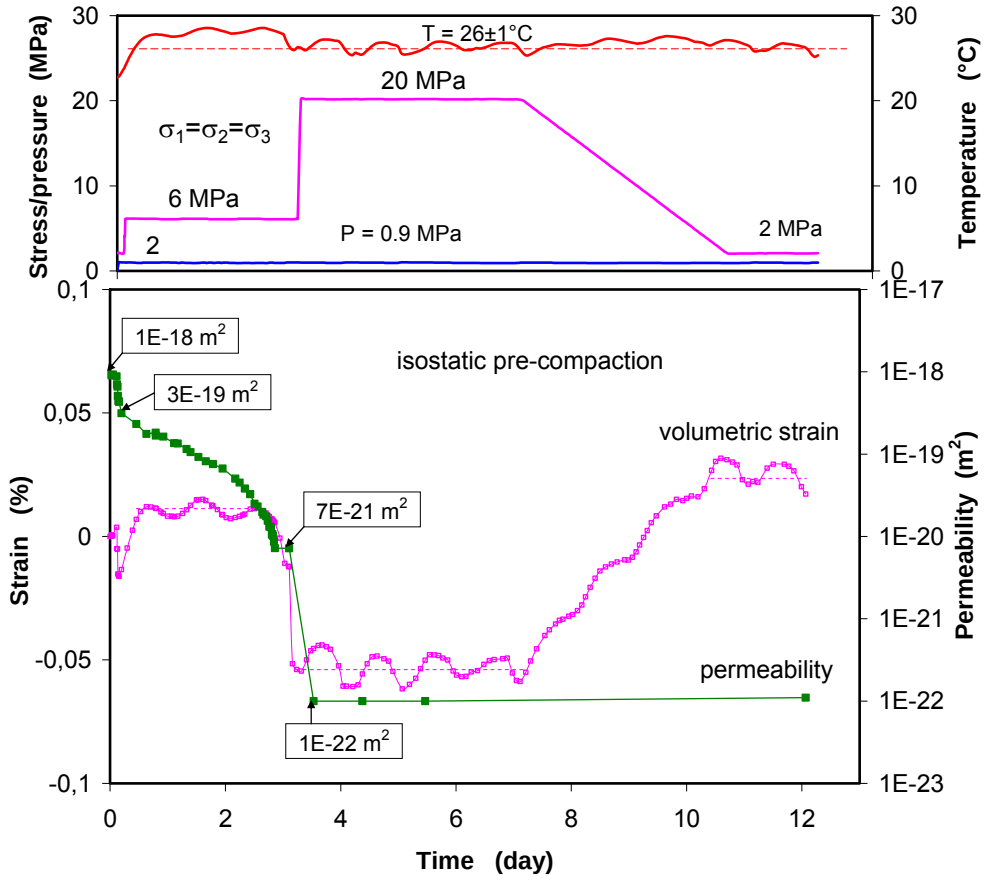

Fig. 3.3 Volume and permeability changes of a salt sample under isostatic compaction

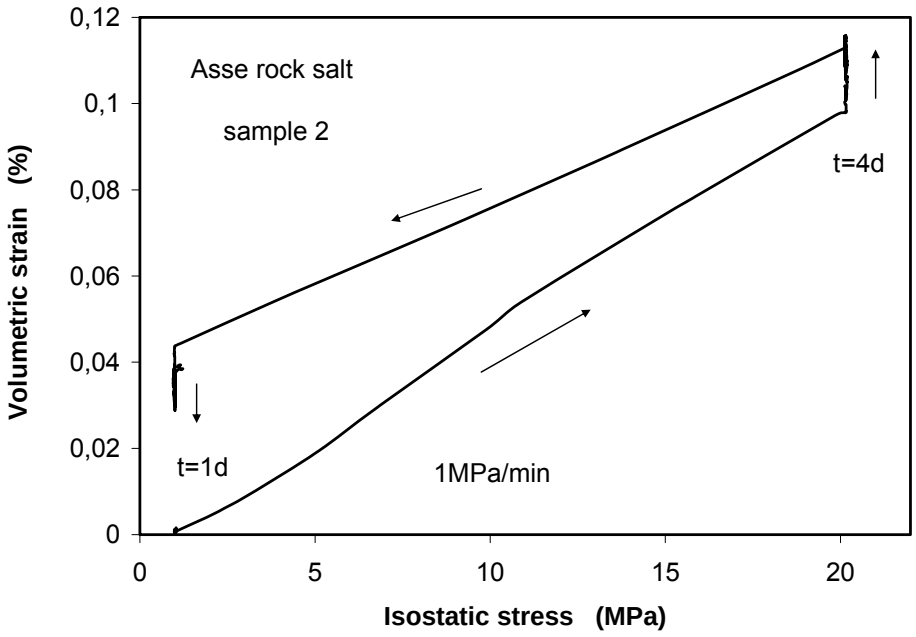

Fig. 3.4 Isostatic pre-compaction behaviour of a salt sample

3.1.2.2 Deviatoric compression

Following the pre-compaction and keeping the radial stress constant, the axial stress was increased at a low strain rate of $\dot{\varepsilon}_a$ = 1·10^{-7} s^{-1}. The measured stress-strain curves and the permeability changes due to the deviatoric loading are illustrated in fig. 3.5 for sample 1 at σ_r = 2 MPa and fig. 3.6 for sample 2 and 3 at σ_r = 1 MPa.

As mentioned before, the volumetric strain was determined directly by the balance calculation of the confining oil in the cell and indirectly by the radial strain measured with strain gauges. A comparison of the ε_v–ε_a curves obtained by both the detecting methods indicates a good agreement in a small deformation range to ε_a ≈ 0.4 %. Beyond that, they diverge with further deformation because the salt cylinders at $\sigma_a > \sigma_r$ deformed more or less to a “drum shape” with a maximum cross section at the middle. This shape is a consequence of the friction resistance at the contact faces at top and bottom between sample and porous discs.

As the $\Delta\sigma - \varepsilon_a$ curve in fig. 3.5 shows, the deformation rate of sample 1 was increased to $\dot{\varepsilon}_a$ = 1·10^{-6} s^{-1} after a large strain of ε_a ≈ 6.0 % in order to create a great damage and an increase in permeability. This was only achieved by further decreasing the radial stress to 0.6 MPa. At a high deviatoric stress $\Delta\sigma = \sigma_a - \sigma_r$ = 34 MPa, close to the failure strength, a sudden increase of the permeability from 1·10^{-22} m^2 to 1·10^{-19} m^2 was recorded. It is to be noted that both end faces of the sample were directly covered with the porous discs and the high strain resistance by the rough surface of the discs resulted in local consolidation at the ends, which might be the reason for this largely delayed permeation. This effect was then minimised in the next two tests by application of thin sand or silicon layers at the top and bottom of the samples.

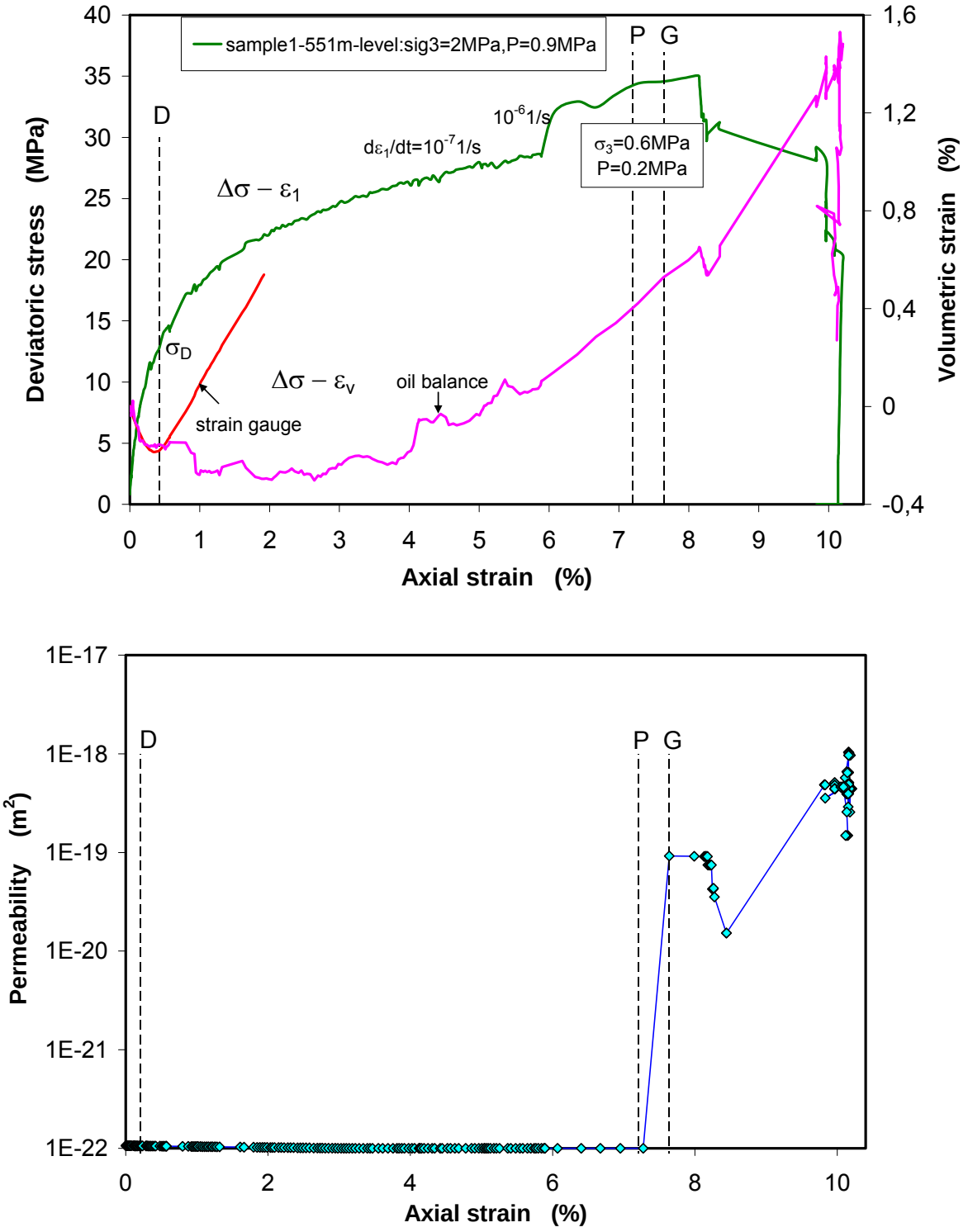

Fig. 3.5 Stress-strain-permeability behaviour of a salt sample deformed by deviatoric loading at confining stress of 2 MPa

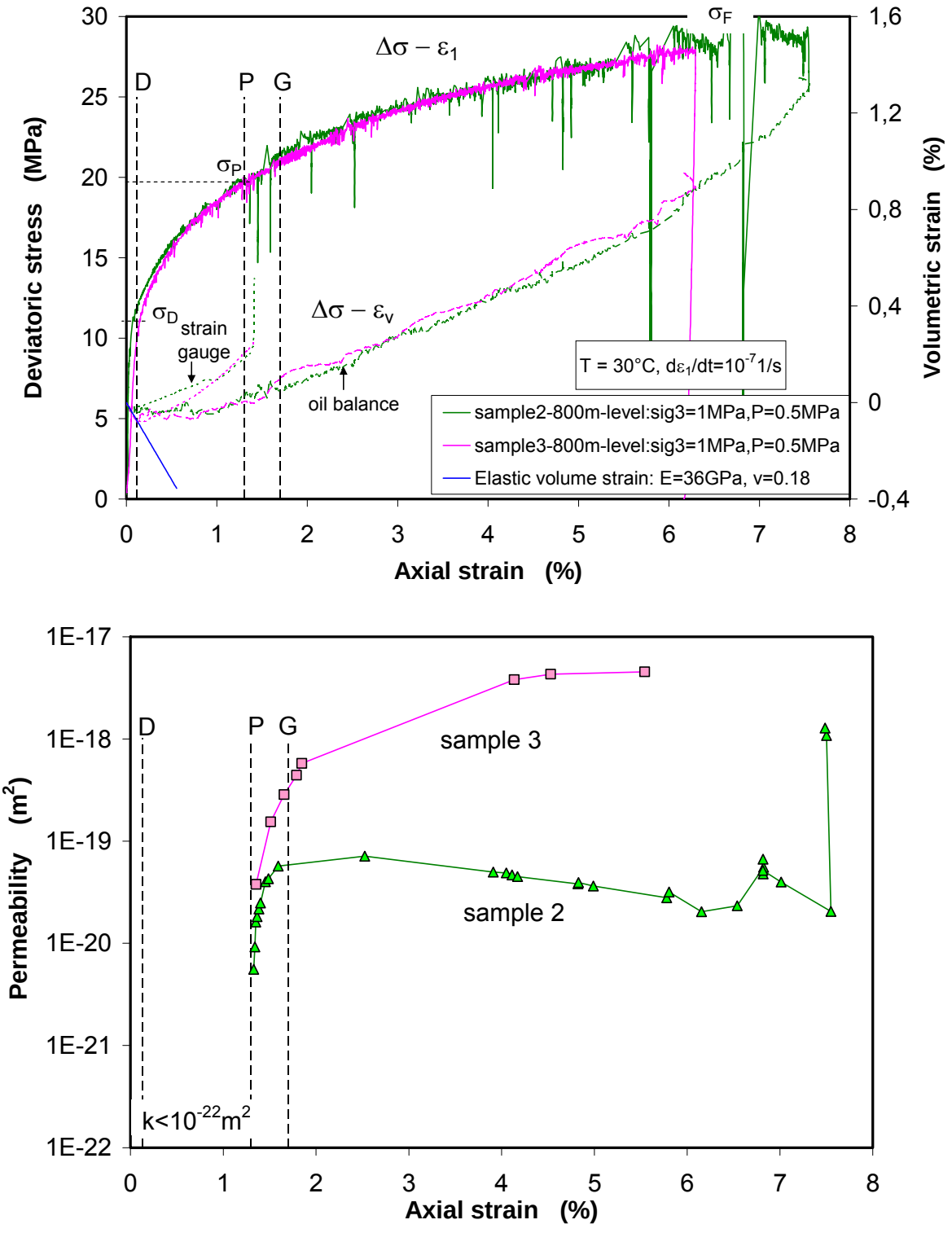

Fig. 3.6 Stress-strain-permeability behaviour of two salt samples deformed by deviatoric loading at confining stress of 1 MPa

The results obtained on samples 2 and 3 are summarized in fig. 3.6. First, one can clearly recognise that the stress-strain curves are excellently coinciding with each other. The typical stress-strain behaviour of rock salt under triaxial compression is also

well reproduced by the tests. The deviatoric stress-deformation and the damage-permeability behaviour of the salt samples may be successively described as follows:

1. The isostatic pre-compaction up to 20 MPa is mainly dominated by elastic closure of the pre-existing micro-cracks/pores (figs. 3.3, 3.4). The subsequent application of deviatoric stress to the pre-compacted samples produces only a small linear strain of ε_a < 0.1 % and then yields. The ε_v–ε_a curve departs from the elastic compaction and shows a minimum point at ε_a ≈ 0.13 % (marked by line D in the figure), i.e. the volume strain starts to transit from the compaction to dilatancy. The detail of the transition phase is illustrated in fig. 3.7. At this onset point of dilatancy, the volume strain reaches the minimum at ε_v = 0.1 % while the deviatoric stress is determined to $\Delta\sigma_D$ = 10.5 MPa.

2. From the dilatancy point, increasing the deviatoric stress results in opening and growth of micro-cracks along the grain boundaries and thus the volume increases. But the individual micro-cracks may be isolated at the beginning, which does not generate pathways, so that a permeability increase is impossible. As the micro-cracks growth to coalescence and connection, flow paths will build up through the sample. This critical point is defined as percolation threshold (/ALK 07/, /ALK 08/). At this point (P), the permeability starts to increase rapidly. The present and other experiments made by Pusch et al. /PUS 02/ and Düsterloh & Lux /ALK 08/ indicate certain distances from the dilatancy point (D) to the percolation threshold (P), depending on the confining stress. For the tested samples shown in fig. 3.6, the distance from D to P should be characterised not only by the stress difference (σ_P - σ_D = 20 – 10.5 = 9.5 MPa), but also by the dilatancy increase (in our case ε_{vP} - ε_{vD} = 0.012 %) and even the axial strain (ε_{aP} - ε_{aD} = 1.2 %). This test finding of difference between dilatancy and percolation thresholds seems to reject the assumption of the dilatancy concept saying that the permeability increase begins at the onset point of dilatancy (coincidence of both points D and P).

3. Beyond the percolation threshold, more and more cracks are rapidly interconnected without significant crack opening (indicated by small dilatancy increase). The connection of cracks forms pathways and therefore results in a drastic increase in permeability. As a full network is reached, the rapid increase of the permeability slows down. This turnover point may be defined as the termination of the percolation process, which is remarked by line G in fig. 3.6. As observed, the major part of the damage-induced permeability increase by several orders of magnitude takes place during this short percolative permeation phase. In case of

our tests, below the percolation threshold (P) no permeability changes were detected, and after transgressing the percolation threshold the permeability increased instantly from 10^{-22} m^2 to $5 \cdot 10^{-20}$ ~ $5 \cdot 10^{-19}$ m^2 at the end of the percolation process (G).

4. After the full connection of the micro-cracks, increasing the deviatoric stress opens the connected cracks further, forming macro-fractures until failure. In this phase, the permeability of fractured rock is mainly dependent on fracture geometry and topology characterised by the fracture aperture and roughness of the fracture walls (/SCH 07/, /ALK 08/). The changes of the fracture geometry just result in a slow increase in permeability. For instance, the permeability measured on sample 2 increases from $5 \cdot 10^{-19}$ to $5 \cdot 10^{-18}$ m^2 even with a large dilatancy increase of $\Delta\varepsilon_v$ = 0.9 % and axial strain of $\Delta\varepsilon_a$ = 4.5 %.

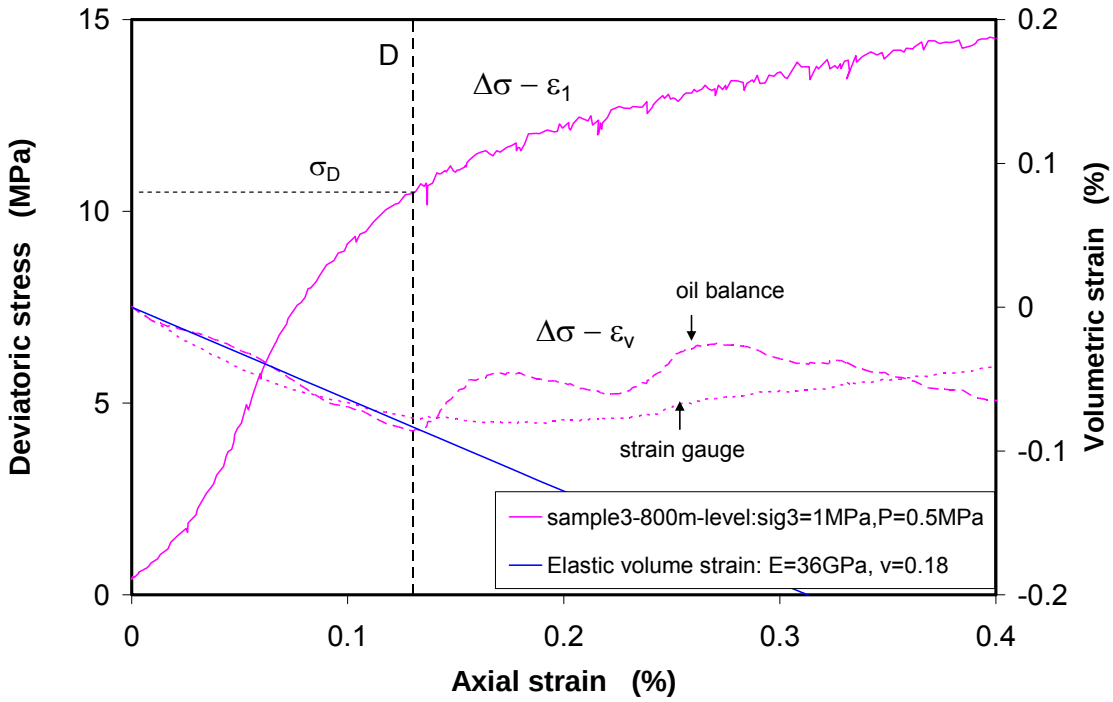

Fig. 3.7 Determination of dilatancy point by detecting the minimum of volumetric strain

Two points are to be noted in regard to our tests. The first one is that the deviatoric loading phase was terminated as significant damage was observed. The other point is that the permeability observed on sample 2 after the percolation phase decreases slightly with deviatoric deformation. The k-values are even one to two orders of magnitude lower than that of sample 3. The difference might be induced by the

different test configurations. On sample 2 thin silicon strips were placed between the load pistons and the end faces, which might be so highly compressed that the part of the interface could be sealed and gas tight. As a consequence, the gas injection might only cover the rest of the cross section and the k-data would therefore be underestimated.

3.1.2.3 Re-compaction

The previously damaged samples were isostatically re-compacted. Figure 3.8 presents the permeability change on sample 1 in relation to the porosity. The re-compaction was conducted from 1 to 2.3 MPa at a low loading rate of 0.4 MPa/d, corresponding to a volumetric strain rate of $\dot{\varepsilon}_v \approx 3 \cdot 10^{-8}\ s^{-1}$. The gas permeability was measured during the re-compaction phase at pressure of 0.6 MPa. The permeability-porosity data are fitted by the power law $k = k_o \cdot \phi^n$ with two sets of parameter values. Because of the relatively large data scatter, the curve slope (n-value) is hard to determine. The high power n = 8 seems to fit the data well.

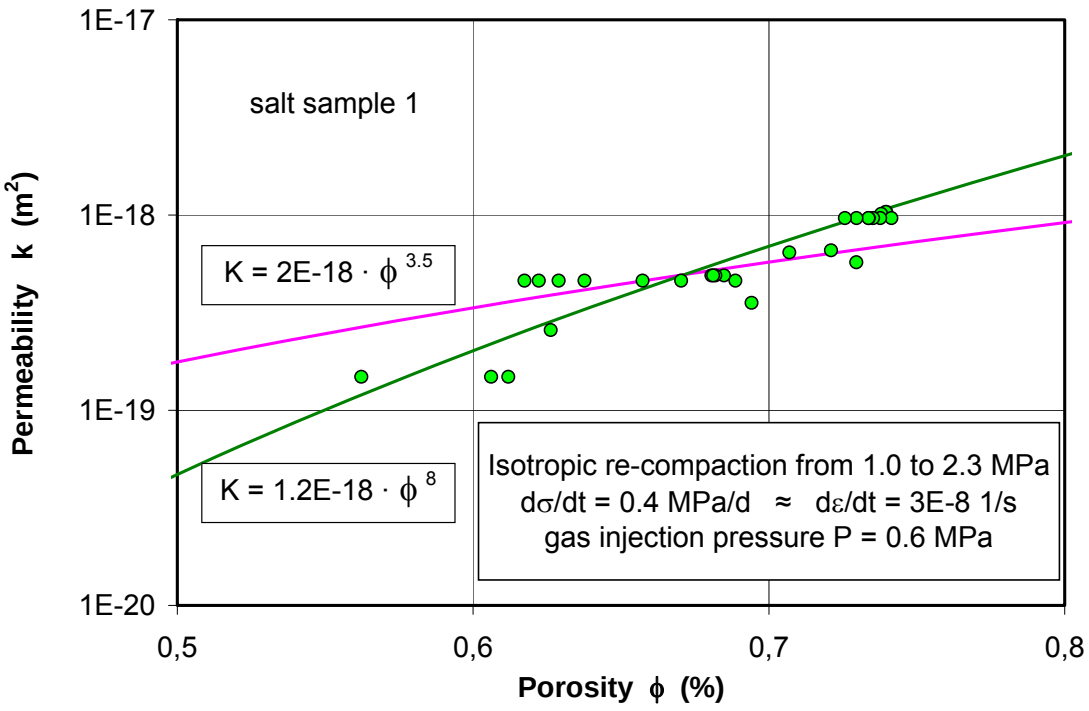

Fig. 3.8 Permeability–porosity relation obtained by re-compaction of damaged salt

Figure 3.9 shows the porosity and permeability changes measured by re-compaction of the damaged sample 2 as a function of the confining stress. Increasing the confining

stress from 1 to 14 MPa led to a reduction of the porosity from ϕ = 0.73 % to 0.65 % and a strong decrease of the permeability from $1 \cdot 10^{-18}$ m^2 to $6 \cdot 10^{-21}$ m^2. Under the constant stress of 14 MPa, the porosity decreased with time to 0.55 % after 3 days, while a permeability change could not be detected. During the unloading phase, the pore volume was partly expanded to a value of ϕ = 0.59 % at 1 MPa. This resulted in an increase of the permeability to $8 \cdot 10^{-20}$ m^2. The *k*-values measured along the unloading path are about one order of magnitude lower than that obtained along the previous loading path. The decreased porosity and permeability after unloading indicates a pronounced plastic closure of the fractures produced by the previously applied deviatoric stress.

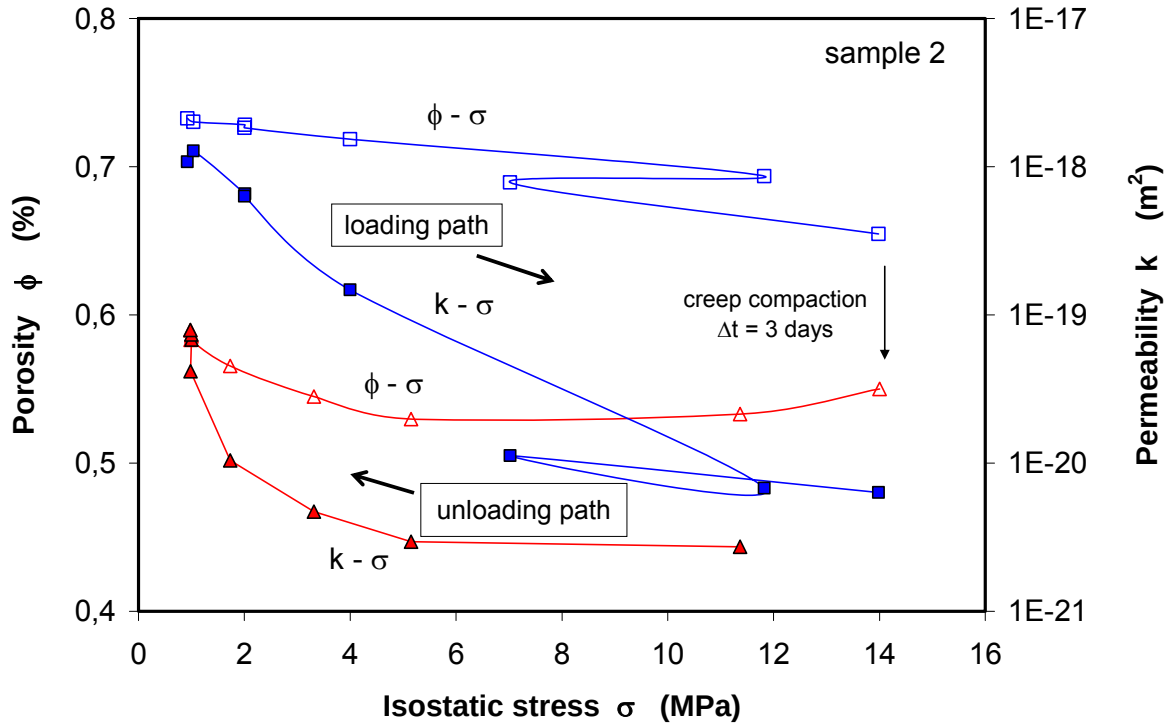

Fig. 3.9 Porosity and permeability changes by re-compaction of damaged salt

3.2 Large-scale tests

A laboratory benchmark test (BMT) was envisaged to be performed on a large salt hollow cylinder, in which relevant THM conditions, especially the evolution and recovery of the EDZ around HLW in rock salt such as excavation, backfilling, heating and cooling, had to be simulated. The coupled THM processes occurring in the sample were to be numerically simulated by the project partners for validation of the constitutive models and computer codes.

3.2.1 Tested material

The reference salt material, Asse Speisesalz, was used in the tests because of the existence of a sound database available. Two big cores of 300 mm diameter and ~ 0.7 m length and normal-sized samples of D = 90 mm / L = 200 mm were provided by BGR to GRS for laboratory tests, as shown in fig. 3.10. They were extracted from the 800-m level of the Asse salt mine. The porosities of the samples varied in a range from 0.1 % to 0.4 %. A very low water content of 0.01 % was measured by drying at 105 °C.

core 1 *core 2*

Fig. 3.10 Large salt cores of 300 mm diameter and ~ 0.7 m length from the Asse mine

3.2.2 Test design

The large-scale test was originally designed to be carried out on a hollow salt cylinder of 280 mm diameter and 525 mm length with an axially-drilled central borehole of 100 mm diameter using the GRS's big triaxial apparatus. The testing apparatus comprises a triaxial cell designed for a maximum cell pressure of 50 MPa and a

maximum axial load of 70 MPa, a heating system for generating temperature up to 150 °C, a hydraulic system for fluid supply up to 15 MPa, a data acquisition system, and various instruments for measurement and control of testing parameters, such as axial/radial stress, axial/radial strain, gas/water injection pressure, inflow and outflow, and temperature.

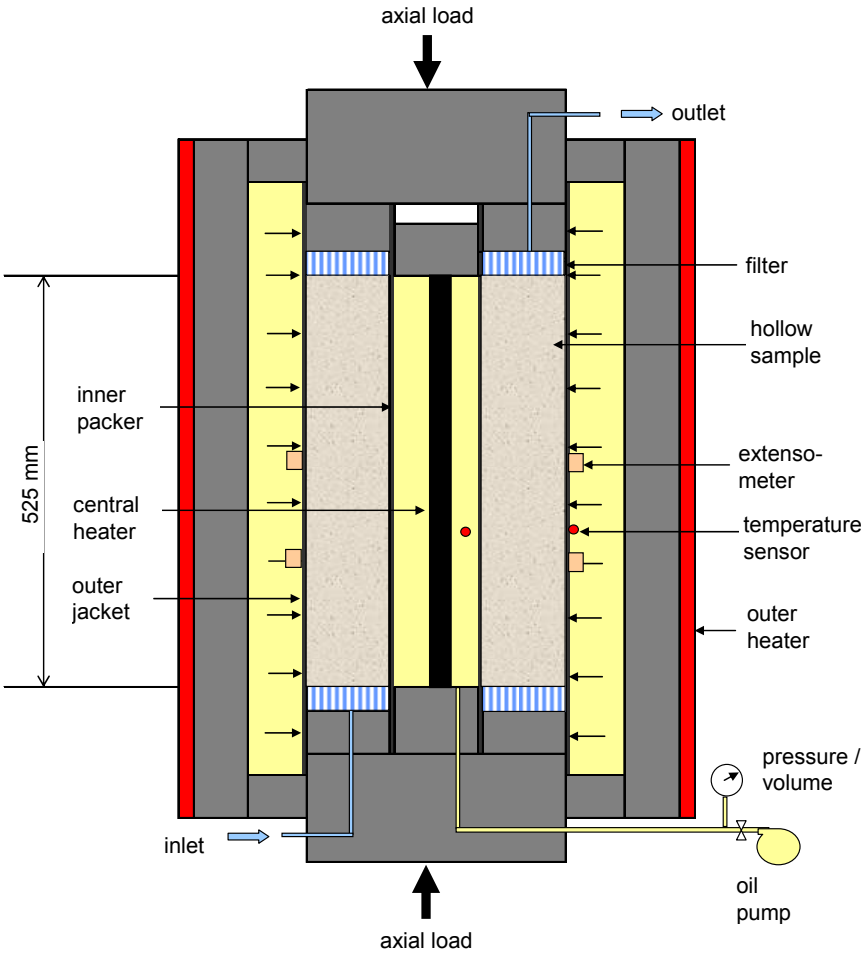

Fig. 3.11 Principle of the large-scale THM-test on a hollow salt cylinder

Figure 3.11 shows schematically the sample assembly for the test. An inflation packer is installed in the borehole for simulating the backfill support, which allows a maximal pressure of 15 MPa and is controlled by a precise syringe pump with oil supply. The external stress around the borehole is applied by regulating the outer axial load and lateral pressure in the cell. Thermal loading is simulated by means of the outer heater mounted around the outer surface of the cell. During the test, outer radial strain is recorded by a circumferential extensometer, while axial strain is measured by a LVDT deformation transducer mounted in the lower piston outside the cell. Additionally, borehole convergence or divergence is monitored by measuring changes of the oil

volume in the central packer. The temperature is recorded by two PT100 sensors in the borehole and on the outer surface of the sample, respectively. Permeability changes in the salt cylinder are monitored in axial direction by injecting nitrogen gas to the bottom at constant pressure and by measuring outflow at the top. The above mentioned parameters are evaluated according to the following definitions:

- Axial stress:

$$\sigma_a = \frac{F}{A_{ring}} = \frac{4 \cdot F}{\pi\left(D^2 - d^2\right)} \tag{3.2}$$

where F = axial force, A_{ring} = cross section of the hollow sample, D = outer diameter of the sample, d = diameter of the borehole

- Outer radial stress: σ_r = applied oil pressure in the triaxial cell

- Inner pressure in the borehole: p = applied oil pressure in the inner packer

- Axial strain:

$$\varepsilon_a = \frac{\Delta L}{L_o} = \frac{L_o - L}{L_o} \tag{3.3}$$

where L = length of the sample, Lo = initial length of the sample

- Outer radial strain:

$$\varepsilon_r = \frac{\Delta D}{D_o} = \frac{D_o - D}{D_o} \tag{3.4}$$

where D = outer diameter of the sample, D_0 = initial value of the outer diameter

- Borehole convergence:

$$\varepsilon_c = \frac{\Delta d}{d_o} = \frac{d_o - d}{d_o} = 1 - \sqrt{\frac{V_b / L}{V_{bo} / L_o}} \tag{3.5}$$

where d = diameter of the borehole, d_0 = initial diameter of the borehole, V_b = volume of the borehole, which is determined by measuring the oil volume in the packer, V_{b0} = initial value of the borehole volume

- Volumetric strain:

$$\varepsilon_v = \frac{\Delta V}{V_o} = \frac{V_o - V}{V_o} = 1 - \frac{L}{L_o}\frac{\left(D^2 - d^2\right)}{\left(D_o^2 - d_o^2\right)} \tag{3.2.5}$$

- Gas permeability:

$$k = 2\mu \frac{p_o \cdot Q}{\left(p_g^2 - p_o^2\right)} \cdot \frac{L}{A_{ring}} \tag{3.2.6}$$

where k = gas permeability (m^2), Q = flow rate of the gas (m^3/s), μ = dynamic viscosity of the gas (Pa·s), L = sample length (m), A_{ring} = the section of the hollow sample (m^2), p_0 = atmospheric pressure (Pa), p_g = injection pressure (Pa)

A general test procedure was proposed by the project partners in the following steps:

1. Determination of initial state of the sample
2. Pre-consolidation of the sample at increased compressive load to minimize the micro-cracks induced by sample preparation
3. Simulation of borehole excavation by reduction of inner pressure in the borehole
4. EDZ extension by introducing an outer stress deviator, if the previous step does not lead to a significant permeability increase
5. Re-compaction by increasing external confining stress and inner pressure in the borehole
6. Heating the sample by increasing the temperature from 30 °C to 70 °C
7. Cool-down to 30 °C
8. Unloading, dismantling and inspection of the sample

Obviously, conducting such a very complicated experiment is a great challenge for the experimenter. A programme was proposed to be performed with two large salt hollow cylinders: The first one serves to test the functions of the testing system and to obtain first experiences with sample preparation, instrumentation, and feasibility of the techniques; and the second one is used for the providing the data for modelling. In reality, the designed test procedure was more or less modified. Especially, the second large-scale test was followed by two additional triaxial compression tests (TC) on normal-sized samples of 100 mm diameter and 190 mm length which were used for the benchmark simulation.

3.2.3 First large-scale test

The first test was carried out on a big hollow salt cylinder of D = 280 mm / d = 100 mm / L = 525 mm. The initial porosity was determined to be ϕ = 0.4 %. Figure 3.12 shows photos of the prepared sample, the packer installed in the central borehole and a filter plate covering the sample end face. One can see that a macro-crack appeared on the surface along the sample length, which was produced during drilling of the central borehole. In order to gather a homogeneous distribution of gas flow and to reduce friction resistance across the end faces, thin teflon sheets with small holes were inserted between the sample and the filter platen at the bottom and the top. It is to be noted here that the sample was actually prepared too long so that the central borehole covered not only the jacket but also some part of the upper steel cap of the inner packer. This faulty assembly was unfortunately recognized too late during the test. As a consequence, the test had to be finished early.

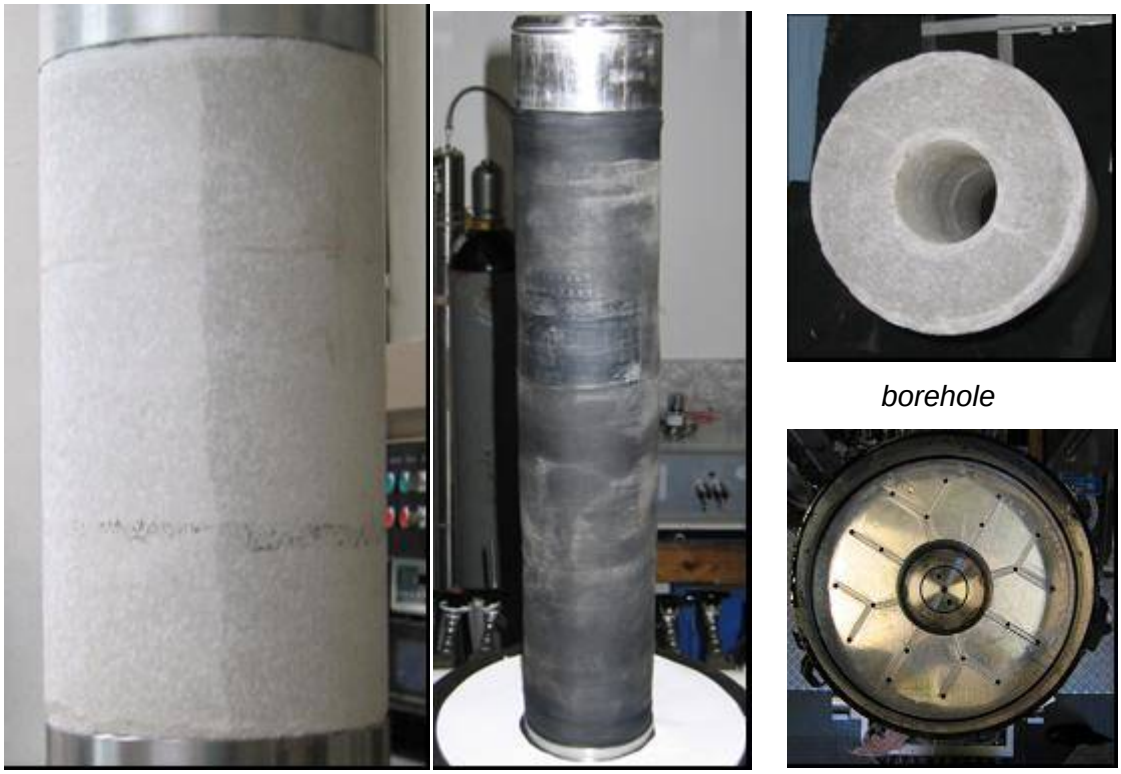

Fig. 3.12 Photos of a large hollow salt sample 1, inner packer and filter plate

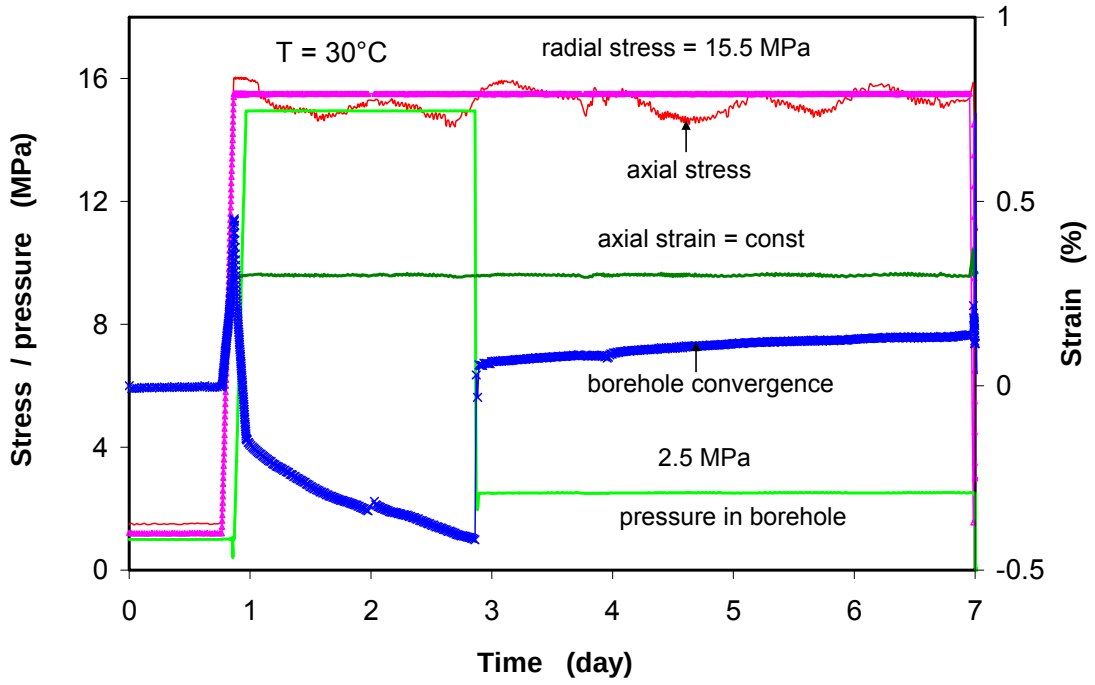

(a) response of borehole convergence to the loading

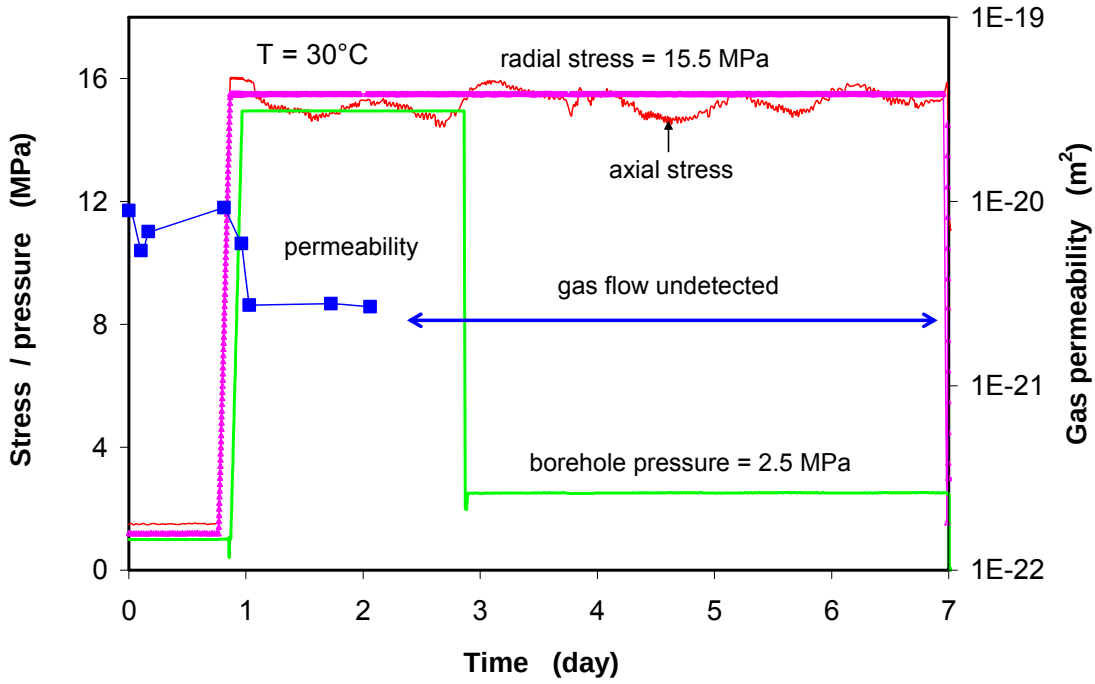

(b) response of gas permeability to the loading

Fig. 3.13 Results of the first part of the first large-scale test

Figure 3.13 illustrates the measurements of borehole convergence (fig. 3.13 (a)) and gas permeability (fig. 3.13 (b)) in response to the applied confining stresses and the borehole pressure. The test was started at a low isostatic stress of about 1.2 MPa and

at temperature of 30 °C. A reconsolidation phase followed by successively increasing the axial stress to σ_a = 16 MPa, the radial stress to σ_r = 15.5 MPa and the inner pressure to p = 15 MPa at a rate of 6 MPa/h. The first external loading led the salt to deform into the borehole. The convergence was then recovered by the subsequent increase of the borehole pressure. On the other hand, the increase of the borehole pressure reduced the permeability from the initial value of $1 \cdot 10^{-20}$ m^2 to $3 \cdot 10^{-21}$ m^2. Following the reconsolidation phase, the borehole was excavated by decreasing the borehole pressure to 2.5 MPa, resulting in a sudden convergence of the borehole which further continued with time. Unexpectedly, no gas flow could be observed during the borehole excavation phase. Possible failure of the gas flow system was suspected, but no failure was found during an inspection after 7 days.

The test was restarted again at a low isostatic stress of $\sigma_a = \sigma_r = p$ = 1.2 MPa. After increasing the axial load to 5 MPa shortly, the axial strain was controlled to be unchanged, i. e. $\Delta\varepsilon_a$ = 0. At p = 1.2 MPa and $\Delta\varepsilon_a$ = 0, the outer radial stress was increased to 20 MPa for 4 days and then to 30 MPa for another 2 days, leading to a borehole convergence and an increase of the axial stress (fig. 3.14).

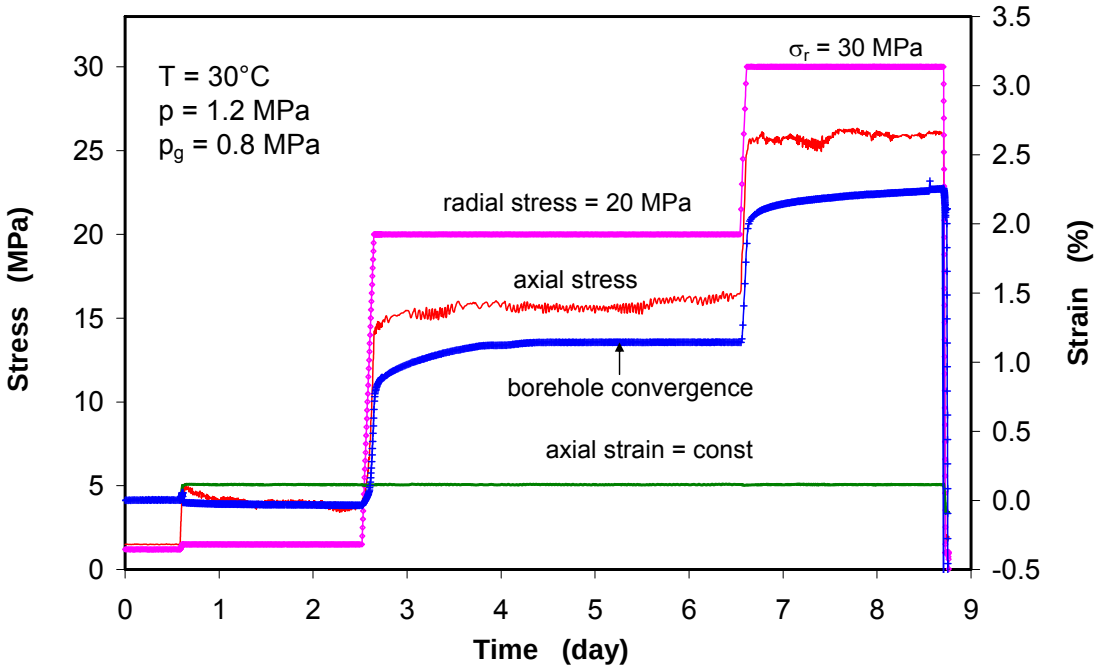

Fig. 3.14 Results of the second part of the first large-scale test

But there was no gas outflow observed at an injection pressure of 0.8 MPa. Removing the sample from the cell again, a tight contact between the sample and the steel cap

was recognized, being the reason for no gas flow through the sample. After dismantling, the macro-crack on the sample surface could still be identified (fig. 3.15).

Fig. 3.15 Photos of the large hollow salt sample 1 after dismantling

3.2.4 Second large-scale test

The second large-scale test followed with another hollow salt cylinder of D = 280 mm / d = 102 mm / L = 460 mm. The sample length of 460 mm allowed the central borehole wall to contact only with the packer jacket but not with the steel caps, and the relatively wide borehole made the installation of the packer easier. Figure 3.16 shows the test layout and photos of the sample. The drilling of the borehole produced some cracks, most of which appeared on the sample surface, particularly in the central part. They did not penetrate through the sample. The initial porosity was determined to be ϕ = 0.3 %.

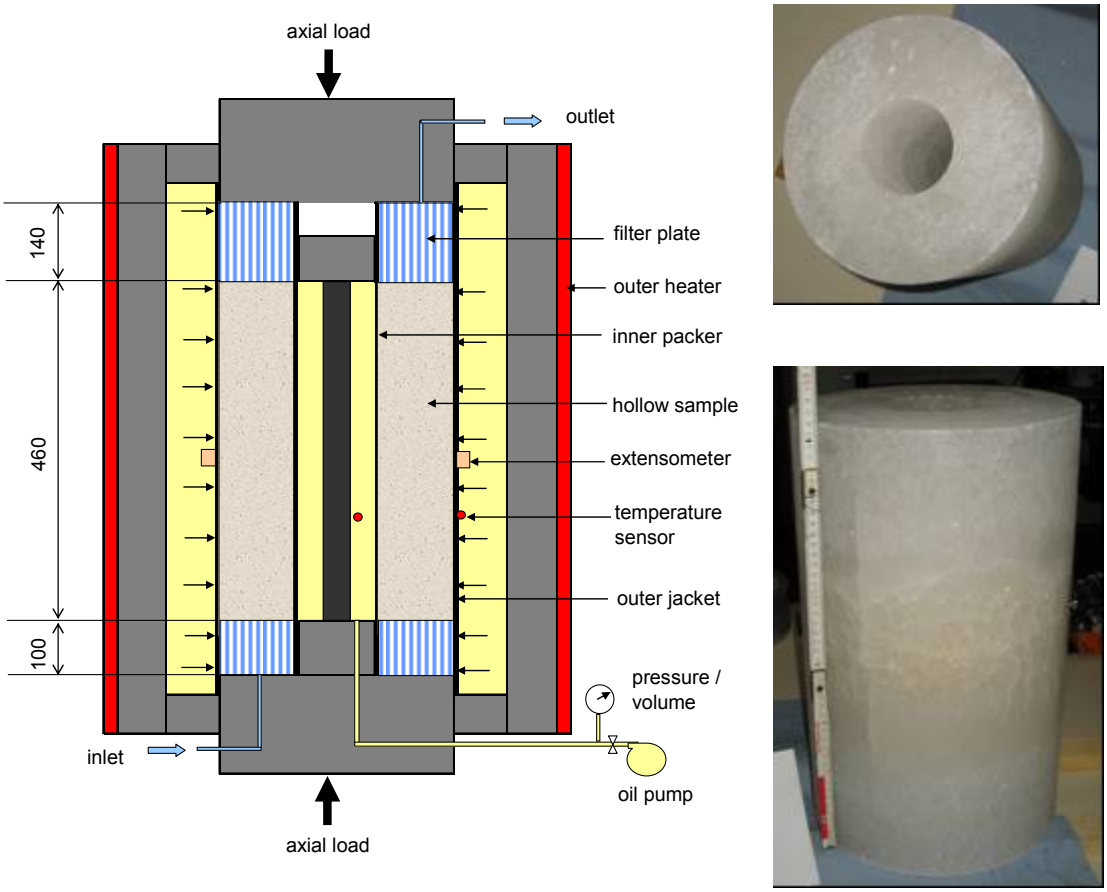

Fig. 3.16 Layout of the large-scale test 2 on a hollow salt cylinder (D = 280 mm / d = 102 mm / L = 460 mm)

Figure 3.17 shows the test procedure performed in six phases with the respective boundary conditions, i.e. initial stabilization, borehole excavation, damage intensification, re-compaction, heating and cooling phases. Responses of borehole convergence and gas permeability are illustrated in fig. 3.18. Test results are described and interpreted as below.

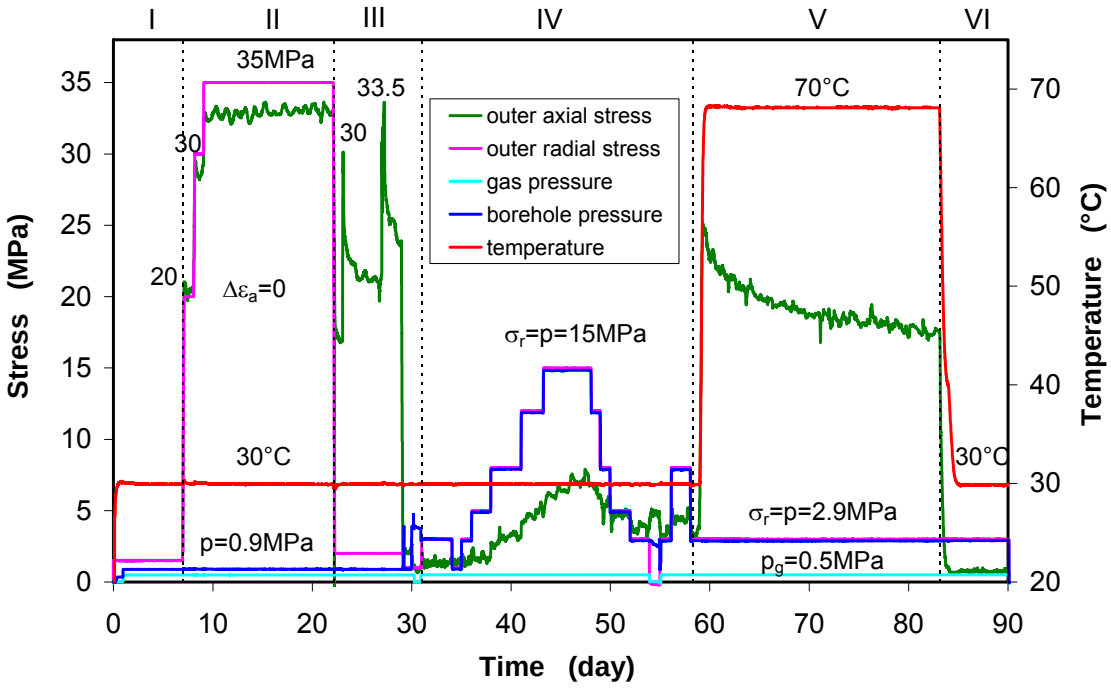

Fig. 3.17 Loading history applied to a large hollow salt cylinder in the BMT test

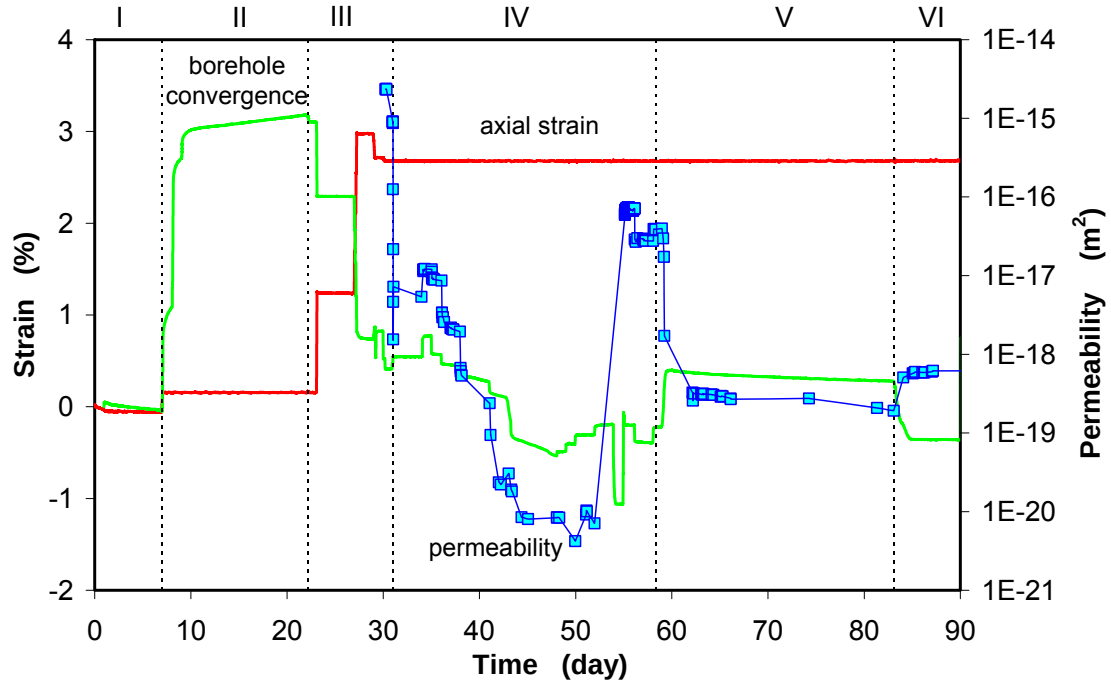

Fig. 3.18 Responses of borehole deformation and gas permeability to the loading

1. Initial state: The test started from the initial conditions of axial stress σ_a = 1.5 MPa, radial stress σ_r = 1.5 MPa, borehole pressure p = 0.9 MPa, gas inlet pressure at

the bottom p_g = 0.5 MPa, gas outflow pressure at the top p_o = atmosphere (0), and temperature T = 30 °C. The stabilization phase lasted over t = 7 days.

2. Borehole excavation: Without pre-consolidation as planned, the borehole excavation was simulated by increasing the axial stress to σ_a = 20.8 MPa and the radial stress to σ_r = 20 MPa under the borehole pressure p = 0.9 MPa. A load rate of 6 MPa/h was applied. The axial strain reached to 0.2 % and then was fixed, i. e. $\Delta\varepsilon_a$ = 0. The external stress corresponds to the lithostatic pressure in a salt formation at a depth of ~ 800 m. The compression resulted in a borehole convergence of 1.1 % (fig. 3.18). A damaged zone around the borehole should have been generated. But unexpectedly, no gas outflow parallel to the cylinder axis could be observed. In order to intensify the EDZ, the outer radial stress was subsequently increased to σ_r = 30 MPa and 35 MPa. Correspondingly, the borehole converged to 3.0 % and continued to 3.15 % over the following creep phase of 11 days. But still no gas outflow could be detected.

3. EDZ-intensification: In order to create pathways, the outer radial stress was lowered to 2 MPa and then the outer axial stress was stepwise elevated at a strain rate of 10^{-6} s^{-1}. At each of the stress levels of σ_a = 23.5, 30 and 33.5 MPa, a relaxation phase with fixed axial strain ($\Delta\varepsilon_a$ = 0) followed, during which the axial stress dropped down (fig. 3.17). At the axial stress σ_a = 33.5 MPa, an axial compression of 3.0 % was recorded and the borehole convergence recovered to 2.5 % (fig. 3.18). Since the upper limit of the testing system for axial strain was met but still no gas outflow occurred, a “fracturing” process had to be carried out for generating pathways. Figure 3.19 shows this “fracturing” phase in more detail. After reducing the axial stress to σ_a = 2 MPa (then $\Delta\varepsilon_a$ = 0) and radial stress to σ_r = 1 MPa, the borehole pressure was increased rapidly to p = 3.8 MPa. But this did not produce gas outflow. After decreasing the confining stresses again to σ_a = 1 MPa (then $\Delta\varepsilon_a$ = 0) and σ_r = 1 MPa, the second increase of the borehole pressure to p = 4.7 MPa caused a drastic gas outflow. The corresponding permeability was quite high ($2\cdot10^{-15}$ m^2). Immediately after gas break-through, the borehole pressure was regulated to the same level of 3 MPa as the outer radial stress, at which a sudden reduction of the permeability to $5\cdot10^{-18}$ m^2 was detected.

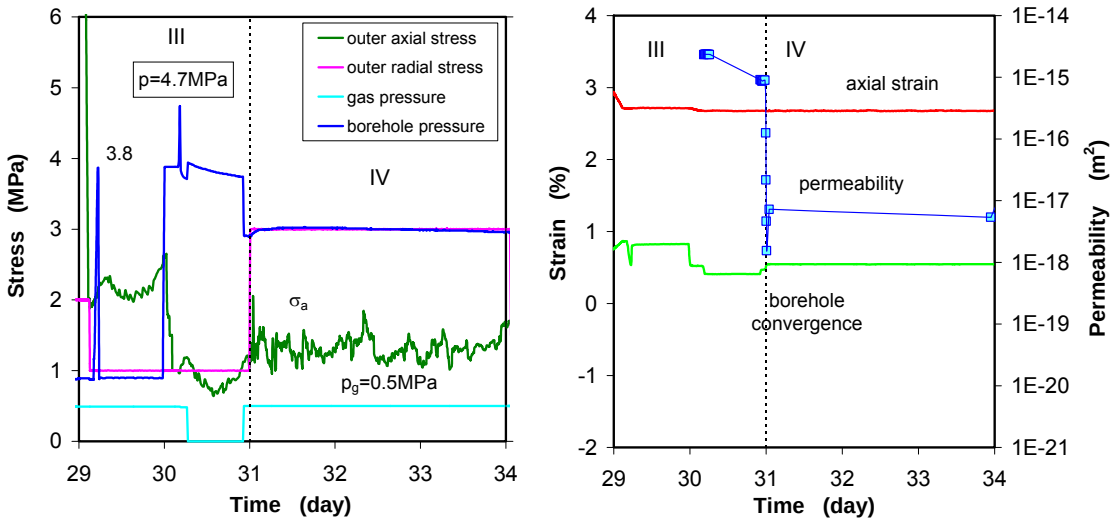

(a) borehole pressure *(b) deformation / permeability*

Fig. 3.19 Details of fracturing by increasing the inner pressure in the borehole

4. Re-compaction: At $\Delta\varepsilon_a$ = 0, the outer radial stress and the borehole pressure were simultaneously increased to investigate the sealing behaviour of the previously generated fractures. Possible permanent closure of the fractures was then examined by increasing the confining pressure. The loading was performed step by step to $\sigma_r = p$ = 1, 3, 5, 8, 12, 15 MPa, each step lasting for 1 to 3 days, respectively. The unloading followed to $\sigma_r = p$ = 12, 8, 5, 3 MPa, each step lasting for 1 day. Figure 3.2.9 shows that the re-compaction led to a significant reduction of the permeability from $1 \cdot 10^{-17}$ m^2 at p = 1 MPa to $8 \cdot 10^{-21}$ m^2 at p = 15 MPa. Even though the applied outer radial stress and the inner borehole pressure are the same, a borehole divergence was recorded to ~ 1.3 % at p = 15 MPa. Very interesting is that the subsequent decrease of the confining pressure down to 4.4 MPa did not give a rise in permeability. This finding strongly suggests a plastic closure of the fractures. The dependence of permeability change on the applied confining pressure is more clearly illustrated in fig. 3.20. Unfortunately, at the last step of $\sigma_r = p$ = 3 MPa, an interruption of the electric power supply resulted in a drop of the outer radial stress but the inner borehole pressure remained nearly at 3 MPa. The stress difference reopened the fractures, indicated by a sudden extension of the borehole and a drastic gas outflow. After reloading to $\sigma_r = p$ = 2.9 MPa at $\Delta\varepsilon_a$ = 0, the gas permeability was determined to $7 \cdot 10^{-17}$ m^2. Further increasing the radial pressure to 8 MPa led to a reduction of the permeability to $3 \cdot 10^{-17}$ m^2.

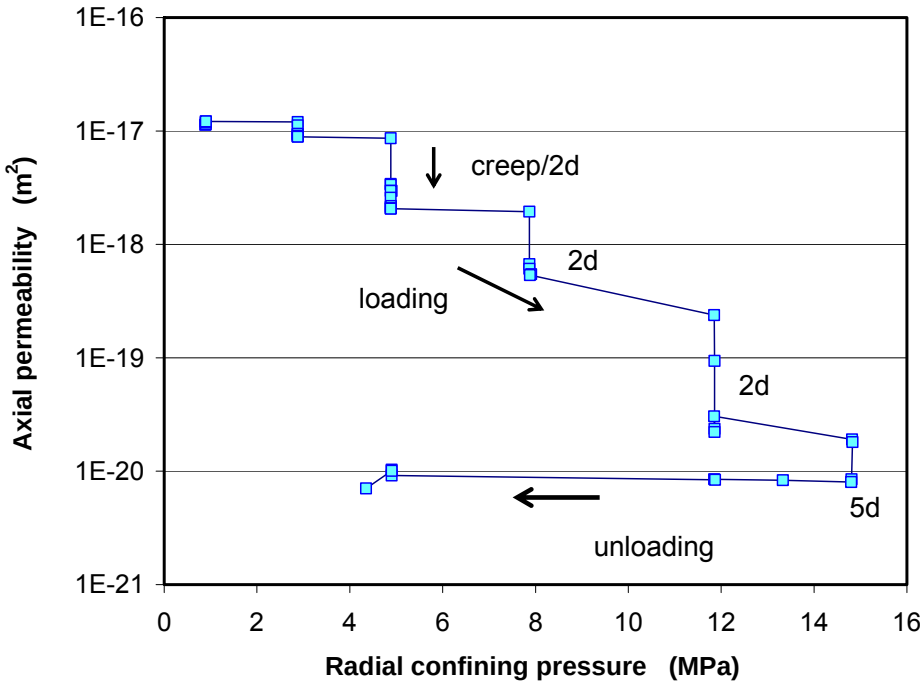

Fig. 3.20 Dependence of fracture permeability on confining pressure

5. Heating was performed by increasing the temperature from 30 °C to 70 °C in 1 day at $\Delta\varepsilon_a$ = 0 and σ_r = p = 2.9 MPa, thus, thermal expansion was not compensated. During the heating phase, a borehole convergence was observed, and the permeability decreased sharply from $4 \cdot 10^{-17}$ m^2 to $3 \cdot 10^{-19}$ m^2 (fig. 3.18). Within the following creep period of 3 weeks at 70 °C, the borehole diameter remained nearly constant, only a slight decrease in permeability was monitored, but the axial stress fell significantly. These observations indicate that the temperature-accelerated deformation contributes to the sealing of fractures in salt significantly.

6. Cooling phase followed by reducing the temperature down to 30 °C in 2 days. This resulted in a borehole divergence, a rapid reduction of the axial stress, but a slight increase of the permeability from $2 \cdot 10^{-19}$ m^2 to $6 \cdot 10^{-19}$ m^2, suggesting an insignificant effect of cooling on the sealing of fractures in salt.

7. Dismantling: Figure 3.21 compares the photos of the salt sample before and after testing. Most of the pre-existing micro-cracks on the surface disappeared, except the macro-fracture which penetrated along the sample length. The permeability changes observed might be dominated by this single fracture.

(a) before testing *(b) after testing*

Fig. 3.21 Comparison of the large hollow salt cylinder before and after testing

Obviously, the test procedure became very complicated due to the unexpected observations, particularly due to the lack of a gas outflow by the “borehole excavation” and the “EDZ-extension”. Reasons for these are unclear. Although a single or a few macro-fractures are often observed in the contour area around underground openings, the fractures generated in the sample certainly are very difficult to be handled in the modelling, especially for those models based on the continuum theories.

3.3 Benchmark tests

Since the only way to produce a permeability increase in the large-scale test had been to load the central borehole, with the consequence of producing a tension fracture instead of the expected microcracks attributed to dilatant behaviour of the EDZ, it was decided that for the benchmark calculation another test was needed. Due to the experiences of the hollow cylinder test and because no new large sample could be made available, two normal-scale samples of 100 mm diameter and 190 mm length

were used for new tests. The second of these experiments was chosen for the benchmark simulation, because a distinct permeability increase under deviatoric load could be detected.

3.3.1 Testing method

The normal triaxial compressive tests (TC) accompanying the large-scale tests were carried out on two salt samples of 100 mm diameter and 190 mm length in another triaxial apparatus at GRS' laboratory. The samples were extracted from the big core used for the second large-scale BMT test. They had an initial porosity of ~ 0.1 %. Figure 3.22 shows the schematic of the test and a photo of a sample. The apparatus essentially comprises a cell for a maximum pressure of 50 MPa. The sample can be heated by means of a heater mounted outside around the cell for temperatures up to 150 °C. While axial deformation is recorded by a LVDT deformation transducer installed inside the cell between the top and bottom, radial strain is measured by a circumferential extensometer mounted around the sample outside the jacket at mid-height. The volumetric strain can be approached by using an averaged diameter along the sample usually deformed in a "drum shape", as illustrated in fig. 3.23. In addition to the strain measurements, this apparatus is also equipped with an ultrasonic device and a hydraulic system for simultaneously detecting damage and sealing of the sample during various loading processes. The sample is inserted in a rubber jacket and located between two load pistons, in which piezo-electric P wave and S wave transducers and stainless steel tubes were introduced. To avoid effects of local consolidation near the sample ends on gas connection to the inlet and outlet, thin filter sheets of 1 mm thickness are inserted between sample and jacket in the upper and lower section of 35 mm. Nitrogen gas is introduced into the bottom at constant pressure and the gas outflow is recorded at the top by means of a burette. Taking the whole length and the total cross section of the sample into account, the gas permeability can only be approximately determined according to Darcy's law. A similar test procedure as that of the large-scale tests was designed for the additional tests. Thus, the focus in TC1 had been primarily on the mechanical side only, while TC2 dealt with all previously named aspects as preconsolidation, deviatoric stressing, re-compaction, heating and cooling.

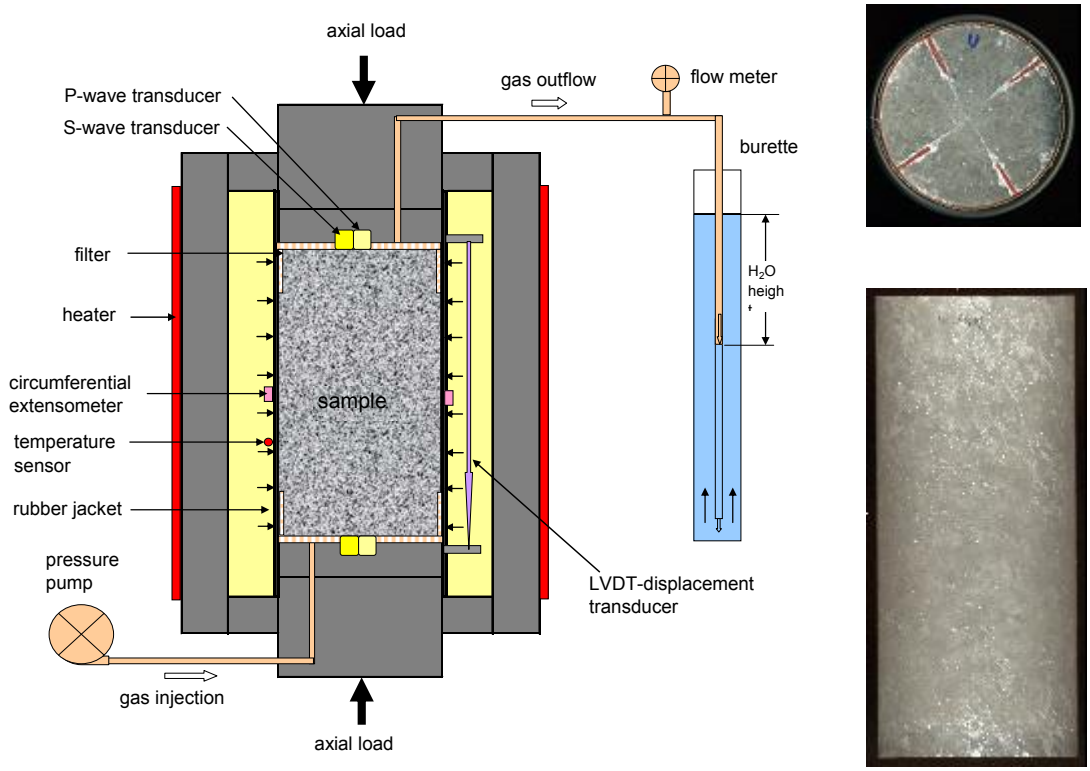

Fig. 3.22 Schematic assembly of a salt sample in triaxial cell

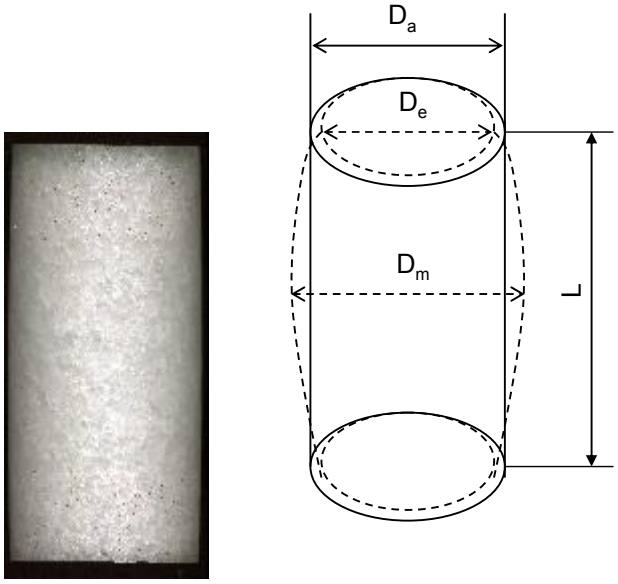

$$D_a = \frac{D_m + D_e}{2} = \frac{D_m(1+\lambda)}{2}$$

$$\lambda = \frac{D_e}{D_m}$$

$$\varepsilon_r = \frac{\Delta D_m}{D_{mo}}$$

$$\varepsilon_{r-a} = \frac{\Delta D_a}{D_{ao}} = \frac{1}{2}(1+\lambda)\varepsilon_r$$

$$\varepsilon_a = \frac{\Delta L}{L_o}$$

$$\varepsilon_v \approx \varepsilon_a + 2\varepsilon_{r-a}$$

Fig. 3.23 Determination of volumetric strain of a “drum shape” sample

3.3.2 TC test 1

TC test 1 was performed without filter sheets around the sample in the upper and lower sections. Filter sheets were inserted just between the pistons and the sample ends. Figure 3.24 presents the results of isostatic compression up to 30 MPa in terms of axial/radial/volumetric strains and P wave velocity as a function of the applied mean stress. The compression resulted in a volume reduction of ~ 0.1 %, which was only partly recovered after the unloading. The remaining part was contributed by the plastic closure of the pores. The wave velocity is less dependent on the load and kept nearly constant at $v_p \approx 4600$ m/s.

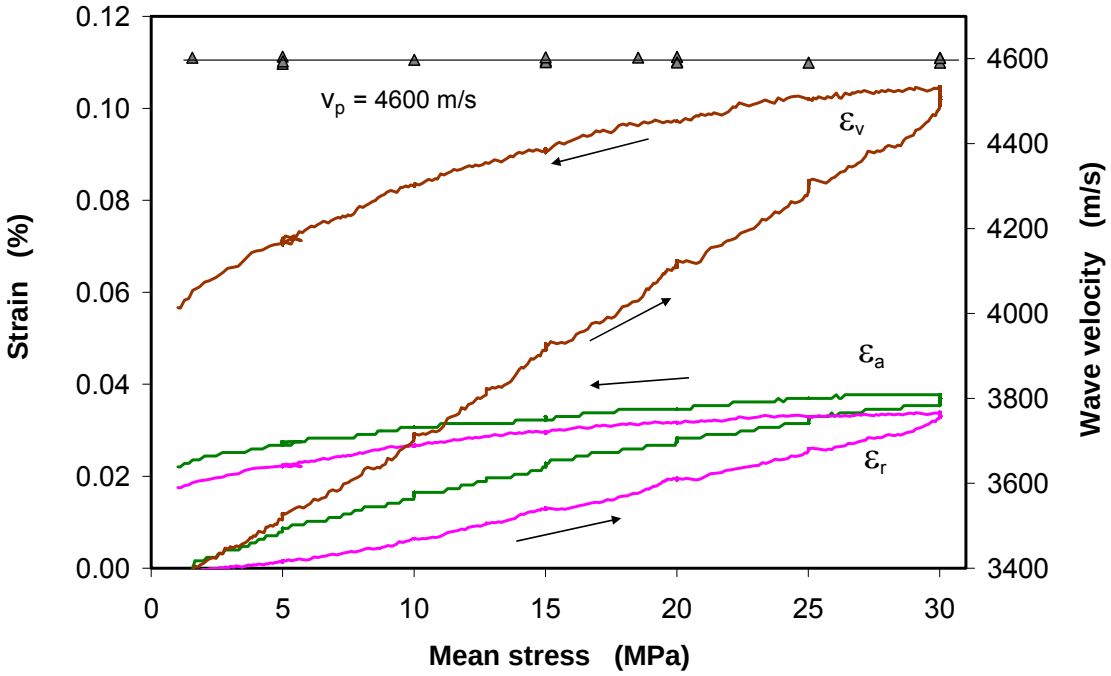

Fig. 3.24 Responses of deformation and wave velocity to isostatic compression on sample TC1

A deviatoric loading phase followed by stepwise increasing the axial stress to different levels of 12, 20, 25, 32 MPa at σ_r = 1 MPa. Figure 3.25 shows the evolution of strains as a function of the deviatoric stress ($\Delta\sigma = \sigma_a - \sigma_r$). At the stress level of $\Delta\sigma$ = 11 MPa over 3 days, the sample was slightly compacted to ε_v = 0.06 %. The subsequent stress increase initiated dilatancy due to the relatively large extension in radial direction. The dilatant stress lies in the range from 11 to 13 MPa. Further stressing increased more radial extension and dilatancy. Unfortunately, the upper limit of the radial strain measurement was reached at ε_r = -2.0 % at $\Delta\sigma$ = 28 MPa, yielding a volume increase

of ε_v = 1.0 %. At $\Delta\sigma$ = 31 MPa, the axial compressive strain reached to ε_a = 5.3 % without recording the radial/volumetric strains. The evolution of dilatancy or damage was also detected by the measurement of wave velocity. A very clear correlation between dilatancy and wave velocity was obtained (see fig. 3.26). The wave velocity decreases with the dilantacy. But unexpectedly, no gas outflow at injection pressure of 0.5 MPa could be detected during the test even though the dilatancy was rather large and close to failure. In order to check possible technical reasons for the lack of gas flow, the sample was removed from the cell. Cracks between salt grains were visually recognized on the sample surface (see the photo of the sample in fig. 3.23). The sample deformed quite homogeneously to a length of 180.8 mm, a diameter of 103.9 mm at the mid-height and 101.4 mm at the top and 101.6 mm at the bottom. But no technical problems were indentified.

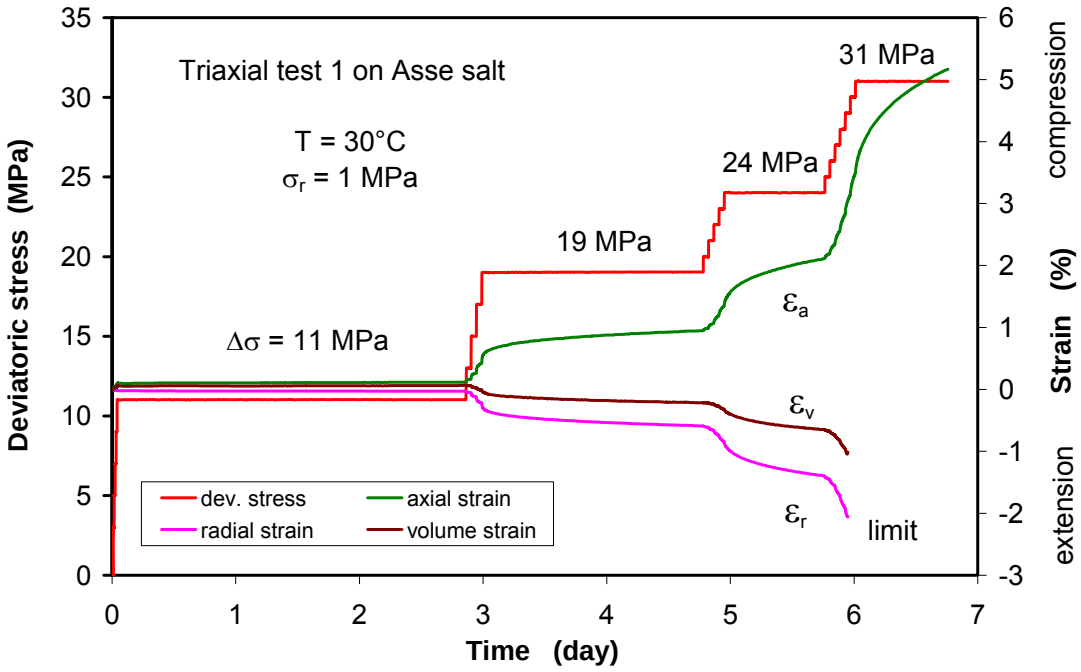

Fig. 3.25 Evolution of strains measured on sample TC1 under deviatoric stresses

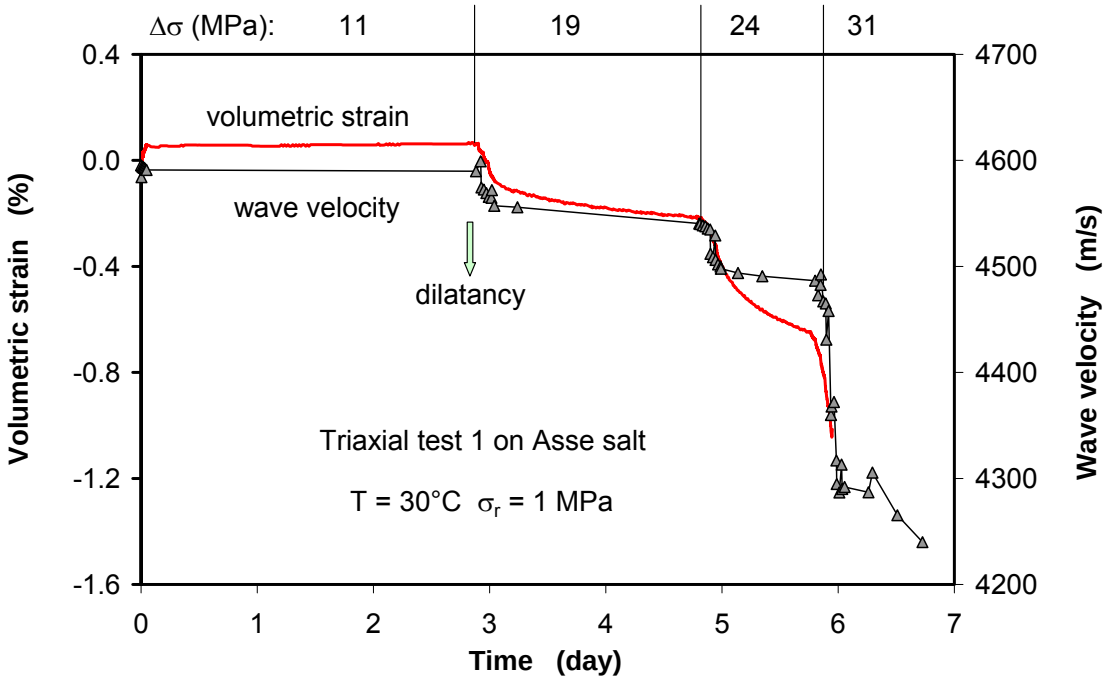

Fig. 3.26 Correlation between volumetric strain and wave velocity (TC1)

3.3.3 TC test 2

TC test 2 began directly with deviatoric loading without the preconsolidation as performed in TC test 1. At a temperature of 30 °C and a radial stress of 1 MPa, axial load was increased step by step to stress differences of $\Delta\sigma$ = 11 and 19 MPa. The resulting strains are depicted in fig. 3.27. A comparison with the data on sample TC1 (fig. 3.25) indicates an excellent agreement. Dilatancy in both samples took place by increasing the deviatoric stress from 11 to 13 MPa. The evolutions of dilatancy and wave velocity are also well correlated (fig. 3.28). Although the dilatancy gradually developed to ~ 0.2 %, no gas outflow could be observed at injecting pressure of 0.5 MPa. The creep phase at $\Delta\sigma$ = 19 MPa lasted over 5 days and was then unfortunately interrupted due to an electric power failure. An inspection after unloading indicted micro-fractures between grains on the sample surface, and the deformation was quite homogeneous to a length of 188.40 mm, a diameter of 100.70 mm at the mid-height and 100.26 mm at both the ends. Based on these data the porosity was determined to ϕ = 0.22 %.

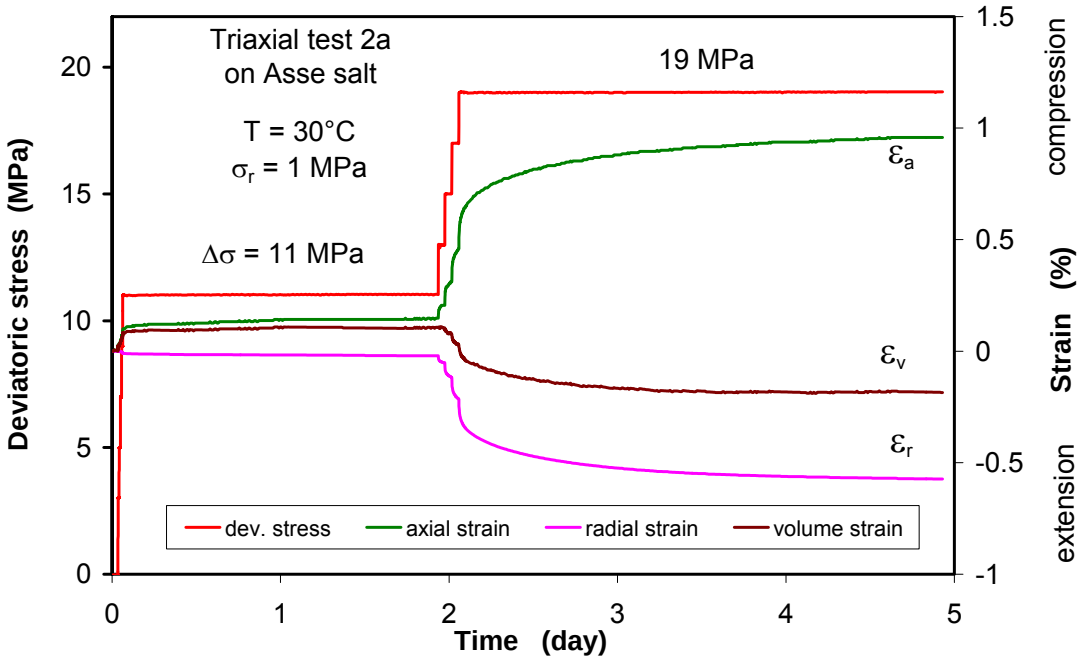

Fig. 3.27 Evolution of strains measured on sample TC2 under deviatoric stresses (TC test 2, first part; TC2A)

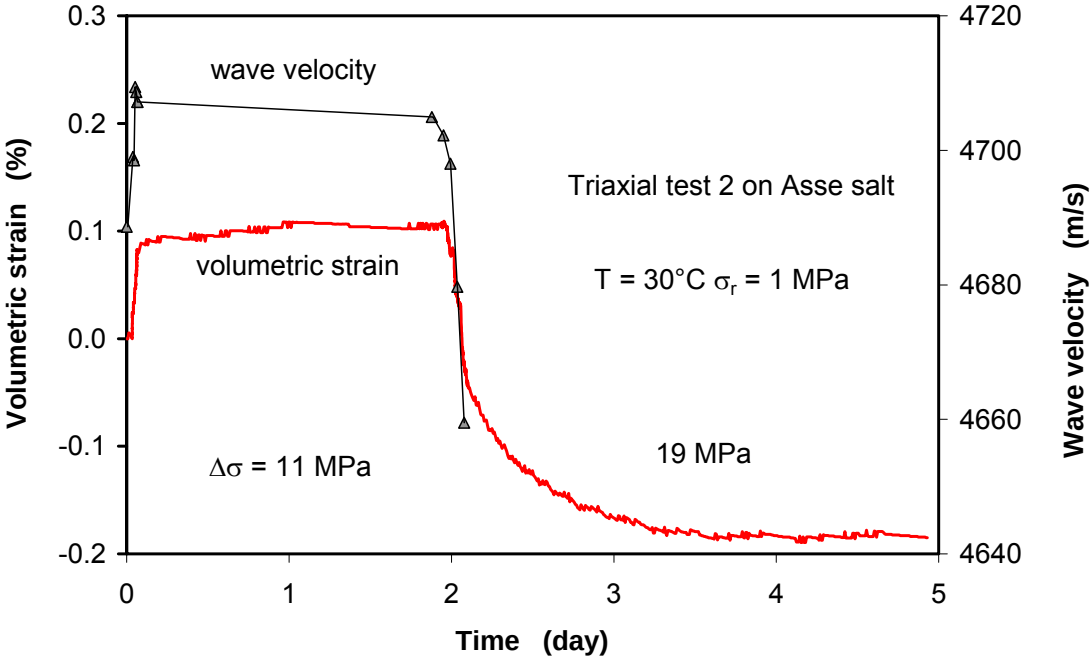

Fig. 3.28 Correlation between volumetric strain and wave velocity (TC2A)

With the deformed sample the test was restarted again. The test procedure including several loading steps is illustrated in fig. 3.29 showing the respective stress and temperature conditions applied. Responses of the salt sample in terms of deformation,

wave velocity and permeability are shown in figures 3.30, 3.31, and 3.32, respectively. The results are interpreted as follows.

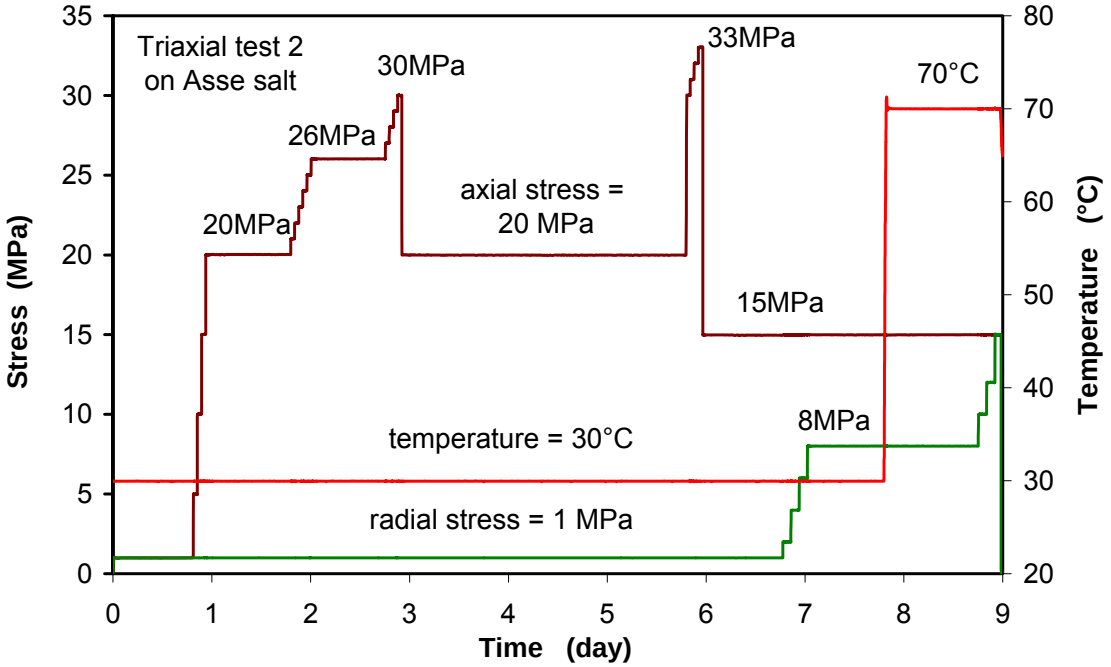

Fig. 3.29 Load conditions applied to the previously deformed sample in TC test 2 (TC2B)

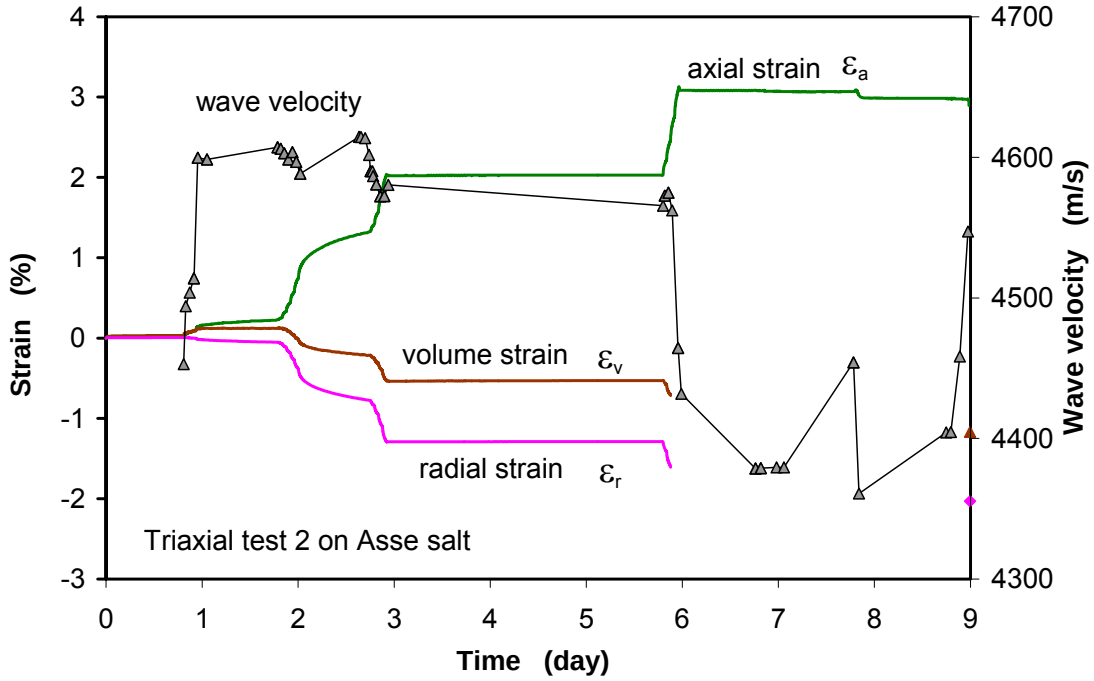

Fig. 3.30 Responses of deformation and wave velocity to loading and heating on the previously deformed sample (TC2B)

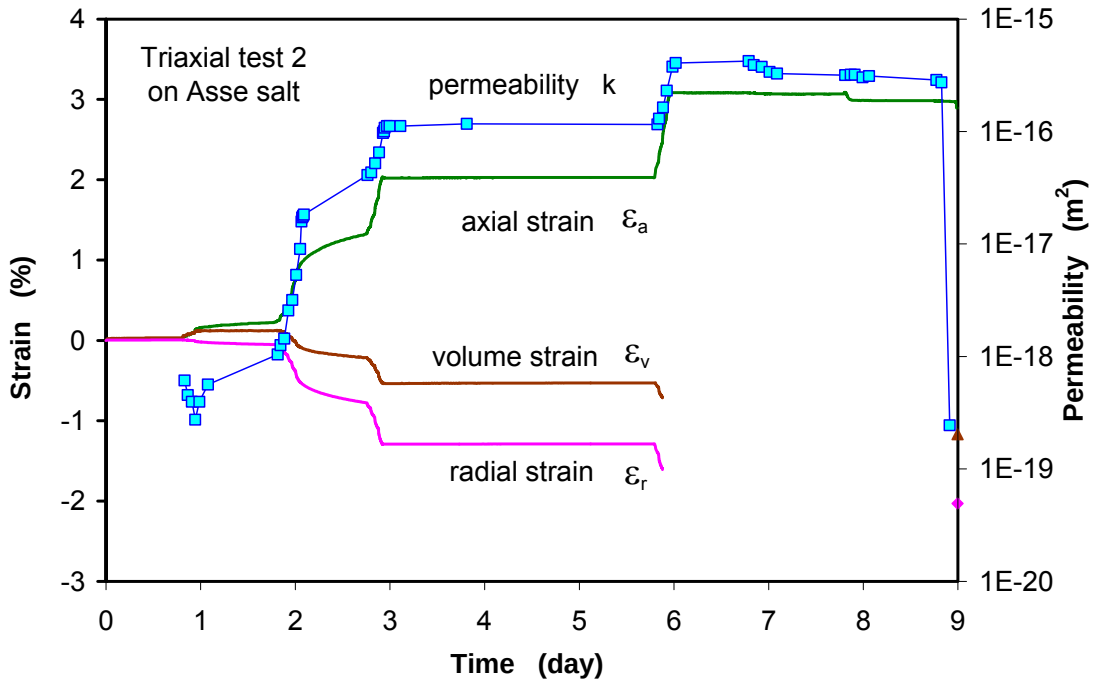

Fig. 3.31 Response of permeability to loading and heating on the previously deformed sample (TC2B)

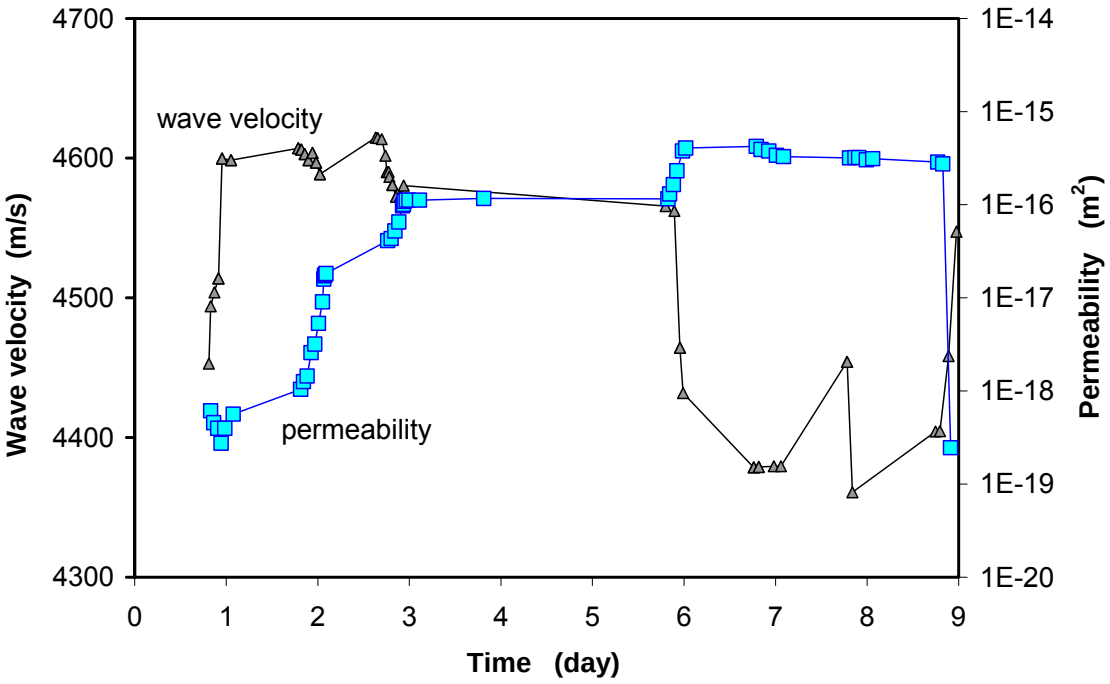

Fig. 3.32 Correlation between permeability and wave velocity (TC2B)

1. Initial state: The test restarted on the previously deformed sample from the initial point of σ_a = σ_r = 1 MPa, gas inflow pressure at the bottom p_g = 0.5 MPa, outlet pressure at the top p_o = atmosphere (0), and temperature T = 30 °C. Interestingly,

a steady gas flow could be observed. The corresponding permeability was determined to $k = 6 \cdot 10^{-19}$ m^2.

2. Damaging: The axial stress was increased step by step at average rates of 0.01 to 0.02 MPa/min to different levels of σ_a = 20, 26, 30 MPa. The first loading to 20 MPa led to a volumetric compaction of ~ 0.12 %. Correspondingly, the wave velocity increased from 4450 m/s to 4600 m/s, and the permeability decreased slightly. The compaction turned over to dilatancy just at the beginning of the next loading phase from σ_a = 20 MPa to 26 MPa. While the wave velocity dropped slightly, the permeability began to rising significantly by about two orders of magnitude, indicating a percolation process. Further increasing the stress to 30 MPa produced more dilatancy, higher permeability, but lower wave velocity. When the axial stress was reduced to 20 MPa again, the damaged structure in the sample seemed to be unchanged, indicated by constant strains, wave velocity and permeability. Reloading to a higher stress of 33 MPa resulted in more damage characterized by the increased dilatancy and permeability but the decreased wave velocity. Because the upper limit of the radial strain measurement was touched, there were no more data of volume changes available. Finally, the axial stress was reduced to 15 MPa again, resulting in no structure changes.

3. Re-compaction: At σ_a = 15 MPa, the radial stress was increased stepwise to σ_r = 2, 4, 6, 8 MPa, causing a slight reduction of the permeability from $4 \cdot 10^{-16}$ to $3 \cdot 10^{-16}$ m^2 while the wave velocity remained constant. The effect of the re-compaction to $\Delta\sigma = \sigma_a - \sigma_r$ = 7 MPa seemed to be insignificant.

4. Heating: At σ_a = 15 MPa and σ_r = 8 MPa, the temperature was rapidly elevated to 70 °C, generating a small amount of expansion, a negligible permeability reduction, but a sudden increase in the wave velocity for a short period of time, which turned down again. During the 1-day creep phase at T = 70 °C, the strain, permeability and wave velocity maintained relatively constant. After approximately another day the radial stress was increased stepwise to σ_r = 10, 12, 15 MPa. This resulted in a strong increase of the wave velocity and a drastic drop down in permeability by three orders of magnitude from $3 \cdot 10^{-16}$ m^2 at σ_r = 8 MPa to $2 \cdot 10^{-19}$ m^2 at σ_r = 12 MPa. The final permeability is comparable with the initial value at the beginning of the test, suggesting the recoverability of fractures in salt under the combined thermal and mechanical impact.

At the last step of σ_r = 15 MPa, the rubber jacket failed and thus the test had to be finished. The final geometry of the sample was measured to a length of 183.13 mm, a diameter of 102.90 mm at the mid-height and 101.22 mm at the bottom and 101.11 mm at the top. The final radial strain of ε_r = -2.0 % and the volumetric strain of ε_v = -1.2 % were established in relation to the state before the second testing.

4 Description of models and improvements

The following sections contain descriptions of the models and the respective calibration works of the different modelling teams. The codes employed were CODE_BRIGHT (used by CIMNE, section 4.1), FLAC (used by IfG, section 4.2), FLAC3D (used by DBE TEC, section 4.3) and PFC^{3D} (tested by DBE TEC, section 4.4). The content of this chapter follows the respective sections in deliverable D6, “Calibration of Thermal-Hydraulic-Mechanical (THM) Models of the Excavation Disturbed Zone (EDZ) in Rock Salt” /WIE 08/.

4.1 CODE_BRIGHT (CIMNE)

4.1.1 Model description

The following section contains a description of the constitutive model for saline materials that is implemented in CODE_BRIGHT and a description of the work done for its application to EDZ problems. The constitutive model has been described in Olivella and Gens /OLI 02/ and the main purpose was to understand and simulate crushed salt deformations both under dry and wet conditions, for general stress states. In this sense the model is macroscopic and can be applied for any stress state. Although the model was calibrated in a comprehensive way for crushed salt compression it is also able to produce dilatant deformations under certain deviatoric stress states.

In what follows the main mechanisms of deformation included are described and the corresponding equations given. The model has three contributions corresponding to FADT creep, dislocation creep and viscoplasticity.

Fluid Assisted Diffusional Transfer (FADT)

As shown in fig. 4.1, FADT is a deformation mechanism assisted by brine (small amounts) and is based on dissolution at contacts (induced by chemical potential increases due to compression) plus molecular diffusion and final precipitation in pores. This means from contact to pore migration of salt, however it can also take place from contact to contact in the case that the material is subjected to deviatoric stress states. Migration of salt from contact to pore is associated with a volumetric deformation while migration from contact to contact produces deviatoric deformations. In this sense, as

porosity decreases the deviatoric part remains active while the volumetric deformation also disappears progressively.

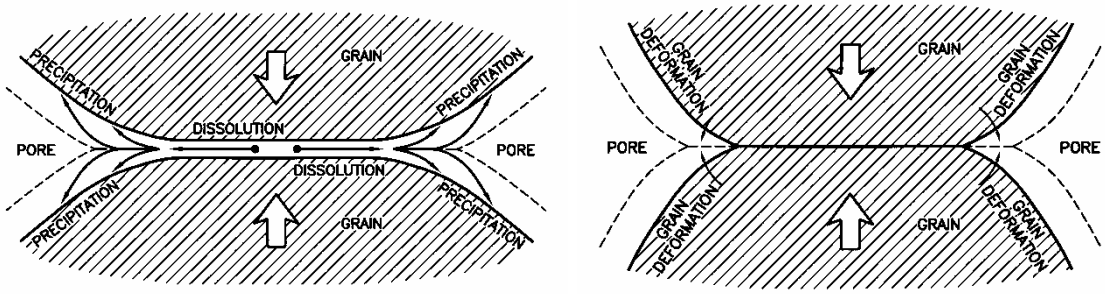

Fig. 4.1 Representation of FADT (dissolution, diffusion and precipitation of salt) and DC creep (particle deformation through crystal dislocation processes)

The final equations for FADT mechanism express strain rate as a function of several variables. These are: stresses, void ratio, grain size, temperature and medium properties. The linear dependence on stresses allows postulating a viscoelastic form.

$$\frac{d\varepsilon_{ij}^{FADT}}{dt} = \frac{1}{2\eta_{FADT}^{d}}(\sigma'_{ij} - p'\delta_{ij}) + \frac{1}{3\eta_{FADT}^{v}}p'\delta_{ij} \tag{4.1}$$

where σ'_{ij} is the effective stress tensor (defined as $\sigma'_{ij} = \sigma'_{ij} - \delta_{ij} P_f$), P_f is fluid pressure, (gas if unsaturated and liquid if saturated), p' is the mean effective stress ($p' = (\sigma'_{11} + \sigma'_{22} + \sigma'_{33}) / 3$) , δ_{ij} is the Kronecker delta, and the volumetric and deviatoric viscosities are defined as:

$$\begin{aligned}
\frac{1}{\eta_{FADT}^{v}} &= \frac{16B(T)\sqrt{S_l}}{d_0^3} g_{FADT}^{v}(e) = C(T,S_l,d_o) g_{FADT}^{v}(e) \\
\frac{1}{2\eta_{FADT}^{d}} &= \frac{16B(T)\sqrt{S_l}}{d_0^3} g_{FADT}^{d}(e) = C(T,S_l,d_o) g_{FADT}^{d}(e)
\end{aligned} \tag{4.2}$$

$$g_{FADT}^{v}(e) = \frac{3g^2e^{3/2}}{(1+e)} \quad g_{FADT}^{d}(e) = \frac{g^2}{(1+e)} \quad g = \frac{1}{(1-f)^2} \qquad f = \sqrt{\frac{2e}{3(1-e^{3/2})(1+e)}} \tag{4.3}$$

The function $C(T,S_l,d_o)$ includes the information related essentially to grain size, brine content and temperature. The functions g^{v}_{FADT} and g^{d}_{FADT}, g and f are geometry-

dependent. In principle, change to other grain shapes would modify these functions, while the other dependences would remain unchanged. From experimental data the model parameters determined by Olivella and Gens /OLI 02/ are:

$$B(T) = \frac{6\times10^{-13}}{RT}\exp\left(\frac{-24530}{RT}\right)\mathrm{s}^{-1}\mathrm{MPa}^{-1}\mathrm{m}^{3}$$

Obviously this part of the model should not be included if the medium is considered dry. This, however, becomes in a natural way as degree of saturation is equal to zero. In such case, both viscosities tend to infinity and this part of the model vanishes.

Dislocation Creep (DC)

Dislocation creep is an intracrystalline deformation mechanism (fig. 4.1). The rock grains deform when subjected to deviatoric stress states. Also the crushed salt grains deform when subjected to deviatoric stress states. The deviatoric deformation of grains produces porosity changes and thus volumetric creep deformations of the material which are only possible if there is some porosity available.

The following general form, based on viscoplasticity theories for geological materials, was proposed:

$$\frac{d\varepsilon_{ij}^{DC}}{dt} = \frac{1}{\eta}\Phi(F)\frac{\partial G}{\partial\sigma'_{ij}} \tag{4.4}$$

This is a viscoplastic equation with a flow rule but without a yield condition, so it is active for any stress level. In this equation it has been included: a viscosity parameter, a flow rule (*G*), a stress function (*F*) and a scalar function (Φ). In Equation (4.1.4) *G* and *F* should be taken as functions of stress invariants. The following form was proposed:

$$F = G = \sqrt{q^2 + \left(\frac{p}{\alpha_p}\right)^2} \qquad \Phi(F) = F^n \tag{4.5}$$

where *n* is the power of the rock creep law and α_p is a material parameter. Figure 4.2 shows the shape of the flow rule in the (*p'*, *q*) plane depending on *F* and α_p values.

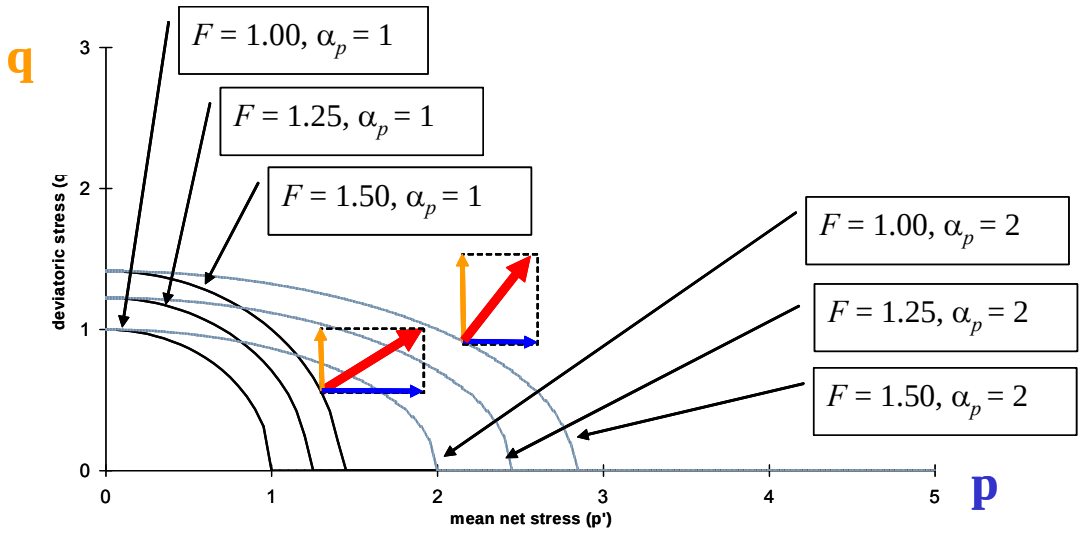

Fig. 4.2 Stress function and flow rule $F = G$ used for the viscoplastic generalization of the creep model (DC mechanism)

(Note that depending on the mean stress and deviatoric stress levels, deformations are different)

Since $\Phi(F)$ is always positive, no threshold is considered in this law. This is consistent because saline rocks develop viscous deformations under any stress level. In order to exploit the theoretically derived equations this generalization of the model is complemented with definitions for η and α_p:

$$\eta = \eta^{d}_{DC} \qquad \alpha_p = \left(\frac{\eta^{v}_{DC}}{\eta^{d}_{DC}} \right)^{\frac{1}{n+1}} \tag{4.6}$$

When void ratio vanishes α_p tends to infinity and the mathematical expression of G (eq. 4.5) reduces to the von Mises case. In this way the creep law for rock salt with von Mises flow rule is recovered. Therefore α_p can be seen as a hardening paramenter for volumetric creep behaviour. With the flow rule adopted, the model does not allow any dilatancy behaviour.

Additional relationships for the creep model are the viscosities and the void ratio functions:

$$\frac{1}{\eta^{v}_{DC}} = A(T) g^{v}_{DC}(e) \qquad \frac{1}{\eta^{d}_{DC}} = A(T) g^{d}_{DC}(e) \tag{4.7}$$

$$g^{v}_{DC}(e) = 3(g-1)^{n} f \qquad g^{d}_{DC}(e) = \left(\sqrt{\frac{1+g+g^{2}}{3}}\right)^{n-1} \left(\frac{2g+1}{3}\right) f + \frac{1}{\sqrt{g}} \qquad (4.8)$$

$$g = \frac{1}{(1-f)^{2}} \qquad f = \sqrt{\frac{2e}{3(1-e^{3/2})(1+e)}}$$

The parameters for the dislocation creep component are:

$$n = 5, \quad Q_{DC} = 54000 \text{ J/mol}, \quad A_{DC} = 5.8\times10^{-6} \text{ 1/s}$$

This creep part of the model is based on dislocation theory or, in other words, on power law for rock salt. Therefore the same parameters that are used for rock salt can be used for crushed salt. As porosity tends to 0, the creep power law for rock salt is recovered. This is a purely creep model. The initial void ratio gives the initial creep compressibility of the material.

The two creep components to the model (FADT and DC) share the same geometry for equation development and the internal variable void ratio (*e*). As void ratio (or porosity) changes, the FADT and the DC functions are modified. Figure 4.3 shows that hardening takes place when void ratio decreases but variations depend on the range.

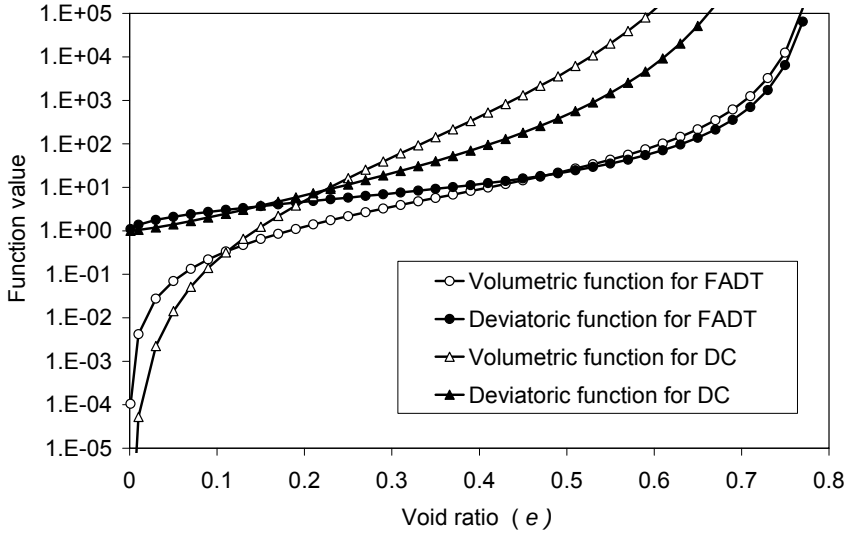

Fig. 4.3 Auxiliary functions g^{v}_{FADT} , g^{d}_{FADT} , g^{v}_{DC} and g^{d}_{DC} that appear in the viscosities

Additional viscoplastic term enabling dilatancy

The constitutive model of Olivella and Gens (2002) described above was developed for crushed salt deformation. When the crushed salt becomes dense it resembles the rock salt and following this idea it seems that a constitutive model may be applicable to both crushed salt and rock salt. However, the model for crushed salt is essentially a model for compaction under isotropic and deviatoric stress states. This model is in fact appropriate for the simulation of deformations under stress states falling in regions (2) and (3) in fig. 4.4. This implies relatively low deviatoric / mean stress ratio (low *q*/*p*). In fact, the model was only able to calculate volumetric deformations of compression in addition to deviatoric, but not in dilatant conditions.

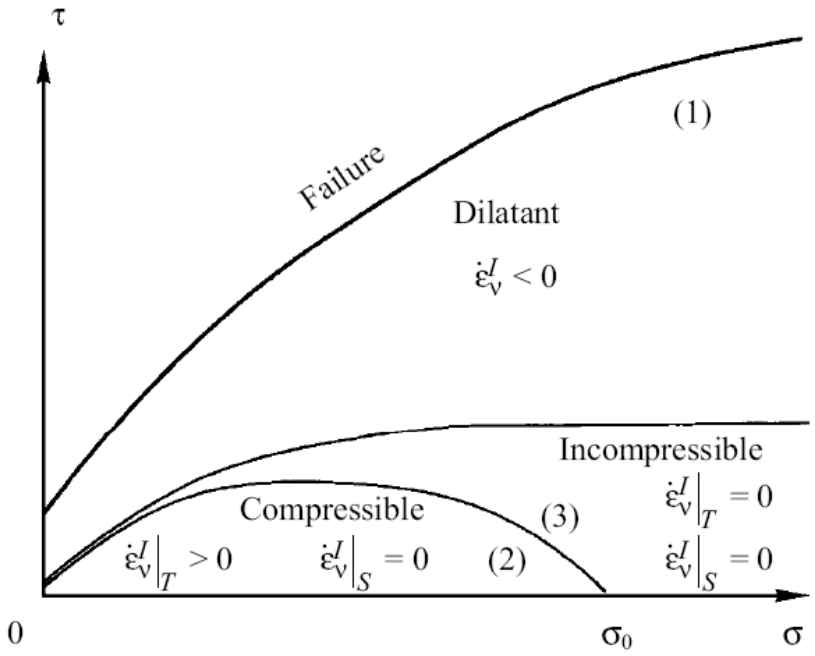

Fig. 4.4 Different deformation types depending on the stress state /CRI 02/

In order to simulate the behaviour of rock salt under dilatant conditions, i. e. for stress states falling in the region (1) in fig. 4.4, it is necessary to consider an additional term to the model. In this way, the overall model equations have the form:

$$\frac{d\varepsilon_{ij}}{dt} = \left(\frac{d\varepsilon_{ij}}{dt}\right)^{elastic} + \left(\frac{d\varepsilon_{ij}}{dt}\right)^{FADT} + \left(\frac{d\varepsilon_{ij}}{dt}\right)^{DC} + \left(\frac{d\varepsilon_{ij}}{dt}\right)^{VP} \tag{4.9}$$

$$\frac{d\varepsilon_{ij}}{dt} = D^{-1}\frac{d\sigma'_{ij}}{dt} + \frac{1}{2\eta^{d}_{FADT}}\left(\sigma'_{ij} - p'\delta_{ij}\right) + \frac{1}{3\eta^{v}_{FADT}}p'\delta_{ij} + \\ + \frac{1}{\eta^{d}_{DC}}\Phi^{DC}\left(F^{DC}\right)\frac{\partial F^{DC}}{\partial\sigma'_{ij}} + \frac{1}{\eta^{d}_{VP}} < \Phi\left(F^{VP}\right) > \frac{\partial G^{VP}}{\partial\sigma'_{ij}} \tag{4.10}$$

The additional viscoplastic term (VP) is useful for rock salt and for crushed salt. The decomposition of this term has to be chosen depending on the stress state. In Olivella and Gens /OLI 02/ the viscoplastic part was included to model compaction of crushed salt by grain crushing and reorganization. However, in the case of rock salt under dilatant conditions, the viscoplastic part of the model may require a different shape.

In rock salt creep deformations hardening and dilatancy occur. These are observed when triaxial tests are performed under stress states falling in the region (1) of fig. 4.4. These deformations are represented by the viscoplastic component to the model which is combined with the creep part. This viscoplastic part is quite powerful because several yield functions and flow rules can be used (associated or non-associated) and complemented by hardening and softening laws both for the size and for the shape of these yield and flow rules.

The basic viscoplastic equation is:

$$\frac{d\varepsilon^{VP}_{ij}}{dt} = \frac{1}{\eta^{d}_{VP}} < \Phi(F^{VP}) > \frac{\partial G^{VP}}{\partial\sigma'_{ij}} \tag{4.11}$$

The brackets <Φ> indicate that this mechanism is only active when Φ > 0. The yield function (*F*) and the viscoplastic flow rule (*G*) have been adopted to model the response of rock salt under triaxial conditions in the following way:

$$\begin{aligned} F &= a_1 q - bp \\ G &= a_1 q - \alpha bp \\ \Phi(F) &= F^m \ \text{ for } F \geq 0; \quad \Phi(F) = 0 \ \text{ for } F < 0 \end{aligned} \tag{4.12}$$

$$\begin{aligned} b &= a_3 + a_2\left(W_d\right)^{0.25} - a_4\left\langle W_d - W_{d0}\right\rangle^{0.25} \\ \alpha &= a_5 + a_6\left(W_d + \left\langle W_d - W_{d0}\right\rangle^2\right) \\ dW_d &= q d\varepsilon_d \end{aligned} \tag{4.13}$$

This is a relatively simple non-associated model with hardening/softening based on the irreversible work hardening. Because the function *F* is positive for a certain stress states, the viscoplastic contribution is only active in that region.

4.1.2 Calibration work

The first test to be simulated was the triaxial tests that has been performed by GRS at confining stress of 1 MPa, strain rate of 10-7 s-1, T = 30 °C, pore pressure of 0.5 MPa on sample 2 from 800 m level at Asse salt mine (see section 3.1). The measurements and the calculated results are represented in fig. 4.5. Figure 4.6 shows the stress path in the p'-q diagram. The stress path indicates that the failure line has not been achieved, but the final point is relatively close to it.

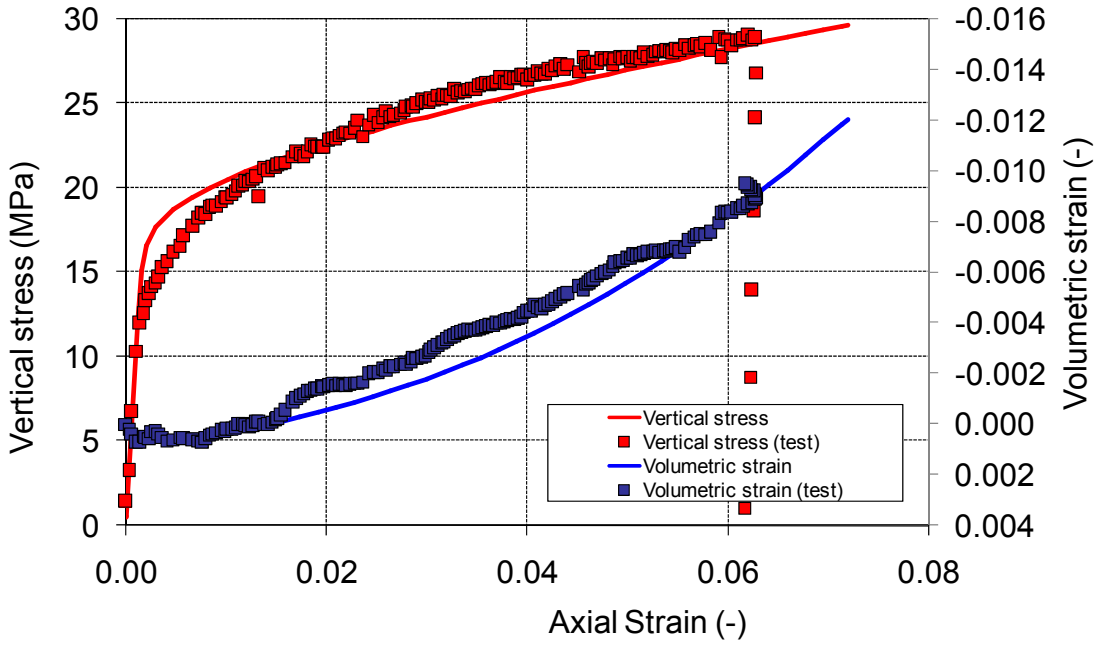

Fig. 4.5 Simulation of a triaxial test at confining stress of 1 MPa, strain rate 10^{-7} s^{-1}, T = 30 °C, pore pressure of 0.5 MPa on a sample from 800 m level at Asse (sample 2)

The parameters that have been used for the model calculations shown in fig. 4.5 are the following (tab. 4.1):

Tab. 4.1 Parameters for simulation of the test on sample 2

Elastic	E = 10000 MPa	ν = 0.3	
Dislocation creep	n = 5	A = 2 · 10^{-6} $MPa^{-n}s$	Q = 54 kJ/mol
Viscoplastic	m = 8	A = 2 · 10^{-9} $MPa^{-n}s$	Q = 54 kJ/mol
	a_1 = 2.5	a_2 = 1.8	a_3 = 2.5
	a_4 = 0.7	a_5 = 0.02	a_6 = 0.02
	W_{d0} = 3.5		

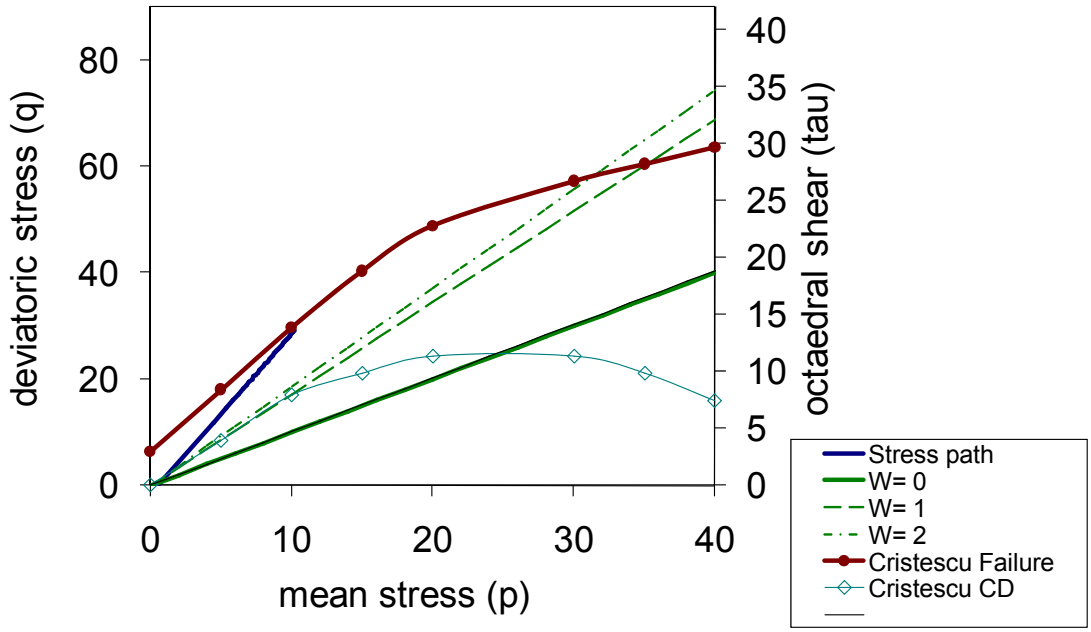

Fig. 4.6 Stress path corresponding to the test simulated in fig. 4.5 (sample 2)

Figure 4.6 shows some lines of viscoplastic yield function for different accumulated deviatoric plastic work calculated as $dW_d = qd\varepsilon_d$. As can be seen in the results the test remains under conditions of hardening.

Another test (the test on sample 1) is simulated below. The triaxial test was performed on a sample deformed by deviatoric loading at confining stress of 2 MPa (decreased to 0.6 after 8 % of axial deformation), strain rate of 10^{-7} s^{-1} (increased to 10^{-6} s^{-1} after 6 % of axial deformation), pore pressure of 0.9 MPa (decreased to 0.2 after 8 % of axial deformation) on a sample from 551-m-level at Asse salt mine. The results are plotted in fig. 4.7 and the stress path is represented in fig. 4.8.

The following parameters have been used in the present calculations (tab. 4.2):

Tab. 4.2 Parameters for simulation of the test on sample 2

Elastic	E = 10000 MPa	$\nu = 0.18$	
Dislocation creep	n = 5	$A = 2 \cdot 10^{-6}$ MPa^{-n}s	Q = 54 kJ/mol
Viscoplastic	m = 8	$A = 5 \cdot 10^{-9}$ MPa^{-n}s	Q = 54 kJ/mol
	$a_1 = 2.5$	$a_2 = 1.8$	$a_3 = 2.5$
	$a_4 = 0.7$	$a_5 = 0.02$	$a_6 = 0.02$
	$W_{d0} = 3.5$		

Only the Poisson ratio and the constant *A* (for the viscoplastic model) have been changed somewhat with respect to the previous case.

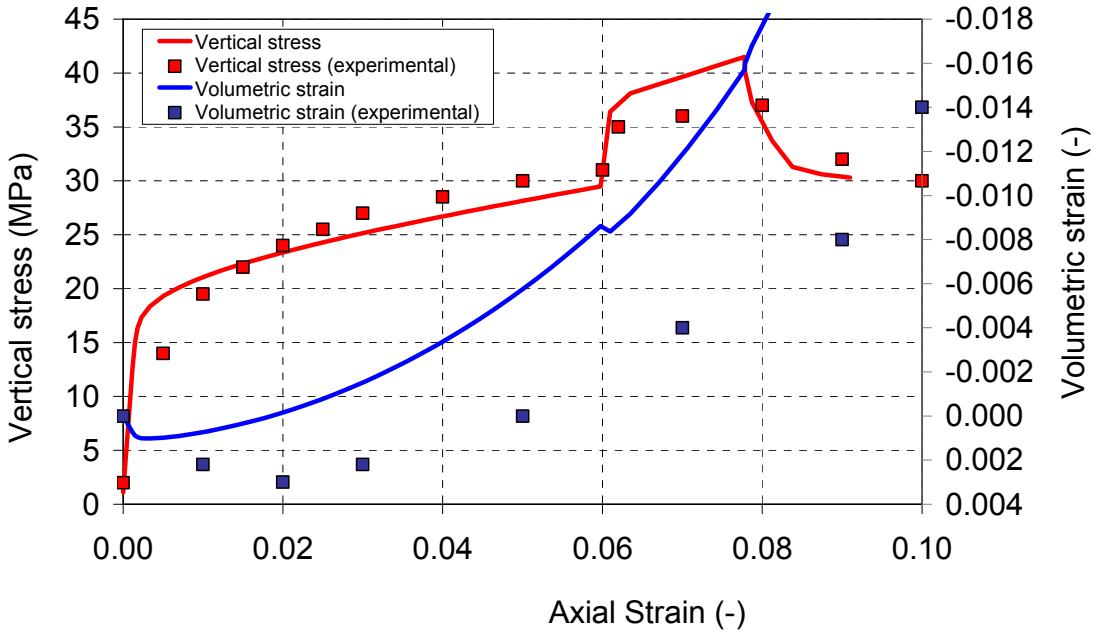

Fig. 4.7 Simulation of a triaxial test at salt sample deformed by deviatoric loading at confining stress of 2 MPa (decreased to 0.6), strain rate of 10^{-7} s^{-1} (increased to 10^{-6} s^{-1}), pore pressure of 0.9 MPa (decreased to 0.2) on a sample from 551 m level at Asse (sample 1)

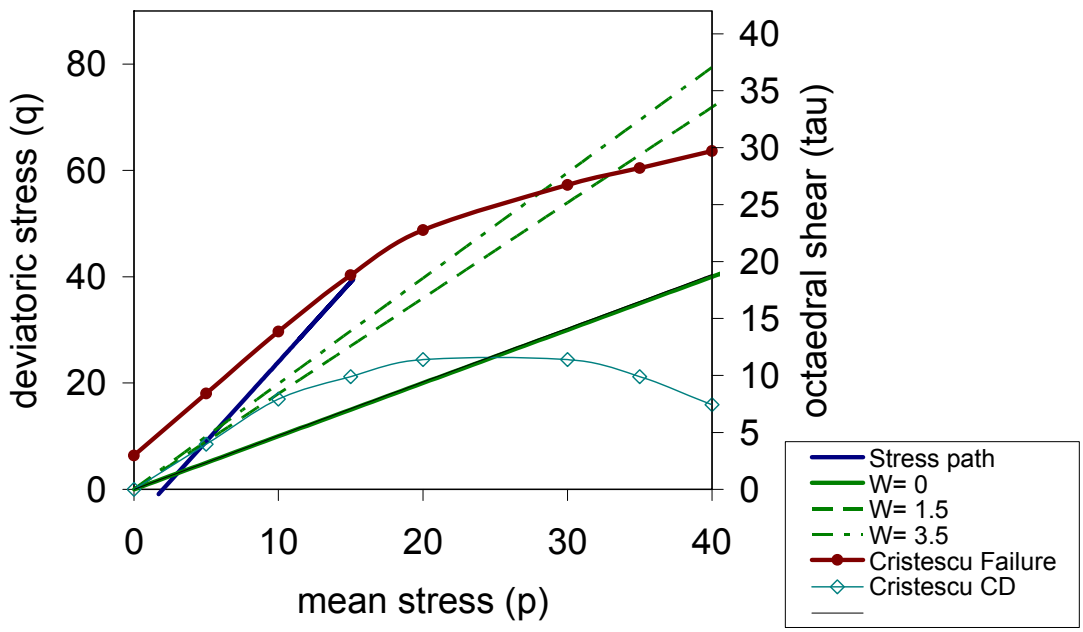

Fig. 4.8 Stress path corresponding to the test simulated in fig. 4.7

In order to evaluate the predictive capabilities of the model, calculations with varying the confinement stress have been performed. The parameters used for modelling of sample 2 have been used in the calculations. The results are shown in fig. 4.9 and fig. 4.10.

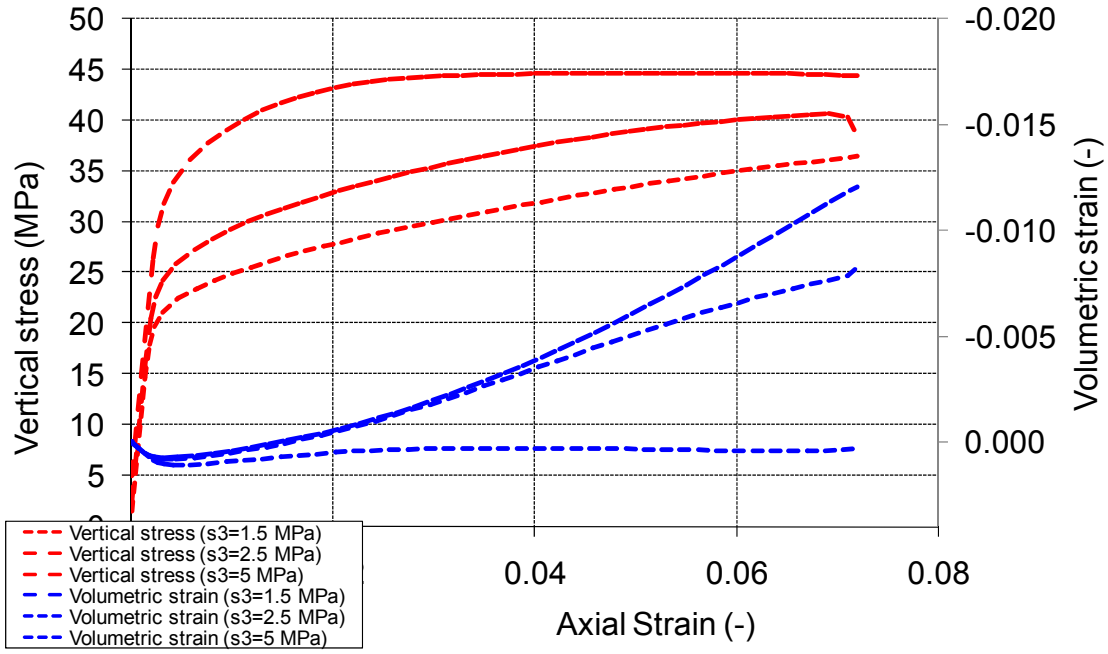

Fig. 4.9 Stress-strain curves for the simulation of triaxial tests under different confinement stresses and strain rate of 10^{-7} s^{-1}

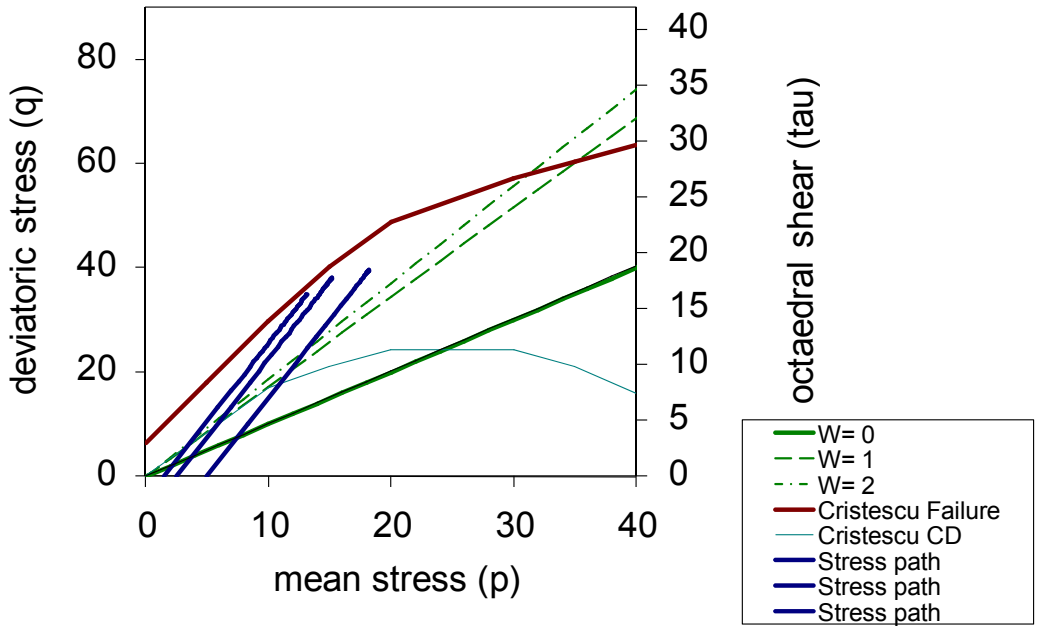

Fig. 4.10 Stress paths for for the simulation of triaxial tests under different confinement stresses and strain rate of 10^{-7} s^{-1}

4.2 FLAC (IfG)

4.2.1 Model description

4.2.1.1 Explanation of using two different material laws

In the frame of THERESA at IfG Leipzig the two different constitutive laws Günther-Salzer /GUE 09/ and Minkley /MIN 04/ were used. Both material laws were developed in the recent years. The initial status of the first one was mainly the modelling of long lasting ductile deformations, whereas in the second one the basic idea was more the simulation of plastic deformations accompanied by brittle fracturing. Both processes take place in the EDZ of underground drifts in rock salt and hence the opportunity was taken for application of IfG's numerical modelling capabilities in the field of assessing the performance and safety of nuclear waste repositories. The calculation of softening, dilatancy and damaging (in combination with creep) as typical processes in the EDZ, coupled with thermal-hydraulic interactions, is a challenge in geomechanics and therefore it was a reasonable decision to regard the EDZ generation from different physical viewpoints.

4.2.1.2 Short description of constitutive law Günther-Salzer

The basics of the constitutive law are the simulation of transient (primary) and stationary (secondary) creep resp. of creep failure (tertiary phase). These processes are in a close relation to each other and result from intracrystalline deformation. Primary creep at the beginning is characterized by high deformation rates. They are caused by dislocations which are present within the lattice structure and which start to move when stress increases. If deformation continues, new dislocations occur within the lattice. Thus, the dislocation density rises (accumulation of dislocations) and the process will cause an increasing resistance against deformation itself so that for maintaining a constant deformation rate an increasingly higher force is necessary or the deformation rate will decrease even when the load is kept constant. This material hardening, which goes up with increasing deformation, is counteracted by the recovery of dislocations. Stationary creep develops by the fact that deformation rate and recovery rate of the dislocations tend to approach equal values, whereas the hardening rate tends to zero. In this phase of creep the magnitude of dislocations, the deformation resistance and consequently also the creep rates evolve to constants. When damage processes and softening processes, which are linked to them and which start in the stress space above the dilatancy boundary, achieve a critical value, creep will pass into its tertiary phase so that creep failure takes place.

The following bullets and fig. 4.11 highlight the basic idea and structure of the constitutive law. More detailed information can be found in /WIE 07/. The material law is implemented in code FLAC as DLL-File.

- Creep (primary, secondary, tertiary phase) and strength behavior with hardening/softening including volumetric dilatancy can be described by microstructural processes. For these the rate of effective hardening ε^{hd}_{eff} is the governing parameter which is influenced by the rates of effective recovery ε^{re}_{eff} and effective damaging ε^{dm}_{eff}.

- Material behavior is explained by internal microstructural processes whose external (integral) phenomena hardening, softening, damaging and dilatancy can be described by physical formulations.

- The parameters for the physical formulations are found by approximation on laboratory curves of creep and strength tests.

tensor of deformation rate: $\dot{e}_{ij} = 3/2\ \dot{\varepsilon}_{eff}\ S_{ij}/\sigma_{eff}$

rate of total deformation: $\dot{\varepsilon}_{eff}^{cr} = \frac{A_p \cdot \sigma^{n_p}}{(\varepsilon_{eff}^{hd})^{\mu}}$ ε_{eff}^{hd} : **effective hardening**

primary creep: $\dot{\varepsilon}_{eff}^{hd} > 0 \Rightarrow \dot{\varepsilon}_{eff}^{hd} = \dot{\varepsilon}_{eff}^{cr} - \dot{\varepsilon}_{eff}^{re} \Rightarrow$ creep rate ↓

secondary creep: $\dot{\varepsilon}_{eff}^{hd} \to 0 \Rightarrow \dot{\varepsilon}_{eff}^{cr} \approx \dot{\varepsilon}_{eff}^{re} \Rightarrow$ creep rate constant

failure, post-failure: $\dot{\varepsilon}_{eff}^{hd} < 0 \Rightarrow \dot{\varepsilon}_{eff}^{hd} = \dot{\varepsilon}_{eff}^{cr} - \dot{\varepsilon}_{eff}^{re} - \dot{\varepsilon}_{eff}^{dm} \Rightarrow$ creep rate ↑

damaging: is set equivalent to dilatancy $\dot{\varepsilon}_{eff}^{dm} = \dot{\varepsilon}_{Vol} = f(\sigma_3, U_{Dil})$

Fig. 4.11 Modelling of different creep phases in material law Günther-Salzer

4.2.1.3 Short description of constitutive law Minkley

In the constitutive model of Minkley the plastic behaviour implying softening and dilatancy is described by a modified non-linear Mohr-Coulomb yield or failure criterion connected with a non-associated flow rule. The Mohr-Coulomb fracture hypothesis depends on the minimum principal stress σ_3 and, if the failure envelope is reached, on the plastic deformation. The dilatancy function depends on σ_3 and plastic deformation as well. Furthermore, the elasto-plastic softening model with dilatancy has been combined with the Burgers creep model. The primary creep phase is modeled by the Kelvin model, and the secondary creep is controlled by the Maxwell model. The tertiary creep is governed by a dilation softening mechanism. In the constitutive model the short-time and the long-time strengths are taken into consideration by a yield limit which depends on the deformation rate.

In fig. 4.12 the concept of the model is illustrated. This model makes differences between the diverse deformation components which sum provides the total magnitude of deformation ε. Salt rocks pose elastic as well as plastic and viscous properties which are superimposed each other. The presented concept of the visco-elasto-plastic constitutive model is based on the acknowledged standard models of mechanics and is applicable in a universal manner to both salt rocks and non-saline rock materials too. The explained constitutive model is suitable for describing the time-dependent mechanical behaviour of salt rock presenting both ductile and brittle material behaviour.

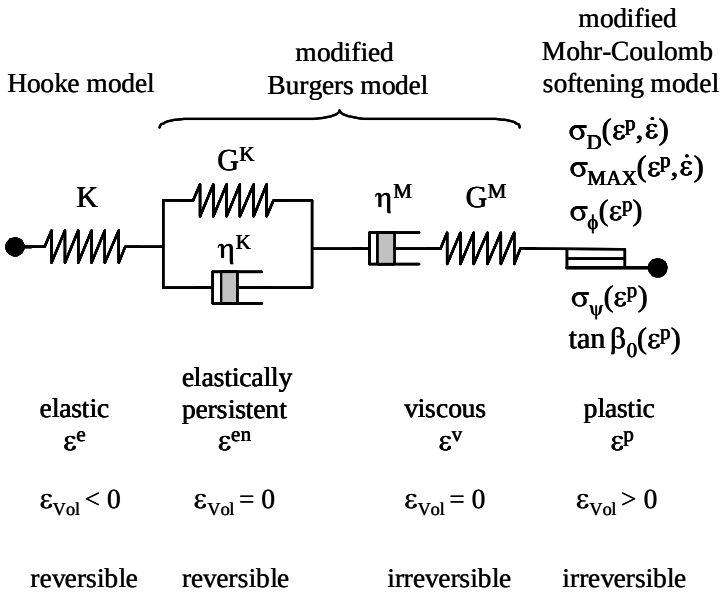

Fig. 4.12 Visco-elasto-plastic model concept in material law Minkley

Again, the material law is implemented as DLL-file in code FLAC. More detailed information and the parameter sets can be found in /WIE 07/.

In /WIE 07/ the two at IfG Leipzig developed constitutive laws Minkley and Günther/Salzer were explained and for both Asse-Speisesalz (Na2) parameters were determined. It was found that the stress-strain behaviour of Na2 rock salt including strain-softening and dilatancy as significant processes in the EDZ could be modelled in a good manner. The calibration in /WIE 08/ took place on special laboratory tests performed on rock salt Asse Na3 which was investigated in frame of the stability proof of the Asse mine. In that project the special topics were the generation of dilatant zones in rock salt Na3 and strength investigation in the dilatant domain. It was not necessary to change the Na2 data sets, the same parameters could be used for Na3 as well.

4.2.2 Calibration work

The calibration work took place by comparing the numerical results to experimental laboratory tests. In fig. 4.13, left hand side, the principle of a triaxial test is depicted in which the axial stress σ_{Ax} is generated by a constant deformation rate (usually under $5 \cdot 10^{-6}$ s^{-1}) and the confining pressure p_c is applied in the triaxial cell using oil pressure (the sample is covered by a rubber mantle). At the right hand side, the numerical model

of a typical cylindrical specimen in a deformed state (height 22 cm, radius 4.5 cm) is sketched.

Figures 4.14 to 4.19 verify the ability of modelling softening and dilatancy as significant processes in the EDZ. In the figures the differential stress curves and the volumetric deformation, each versus axial deformation, of rock salt Na3 at three different confining pressures 0.2, 1 and 2 MPa are depicted. The differential stress is the difference between axial stress σ_1 and confining pressure σ_3. The tests were driven at a deformation rate of $\dot{\varepsilon}_1 = 5 \cdot 10^{-6} s^{-1}$. The sample dimensions were 90 mm diameter and 220 mm length. The curves show typical strain hardening until failure occurs.

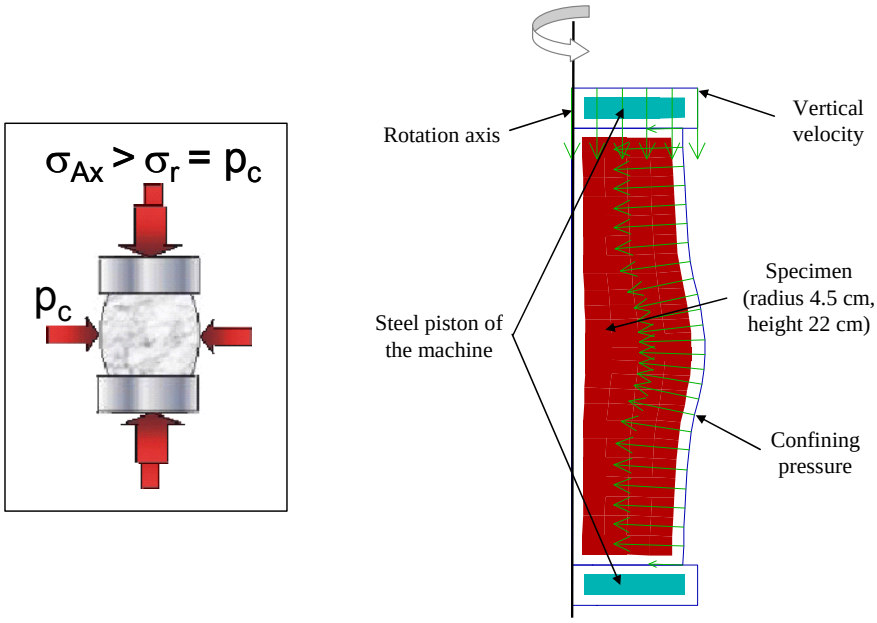

Fig. 4.13 At left hand side, principle of a triaxial test and at right hand side, numerical model of a cylindrical specimen in a deformed state

After exceeding the maximal stress (peak strength) a strain softening, accompanied by a remarkable dilatancy, is visible. At the shear failure the dilatancy curves rise steepest in the domain of the most weakening (strongest damaging). After it a residual strength with a more or less constant value up to deformations of 20 % exists in which the volumetric deformation increases with approximately constant slope. It means, damaging in the specimen proceeds, but is concentrated in a fracture plane.

For each confining pressure 2 resp. 3 curves are drawn (black colour). The numerical results (red and blue colour) fit the scattering range of the experiments very well and justify the application of the constitutive laws for the planned THMC-simulations.

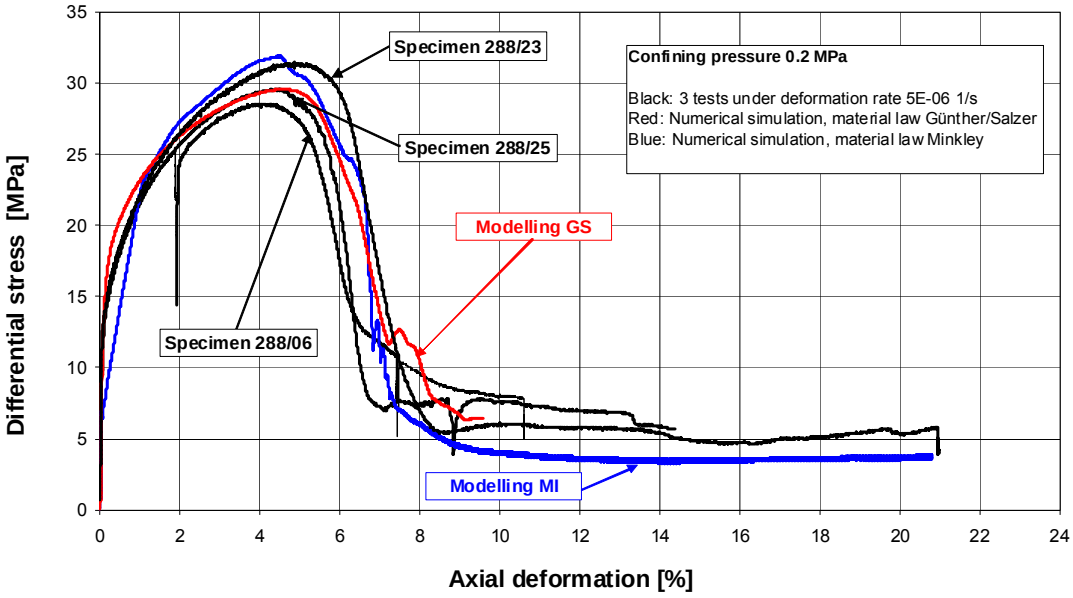

Fig. 4.14 Evolution of differential stress (σ_1 - σ_3) versus axial strain, hardening until peak strength and softening in the dilatant domain, measured and calculated on Na3 from Asse mine, confining pressure 0.2 MPa

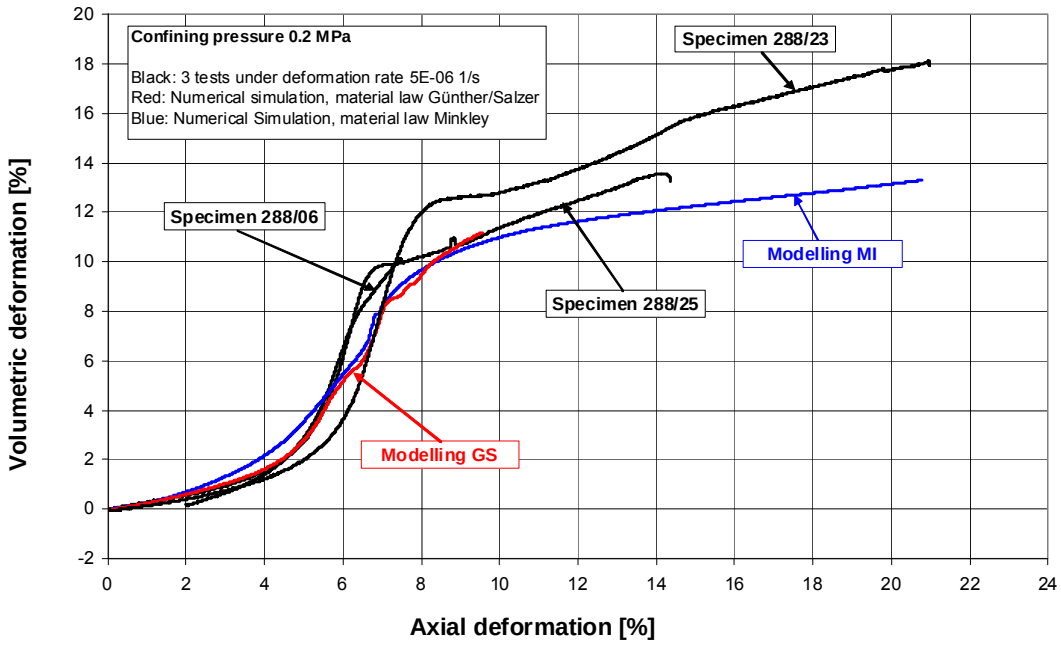

Fig. 4.15 Evolution of volumetric deformation versus axial strain, strong dilatancy increase while fracturing and slight increase after generation of shear bands in the dilatant domain, measured and calculated on Na3 from Asse mine, confining pressure 0.2 MPa

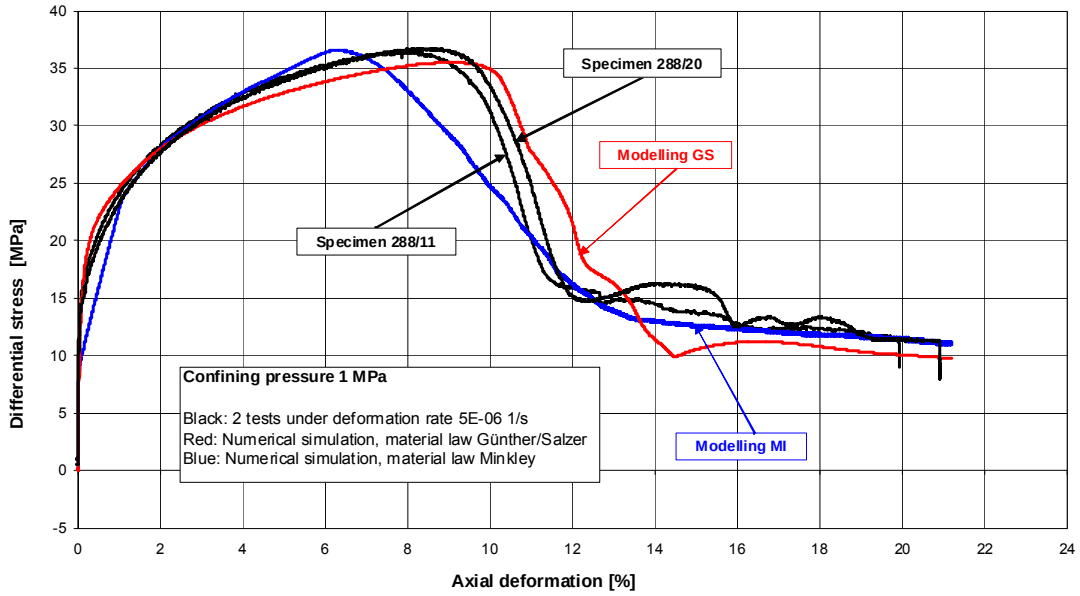

Fig. 4.16 Evolution of differential stress (σ_1 - σ_3) versus axial strain, hardening until peak strength and softening in the dilatant domain, measured and calculated on Na3 from Asse mine, confining pressure 1 MPa

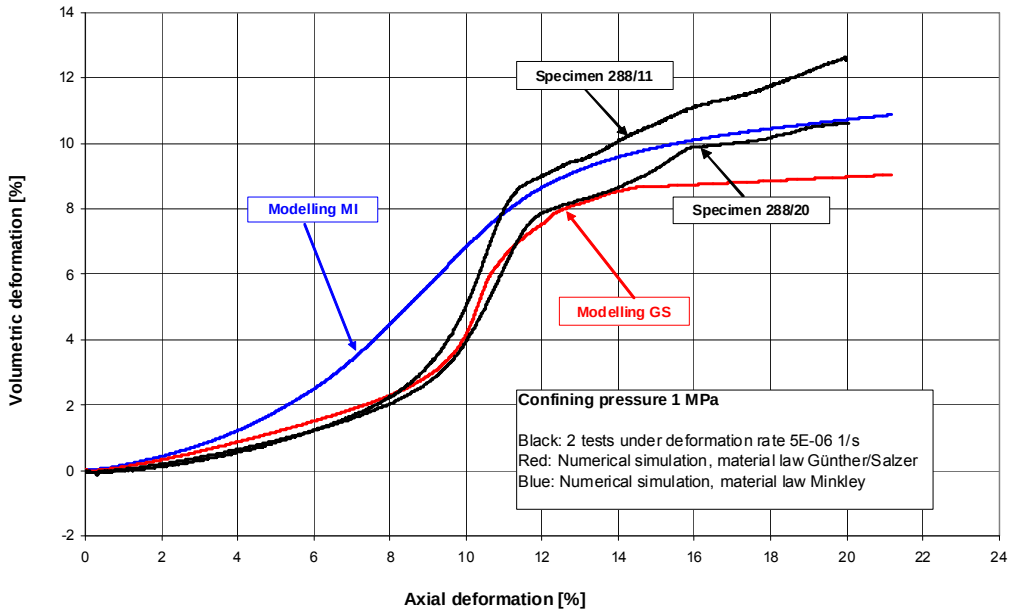

Fig. 4.17 Evolution of volumetric deformation versus axial strain, strong dilatancy increase while fracturing and slight increase after generation of shear bands in the dilatant domain, measured and calculated on Na3 from Asse mine, confining pressure 1 MPa

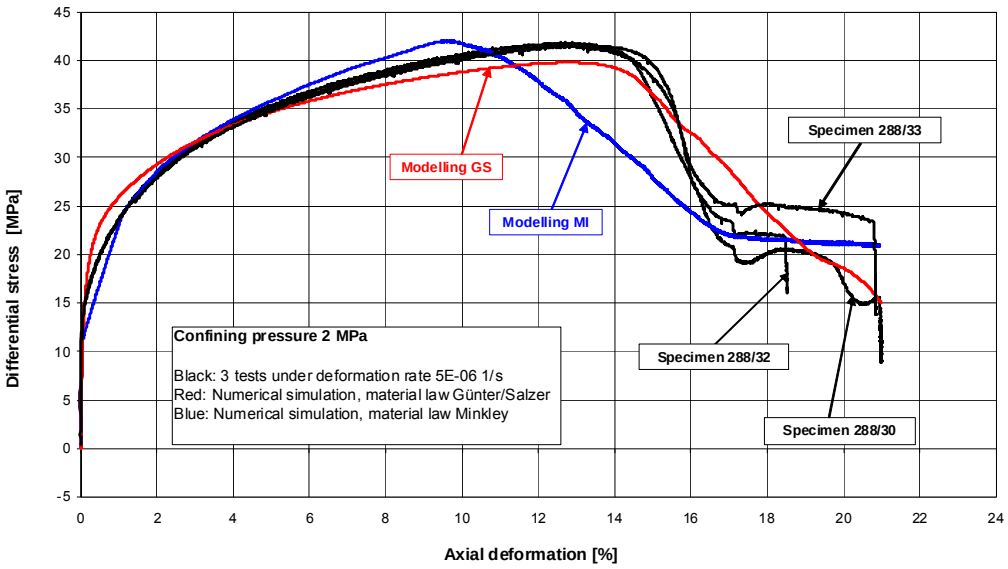

Fig. 4.18 Evolution of differential stress (σ_1-σ_3) versus axial strain, hardening until peak strength and softening in the dilatant domain, measured and calculated on Na3 from Asse mine, confining pressure 2 MPa

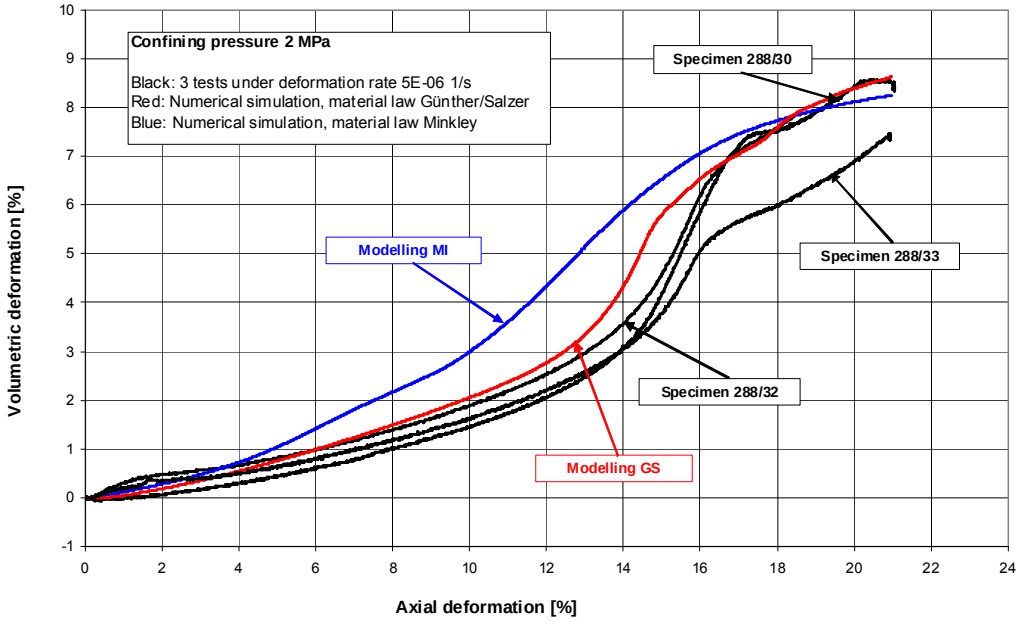

Fig. 4.19 Evolution of volumetric deformation versus axial strain, strong dilatancy increase while fracturing and slight increase after generation of shear bands in the dilatant domain, measured and calculated on Na3 from Asse mine, confining pressure 2 MPa

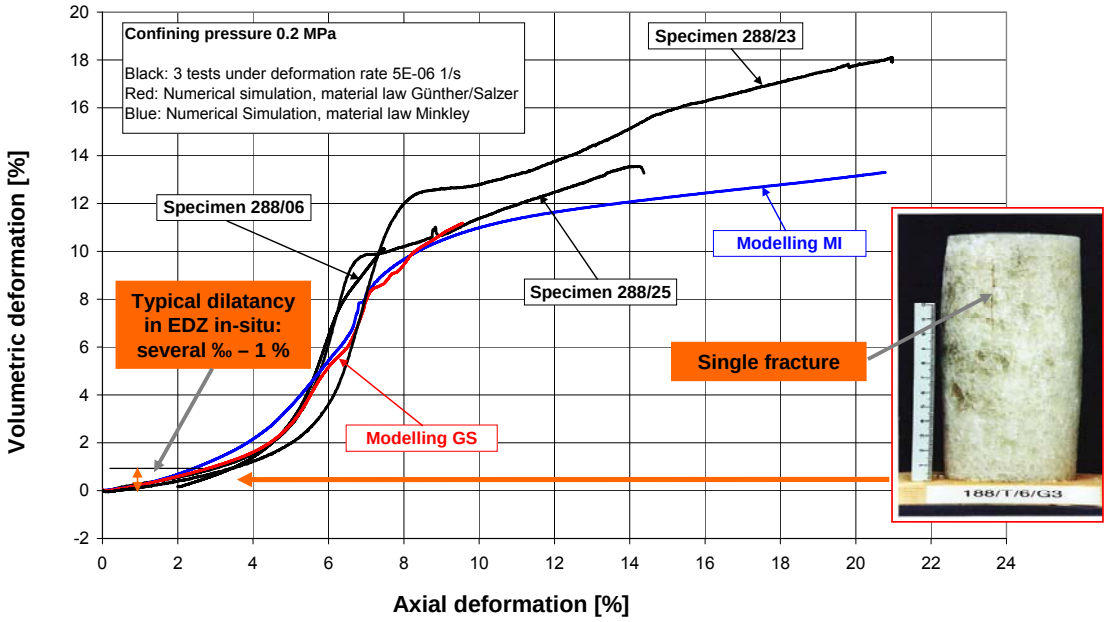

Fig. 4.20 Relevance of the laboratory test at 0.2 MPa for EDZ in-situ, relevance is mostly given for the domain of volumetric deformation < 1 % (axial deformation < 3 %)

It has to be clarified that only a dilatancy domain up to about 1 % is relevant for the EDZ in an underground drift contour. Broken contour plates which are generated after open creep times of decades (pillar splitting in the contour zone) are usually reworked by machine cutting. This is necessary in the operating phase of the mine for safety reasons and, furthermore, before the installation of engineered barriers for reasons of fluid flow retention. From this point of view, only the dilated domain with possible single fractures, not the domain with significant shear bands, is relevant for long-term predictions of performance assessment. In fig. 4.20 the domain is marked and a rock salt sample after volumetric deformation up to 1 % is depicted.

In fig. 4.21 the hydraulical consequences of dilatancy in a range from several per mill up to 1 % is visible. The relation between porosity (hydraulical accessible pore and fissure space, equivalent to volumetric dilatancy) and permeability is based on laboratory tests on rock salt at different confining pressures /POP 02/. On this basis a mathematical expression was developed /HEE 04/ which can be used for graphical representation relevant for EDZ at low minimal principal stresses. The conclusion that can be drawn is a lowest expectation range for permeability of about $1 \cdot 10^{-19}$ m^2 and a highest range of about $1 \cdot 10^{-15}$ m^2.

$$k = \frac{k_{tp}}{\left[\left(\frac{\phi}{\phi_{tp}}\right)^{-4} + \left(\frac{\phi}{\phi_{tp}}\right)^{-1,07} \right]}$$

$$k_{tp} = a_k \cdot \exp(b_k \cdot \sigma_{min})$$

$$\phi_{tp} = a_\phi \cdot \exp(b_\phi \cdot \sigma_{min})$$

$a_k = 4{,}27E-14\ m^{-2}$

$b_k = 1{,}26\ MPa^{-1}$

$a_\phi = 0{,}0263$

$b_\phi = 0{,}3093\ MPa^{-1}$

U. Heemann,
S. Heusermann
(modified after T. Popp
for low porosities)

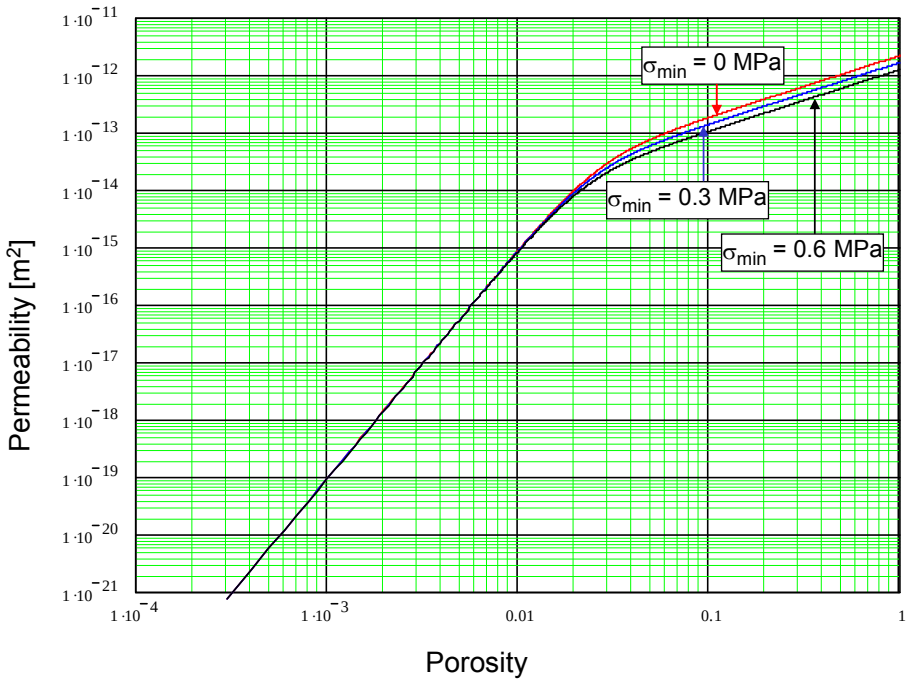

Fig. 4.21 Hydraulical consequences of mechanically induced dilatancy at minimal stresses 0 – 0.6 MPa

In fig. 4.22 the calculation results of the volumetric deformation in the contour zone of a drift in rock salt (area of cross cut ≈ 15 m^2, depth = 775 m) are depicted. The open creep time was 30 years. The calculated dilatancy in the EDZ is several per mill which is indicated in-situ by single open fractures (see photographs at the left and right hand side in fig. 4.22).

After reworking of broken contour plates by machine cutting the area of cross cut was expanded to about 20 m^2. Four month after reworking a measurement campaign took place and the in fig. 4.23 demonstrated permeabilities were found. They represent the above discussed lowest expectation range for permeability of about $1 \cdot 10^{-19}$ m^2 (fig. 4.21) and confirm the success of EDZ reworking. The calculated dilatancy and hereby caused permeability is valid for in-situ as well.

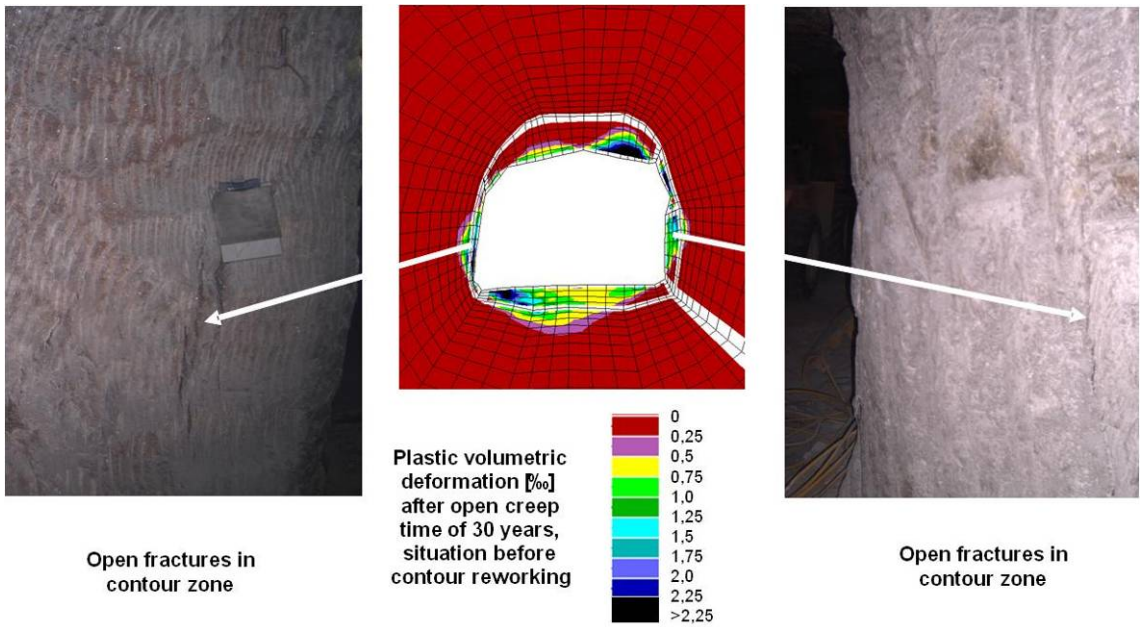

Fig. 4.22 Cross section of single drift in halite mine, situation before reworking of contour zone, depth 775 m, A ≈ 15 m^2

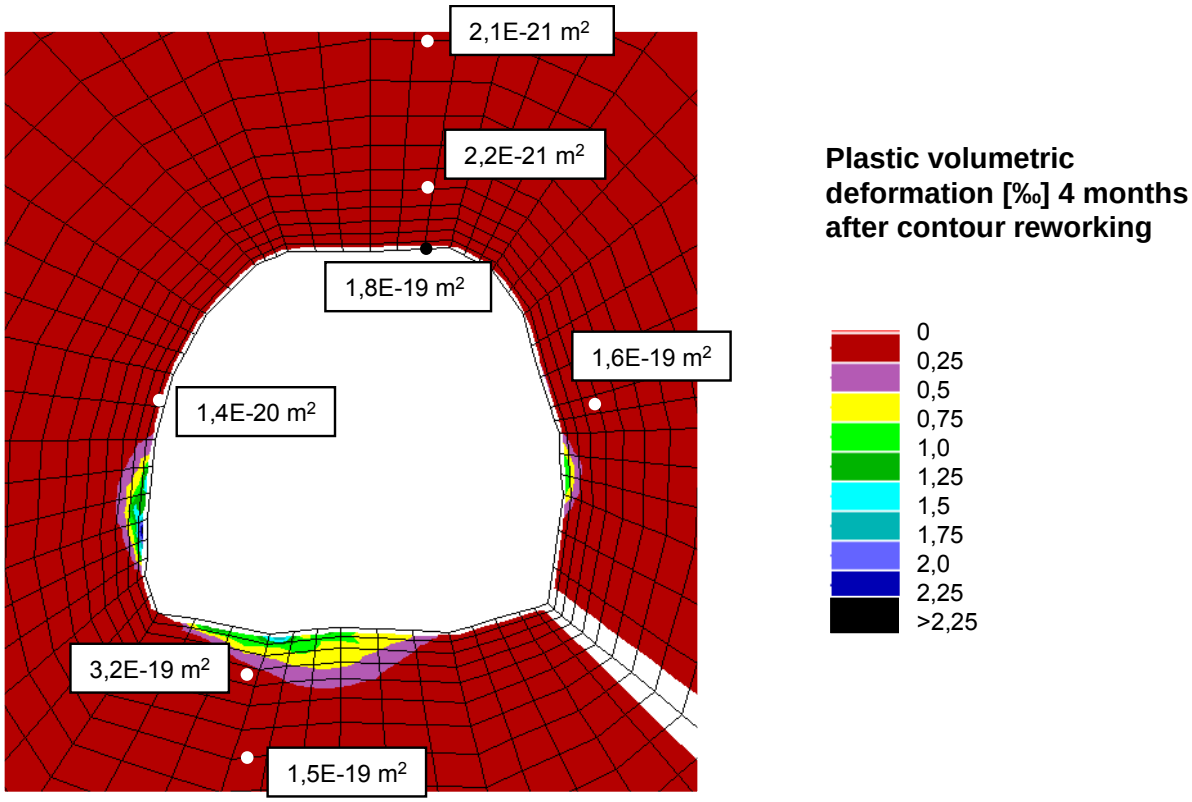

Fig. 4.23 Cross section of single drift in halite mine, 4 months after reworking of contour zone, results of borehole permeability tests, depth 775 m, A ≈ 20 m^2

4.3 FLAC^{3D} (DBE TEC)

4.3.1 Model description

The deformation of rock salt is subject to various processes which take place within the inter- and intra-crystalline structures of this type of rock. DBE TEC intended to apply the WIPP-model provided by FLAC^{3D} to non-dilatant rock salt /ITA 06/ and a modified model by Hein /HEI 91/ to dilatant rock. Originally, the constitutive model by Hein had been developed dealing with crushed salt under conditions of compaction and not for rock salt under dilatant conditions. Pudewills /PUD 07/ successfully applied a modified version of this model to dilatant rock, although this process seems to be the opposite of the compaction of crushed salt. It was intended to decide by means of a dilatancy criterion which of the laws, WIPP or modified Hein, is to be applied to each time step within each element.

Both models consider the thermo-elastic response of the material. In addition, the WIPP-model takes transient and secondary creep into account, while the modified crushed salt model considers porosity-dependent viscoplastic behaviour. The processes will be only discussed phenomenologically here by distinguishing elastic behaviour, non-dilatant creep (dislocation creep) which comprises into stationary and transient behaviour, and dilatant creep. An additive decomposition of the total strain rate tensor by all these processes is assumed

$$\begin{aligned} \dot{\varepsilon}_{ij} &= \dot{\varepsilon}_{ij}^{thel} + \dot{\varepsilon}_{ij}^{vpl} + \dot{\varepsilon}_{ij}^{dil} \\ \dot{\varepsilon}_{ij}^{vpl} &= \dot{\varepsilon}_{ij}^{tr} + \dot{\varepsilon}_{ij}^{stat} \end{aligned} \tag{4.14}$$

Typically, thermo-elastic behaviour is described by linear stress-strain behaviour, depending on Young's modulus E and Poisson's ratio ν, and thermal strain, depending on constant thermal expansion coefficient α_{th}.

The theory of classical plasticity is adopted in both cases of viscoplastic creep, non-dilatant and dilatant creep

$$\dot{\varepsilon}_{ij}^{vpl} = \gamma(T) < \phi(f) > \frac{\partial G}{\partial \sigma_{ij}} \tag{4.15}$$

where $\gamma(T)$ is a temperature-dependent viscosity coefficient. The brackets denote a function which gives $\phi(f)$ for f>0 and 0 in all other cases. f is the yield function $F-F_0$, F_0 the yield stress and G the flow rule. F and G are identical in case of an associated flow rule.

Dislocation creep

The yield stress F_0 is typically set at 0 MPa in case of dislocation creep. The creep rate is commonly described by a J2 flow potential, where J2 is the second invariant of the deviatoric stress tensor, thus, no volumetric component exist. The non-dilatant strain is devided into transient and stationary creep as already described in equation 4.14. The amount of stationary creep $\dot{e}^{stat}$ is given by a multiplicative composition of a stress part by Norton's power law and a thermal part by an Arrhenius term /CRI 98/.

$$\dot{e}^{stat} = A \cdot \exp^{-\frac{Q}{RT}} \left(\frac{\sigma_{\text{eff}}}{\tilde{\sigma}} \right)^n \tag{4.16}$$

The creep coefficient A, the activation energy Q, and the exponent n are model parameters, T denotes absolute temperature and R is the universal gas constant of 8.314 J K^{-1} mol^{-1}. The parameter $\tilde{\sigma}$ is used as a universal scaling parameter uniformly set to 1 MPa in all equations.

Transient creep is modelled as strain hardening. Thus, the transient strain rate is related to the amount of transient strain e^{tr} itself and to the stationary creep rate $\dot{e}^{stat}$. The transient creep rate is given by

$$\dot{e}^{tr} = b_0 \dot{e}^{stat} - b_1 \max\left\{ b_2, \dot{e}^{stat} \right\} e^{tr} \tag{4.17}$$

where the coefficients b_i are parameters of the model. The equation shows that stationary creep affects transient creep and that the rate of the latter subsides if the stationary creep rate is constant. Note: $dy/dt = a - b \cdot y$ is solved by $y(t) = c \cdot e^{-b \cdot t}$. Transferred to equation 4.17 and with respect to the identification of the model parameters, the quotient b_0/b_1 controls the amplitude of transient creep and b_1 controls the velocity with which the process subsides.

Dilatant creep

For dilatant creep two different models are introduced, the first according to /PUD 07/ and the second adopted from Olivella /WIE 08/. Both can be expressed within the framework of viscoplasticity, equation 4.15. An associated flow rule and a quadratic yield function are used in case of the first model, while a linear and non-associated approach is used in the second case.

The associated model based on the quadratic yield function is derived from a constitutive model developed by Hein, originally intended for the compaction of crushed salt, /HEI 91/ /BRE 94/, and used in modified version for crushed salt /BEC 99/ /BEC 04/. For the description of dilatant behaviour, it was modified again within the two coefficient functions n_1 and n_2 of the flow rule by FZK-INE, e. g. /PUD 07/,

$$F_q^{dil} = G_q^{dil} = n_1(p,q)\cdot p^2 + n_2(p,q)\cdot q^2 \tag{4.18}$$

where p denotes the mean stress p=-1/3 tr($\underline{\underline{\sigma}}$) and q is the quadratic norm from deviatoric stress $\underline{\underline{S}}$, thus, q=sqrt($\underline{\underline{S}}$:$\underline{\underline{S}}$). The coefficient functions n_1 and n_2 depend on the stress state by

$$n_1 = \bar{c}_1\left(\frac{q^2}{p^2} - \bar{c}_2\,\eta\right) \quad \text{and} \quad n_2 = 1 - \bar{c}_3\, n_1 \cdot \frac{p^2}{q^2} \tag{4.19}$$

$\bar{c}_i$ are constant model parameters, η denotes porosity which changes due to dilatant or compressive conditions. Thus, the expanded version of the flow rule, equation 4.18, with respect to equation 4.19 is

$$F_q^{dil} = G_q^{dil} = \bar{c}_1\left(\frac{q^2}{p^2} - \bar{c}_2\eta\right)\cdot p^2 + \left(1 - \bar{c}_1\bar{c}_3 + \bar{c}_1\bar{c}_2\bar{c}_3\eta\,\frac{p^2}{q^2}\right)\cdot q^2 = \tilde{c}_1\,\eta\; p^2 + \tilde{c}_2\, q^2 \tag{4.20}$$

The result is that the model simplifies to an expression quadratic in p and q but without any stress dependency in the coefficients. This is a significant result with respect to the analysis and the implementation of this model. Another aspect is, that equation 4.20 becomes q^2 with $\bar{c}_3 = 1$ as given in /PUD 07/. The function finally implemented for the

quadratic case is slightly more general, while the model parameters c_i are still constant over time, equation 4.21.

$$F_q^{dil} = G_q^{dil} = -\left(c_3 + c_1\,\eta\right)\,p^2 + \left(c_2 + c_4\,\eta\right)q^2 \tag{4.21}$$

Dilatant creep becomes active for positive F_q^{dil}, so,

$$\tau_{oct} \;>\; \sqrt{\frac{1}{3}\frac{c_3+c_1\eta}{c_2+c_4\eta}}\cdot p \tag{4.22}$$

Another shear stress limitation between dilatant and non-dilatant behaviour is given by the Cristescu-Hunsche criterion /CRI 98/. This criterion leads to dilatant creep if the following condition for the octahedral stress is met,

$$\tau_{oct} \;>\; \begin{cases} 0.8996\,p - 0.01697\,\mathrm{MPa}^{-1}\,p^2, \text{ for } 0 \le \mathrm{p} \le 26.51\ \mathrm{MPa} \\ 11.92\mathrm{MPa} \qquad\qquad\qquad\qquad\quad \text{, for } \quad \mathrm{p} > 26.51\ \mathrm{MPa} \end{cases} \tag{4.23}$$

The second condition expresses the continuation of the parabola by its maximum value obtained at p = 26.51 MPa. The criterion is applied only in case of a compressive stress state, i. e. for p > 0.

In the linear approach with non-associated flow rule for dilatant creep the yield function and the flow rule differ by a single coefficient function α,

$$F_l^{dil} = \sqrt{3}\,a_1\,q - a_p\,p \;\text{ and }\; G_l^{dil} = \sqrt{3}\,a_1\,q - \alpha\,a_p\,p \tag{4.24}$$

The coefficient functions α and a_p depend on irreversible work hardening by means of

$$\alpha = a_5 + a_6\left(\frac{W^{dil}}{\tilde{W}} + \left\langle \frac{W^{dil}}{\tilde{W}} - \frac{W_0^{dil}}{\tilde{W}} \right\rangle^2\right) \text{ and } a_p = a_3 + a_2\sqrt[4]{\frac{W^{dil}}{\tilde{W}}} - a_4\sqrt[4]{\left\langle \frac{W^{dil}}{\tilde{W}} - \frac{W_0^{dil}}{\tilde{W}} \right\rangle} \tag{4.25}$$

The normalization parameter $\tilde{W}$ is set to 1 Ws m^{-3}. The density of the dissipation of plastic energy W^{dil} has to be continuously integrated during the simulation process from the relation function and note that the flow rule differs by a single coefficient function α.

$$dW^{dil} = \sigma_{eff} d\varepsilon_{eff}^{dil} \tag{4.26}$$

If no further yield condition is chosen dilatant creep becomes active for positive F_q^{dil}, so,

$$\tau_{oct} > \frac{a_p}{3a_1} p \tag{4.27}$$

4.3.2 Calibration work

The ability of the models to describe real damage and re-compaction processes in rock salt had to be tested on data which had been taken from laboratory tests gained from salt samples from the Asse mine, so-called *Asse Speisesalz,* /ZHA 09/. The parameters for elasticity and stationary creep are available for this type of salt /BEC 99/, thus, they are set without calibration to the values given in tab. 4.3.

Tab. 4.3 Mechanical parameters for *Asse Speisesalz*

Elasticity	Young's modulus E = 25 GPa	Poisson ratio ν = 0.27
Stationary creep without dilatancy	Activation energy Q = 54 kJ/(kg K) Stress exponent n = 5	Flow factor A = 0.18 d^{-1}

The model parameters for transient creep are determined based on data from BGR (German Federal Institute for Geosciences and Natural Resources) /PUD 04/. The short-term stress-controlled creep test BGR-94097 was carried out on *Asse Speisesalz* loading the cylindrical sample with a lateral confining stress of 25 MPa and an axial stress of 45 MPa. Figure 4.24 shows the simulation results of the laboratory test BGR-94097. The curves for three variations of the parameters b_i are given in fig. 4.24 together with the curve for the experimental data. The parameter b_0 is adapted in such a way that the ratio b_0/b_1 remains constant at 0.34. The model for transient creep seems only to be able to reproduce the initially high creep rates with showing unphysical behaviour during the attenuation phase of transient creep for the case b_0 = 136. Plotting the creep rate over a logarithmic time scale, figure 4.25 (a), reveals that

the slower the attenuation of transient creep takes place the higher the numerical instability in the initial phase.

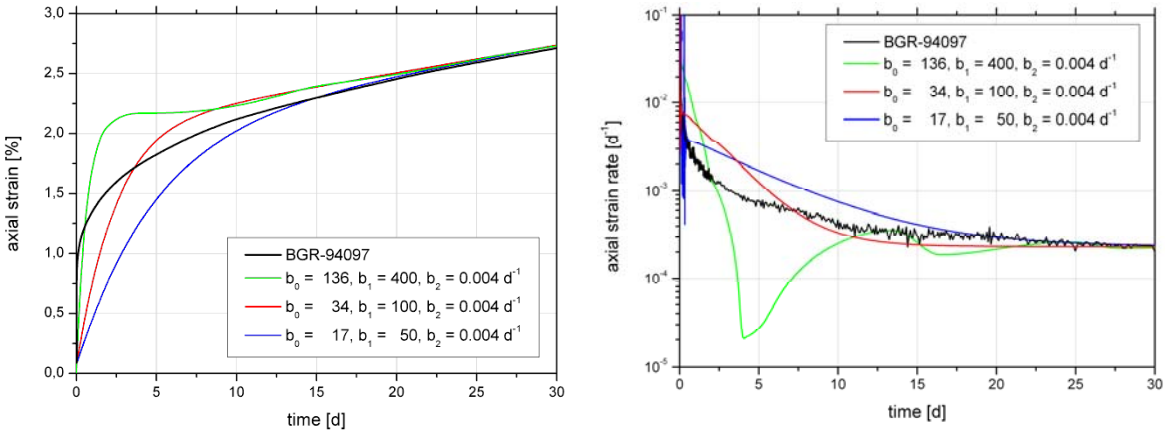

(a) *(b)*

Fig. 4.24 Comparison of measured and calculated axial strain (a) and axial strain rate (b), data set BGR-94097

It could be seen again that the transient approach has some physical limitations if the axial strain rate over time is given in double logarithmic scale, fig. 4.25 (a). The figure also shows that the state at the end of the compaction process is far from a stationary situation. Compared to this, the long-term stress-controlled creep test BGR-95015 is at least close or already under stationary condition, fig. 4.25 (b).

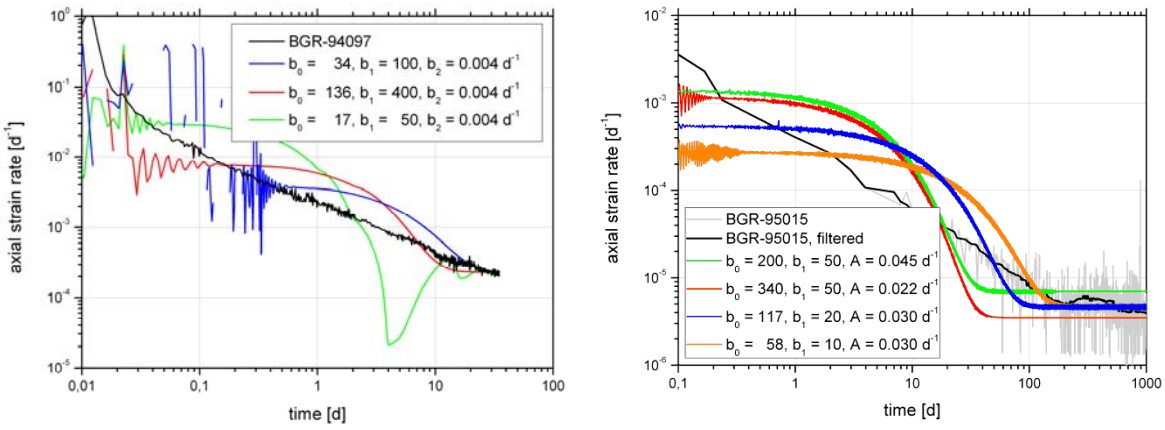

(a) *(b)*

Fig. 4.25 Comparison of measured and calculated axial strain rate on logarithmic time scale, (a) data set BGR-94097, (b) data set BGR-95015

Simulation results for the long-term stress-controlled creep test BGR-95015 over 1250 days are shown in fig. 4.26 for the axial strain and the axial strain rate on a linear time scale. This test was carried out without confining pressure and an axial stress of

14 MPa. The figures demonstrate that within the scope of the chosen parameter settings the constitutive law is not able to model the transient creep behaviour realistically. The best description of the long-term behaviour is achieved by setting the parameter *A* for stationary creep to 0.03 d^{-1}, which means that this value is in-between creep class 2 and 3 according to the classification by BGR, thus, it is approx. 2.5 classes below the assumed class. As for the simulations of BGR-94097, fig. 4.25 (b) shows that the calculations behave numerically in a different way. While the orange and blue lines keep oscillating for the whole run, the stationary part becomes smooth in case of the red and the green line. This is due to the slower attenuation of transient creep expressed by smaller values for b_1 so that this process affects the explicit time integration for a longer period. The smooth behaviour corresponds to longer time steps and significantly shorter calculation times. The logarithmic time scale in fig. 4.25 (b) reveals the insufficient simulation results for transient creep in terms of the axial strain rate and axial strain itself.

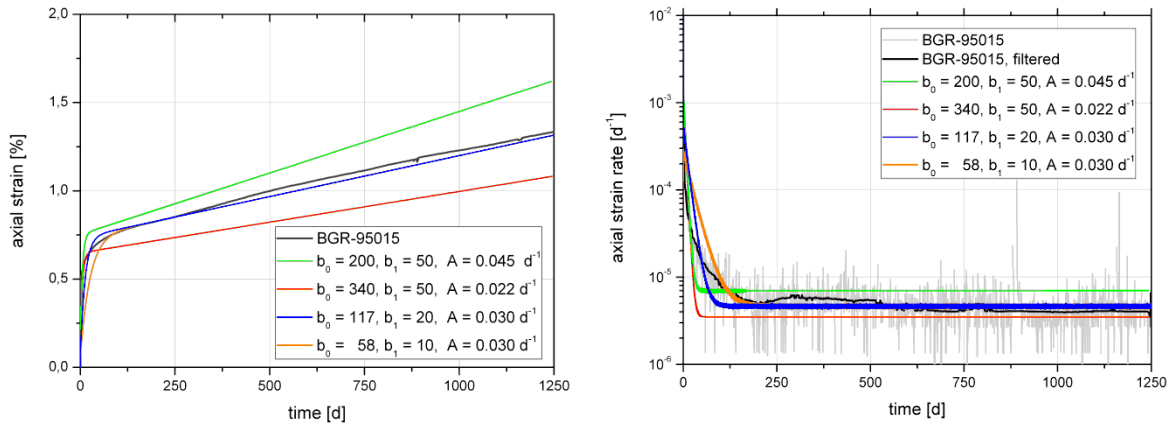

(a) *(b)*

Fig. 4.26 Comparison of measured and calculated axial strain (a) and axial strain rate (b), data set BGR-95015

For strain-controlled experiments with a confining pressure load of 0.5 MPa to 3.0 MPa, the data sets BGR-9070, BGR-9071, BGR-9086 and BGR-9088 were available. The axial strain rate is about 10^{-5} s^{-1} in all cases. It was not possible to reproduce dilatancy as in /PUD 07/, neither with parameters suggested in /PUD 07/, e. g. c_1 = 500, c_2 = 0.7, c_3 = 1, m = 2.25, nor with others. Section 4.3.1 gives some argument why this result is actually not unexpected. The calculations were extremely time-consuming and often terminated in run time errors just after switching the constitutive law. Also, the run time behaviour varied with the version of the software. One hour of simulation time could consume more than a day of computer time. One hour corresponds to an axial strain of

3.6 %. Figure 4.27 shows two examples for a confining pressure of 3 MPa. The parameters given in fig. 4.27 refer to the modified Hein model with settings for the dilatant case. The huge difference between the stresses for the two simulations is due to the different settings for the exponent m.

Figure 4.28 illustrates results from further numerical investigations of the modified Hein law. The exponent was set to m = 2. The curves for the volumetric strain (dotted lines) demonstrate that a negative product of parameters c_1 c_2 (c_3 - 1) leads to a significant limitation in volume change. This agrees with the discussion in the previous chapter. A volumetric increase cannot be observed with the chosen parameter settings, though.

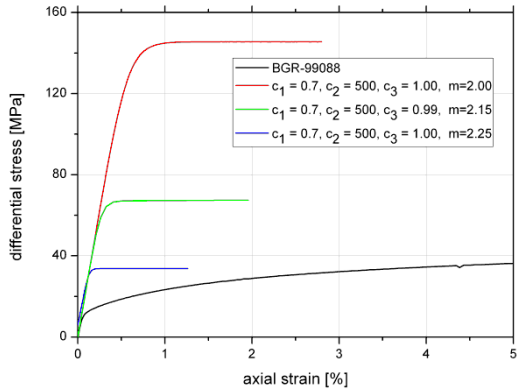

Fig. 4.27 Experimental and calculated stress-strain-behaviour, 3 MPa confining pressure, data set BGR-99088

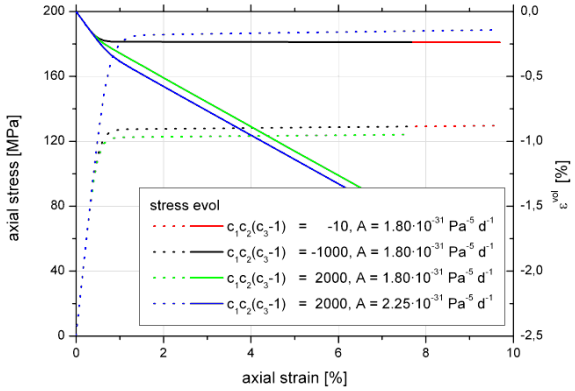

Fig. 4.28 Numerical experiments with the modified Hein law, axial stress (dotted) and volumetric strain (solid)

Data for dilatant behaviour are taken from /WIE 07/ without any further optimization due to the difficulties in non-dilatant behaviour.

4.4 PFC^{3D} (DBE TEC)

Within the continuum mechanical modelling approaches like finite element method (FEM) or finite difference method (FDM), a change in permeability is mainly due to a change in the parameter for expressing porosity and may additionally depend on the stress state. The porosity changes when the volume is changed by plastic, i. e. irreversible processes. The evolution of the rock texture is intentionally not considered in the modelling of damaging and healing processes in this context. The discrete element method (DEM) in contrast tries to grasp these structural impacts by modelling

the mechanical properties of a body by the interactions of objects on a smaller scale. This applies especially to the special type of DEM for granular media considered here. The changing configuration of such an assembly of small objects which may show the formation and closure of cracks explains the change in permeability as a consequence of a structural process on a lower scale. Essentially, the DEM solves the equations of motion of a multi-body system. Thus, DBE TEC has contributed to both approaches, FDM and DEM, within this project.

Different kinds of the DEM with different modelling purposes exist. One representation describes the behaviour of an assembly of distinct and generally polyhedral and geometrically fitting blocks with each of the blocks behaving according to a continuum mechanical constitutive law, /JIN 07/. A block is not an elementar geometric object because it is further discretized into smaller pieces. Contact laws determine how different blocks influence each other. The intention of this method is the simulation of the fracturing of a rock mass or the behaviour of a fracture system. But the fracture system has to be known in advance, at least in a stochastic sense. Simulation tools for this kind of modelling are, e. g., ITASCA's software packages UDEC and 3DEC in two and three spatial dimensions, respectively.

Another approach is derived from the description of granular media as an assembly of rigid geometrical objects. Mostly, but not necessarily, these particles are assumed to be spherical. Due to their rigidity, they do not have to be further discretized, but overlap has to be allowed for a reasonable modelling of their contact behaviour. This granular approach has also been used for the description of rock and rock mass by adapting the geometrical assembly of objects and their contact properties. DBE TEC followed this approach using the software PFC^{3D} /ITA 04/. It should be noted that in this application of a methodology for granular media to a rock mass, the individual particles do not necessarily represent physical entities any more. For our purposes, the number of particles and their sizes were chosen purely by considering available resources and relevance in practice. In the end, the integral behaviour of the system on the macroscopic level, which is determined by its micro-scale properties, determines whether the model is appropriate or not. Mechanical properties of real rock samples are determined by tri-axial tests. Analogously, the macroscopic behaviour of a DEM assembly can be investigated by virtual tri-axial test as presented below.

4.4.1 Model description

Theoretical background of PFC3D

Compared to the continuum-mechanical approaches in the previous chapters, the model description contained here is more general. The acronym PFC stands for particle flow code. The software PFC^{3D} /ITA 04/ uses spheres of different size as the only type of elementary particles. Figure 4.29 shows a typical assembly of such spheres being confined by walls. In the following context, a sphere equipped with a density and other parameters to control its interactive behaviour is referred as a ball. A ball never changes its shape due to “physical” interactions and may be bonded to other balls it is in contact with. Overlapping of balls is allowed, but a repelling force acts between overlapping balls which is the stronger the larger the extension of the overlap is, unless the balls are bonded to each other. This overlapping may also be interpreted as a squeezing of the spheres’ shape.

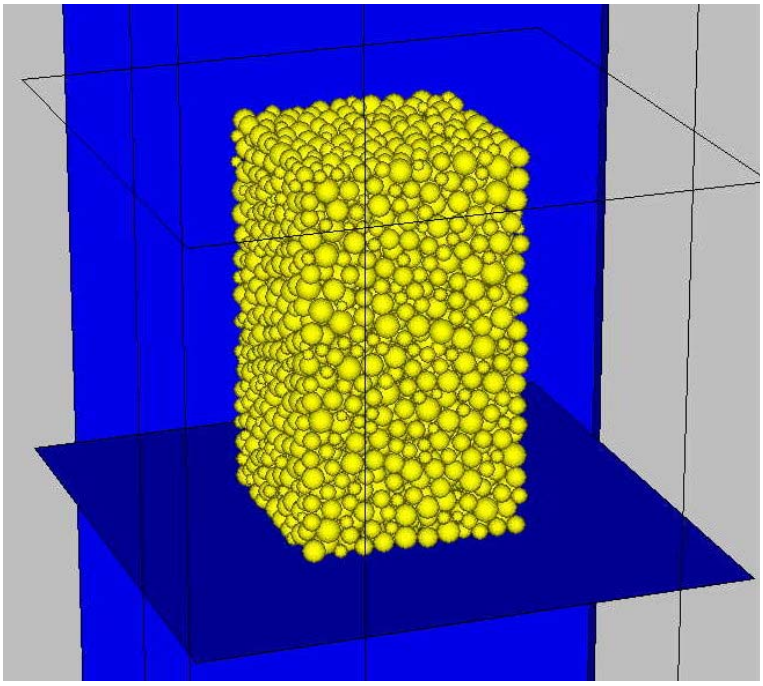

Fig. 4.29 Assembly of particles in PFC3D being confined by walls (3269 balls)

The DEM-code integrates a system of equations of motion for a multi-particle system. For each particle, indexed by *a*, the equations for translational and rotary movement have to be solved with three degrees of freedom for the position of its centre of mass x_i and its orientation α_i, each.

$$m_a \cdot \ddot{x}_a = F_a$$
$$I_a \cdot \ddot{\alpha}_a = M_a \tag{4.27}$$

Mass and momentum of inertia are referred to by m and I_i, respectively. The interaction of particles is represented by the way they contribute to the forces and torques acting on the right side of the above equations. Figure 4.30 shows schematically two particles in contact with each other and introduces the notation used in the presentation of the theoretical background which largely follows /JIN 07/ /ITA 04/.

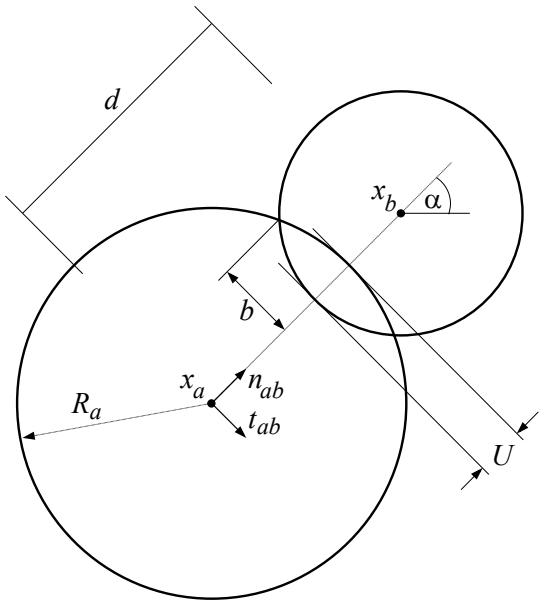

Fig. 4.30 Two particles in contact, see /JIN 07/ /ITA04/

The relative velocity of two particles *a* and *b* to each other is determined by

$$v_{ab} = \left(\dot{x}_a - \dot{x}_b\right) - \left(\dot{\alpha}_a R_a + \dot{\alpha}_b R_b\right) t_{ab} \tag{4.28}$$

which results in a relatively normal and tangential movement affecting the overlap *U* by

$$\Delta U_n = \left(v_{ab} \cdot n_{ab}\right) \Delta\tau$$
$$\Delta U_t = \left(v_{ab} \cdot t_{ab}\right) \Delta\tau \tag{4.29}$$

within a time interval $\Delta\tau$. For the representation of the displacement, the tangential direction has to be chosen in three-dimensional space in such a way that the relative velocity can be described by n_{ab} and t_{ab}, e. g.

$$t_{ab} = \frac{v_{ab} - (v_{ab} \cdot n_{ab}) n_{ab}}{\left\| v_{ab} - (v_{ab} \cdot n_{ab}) n_{ab} \right\|} \tag{4.30}$$

The displacement causes an increment in the normal and tangential component of the force which acts between the particles. In the simplest case these increments are described by Hook's law,

$$\begin{aligned} \Delta F_n &= K_n \Delta U_n \\ \Delta F_t &= K_t \Delta U_t \end{aligned} \tag{4.31}$$

These increments update the normal and shear forces in time step *j* via

$$\begin{aligned} F_n^j &= F_n^{j-1} + \Delta F_n \\ F_t^j &= F_t^{j-1} + \Delta F_t \end{aligned} \tag{4.32}$$

So, particle *b* acts with force F_{ab} on particle *a* and induces also a torque $M_{ab} = R_a F_{t,ab}$ by its tangential component of F_{ab}. The total translational and angular acceleration of particle *a* is a result of the interaction with all adjacent particles *b* by

$$\begin{aligned} \ddot{x}_a^j &= \frac{1}{m_a} \sum_b F_{ab}^j \\ \ddot{\alpha}_a^j &= \frac{1}{I_a} \sum_b M_{ab}^j \end{aligned} \tag{4.33}$$

With these quantities, the equations of motion are integrated by an explicit integration scheme for particle translation and rotation

$$\begin{aligned} \dot{x}_i^{(j+1/2)} &= \dot{x}_i^{(j-1/2)} + \ddot{x}_i^j \Delta\tau \\ x_i^{j+1} &= x_i^j + \dot{x}_i^{(j+1/2)} \Delta\tau \end{aligned} \quad \text{and} \quad \begin{aligned} \dot{\alpha}^{(j+1/2)} &= \dot{\alpha}^{(j-1/2)} + \ddot{\alpha}^j \Delta\tau \\ \alpha^{j+1} &= \alpha^j + \dot{\alpha}^{(j+1/2)} \Delta\tau \end{aligned} \tag{4.34}$$

Apart from the interactive forces, body forces, e. g. gravity, and boundary stresses have to be considered within the integration process. Forced strain rates can be imposed by fixed or moving walls on an assembly as well. The complete calculation process of PFC^{3D} is schematically shown in fig. 4.31.

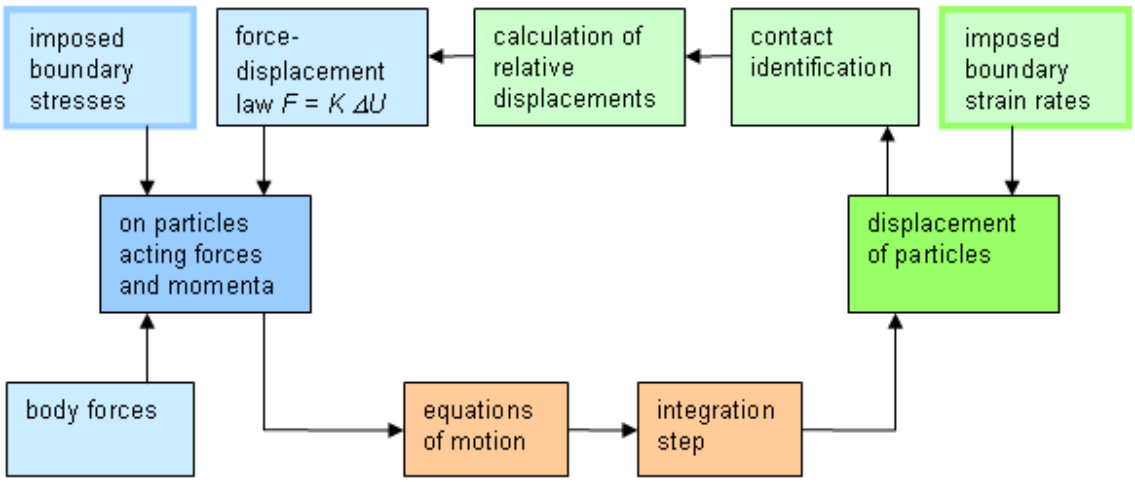

Fig. 4.31 Calculation cycle in PFC^{3D}

In reality, the interaction of two particles is more complicated than as described by Hook's law. In fact, it is determined by sub-models for contact, bonding, and friction which are sketched below roughly.

For the linear contact-model, each particle is parameterized by a normal and shear stiffness k_n and k_t. The effective moduli of the interaction are calculated from the particles' parameters by

$$K_n = \frac{k_{n,a}k_{n,b}}{k_{n,a}+k_{n,b}} \quad \text{and} \quad K_t = \frac{k_{t,a}k_{t,b}}{k_{t,a}+k_{t,b}} \tag{4.35}$$

A contact force acts if the particles overlap. Non-overlapping particles interact only if they are bonded. Bonds between particles are mainly characterized by their bond strength. If two particles are driven apart by forces exceeding the bond's strength, the bond breaks and the interaction ceases to exist. The bond is actually parameterized by two different parameters for normal and shear strength. The normal and tangential displacement of two bonded particles, as shown in fig. 4.32 (a), causes an interaction that tries to drive the particles back into the initial relative configuration. Such, the simple linear bond model represents a connection by two springs in normal and tangential direction. In the so called *parallel-bond model*, the particles interact additionally by their torques in such a way that they behave as being glued together by a layer of cementitious material as shown in fig. 4.32 (b). The radius of the gluing layer is a parameter of the bond model, called the *bond radius*. The bond radius is given relative to the balls' radii and such takes values in the range between 0 and 1.

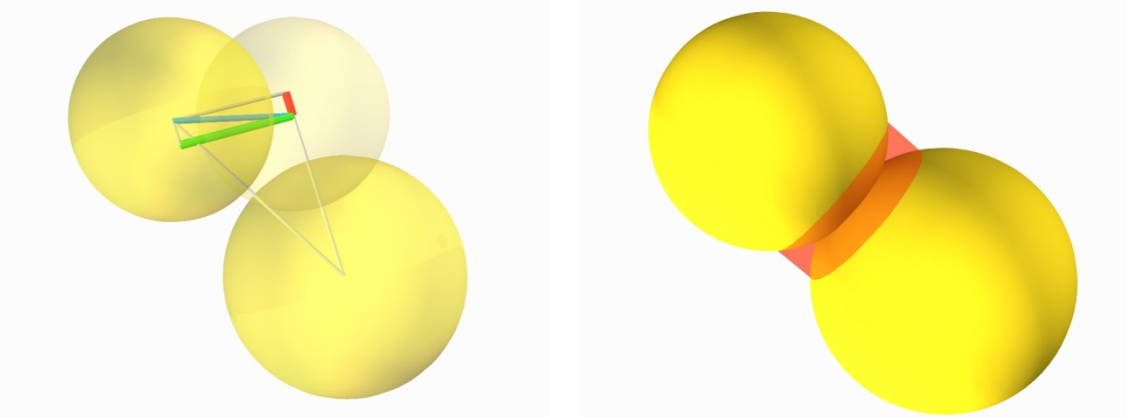

(a) *Relative movement (blue) of a bonded ball with effective normal (red) and shear (green) displacement increments*

(b) *visualization of a parallel bond with gluing layer*

Fig. 4.32 Balls in contact

The *slip model* for two particles in contact suppresses the interacting shear force $F_{t,ab}$ as long as $\left|F_{t,ab}\right| \leq \mu_a \left|F_{n,ab}\right|$ holds for a given friction parameter μ_a.

Generation of particle assemblies

The particles of the model do not necessarily represent physical particles but can be seen as sub-entities of the rock similar to a finite element representing a piece of rock in the continuum approach. The number of particles is also limited by the given computational resources, thus, not every desirable configuration can be handled. Furthermore, only the integral behaviour of the system on the macroscopic level, which is determined by its micro-scale properties, appoint whether the model is appropriate or not. Rock properties necessary for its continuum mechanical modelling are experimentally determined by tri-axial tests. In the same way macroscopic properties of a DEM-assembly are determined by virtual tri-axial tests.

The geometrical assembly of particles itself is decisive for the overall behaviour of the system in addition to the choice of sub-models and their parameterizations. The distribution of sphere radii and the density of their packing is of vital importance. Usually, it is desired that the assembly fulfills additional geometric conditions. E. g., the porosity of the rock matrix is of major interest in the case of hydro-mechanical

interactions; so it seems natural to claim that the DEM assembly possesses the porosity of the investigated rock. Moreover, the degree of overlap within an assembly is crucial for its internal stress state. A largely randomly generated setting of geometry, models, and parameters does not result in a dynamically equilibrated system. It has to be joggled into an equilibrium before it is suitable for the mechanical simulation of a deformation process of a solid body. Here, the assemblies are created in a first step by a purely random distribution of particles within a cuboid. In this initial stage the balls cannot overlap according to the conditions of PFC^{3D}. In a second step the balls are inflated to their desired size. Balls may overlap only after inflation. Overlapping balls are bonded to each other by the parallel-bond law so that this initial overlapping does not contribute to the internal pressure of the assembly generated by repulsive forces.

4.4.2 Calibration work

Two different particle assemblies with varying parameterizations are investigated by virtual tri-axial tests. Figure 4.29 has already shown an example of an assembly of spheres prepared for the test within a square cuboid of 0.4 m height and a square base of 0.2 m side length. The two assemblies investigated consist of 3269 and 5664 balls respectively and they are similarly parameterized according to the reference case given in tab. 4.4. Both possess the same distribution of radii between 0.005 m and 0.012 m, but the degree of overlapping and the number of bonds differ. Initially overlapping spheres are attached to each other by the parallel bond law.

Figure 4.33 shows a virtual tri-axial test where the speed from the top and the lateral walls of the assembly are controlled. The lid moves with a given constant speed of 0.1 m·s^{-1} downwards while the bottom is fixed. The lateral walls are movable and their movement is adjusted with respect to the pressure to which they are subjected. The moving lid tends to increase the overlap and the repulsion within the assembly, but the position of the lateral walls is controlled in such a way that the confining lateral pressure is remaining close to 2 MPa. Because the walls are rigid no curvature as it can be observed in real laboratory tests is possible.

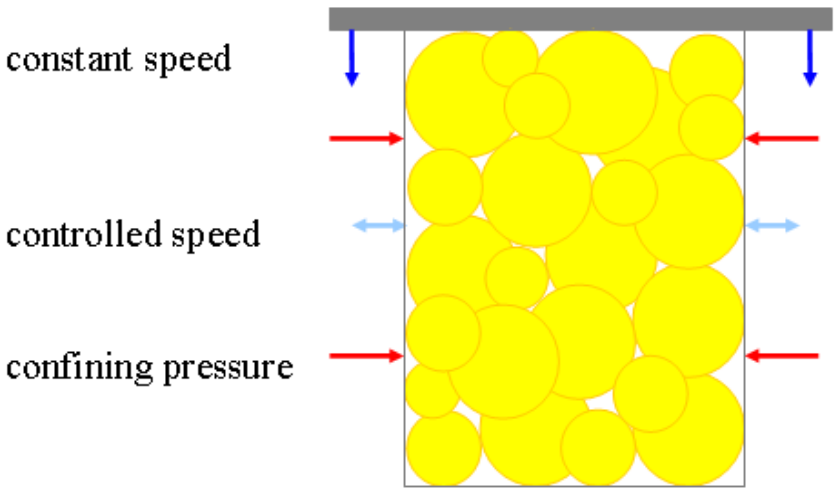

Fig. 4.33 Sketch of a strain-controlled tri-axial test

The virtual tri-axial tests are carried out with different parameter settings in order to investigate their influence on the macroscopic properties. The parameterization and its variations is shown in tab. 4.4 for the first assembly of 3269 balls.

Tab. 4.4 Variation of bond properties for 3269 balls

parameter		unit	reference case	increased bond strength	increased bond stiffness
assembly	number of balls	-	3,269		
	initial number of bonds	-	8,449		
	confining pressure	MPa	2.0		
ball	density	kg m^{-3}	2,000.0		
	radius	M	(uniformly distributed) 0.005 - 0.012		
contact	normal stiffness	GN m^{-1}	0.1		
	shear stiffness	GN m^{-1}	0.0		
	friction	-	1.00	0.58	0.58
bond	normal stiffness	GN m^{-1}	970	970	9 700
	shear stiffness	GN m^{-1}	370	370	3 700
	normal strenght	GN	0.01	0.1	0.05
	shear strength	GN	0.03	0.3	0.1
	bond radius	-	0.7		

Figure 4.34 demonstrates the influence of bond parameters on the mechanical behaviour (solid line) and relates them to the ratio of broken bonds (dotted line) in the assembly. The maximally loadable stress is closely related to the steepest increase in bond breakage. A residual fraction of bonds remains after failure, characterising the residual strength. Increasing the bond strength by one order of magnitude strengthens the material in the same order, as shown by the red and the green lines.

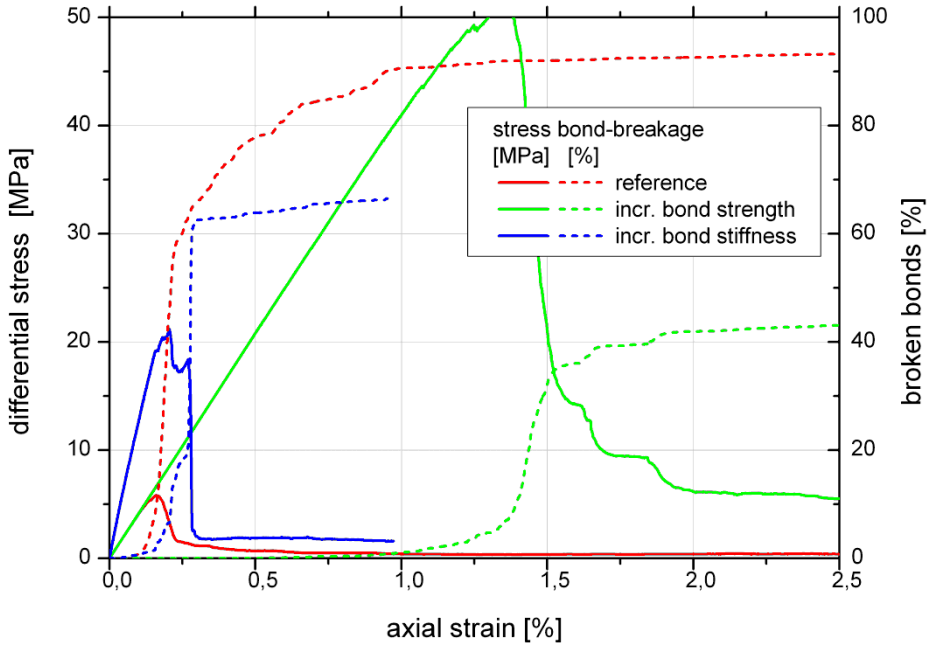

Fig. 4.34 Influence of bond parameters on mechanical behaviour (3269 balls)

A variation of the contact properties demonstrates that an increase in contact stiffness increases the potential for material damage, fig. 4.35. When the contact stiffness is increased above a certain level, the assembly is able to resist ever higher loads. This is due to the ever higher repelling contact forces within the assembly which are induced by the axial load. But when loaded beyond its strength the assembly falls apart, i. e. nearly all the bonds break simultaneously. This behaviour is far from that of rock but it illustrates the effects that have to be considered when applying the discrete element approach.

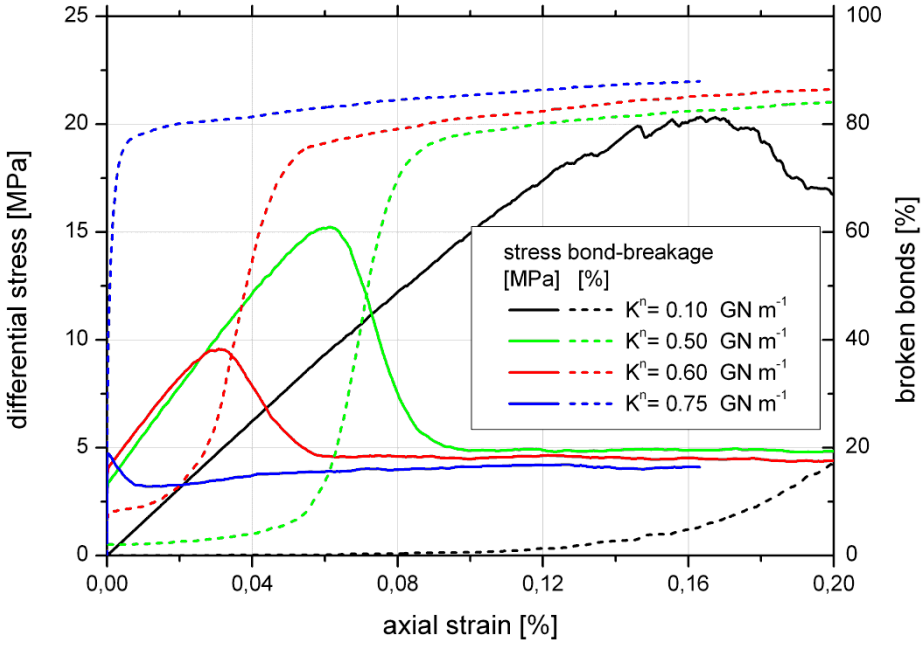

Fig. 4.35 Variation of contact-stiffness (5664 balls)

4.4.3 Conclusions from experience with DEM

The DEM-systems analyzed are far from suitable for the mechanical modelling of rock salt with all its THM-related processes. It was not possible to tune all the possible degrees of freedom towards a more realistic system within the time available. Nevertheless, general effects of model parameters could be analyzed.

The geometric effects of the damaging process on the assemblies and its influence on permeability could not be investigated here. Thus, certain features of the software, e. g. the use of fixed ball clusters, were not considered in the presented calculations. The software also allows the replacement from laws for contact and bonding with user defined models. This could be used for realizing plasticity on a micro-scale. But these approaches were far beyond the possibilities with respect to the available resources.

Nevertheless, the results obtained give a first insight into how the method works and how such systems behave. The approach seems to be promising with regard to the evolution of the EDZ. However, a lot of experience is still needed with regard to the methodology of the DEM and the software PFC^{3D} itself in order to obtain reliable results. /JOB 10/ has shown that it is possible to describe the permeability of a porous structure with code PFC, here for clay as host rock, by using of a fractal approach.

5 Benchmark simulation

As discussed in section 3.3, the modelling benchmark based on the experiment with a normal-scale salt cylinder. This test was performed in two steps (test case 2A and 2B, respectively). After two load steps at 11 MPA and 19 MPa deviatoric load without permeability increase, the sample was removed from the apparatus and inspected. Afterwards, the sample was installed again and the experiment was resumed with several deviatoric load steps, a re-compaction phase and a phase of elevated temperature. Details of the test are given in section 3.3.

The second hollow cylinder test was modelled by CIMNE as an optional exercise, since EDZ formation by dilatancy was not considered the relevant process in this test.

Modelling of the tests was performed in two steps: On February 09, 2009 the modelling teams received the load history of the benchmark test case (TC2A and B) and of the second hollow cylinder test; the strain and permeability responses were held back so that the modellers had the possibility to perform a blind prediction calculation. On April 03, 2009 the test results were distributed to the modellers and an interpretation modelling phase followed.

5.1 CODE_BRIGHT simulation (CIMNE)

For the test case simulation with CODE_BRIGHT the model described in section 4.1.1 was used, with parameters derived from the simulation of sample 2 (see section 4.1.2).

5.1.1 Simulation of TC2A and TC2B

CIMNE simulated TC2A and TC2B, with TC2B actually being the continuation of TC2A with the same sample but with additional stress and temperature paths, as described in section 3.3. Figure 5.1 shows the measured and simulated results of deformations for the TC2A (including the stress variation applied). The deviatoric stress applied shows an initial up to 11 MPa and later increase up to 19 MPa. Variations of stress are performed.

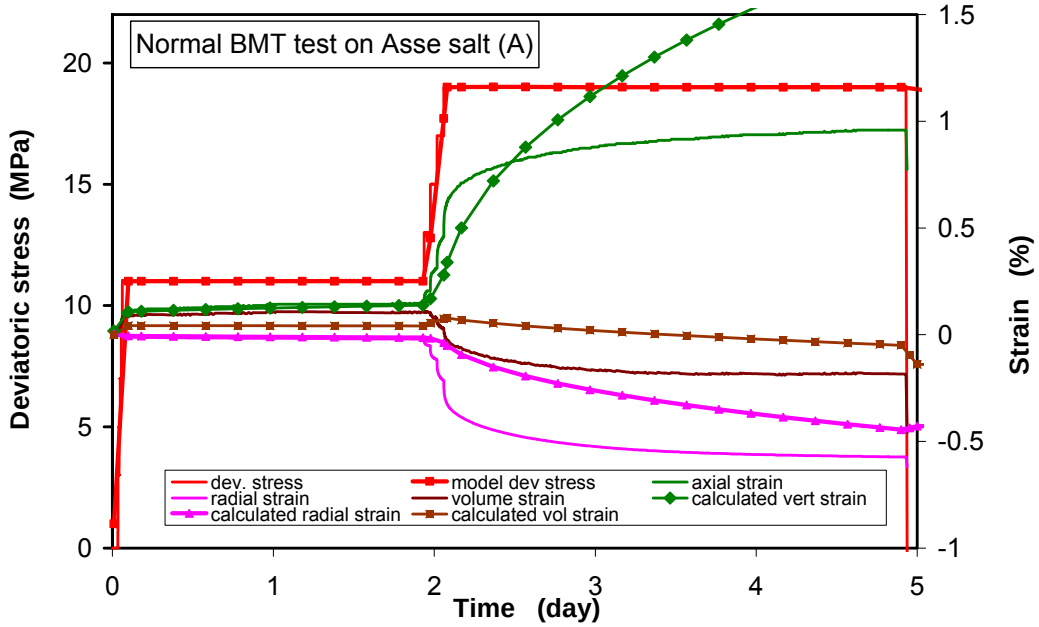

Fig. 5.1 Simulated and measured results for TC2A

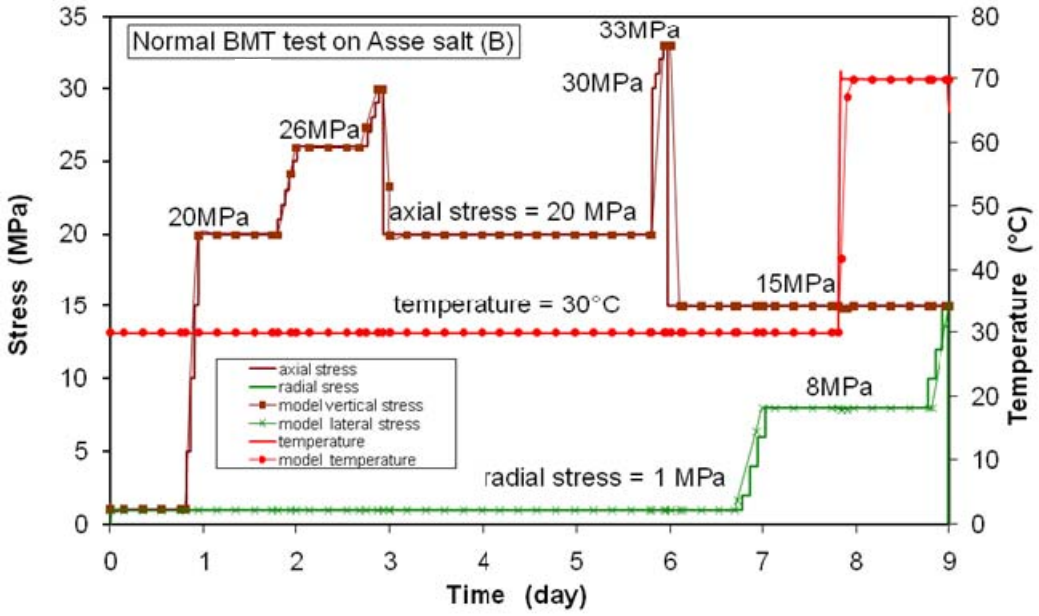

Fig. 5.2 Stress variation and temperature variation in the experiment TC2B (the variation used in the model is also shown)

The continuation of TC2A is TC2B, with the stress and temperature evolution described in fig. 5.2. It can be seen that several axial and radial stress changes take place, and the temperature is raised to 70 °C during the last day. Figure 5.3 shows the deformations measured and calculated for TC2B. Parameters are the same as in TC2A

(taken from previous calibration of the test on sample 2). It can be observed that the axial stress is well captured in the different stages of the test. However, the lateral stress is underpredicted by the model and this implies also some overprediction of the dilatancy. The overall results are relatively good but further refinement is possible in order to improve the model calculations.

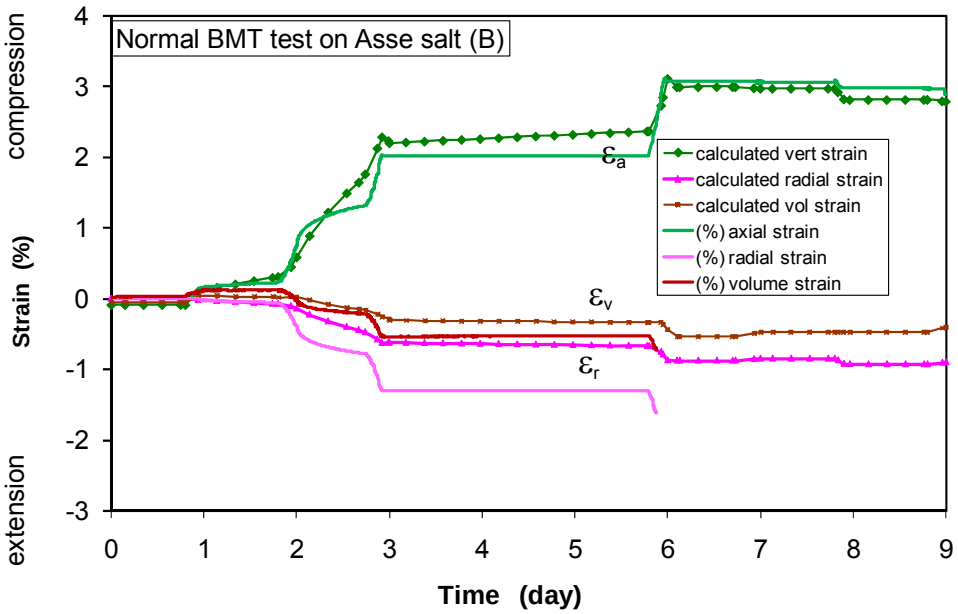

Fig. 5.3 Comparison of measured and calculated deformations during TC2B

Following the results of deformations, and specially dilatancy, the modeled results permit to determine the evolution of permeability. Figure 5.4 shows the evolution of permeability calculated with two possible equations. Model I consists in the simple application of a permeability as a function of porosity to the power of n = 3.

$$k = k_o \left(\frac{\phi}{\phi_o} \right)^n \qquad \phi_o = 0.0025 \qquad n = 3 \qquad k_o = 5 \times 10^{-20} \ \mathrm{m}^2 \tag{5.1}$$

In this equation the reference porosity is equal to 0.0025 and corresponds to the initial value in the sample before testing.

Model II is an interpretation of permeability as a function of microfractures which are characterized by an aperture (*b*) and a constant spacing (*s*). This model is described in more detail in /OLI 08/.

$$k = k_{matrix} + \frac{b^3}{12s} \qquad b = b_o + \Delta b \qquad \Delta b = s\Delta\varepsilon$$
$$k_{matrix} = 10^{-20}\ \mathrm{m}^2 \qquad (5.2)$$
$$b_o = 10^{-8}\ \mathrm{m}$$
$$s = 0.0002 \text{ and } s = 0.0001 \text{ and } s = 0.01$$

In this model, it is assumed that the changes in aperture can be calculated as a function of deformations. When dilatancy takes place, permeability increases. Compression under the initial aperture does not produce further decrease of permeability as it is assumed that the matrix permeability is constant.

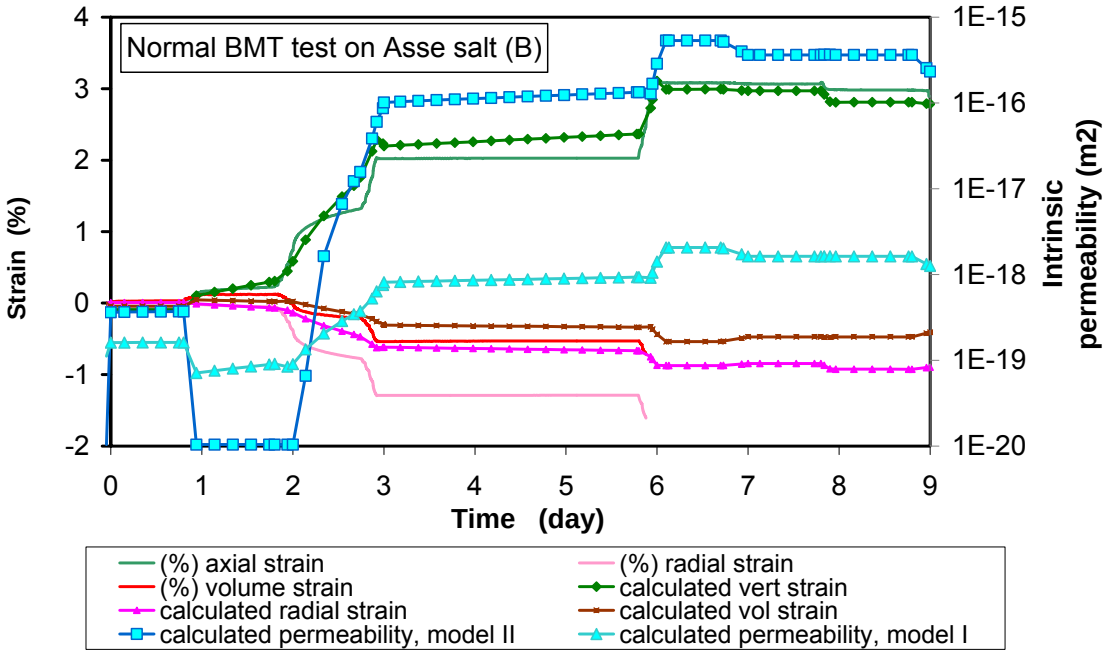

Fig. 5.4 Evolution of calculated deformations and calculated permeability (with Model I and Model II) during TC2B

5.1.2 Simulation of TC2B with alternative parameters

Because the volumetric strain of expansion is underpredicted, a modified analysis was performed using a_5 = 0.04 instead of 0.02 that was the value used before (see eq. 4.13 and 4.14). From model equations it can be seen that larger values of this parameter should produce larger dilatancy. The results with a modified parameter (a_5) are shown in fig. 5.5 and fig. 5.6. In order to readjust the permeability prediction, the spacing is now larger than s = 0.0001 m. The permeability model assumes a series of fractures,

parallel and ideal with very low spacing (0.0002 m or 0.0001 m) adjusted depending on the dilatance calculated. The asperity and tortuosity of the real fractures would modify the spacing, actually increasing it. In any case, the aperture and spacing correspond to the model and in reality other factors such as roughness, tortuosity and connectivity could be incorporated in the model.

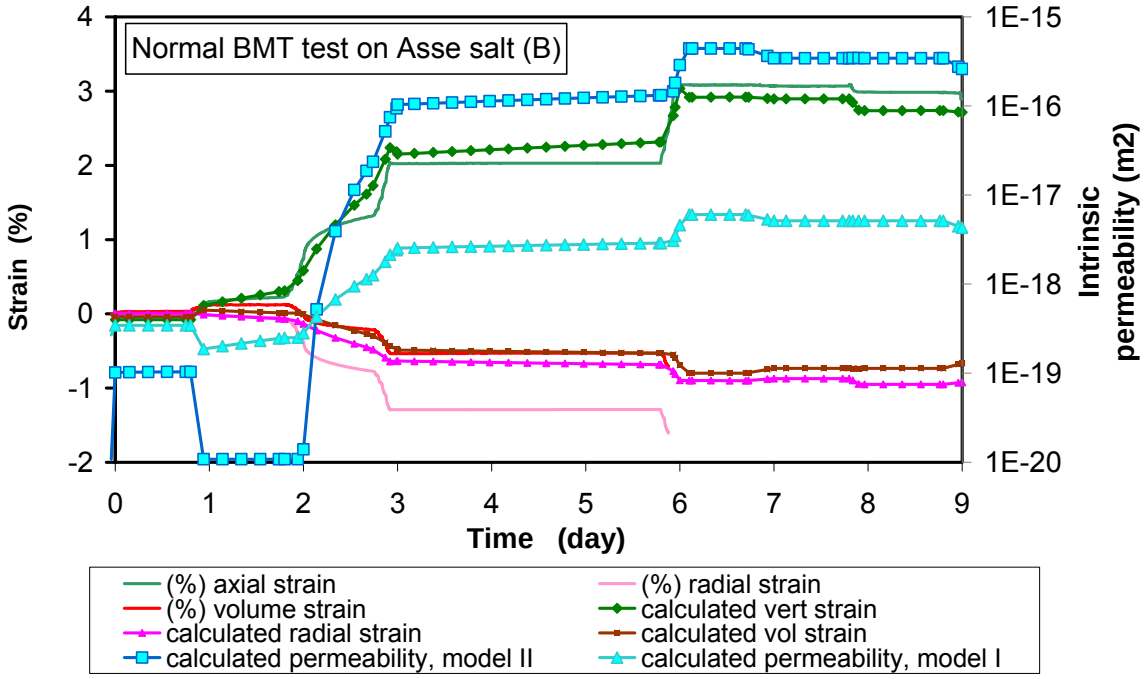

Fig. 5.5 Evolution of calculated deformations and calculated permeability (with Model I and Model II) during Test B. Modified parameter (a_5 = 0.04)

The vertical strain is well predicted in relative terms. In contrast, the lateral strain is underpredicted. In order to check that the total strain corresponds with the sum of deformations is still necessary to obtain the circumferential stress which directly comes as *u/r* i. e. displacement divided by radius. In any case, here the volumetric strain is calculated independently from porosity.

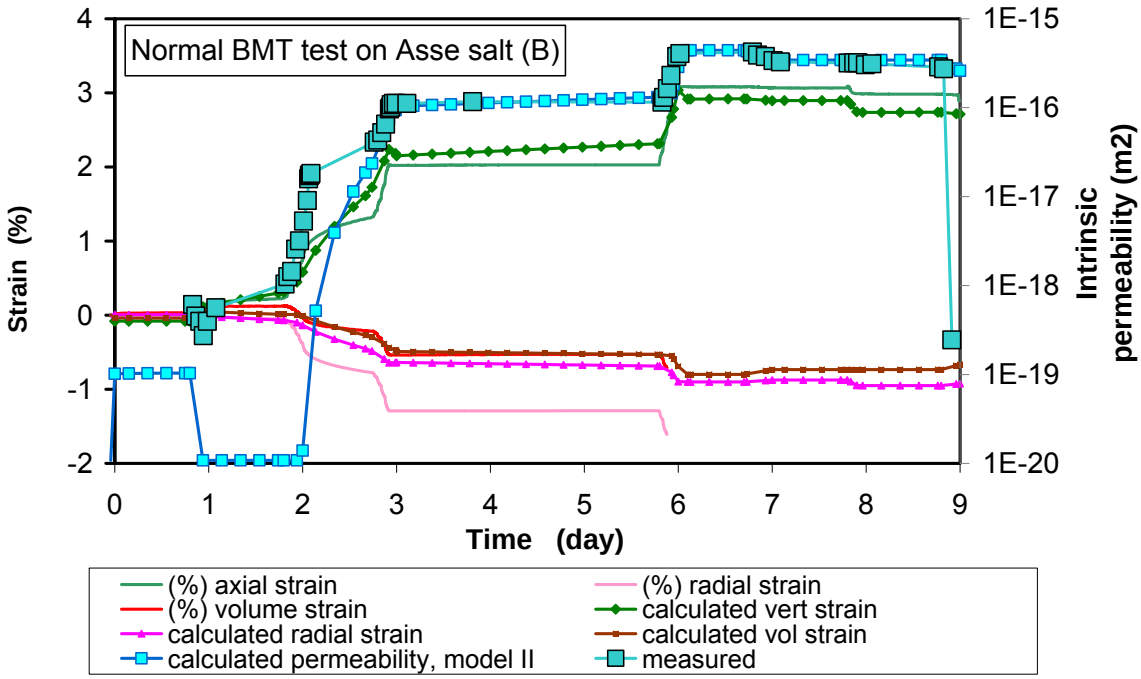

Fig. 5.6 Comparison of measured and calculated permeability

5.1.3 Simulation of the large hollow cylinder test

The test using the hollow cylinder apparatus was performed imposing a complex stress path (fig. 5.7). The stress path was modified during the test in order to achieve permeability increments. Actually, these were only measured when the inner stress was increased above the outer stress. This happens between 30 and 35 days as can be seen in fig. 5.7.

The permeability calculations are shown in fig. 5.8 together with the measured values. The model predictions show some trends which are consistent with measurement such as the starting of permeability increase, the decrease during compression (but at lower rate), further increase of permeability during unloading and decrease of permeability at heating. The values are not fully consistent even though the model has been recalibrated using s = 0.01 m, much higher than in the previous tests. The hollow cylinder conditions (tension) are quite different from the triaxial conditions (shear) to obtain dilatancy, so that may help to explain different spacing of fractures. Actually, a localized fracture in the hollow sample was observed, while in the triaxial tests, the same show failure in a more distributed way.

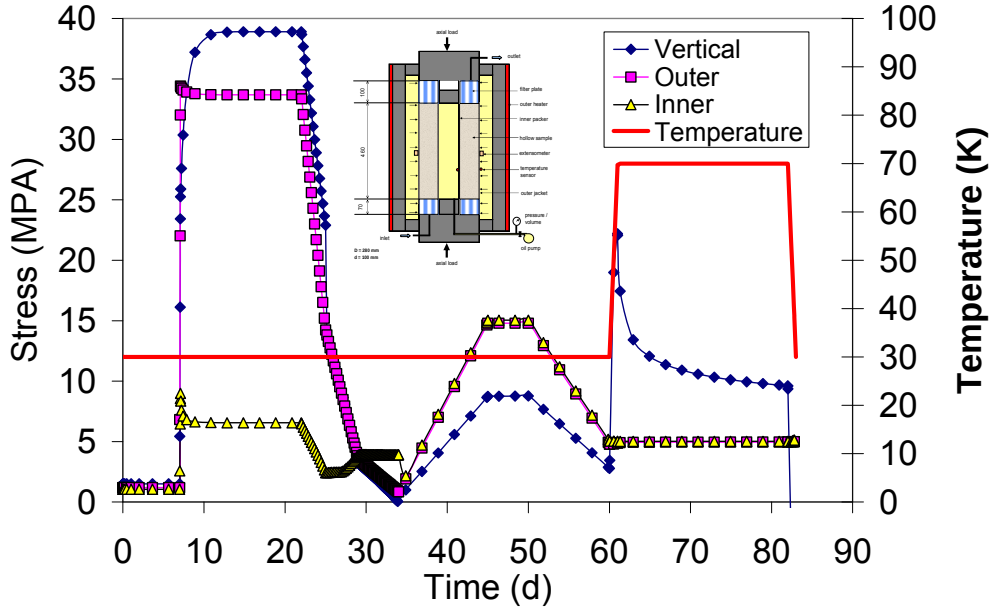

Fig. 5.7 Stress history applied in the hollow test to perform the large scale test

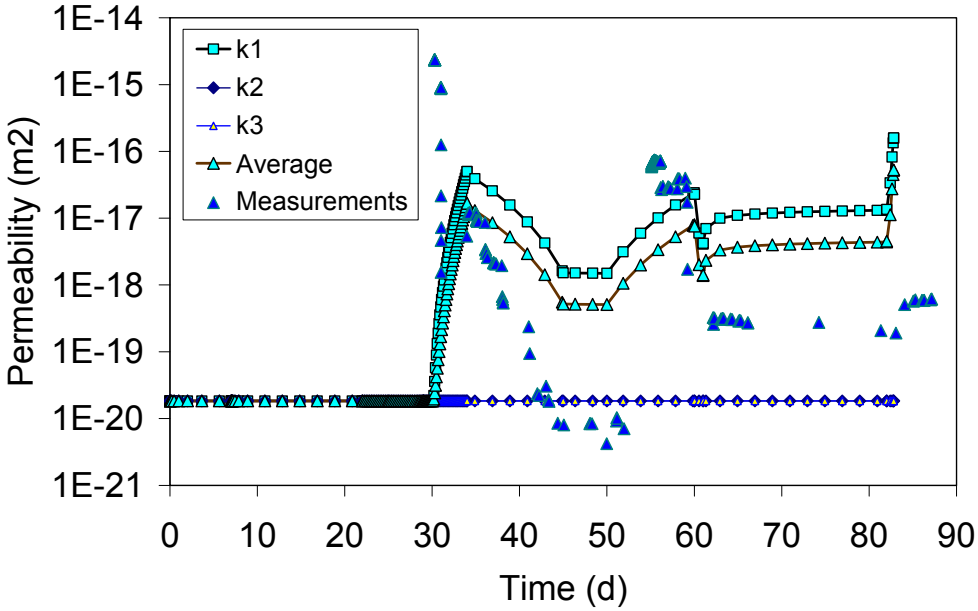

Fig. 5.8 Measured and calculated evolution of permeability (s = 0.01 m)

5.1.4 Conclusions

The predictive capabilities of the constitutive model for saline materials developed originally for crushed salt have been increased by the addition of a contribution to

produce dilatancy deformations. This model is empirical and relatively simple. Hardening is produced by a variable that depends on the dissipated shear work.

With the same parameters for the mechanical constitutive models, different tests were simulated: “GRS-sample 2”, “TC2A and B” and “Hollow Cylinder”. One parameter was modified in order to increase the dilatancy calculated in TC2B and hence improved the results (the permeability function was recalibrated by changing the spacing of microfractures).

In the case of the hollow cylinder, the parameters used up to TC2B were used as well. This gave little dilatancy and hence little change in permeability. In order to get permeability in the order of the measurements, the spacing was increased. This implies fewer fractures in the sample but with higher aperture increase. The fact that triaxial test and hollow test do not give the same function of permeability is not surprising as the deformation mode was very different.

The cubic law applied to apertures derived from deformations is a promising approach because it can be combined with anisotropy; it can be applied to unsaturated conditions by simply using Laplace’s Law to calculate the capillary pressure. However, the determination of the spacing is difficult and assumptions will have to be performed for the predictive application of the model.

5.2 FLAC simulation (IfG)

5.2.1 Blind prediction of the large hollow cylinder test

The blind prediction work on the large hollow cylinder was done in reference to the first large-scale test of GRS, first and second part (see figs. 3.13 and 3.14). Figure 5.9 shows the scheme of the set-up for laboratory testing and also for modelling. The hollow cylinder has a height of 525 mm, an outer radius of 140 mm and the borehole has an inner radius of 50 mm. In the calculation model the steel plates of the testing machine were recognized with a Young’s modulus of 210 GPa, a Poisson’s ratio of 0.28 and a density of $7.7 \cdot 10^3$ kg/m^3. The angle of friction between the rock salt sample and the steel was set to 30° which is equivalent to a friction coefficient of 0.6.

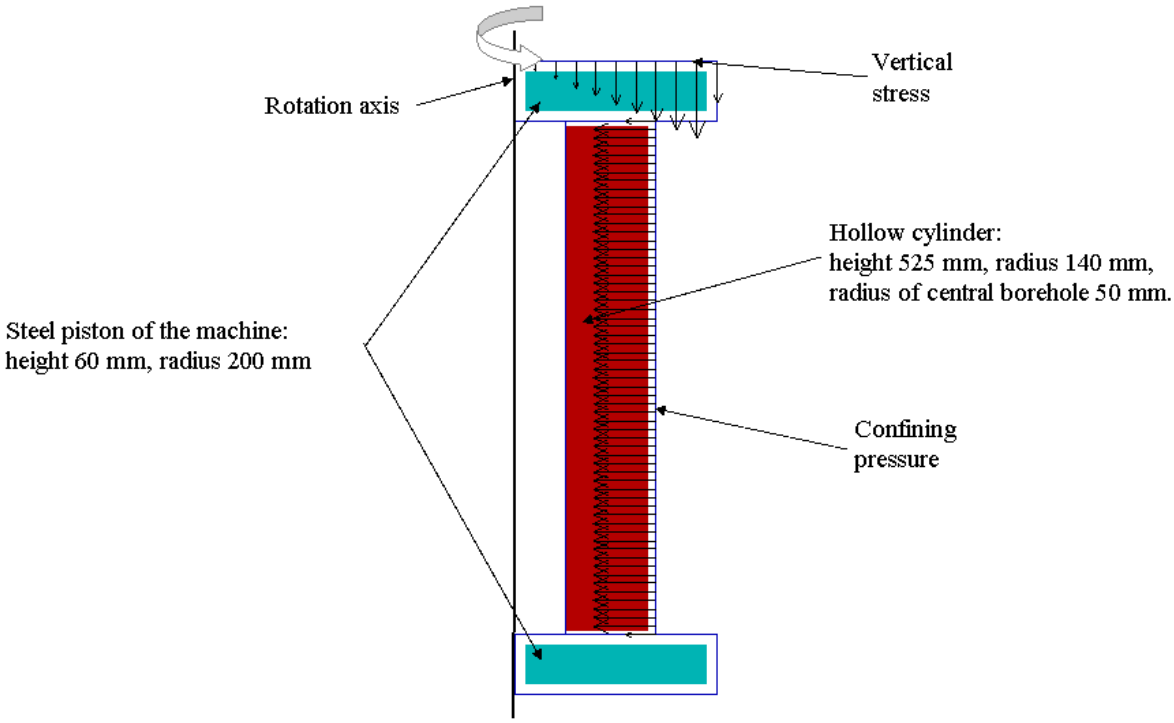

Fig. 5.9 Scheme of set-up for the laboratory test and the calculation model for the large hollow cylinder

Regarding to the symmetry conditions the axisymmetric code of FLAC can be used. The constitutive law was Günther-Salzer with the following parameters for rock salt Na2 *Asse Speisesalz*:

Elastic paramaters: Young's modulus 25 GPa

Poisson's ratio 0.24

Density 2.14·103 kg/m3

Creep: $A_p = 3.98 \cdot 10^{-29}\ d^{-1}$

$\mu = 3.0$

$t_0 = 1000$ d

$$n(\varepsilon_{Vol};\sigma_3) = \frac{n_{\varepsilon_{Vol;0}} + n_1 \cdot \exp(n_2 \cdot \sigma_3) \cdot [1 - \exp(-n_3 \cdot \varepsilon_{Vol})]}{(1-\varepsilon_{Vol})^{n_4}}$$

with $n_{\varepsilon Vol;0}$ = 15.18

n_2 = -0.33 n_4 = 0.3

n_1 = 0.8 n_3 = 2000

Dilatancy boundary: $\sigma_{eff}^{Dil}(\sigma_3) = \sigma_3 \cdot \left[\frac{D_1}{D_2 + \sigma_3} + D_3 \right]$

with D_1 = 8 MPa D_2 = 0.2 MPa D_3 = 3.7 MPa

Tensile strength: 1 MPa

Evolution of damage: $A_1(\sigma_3) = a_1 + a_2 \cdot \exp[a_3 \cdot \sigma_3]$ with $a_1 = 5{,}0 \cdot 10^{-3}$, $a_2 = 0{,}0135$, $a_3 = -0{,}4$

$A_2(\sigma_3) = a_4 + a_5 \cdot \exp[a_6 \cdot \sigma_3]$ with $a_4 = 1 \cdot 10^{-6}$, $a_5 = 2{,}5 \cdot 10^{-4}$, $a_6 = -6{,}25$

$A_3(\sigma_3) = a_7 + a_8 \cdot \exp[a_9 \cdot \sigma_3]$ with $a_7 = 0{,}0$, $a_8 = 5{,}13$, $a_9 = -0{,}3$

Similar to the first part of the first large-scale test of GRS the axial stress and confining pressure were applied with 15 MPa and, expecting a higher dilatancy, the interior pressure was set to zero. In fig. 5.10 is to see that after 7 days of creep the volumetric extension is calculated with 1 ‰ in a very small contour zone of about 5 mm. After an axial and outer stress increase to 20 MPa under further zero-loading of the interior borehole (similar to the second part of the first large-scale test of GRS) in fig. 5.11 the dilatancy goes up to 2 ‰ in a contour depth of 5 mm. The total creep time was 14 days.

Although the stress boundary conditions in comparison to the laboratory test of GRS were changed slightly to get a higher dilatancy it must be concluded from the blind prediction that at these low magnitudes of dilatancy in a very small contour zone of the borehole the proof of significant higher permeability represented an experimental challenge and was not sure. Indeed, a gas flow could not be observed in both parts of the large-scale test.

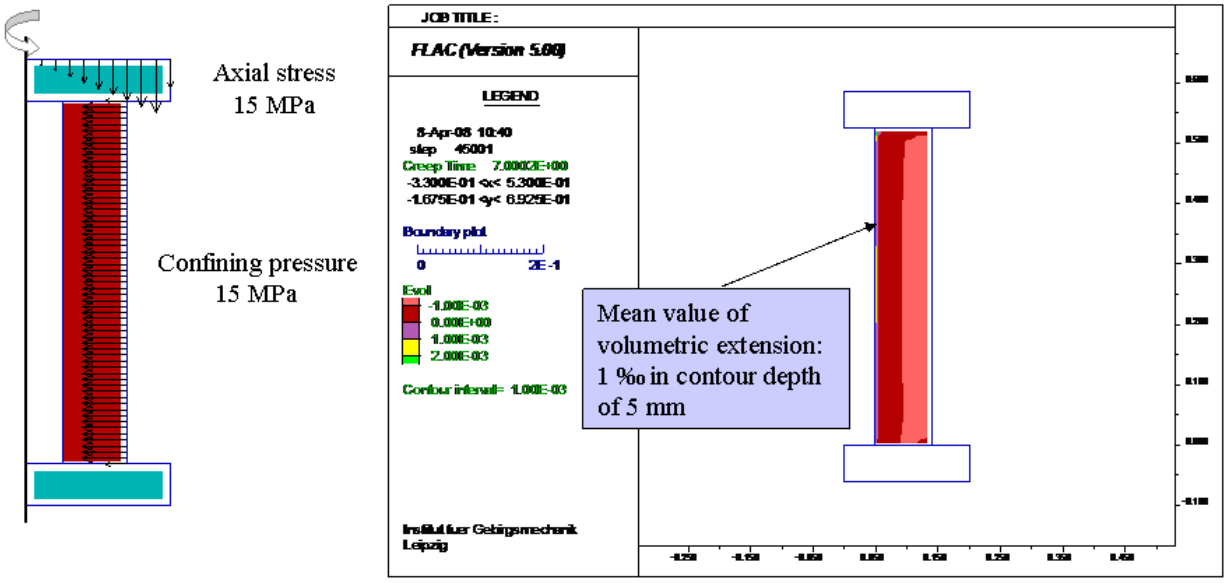

Fig. 5.10 Part 1: Axial stress and confining pressure 15 MPa, no interior pressure, 7 days creep

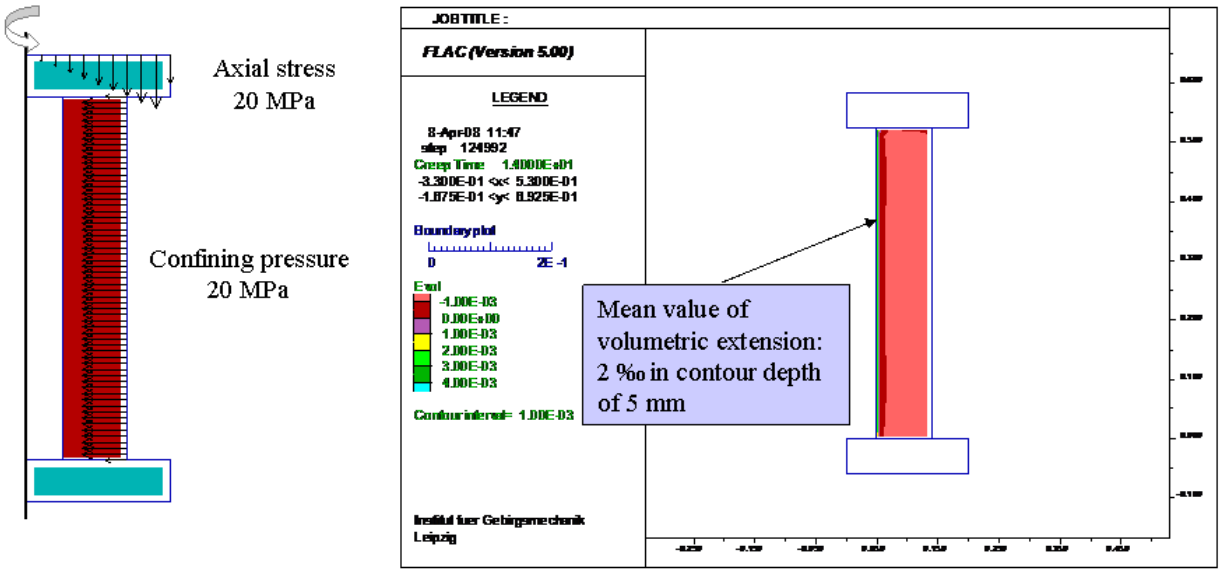

Fig. 5.11 Part 2: Increase of axial stress and confining pressure to 20 MPa, no interior pressure, 7 days creep (total 14 days creep)

Because further load conditions and experimental set-ups were not successful as well for generation of an EDZ relevant permeable contour zone it was decided that for the benchmark calculation two normal-scale samples of 100 mm diameter and 190 mm length were used for new tests. The model calculations regarding TC2A and TC2B are described in the next sections.

5.2.2 Blind prediction and interpretation modelling of benchmark test TC2A

Figure 5.12 shows the scheme of the set-up for triaxial testing and also for modelling. The cylindrical sample has a height of 190 mm and a radius of 50 mm. Again, in regard to the symmetry conditions the axisymmetric code of FLAC can be used.

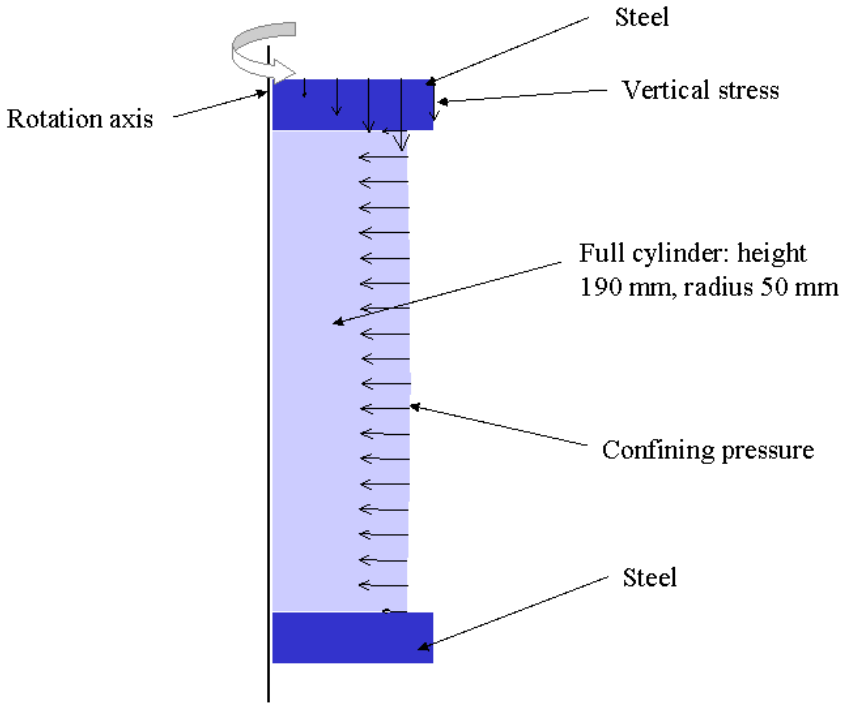

Fig. 5.12 Scheme of set-up for the laboratory test and the calculation model

The steel plates in contact to the top and bottom of the specimen represent the testing machine. The steel was modelled with Young's modulus of 210 GPa, Poisson's ratio of 0.28 and density of $7.7 \cdot 10^3$ kg/m^3. The angle of friction between the rock salt sample and the steel was set to 30°. Furthermore, the arrows along the mantle surface depict the confining pressure generated in the triaxial cell and the arrows at the top side sketch the axial force.

The material parameters for constitutive law Günther-Salzer were equivalent to the blind prediction work on the large hollow cylinder in section 5.2.1.

Figure 5.13 illustrates the test course of TC2A performed at GRS. The confining pressure was 1 MPa and the axial stress was raised after two days from 12 MPa to 20 MPa. The temperature was constant the whole time with 30 °C. The measured axial

deformation after an observation time of 5 days reached 1 %, the radial deformation was about 5 ‰ and the volumetric extension was generated to approximately 2 ‰.

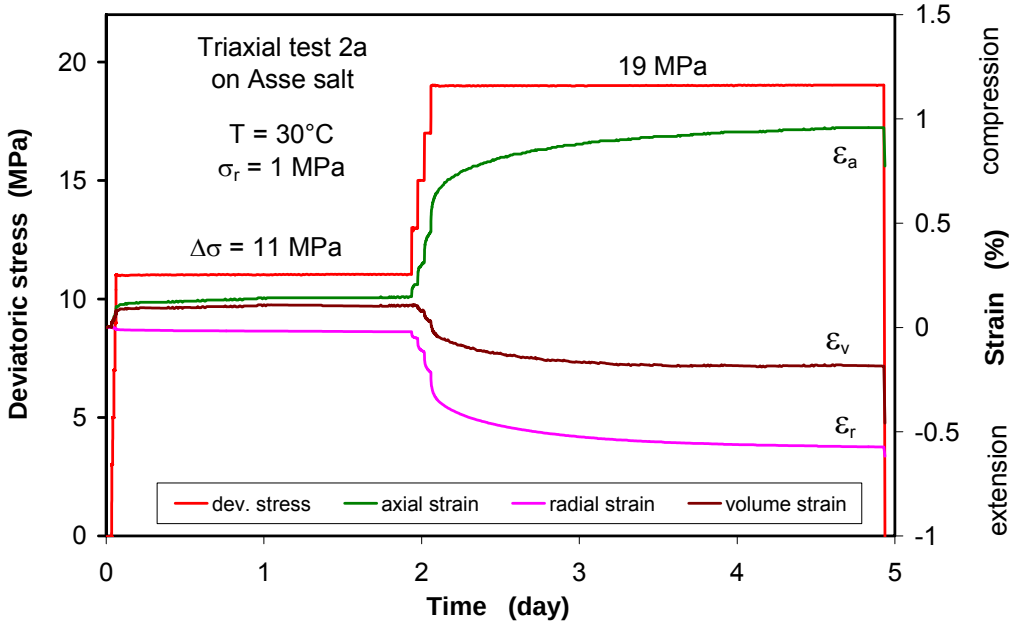

Fig. 5.13 Stress and temperature conditions at TC2A with measured strains versus time

A significant dilatancy with measurable permeability increase can only be expected if the applied stresses cause a loading in the dilatant domain. In fig. 5.14 the two in the last years used dilatancy boundaries are displayed. The dilatancy boundary after Cristescu and Hunsche /CRI 98/ is at a lower level and represents the onset of micro-cracking. At this stage volumetric compaction still exists. The dilatancy boundary after Schulze et al. /SCH 01/ is characterized by the measurable volumetric minimum. It means, after exceeding of the second one the volume goes up due to damaging and permeability increases. In THERESA only the second boundary is relevant.

The stress state σ_3 = 1 MPa, σ_1 = 12 MPa is located at that boundary and the stress state σ_3 = 1 MPa, σ_1 = 20 MPa lies narrow to it. For evaluation, one has to recognise that this boundary condition is more a band than a distinct line /SCH 07/. Consequently, under the both stress states no notable permeability elevation could be expected. In confirmation, in /ZHA 09/ it is stated that although a volumetric increase of ~ 2 ‰ took place, no gas outflow could be observed at injecting pressure of 0.5 MPa.

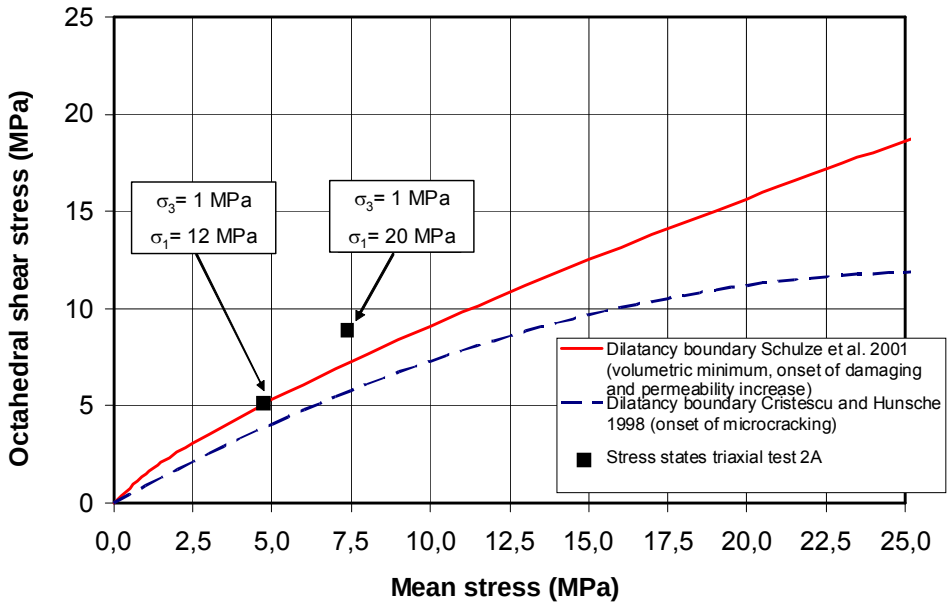

Fig. 5.14 Location of stress states for test TC2A in octahedral stress space

The two stress states can be converted into the octahedral stress space using the equations:

Mean stress $\sigma_o = \frac{\sigma_1 + 2 \cdot \sigma_3}{3}$ and

Octahedral stress $\tau_o = \frac{\sqrt{2}}{3} \cdot (\sigma_1 - \sigma_3)$, σ_1 = axial stress, σ_3 = confining pressure

In fig. 5.15 the in the model applied differential stress (black colour) is drawn. The differential stress denotes the stress difference $\sigma_1 - \sigma_3$. The oscillation is typical for the solution algorithm of code FLAC: FLAC uses the full dynamic equations of motion, even in static calculation problems. Thus, every model change (geometry, boundary conditions, material parameters) causes a disturbance of equilibrium. The oscillation is damped very fast, but in a history plot the excursion is visible.

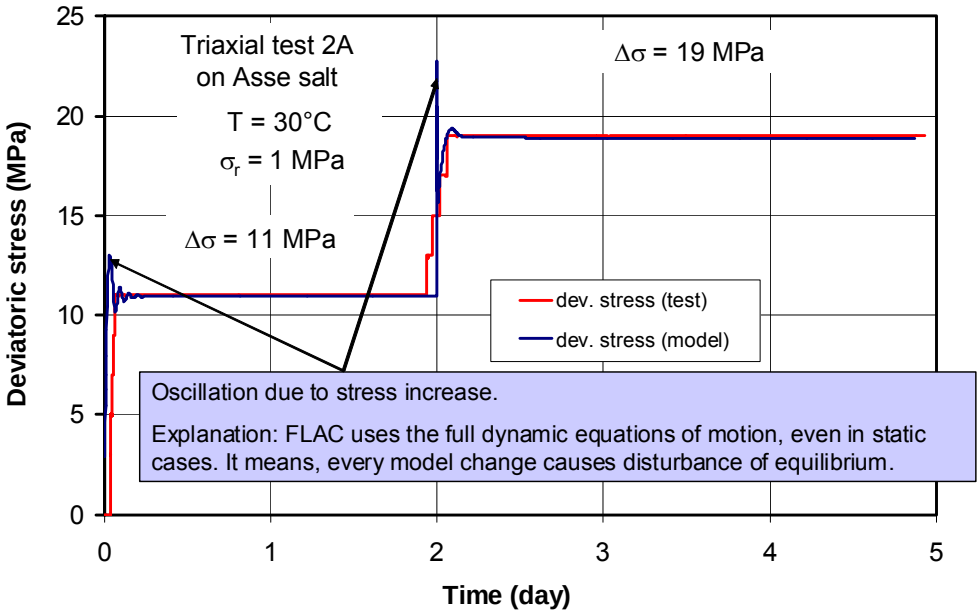

Fig. 5.15 Blind prediction of TC2A: Applied differential stresses (black colour)

Figure 5.16 illustrates the in blind prediction of TC2A calculated axial and volumetric deformation (bold lines) in comparison the later provided test results (thin lines). For the radial deformation no history plot was defined separately, the radial deformation is included in the volumetric strain. The tendency of both blind predicted magnitudes is calculated sufficiently, but the quantitative agreement could be better. Obviously, the in the calibration phase in /WIE 08/ for simulation of strain rate driven laboratory tests used parameter set cannot model all thinkable loading conditions in the same quality.

For better agreement, in the interpretation modelling phase of TC2A a parameter adaptation was made. For that, only the creep parameters described in section 5.2.1 were changed:

$A_p = 1 \cdot 10^{-76}\ d^{-1}$ $\mu = 10$ $n_{\varepsilon Vol;0} = 41$

Furthermore, in fig. 5.17 it can be seen that the applied deviatoric stress (black curve) was increased stepwise. Thus, the stress oscillation could be reduced.

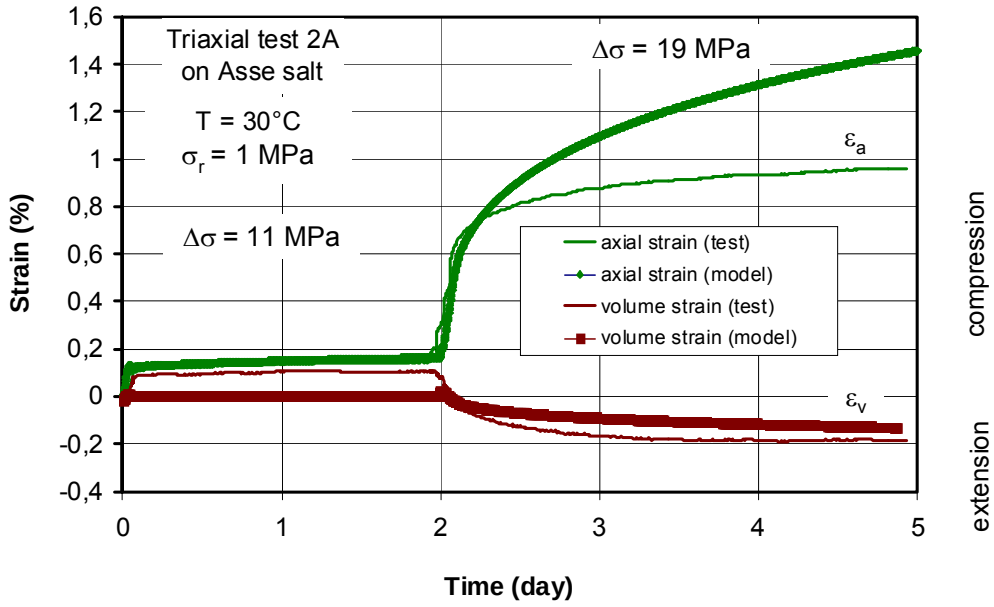

Fig. 5.16 Blind prediction of TC2A: Calculated (bold lines) strains in comparison with later provided test results (thin lines)

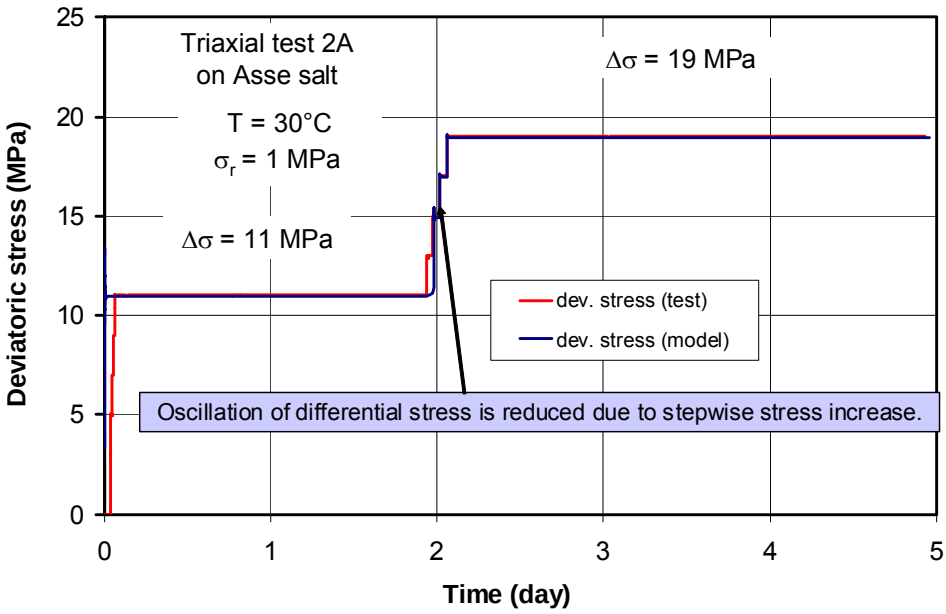

Fig. 5.17 Interpretation modelling of TC2A: Applied differential stresses (black colour)

Figure 5.18 indicates the almost perfect agreement between calculated and measured axial deformation (green colour). The modelled volumetric strain (brown colour) is in a range of about 50 % of the measured magnitude.

From now on the parameter set is not changed anymore. The only new parameterization for simulation of TC2B is the initial strain hardening of about 1 % generated in TC2A. The benchmark test TC2B was restarted with an already deformed sample.

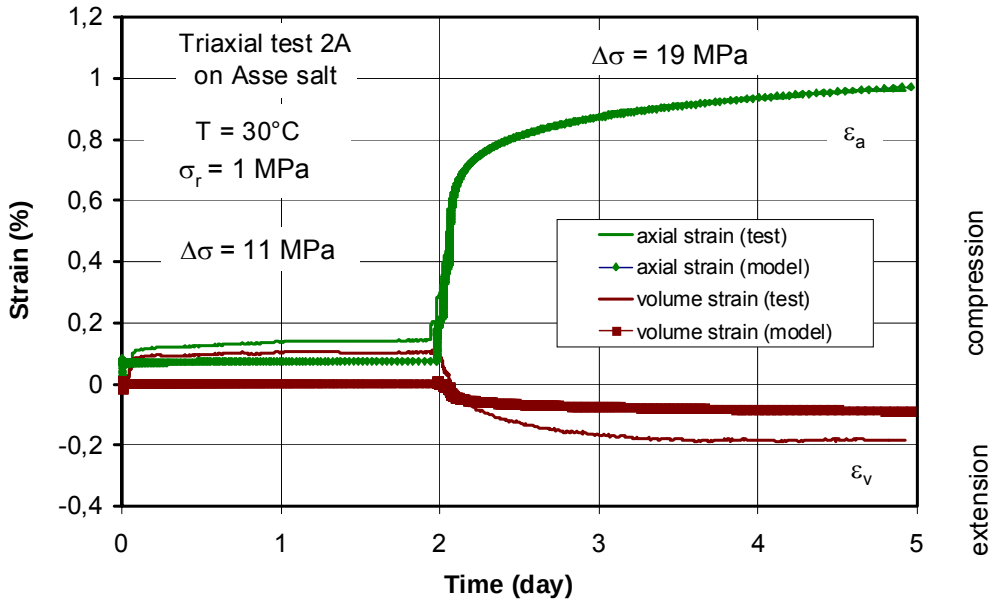

Fig. 5.18 Interpretation modelling of TC2A: Calculated (bold lines) strains in comparison with later provided test results (thin lines)

5.2.3 Interpretation modelling of benchmark test TC2B

Figure 5.19 illustrates the test course of TC2B performed at GRS. The confining pressure was raised after 7 days from 1 MPa to 8 MPa. The axial stress was increased and decreased in several steps which are depicted in fig. 5.19. The temperature was 30 °C up to 7.8 days and then rose to 70 °C.

The locations of all stress states in the octahedral space applied in fig. 5.19 are displayed in fig. 5.20. In recognition of the already generated volumetric deformation of about 2 ‰ in TC2A for all loading phases from the beginning up to 6 days an increased permeability (higher than the initial permeability of undisturbed rock salt) was to suppose. The differential stress reduction in the last 3 days led to an approach to the dilatancy boundary (σ_1 = 15 MPa, σ_3 = 1 MPa) respectively to a shifting in the non-dilatant domain (σ_1 = 15 MPa, σ_3 = 8 MPa). For the last load condition (σ_1 = 15 MPa, σ_3 = 8 MPa) a permeability reduction is to expect.

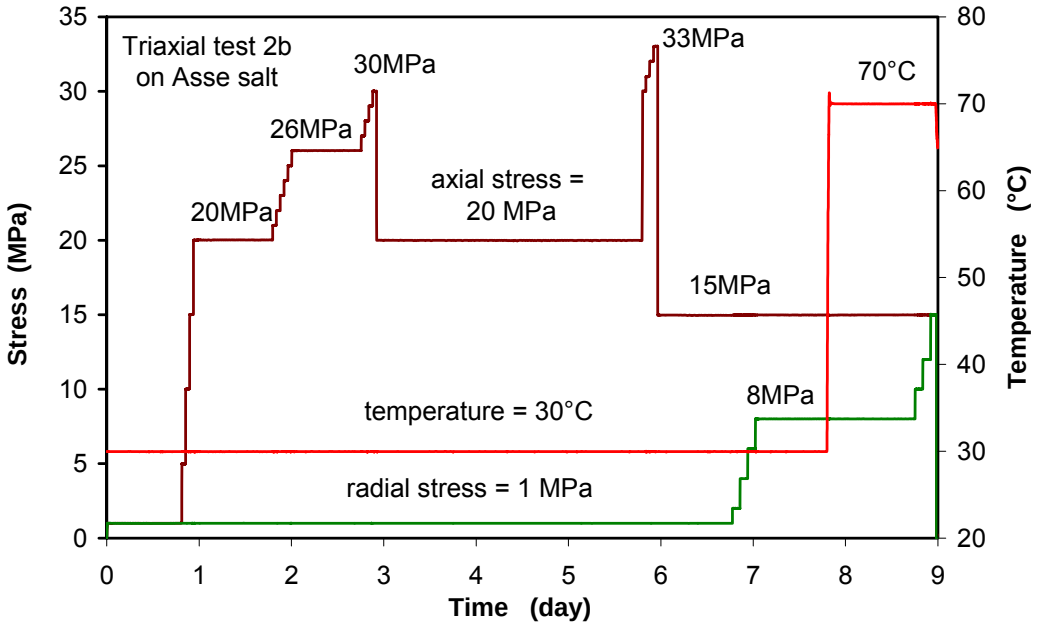

Fig. 5.19 Stress and temperature conditions at TC2B (previously deformed salt sample)

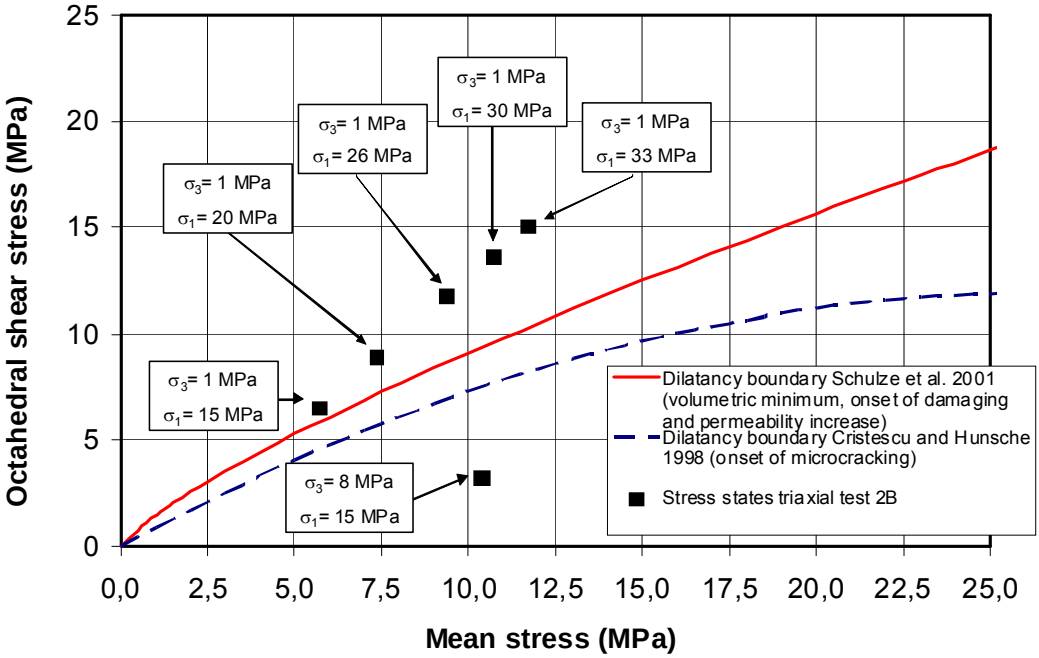

Fig. 5.20 Location of stress states for TC2B in octahedral stress space

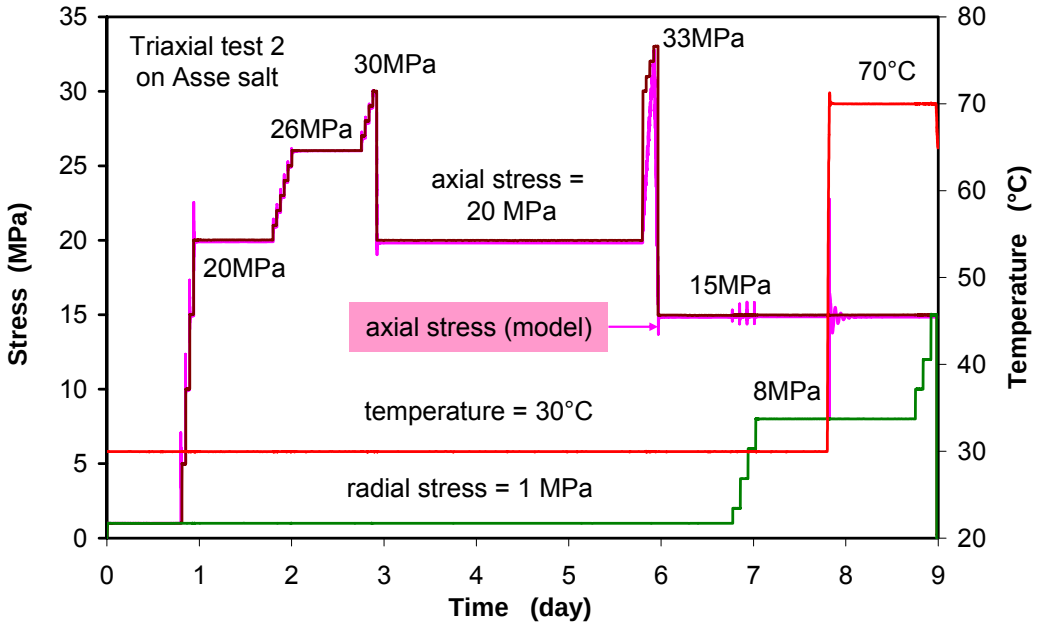

Fig. 5.21 Test course of TC2B, applied axial stress in magenta colour

Figure 5.21 illustrates the test course of TC2B and the calculated axial stress. The confining pressure was raised after 7 days from 1 MPa to 8 MPa and finally to 15 MPa. The axial stress was increased and decreased in several steps. The temperature was 30 °C up to 7.8 days and then rose to 70 °C.

The in the model applied axial stress is drawn in magenta colour. Again, the stress oscillation was reduced due to the stepwise build up of σ_1.

The calculated axial and volumetric strain (bold lines) is visible in fig. 5.22. The agreement to the test results is very good. Unfortunately, the observation of volumetric strain was interrupted after 6 days, but a comparison was made possible because of submission of the final magnitude (red triangle in fig. 5.22).

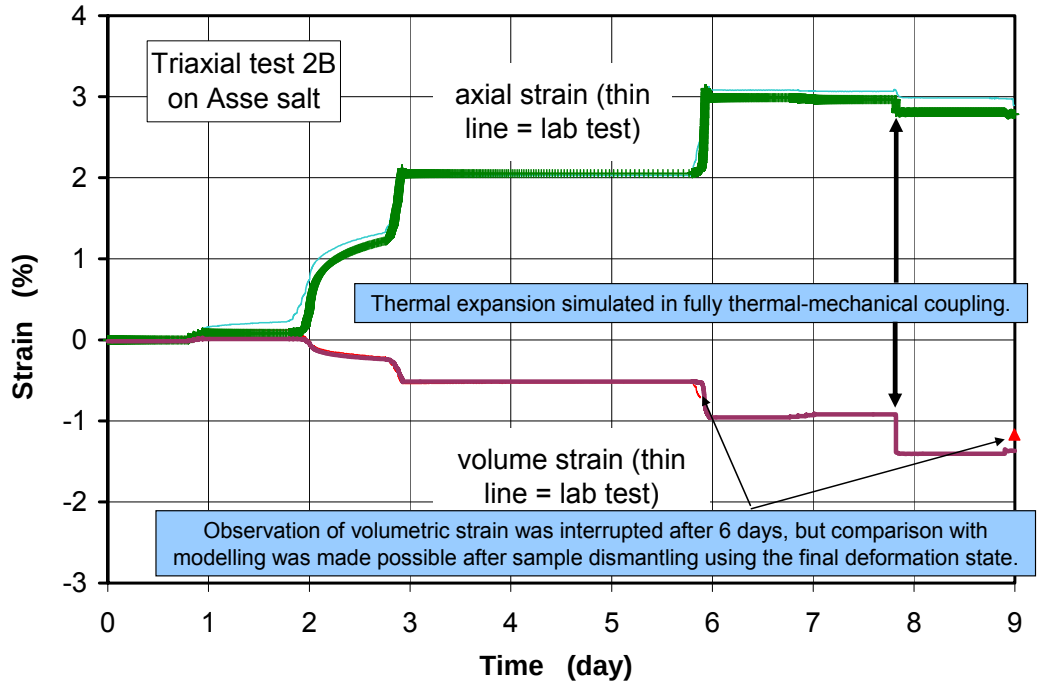

Fig. 5.22 Comparison of measured axial and volume strain with calculation results in TC2B

The thermal expansion after a testing time of 7.8 days was modelled in the fully coupled thermal-mechanical mode of FLAC. It is not caused by higher dilatancy (damaging). The thermal parameters of rock salt for a temperature of 70 °C were taken from the project BAMBUS II /BEC 04/:

- Specific heat = 868 J/(kg·K)
- Isotropic thermal conductivity = 4.6 W/(m·K)
- Coefficient of linear thermal expansion = $40 \cdot 10^{-6}$ 1/K

Additionally, the creep factor A_p is increased by use of the Arrhenius term.

Regarding the porosity-permeability-relation the reference /HEE 04/ was used. Heemann's adaptation is based on the laboratory tests of Popp /POP 02/. Thereby, the dilatancy is set equivalent to the porosity. Both parameters represent the interconnected fluid-accessible pore and micro-fracture space. In fig. 5.23 the relations for the two in TC2B applied confining pressures 1 MPa and 8 MPa are denoted.

$$k = \frac{k_{tp}}{\left[\left(\frac{\phi}{\phi_{tp}}\right)^{-4} + \left(\frac{\phi}{\phi_{tp}}\right)^{-1,07} \right]}$$

$$k_{tp} = a_k \cdot \exp(b_k \cdot \sigma_{min})$$
$$\phi_{tp} = a_\phi \cdot \exp(b_\phi \cdot \sigma_{min})$$

$a_k = 4{,}27E-14\ m^{-2}$
$b_k = 1{,}26\ MPa^{-1}$
$a_\phi = 0{,}0263$
$b_\phi = 0{,}3093\ MPa^{-1}$

U. Heemann,
S. Heusermann
(modified after T. Popp
for low porosities)

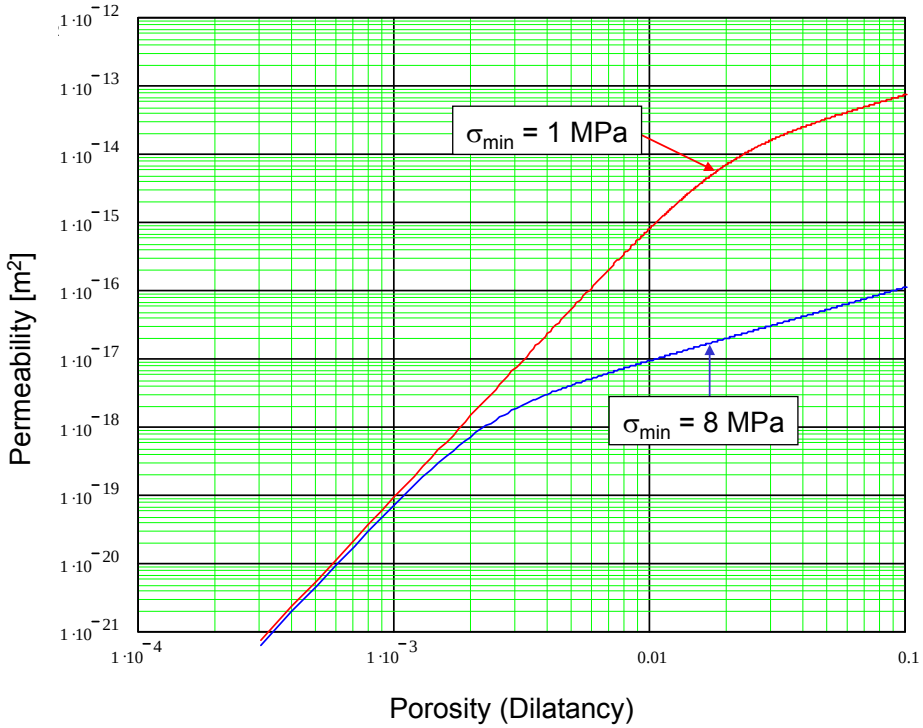

Fig. 5.23 Porosity-permeability-relation: Dependence on dilatancy and confining pressure

The permeability in fig. 5.24 (basis is the porosity-permeability-relation in fig. 5.23) was calculated using the volumetric plastic strain (volumetric deformation caused by damage). The integral sample expansion, calculated using the nodal point displacement of the sample, includes the thermal expansion and would yield an overestimation of permeability. Considering the high sensitivity of permeability tests at complex boundary conditions the agreement between the two curves can be seen as sufficiently. Remarkably, the thermal expansion after 7.8 days causes no permeability increase.

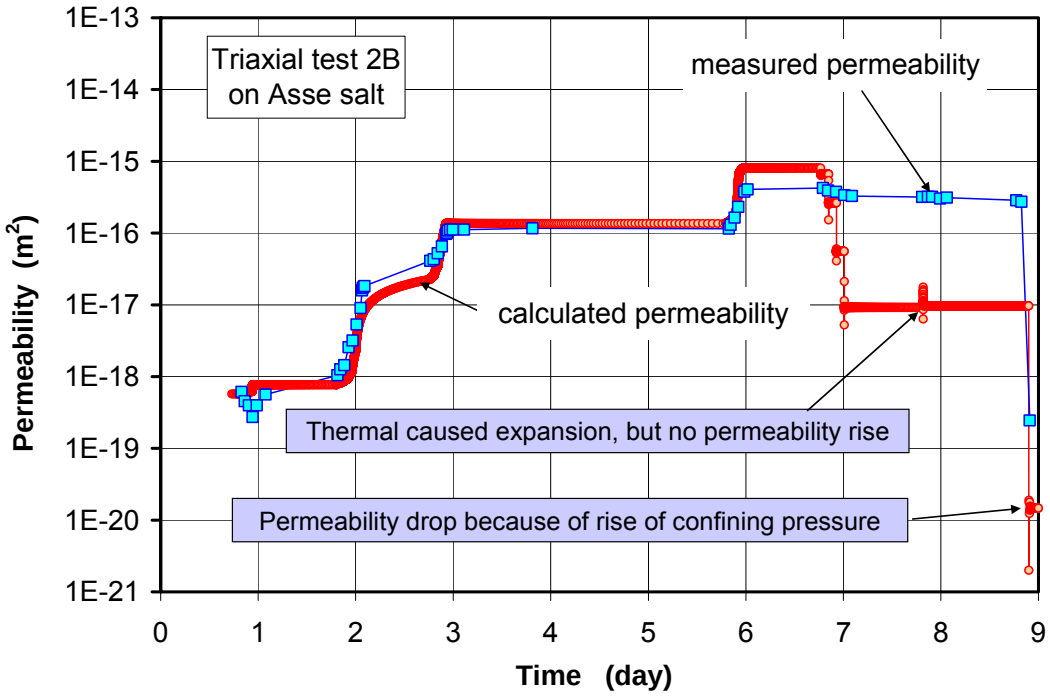

Fig. 5.24 Comparison of in TC2B measured permeability with in dependence on dilatancy calculated magnitudes

5.2.4 Conclusions

The conclusions can be summarized in bullets:

- Blind prediction of laboratory (or in-situ) tests on basis of calibrated parameter sets is possible. The tendency will be given in a correct range, but for better agreement an interpretation modelling may be necessary.
- In FLAC stress changes must be generated stepwise (every model change causes a disturbance of equilibrium).
- For modelling of the temperature expansion thermal-mechanical coupling was used. The thermal expansion was caused elastically, not due to damaging.
- For permeability calculation the volumetric plastic deformation (damaging deformation) must be used (not integral extension). Otherwise, the expansion at heating would pretend a damaging following permeability increase.

5.3 FLAC^{3D} simulation (DBE TEC)

5.3.1 Simulation of TC2A and TC2B

GRS carried out laboratory tests on Asse Speisesalz in order to obtain data that resemble measurements from damaging and re-compaction processes within the EDZ in rock salt, /ZHA 09/. The evolution of the permeability of rock salt when subjected to such processes was of major interest. Unexpected breakage of a sample and power supply failures during the experiment made the data obtained less suitable for comparative benchmarking. Moreover, numerical instabilities induced by the used constitutive laws for dilatant creep did not allow to simulate the tests on hollow cylinders together with their loading conditions. Therefore, the benchmarking was restricted to the obligatory test case TC2 for a plain cylinder. In TC2A, a cylindrically shaped sample with an initial height of 0.19 m and a radius of 0.1 m was loaded with axial and radial stresses and heated to specific temperatures according to a defined time dependent scheme, the loads applied in the two phases are shown in fig. 5.25. After 5 days, the experiment was interrupted due to a failure of the power supply, fig. 5.25 (a). The test was resumed as TC2B with the already damaged sample. Hence, two measurement campaigns of 5 days, fig. 5.25 (a), and 9 days length, fig. 5.25 (b), exist.

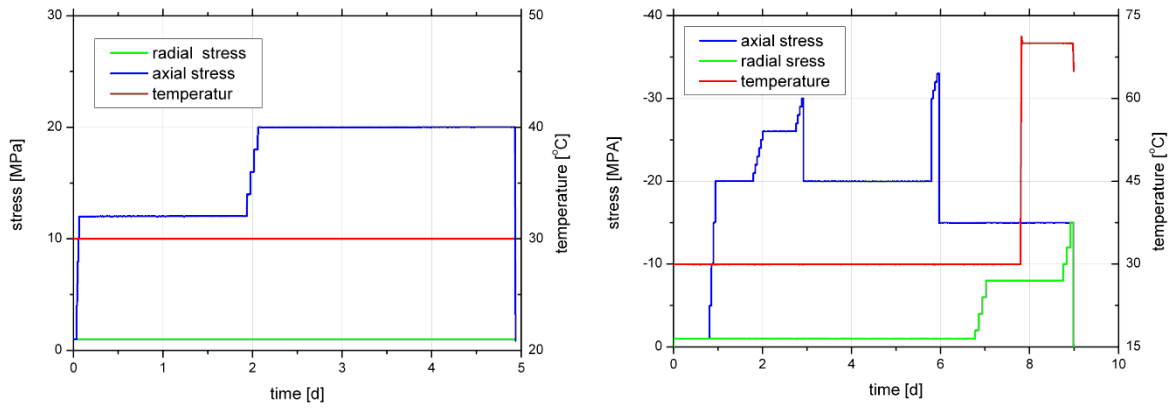

(a) *(b)*

Fig. 5.25 Loading scheme of TC2, phase TC2A (a) and phase TC2B (b)

A purely mechanical model was used to perform the simulations. The changing temperature in phase TC2B was treated as a time-dependent parameter uniformly set within the whole sample. The permeability of the sample was derived from the local permeability distribution by means of an algorithm which is presented below. A quarter

of a cylinder was chosen as a suitable geometry with appropriate boundary conditions on the planes of symmetry, fig. 5.26. In the set-up of the simulation, the distinct bodies of salt sample and piston are rigidly coupled to each other. The load is applied as stress boundary condition on the top surface of the upper piston (axial load) and the lateral cylinder surface of the sample. These two load sections vary independently from each other over time according to the loading scheme of the experiment as shown in fig. 5.25. The displacements on all other boundary surfaces are assumed to vanish in normal direction as shown in figure 5.26 (c).

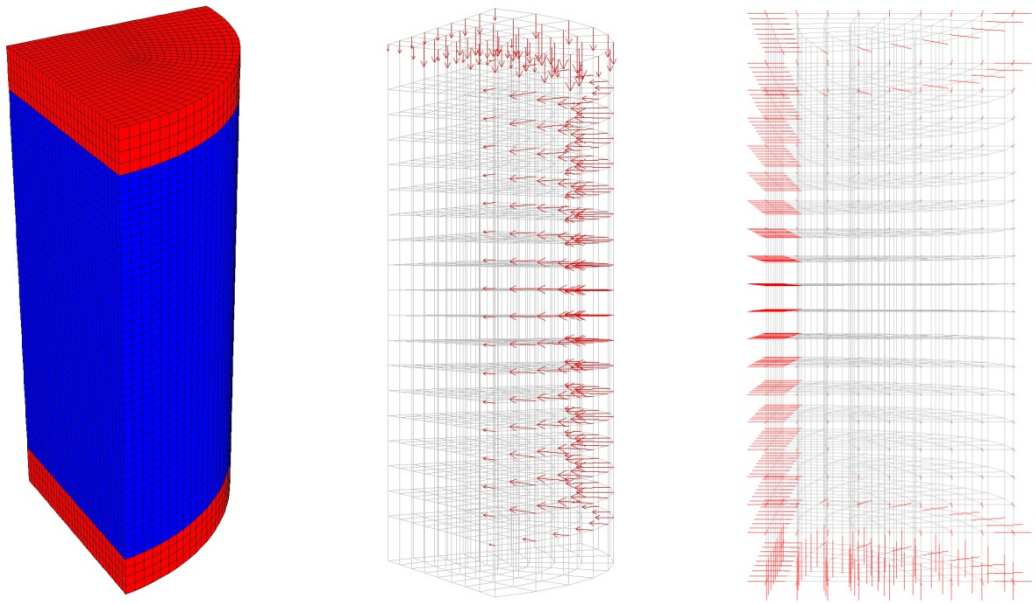

(a) *(b)* *(c)*

Fig. 5.26 (a) Discretization of pistons (red) and sample (blue) on calculation grid
(b) axial and radial loading on the top and the lateral surface (coarse grid)
(c) grid points fixed in normal direction to corresponding planes (coarse grid)

The relevant data concerning the mechanical properties which are derived from the laboratory tests are axial, radial, and volumetric strain of the samples. These three quantities are a measure of the global geometric sample distortion. For the determination of the first two quantities, the grid points marked in orange and red in fig. 5.27 are observed during the simulation process. Three of the points are situated on the centre axis, i. e. at the top, the centre, and the bottom of the line. The fourth point lies on the outer surface halfway up the cylinder, initially. Height and radius of the virtual sample is measured as sketched in fig. 5.27.

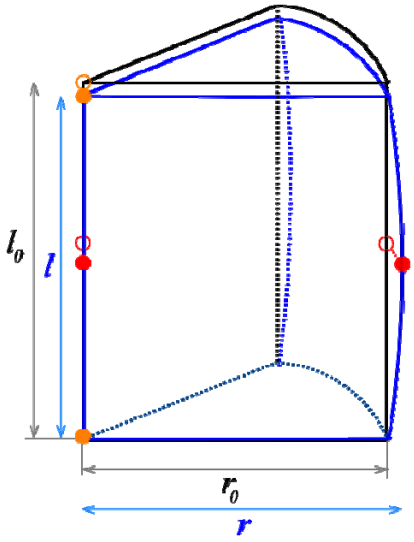

(a)

axial and radial strains

$$\varepsilon^a = \frac{l - l_0}{l_0} \text{ and } \varepsilon^r = \frac{r - r_0}{r_0}$$

volume change

$$V = \sum_{i=1}^{n} V_i \text{ and } \varepsilon^V = \frac{V - V_0}{V_0}$$

with number of zones in the model n

(b)

Fig. 5.27 (a) Observation points for the determination of axial and strain
(b) quantities to be determined

Sets of evaluated parameters were not available for the new models. Unfortunately, they could not be identified in advance for the complete model. Thus, elastic properties are standard values, parameters for stationary and transient creep were taken from BGR-94097 and BGR 95015. For the linear model of dilatant creep, this was done with the parameter settings given in /WIE 08/. For the quadratic model, no reliable input data was available and values had to be determined. All material parameters used in the different calculations are given in tab. 5.1.

Tab. 5.1 Material properties

Elastic properties					
Young's modulus	25.0 GPa				
Poisson's ratio	0.27				
Density of salt	2,187 kg m^{-3}				
Stationary creep					
A	0.18 d^{-1}				
Q/R	6490 K				
N	5				
$\tilde{\sigma}$	1 MPa				
Transient creep					
b0	36	34		34	
b1	220 d^{-1}	100 d^{-1}		100 d^{-1}	
b2	0.004				
Dilatant creep (quadratic model)			**Dilatant creep (linear model)**		
	case Q1	case Q2		case L1	case L2
CH-criterion	no	yes		no	no
C	1.0 d^{-1}		C	1.0 d^{-1}	
m	2.7		m	8	7
c_q	100		a_1	2.5	
c_p	5		a_2	1.8 $Pa^{-1/4}$	
			a_3	2.5	
			a_4	0.7 $Pa^{-1/4}$	
			a_5	0.02	
			a_6	0.02 Pa^{-1}	
			W_0	35 kJ m^{-3}	

Results obtained with the linear dilatancy model

The constitutive law extended by the linear dilatancy model could only be applied to TC2A (fig. 5.28). This is due to the fact that unloading of the sample to the initial conditions of phase B resulted in numerical failure shortly after reaching this state. Different stress paths were tried for unloading the sample but the numerical failure could not be avoided in this stationary phase. Two sets of parameters were tried, where the only variation is the value of the exponent of the dilatancy model which was reduced from 8 (case L1) to 7 (case L2) as the calculated volumetric strain

overestimated the measured one. However, when the exponent is set to 7, the strain is far too small at the end of phase A. With the current parameter settings, the constitutive law is not able to reproduce the sharp increase of strains when the axial load is increased from 12 MPa to 20 MPa. Furthermore, the calculated strains do not become stationary at the end of this phase like the measured ones almost do. The response of the sample during the first two days was expected to be purely elastic as creep does not gain great importance during this period. But the measured data show a volumetric shrinkage which cannot be fully explained by an elastic response only.

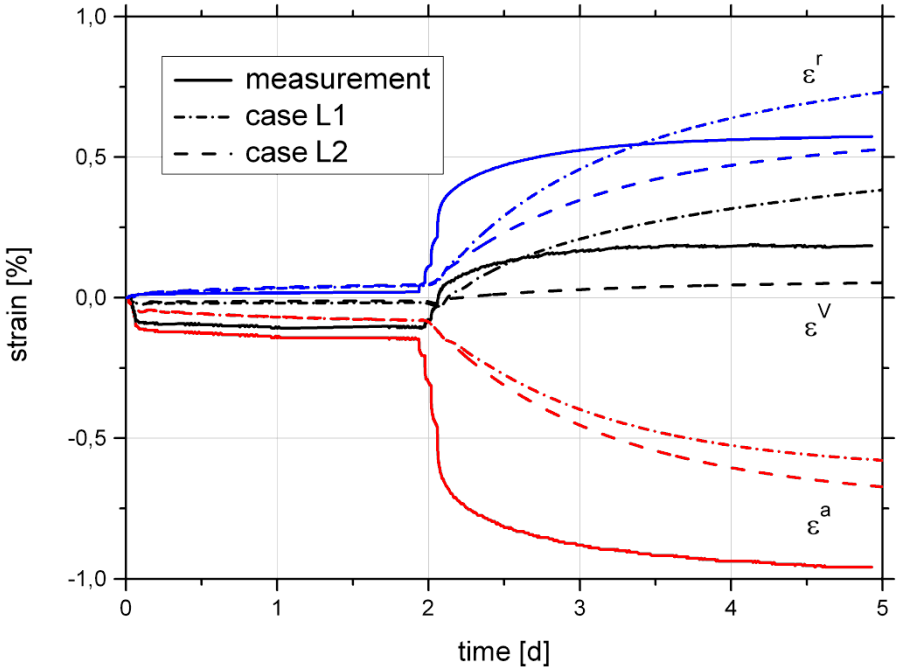

Fig. 5.28 Simulation results with the linear dilatant model for TC2A

Results obtained with the quadratic dilatancy model

The simulation results of the quadratic model for TC2A are shown in fig. 5.29. The development of the volumetric strains of both cases Q1 and Q2 is identical as the stress states induced by the boundary loads lie within the dilatant domain according to the Cristescu-Hunsche-condition (CH-condition). The two cases differ in the parameterization of transient creep as can be seen clearly from the fact that transient creep becomes stationary much faster in case Q1 than Q2 as the parameter b_1 is larger in the first case. As the strain amplitude of transient creep is determined by b_0/b_1, the maximum strain effect is smaller for Q1 than for Q2 as verified by the diagram. As in the cases of L1 and L2, the axial and radial strain response to the increase of differential stress is too slow. The volumetric strain increases with a constant rate. This

is due to the fact that the stress state is largely constant because of stationary boundary conditions. The response of the quadratic dilatant creep model depends on this stress state only as long as the coefficients of the model remain unchanged. This is in contrast to the linear case which considers hardening effects by means of the dissipated energy generated during the damaging process.

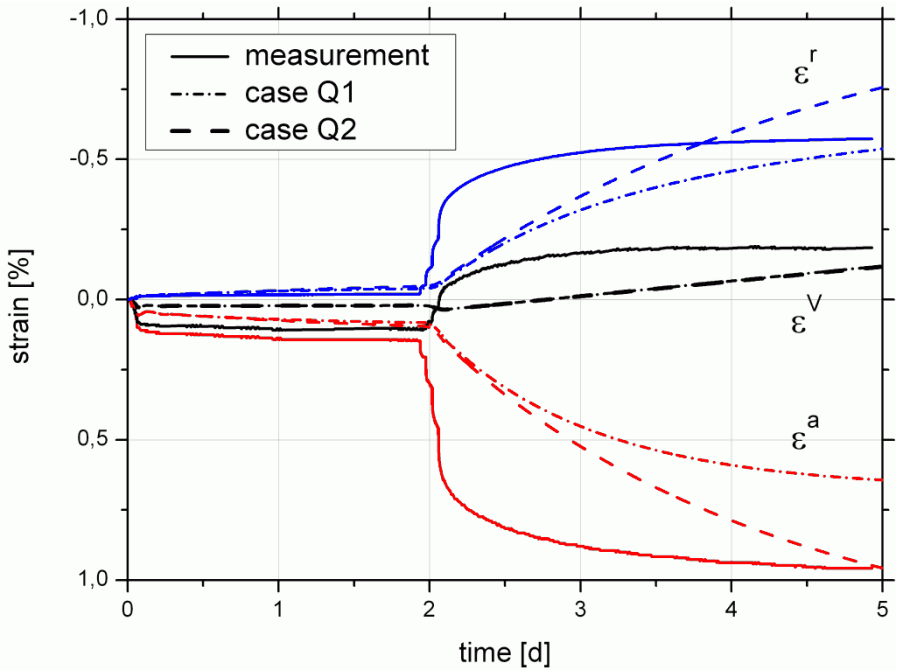

Fig. 5.29 Simulation results with the quadratic dilatant model for TC2A

The constitutive law extended by the quadratic dilatancy model was the only one of the two that was able to compute TC2B. The strain responses from the two parameterizations Q1 and Q2 for TC2B are shown in fig. 5.30. The fit of the calculated radial and volumetric strain looks like to be reasonable. The axial strain differs by a factor of 2 (and more) from the measurement data. But this may also be due to the choice of the grid points taken for the calculation of axial strain. A moderate increase of differential stress produces only a slow increase of axial and radial strain, but phases of sharp acceleration as a response to pressure peaks up to 30 MPa and 33 MPa can be observed at the end of days 3 and 6. Unloading after the first peak of axial pressure from 30 MPa down to 20 MPa causes a different volumetric behaviour of the two cases Q1 and Q2. Dilatancy still occurs in Q2 but slightly delayed. A reason could be that during this phase dilatancy occurs only in one part of the sample while the dilatancy model is switched off by the CH-condition in the other. Figure 5.30 shows the different behaviour by means of the evolution of porosity. After the next axial loading and unloading step, the volumetric strain rates behave similarly again in both simulations.

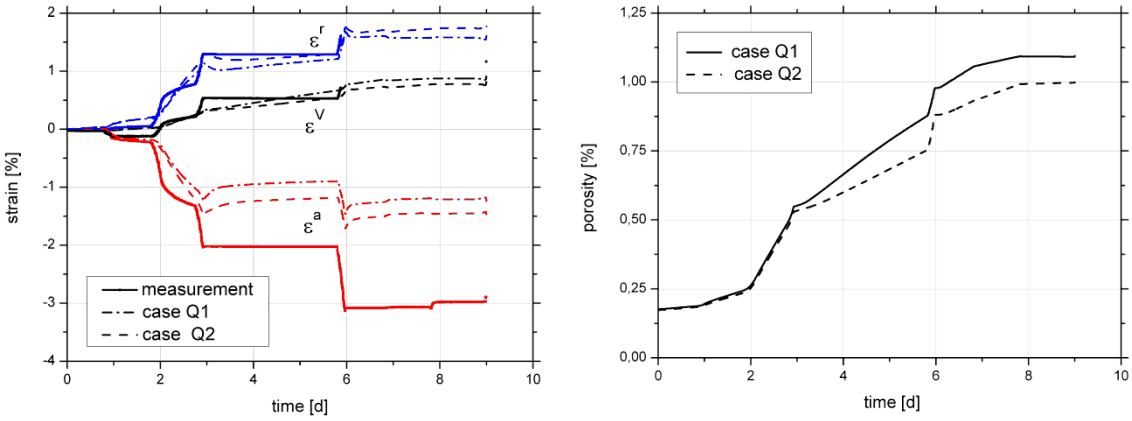

(a) *(b)*

Fig. 5.30 Simulation results with the quadratic dilatant model for TC2B
(a) evolution of strains over time
(b) development of secondary porosity

Hydro-mechanical coupling

Different models have been proposed for the calculation of the permeability depending on changing properties. The dilatancy-induced increase in permeability is often described by a polynomial porosity-permeability relation $k = k_0 \varphi^n$. But experimental data show two different modes of the permeability evolution with respect to porosity which depend on the stress state as well. Therefore, the following relation was proposed, /POP 02/ and /HEE 04/,

$$k = \frac{k_{tp}}{\left(\frac{\phi_{tp}}{\phi}\right)^{n_1} + \left(\frac{\phi_{tp}}{\phi}\right)^{n_2}} \quad \text{where} \quad \begin{aligned} k_{tp} &= a_k e^{b_k \sigma_{\max}} \\ \phi_{tp} &= a_\phi e^{b_\phi \sigma_{\max}} \end{aligned} \tag{5.3}$$

The quantity σ_{max} is the maximum principal stress, i. e. the one of minimal absolute value as long as no tension occurs. The parameters are a_k = 4.27·10^{-14} m^{-2}, b_k = 1.26 MPa^{-1}, a_p = 2.63·10^{-2}, b_p = 3.093·10^{-1} MPa^{-1}, n_1 = 4, n_2 = 1. In an optimized version a_k is set to 8.54·10^{-15} m^{-2}.

The estimation of permeability during a test under mechanical loading condition is actually a hydro-mechanical coupled process in reality. So, the numerical simulation has to be performed on a coupled HM-model. By contrast therefore, the calculations documented in this section were carried out purely mechanically and the hydraulic task

was treated in a post-process. As the dilatancy-induced secondary porosity and the stress state vary locally within the sample, this post-process approach has to be applied to each discretization element. Different approaches to determine an integral permeability of the modelled sample from the local data without a full simulation of the flow process in the sample are possible. Figure 5.31 (a) shows the porosity distribution within a cross section of the sample at the end of phase B of TC2. The derived stress-dependent permeability distribution using the approach from equation 5.3 is given in fig. 5.31 (b).

Different approaches were tested to estimate the overall permeability of the test sample, e.g. average value in each horizontal layer or maximum value in each horizontal layer, because it was assumed that the horizontal layer is normal to the global flow direction. Figure 5.31 (b) shows a connected pathway of high local permeability ranging from the top to the bottom of the sample. This structure seems to be decisive for the overall axial permeability of the sample. Thus, the maximum value approach proved to be the best. Therefore, the permeability of this pathway is calculated by the following heuristic algorithm, where k_{ij} indicates the permeability in the cell situated in the horizontal layer *i* and vertical column *j* for an arbitrary indexation of layers and columns in the sample. Because of the shape of the pathway, the "dominant path approach" can be approximated by the following "maximum permeability algorithm".

- determine the maximum value of permeability in the grid cells j in each horizontal layer i

$$k_i = \max k_{i,j} \tag{5.4}$$

- add the maximum values by layers to the overall value

$$k = \frac{1}{\sum_i \frac{1}{k_i}} \tag{5.5}$$

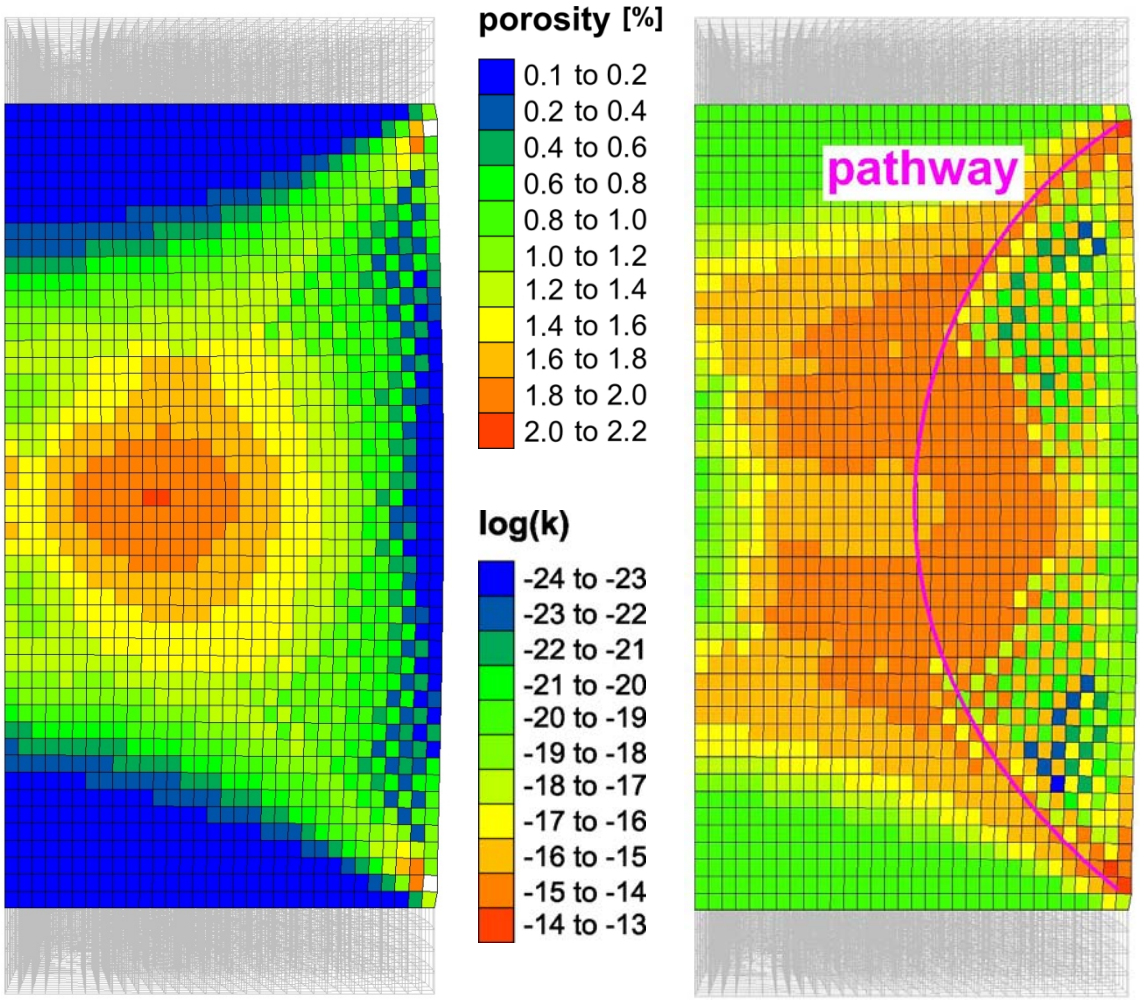

(a) *(b)*

Fig. 5.31 Results at the end of simulation process TC2B, quadratic dilatant model case Q1
(a) distribution of porosity
(b) distribution of logarithmic permeability

This algorithm neglects different heights of elements or layers, which are equal initially. This is justified for the moderate distortion the sample is subjected to. The method leads to the results shown in fig. 5.32. The fitted curve corresponds to a variation of the parameter a_k by a factor of 5. The permeability is too high in the initial phase. Nevertheless, the local permeability model chosen in combination with the dominant-path-algorithm seems to take all the essential mechanical effects on the hydraulic behaviour into account.

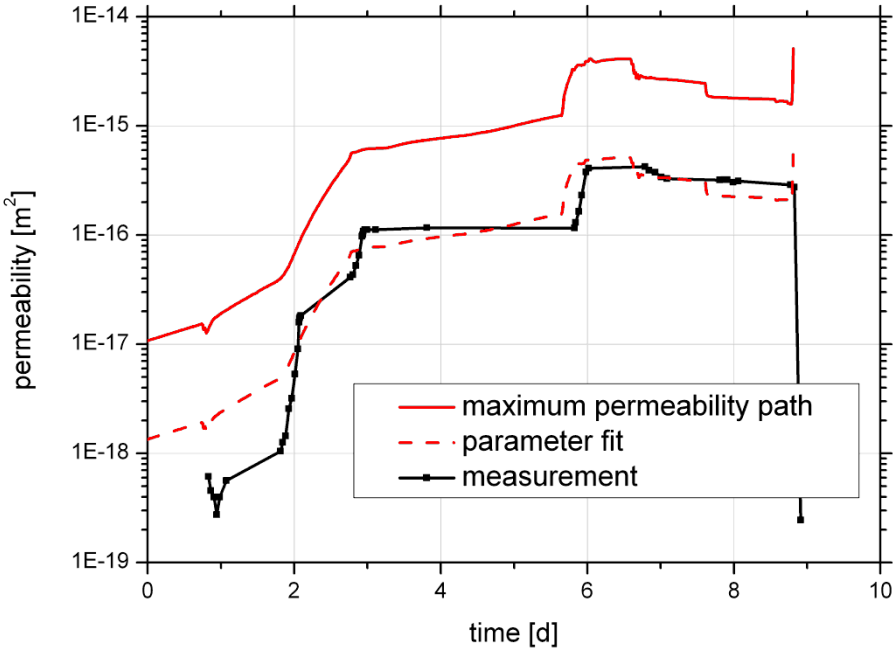

Fig. 5.32 Measured and calculated permeability over time for TC2B (case Q1)

5.3.2 Conclusions

Conclusions from continuous modelling of damaging

When DBE TEC joined into the THERESA project, none of the constitutive models was capable of simulating dilatant behaviour. The constitutive model which was finally implemented comprises two possibilities to simulate dilatancy. The applicability of these variants is limited, though. Better results could probably be achieved by an extended identification of parameters. Hardening should be introduced into the quadratic model for dilatant creep. It is also important to have a better understanding of why the linear model lacks numerical stability in FLAC^{3D} and if this is due to the hardening approach. Robust numerical schemes for the solver that are better adapted to the needs of the creep models applied are desirable.

The approach chosen for the computation of the permeability works in the case presented. But as it relies on the existence of a path of high permeability it cannot be recommended in general. A coupled (T)HM-calculation is recommended for a reliable prediction of the permeability resp. the flow rate.

The work deepened significantly a better insight into the various difficulties to be faced in the numerical description of EDZ evolution.

Overall

The modelling of damaging and healing processes and their effects on the hydraulic properties of the EDZ is a highly challenging task. Even when using the classical continuum mechanical approach, the formulation of a suitable model, its implementation, and the execution of simulation runs proved to be difficult. An analytical comparison of the models applied within this working package would be helpful. Such a study should be extended to an analysis of the numerical requirements of such models. The latter could also be done with respect to the fact that in a real world application, the period to be simulated is significantly longer than in the laboratory tests presented. The simulation of the short-term laboratory tests created significant computational costs.

The question of available computational resources is also of importance for the DEM. Also, the understanding of these types of models for the simulation of the evolution of the EDZ seems to be far less developed than in the continuum case. However, this methodology offers a possibility to better understand the structural processes and consequently to better describe of the evolution of hydraulic properties.

From the point of view of process understanding and description, both approaches have proved to be still improvable for a reliable prediction of EDZ properties with respect to a safety analysis.

6 Reference case simulation

The last task of THERESA was the combination of the results of the process-level codes (PLC) into an integrated total system performance assessment (TSPA) code and the calculation of a repository reference case. Therefore, the reference case for a repository in rock salt was to be defined and its development over time was simulated using PLC and TSPA codes from participating partners. Within this context, the focus in this task had been on predicting the long-term evolution of the EDZ and its impact on the long-term performance assessment of the repository, taking into account coupled THM processes of rock salt.

6.1 Definition of reference case

With the above objective in mind, it was decided that rather than simulating an entire repository with the TSPA codes, it would be more sensible to concentrate on the EDZ in the rock salt around a drift seal. Thus, the schematic model (see fig. 6.1) was to comprise the seal, the EDZ, and the undisturbed salt around EDZ, connecting with the shaft on one side and the disposal field at the other of the seal. The sealed drift is located at a level of 855 m below surface. The drift cross section is 23 m^2, with a realistic geometry provided by DBE TEC. Before construction of the seal, the drift contour is removed up to a depth of 0.5 m. The seal material is assumed to be incompressible concrete with a constant permeability of 10^{-19} m^2.

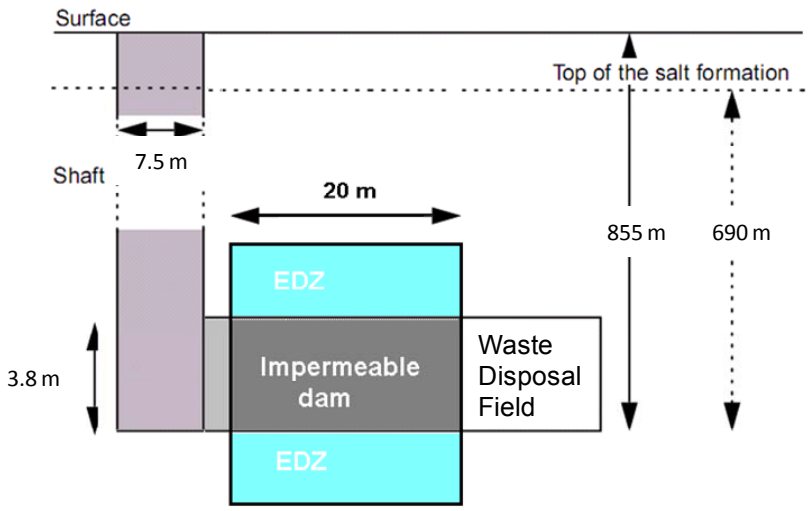

Fig. 6.1 Principle of the configuration considered for the reference case simulation

The shaft is the potential path for brine inflow, thus, the shaft is also considered to be a seal. The disposal field is considered to be a sink of infinite volume. The latter assumption is conservative from the view of brine inflow into the repository via the shaft. In fact, convergence of the disposal field will lead to a reduction of the void volume over time. DBE TEC carried out calculations with different assumptions for the temperature evolution in the repository. The results are summarized in fig. 6.2.

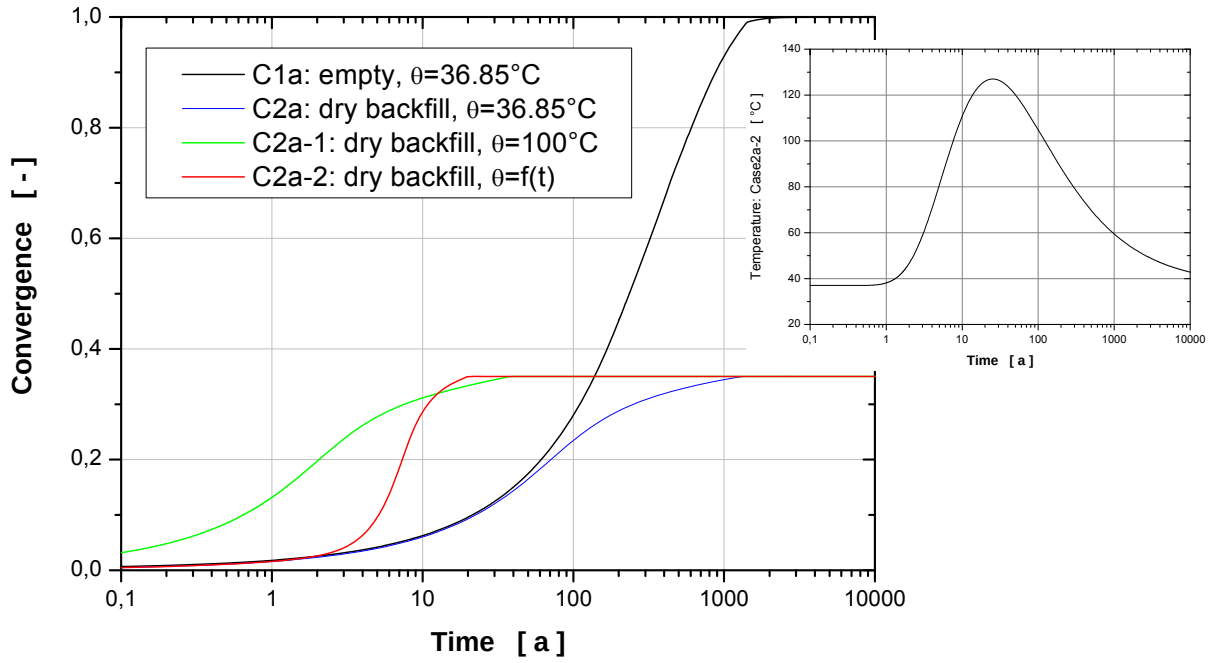

Fig. 6.2 Predicted disposal drift convergence for different cases of thermal behaviour

The cases considered were an open or backfilled disposal drift at ambient temperature, a backfilled drift at a constant temperature of 100 °C, and a more realistic temperature evolution for a disposal drift as shown on the right side of fig. 6.2. The backfill material is assumed to be crushed salt with an initial porosity set to 0.35. Depending on the case studied and with respect to the simplified model used, the void volume in the disposal drift will have vanished after 20 to 2000 years. This is the minimum time for which the EDZ evolution may be relevant for safety considerations. For the reference case simulations, however, convergence of the disposal drift was not considered.

Several cases to be studied were defined:

1. The dry (reference) case: Evolution of permeability with EDZ cut-off before construction of the drift seal and without brine inflow.

2. The first alternative case: same as 1, but the shaft seal fails 50 years after drift seal construction and brine under hydrostatic pressure will be present at the front side of the seal from then on.

3. The second alternative case: same as 2, but there is no shaft seal at all, meaning that brine under hydrostatic pressure is at the front of the seal right after drift seal construction (to test the effectiveness of the drift seal alone).

4. Additional alternative cases 4.1 – 4.3: same as 1 – 3, but without EDZ cut-off before construction of the drift seal.

Since the TSPA codes do not model the mechanical evolution around the drift seal, they have to rely on input from process-level codes. Therefore, the cases 1 and 4.1 have to be modelled beforehand using a finite element code to provide a permeability and porosity evolution that can be used in the integrated codes.

As a simplification the EDZ development was transferred from the dry states on the alternative scenarios and the influence from brine was considered only in the TSPA code. This was due to the limited budget. However, the alternative scenarios show a HM-coupled system behaviour that would have to be treated at PLC level accordingly.

6.2 Process-level modelling of EDZ evolution

For the process-level simulation, GRS used CODE_BRIGHT, originally with the constitutive laws and parameters used by CIMNE for the benchmark simulation (see section 5.1.1). An overview of the finite element model is given in fig. 6.3.

Displacements in normal direction are suppressed at the base line of the model, at the symmetry line (left border), and the right border. From the top line, a stress boundary condition of -15.8781 MPa is applied (the negative sign is caused by sign convention: tension is indicated as positive, pressure as negative, thus, the stress closest to zero without occurring tension is the maximum stress, the stress farthest from zero is the minimum stress). The initial stress field (before excavation of the drift) changes linearly from -15.8781 MPa to -20.1219 MPa depending on the rock salt density. The initial porosity of the salt is set to 0.3 % in accordance with measurement results of the benchmark samples. The schedule for the simulation is shown in tab. 6.1.

Tab. 6.1 Simulation schedule

Time / years	Event
0.0 – 1.0	Start-up, all material is rock salt (equilibration period)
1.0	Drift excavation
31.0	EDZ cut-off (in one of the two simulations)
31.5	Seal construction
31.5 – ~10,000	EDZ self-sealing

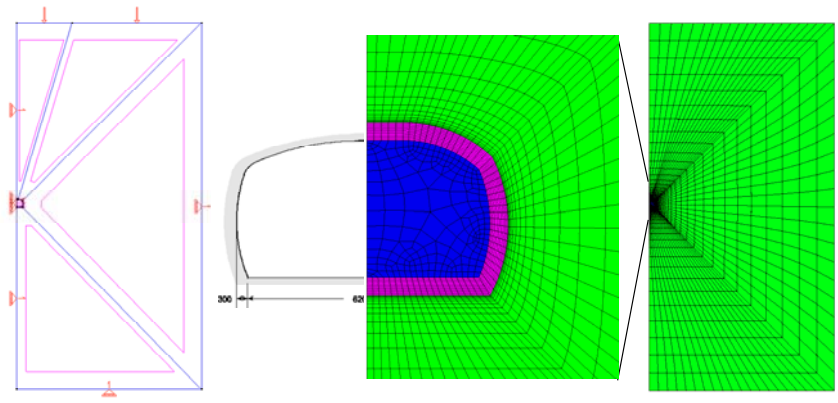

Fig. 6.3 Finite element model of the drift

However, the first simulation of the drift model showed that the above combination of geometry and parameters led to a hardening of the salt surrounding the drift which suppressed any dilatancy. As a consequence, the only porosity increase around the drift was due to elastic unloading. In order to model dilatancy around the drift, as it is observed in situ, the hardening process is switched off in the model. This solution is considered conservative as it produces the highest possible dilatancy with this model.

The simulation results of this modification show the expected evolution of displacements and stresses. Prior to seal construction, zones of maximum principal stress close to zero were found near the drift contour, i. e., dilatancy occurs. The largest extent of dilatancy is under the floor. After seal construction, the maximum stress tends to increasing pressure values again, so, dilatancy reduces. The porosity reaches maximum values of 1.2 % prior to EDZ cut-off in a thin zone near the wall. In the roof and especially in the floor, larger zones of increased porosity can be observed, but the maximum values are about 0.7 % only. Half a year after EDZ cut-off, at the time point when the drift seal is constructed, no new high-porosity zone near the wall exists, and the dilated zones in the floor and the roof are still smaller than before cut-off.

Removing the drift contour does not significantly influence the evolution of the remaining EDZ (fig. 6.4).

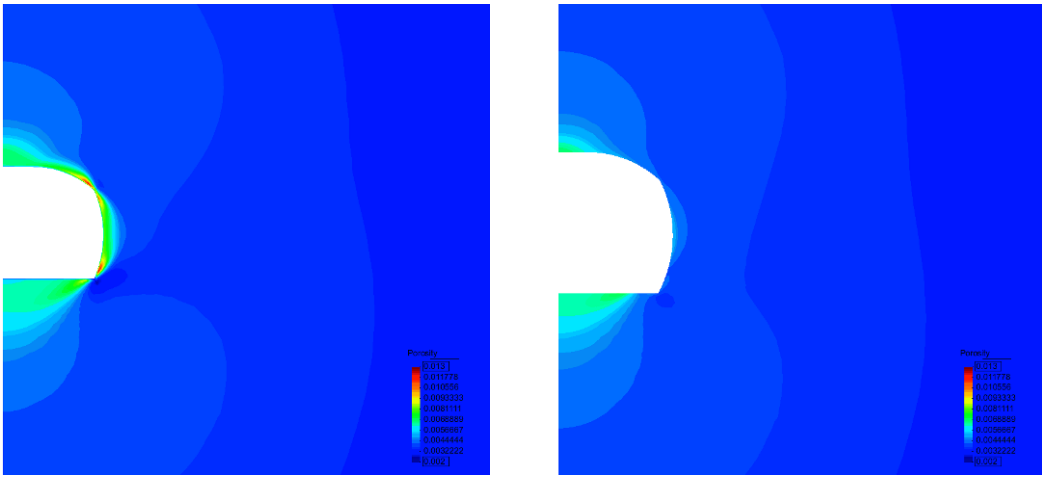

Fig. 6.4 Porosity around the drift before EDZ cut-off (left) and at the time of seal construction, six months after EDZ cut-off (right)

Figure 6.5 shows the porosity profile below the floor at different times for the case with EDZ cut-off. The porosity reduction over time can be taken from this figure. After 200 years, the porosity along the profile has significantly reduced. After 4000 years, it is below the original value of 0.3 % everywhere.

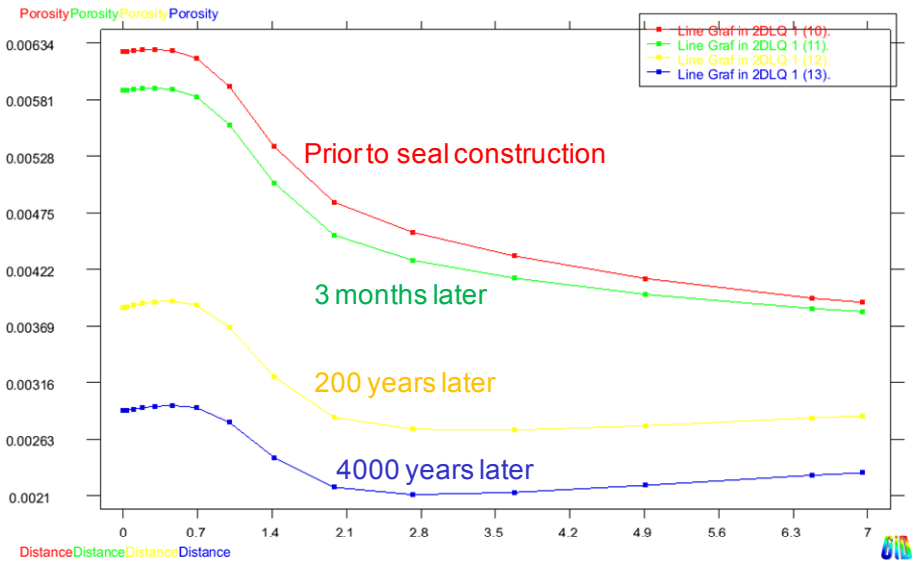

Fig. 6.5 Porosity profile below the drift floor at different times for the case with EDZ cut-off

For the case without EDZ cut-off, the porosity distribution at the time of seal construction is nearly identical to that half a year before, this has already been shown for the case with EDZ cut-off in fig. 6.4 (left). Figure 6.6 shows the porosity profile below the floor at different times for the case without EDZ cut-off. Although the dilated zone below the floor is larger, the porosity is again below 0.3 % along the profile after 4000 years. However, small zones of increased porosity remain in the wall where the contour with higher porosity had not been cut off in this calculation case.

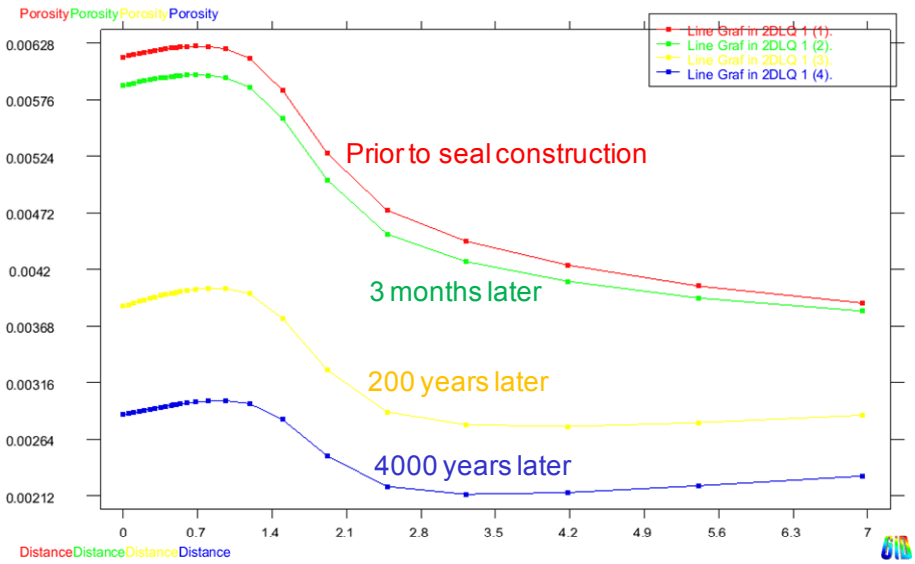

Fig. 6.6 Porosity profile below the drift floor without EDZ cut-off at different times

6.3 Equivalent permeability and porosity as input for TSPA codes

Up to now, EDZ in rock salt has seldom been considered in TSPA simulations. If so, the additional flowpath provided by the EDZ was accounted for by increasing the seal permeability. A time-dependence of EDZ permeability was never modelled before.

In order to achieve this, the GRS TSPA code module LOPOS was modified so that the permeability and porosity of the EDZ could be modelled independently of the seal and with a temporal evolution. The code, however, requires a single (time-dependent) value for permeability and porosity, in contrast to the permeability/porosity distribution that can be provided for each time step by the process-level modelling. Therefore, distributions of permeability and porosity have to be transferred in equivalent permeability and porosity values that would result in the same flow rate. The procedure to do this was:

1. For each time step, the porosity distribution in the EDZ resulting from the PLC simulation was divided into classes with bandwidths of 0.01 %, i. e. the classes 0.3 - 0.31 %, 0.31 - 0.32 % and so on were defined. For each time step the total cross section area of each porosity class was evaluated. The result can be shown in a plot where the area is a function of porosity.

2. For each porosity class the respective permeability was calculated using various permeability-porosity relations. The relations considered were the two used by Olivella in the benchmark simulation (section 5.1; the Kozeny-type relation and the microfracture model) with unchanged parameters, a percolation model as modified by Zhang /ZHA 09/ with a threshold porosity of 0.35 %, and a more conservative version of Zhang's model with a threshold porosity of 0.31 % (see fig. 6.7). The figure shows that Olivella's microfracture relation will produce the highest permeability in nearly the complete porosity range. In that sense it is the conservative assumption. In the low porosity range, Zhang's relation with a percolation threshold of 0.31 % is nearly identical, but at high porosities it yields considerably lower permeabilities. The least conservative relation is that of Kozeny-type, except for porosities slightly above 0.3 %.

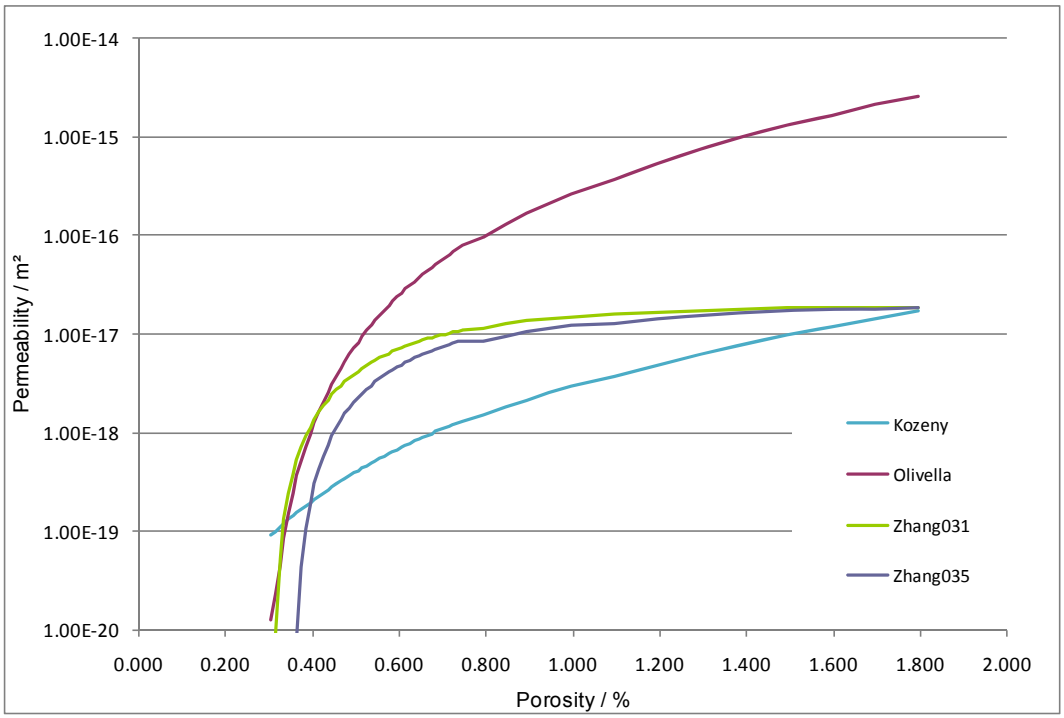

Fig. 6.7 Permeability-porosity relations considered for the determination of equivalent permeability

3. For each time step, the cross section area of each permeability/porosity class was determined. Since the Darcy equation is linear in permeability and cross section, an equivalent permeability for an arbitrarily chosen cross section can be calculated that leads to the same flow rate. In a graph showing cross section as a function of permeability, the product of given cross section and associated equivalent permeability would be marked by a rectangle having the same area as the integrated area below the cross section/permeability class curve. The equivalent permeabilities were calculated for an equivalent cross section of 23 m^2, because this is the value for the drift cross section. Thus, the equivalent permeability values are directly comparable to the seal permeability.

4. The equivalent porosity for an EDZ cross section of 23 m^2 is obtained by integrating the total pore volume increase in the EDZ at each time step and calculating the porosity increase in the 23 m^2 cross section that represents the same pore volume.

All the equivalent permeabilities for an equivalent cross section of 23 m^2 were calculated for the different calculation cases (with/without EDZ cut-off), time steps, and considered permeability-porosity relations. The results, in terms of equivalent permeability versus time after seal construction, are shown in fig. 6.8 and fig. 6.9 in double logarithmic scale for the cases with and without EDZ cut-off.

The figures show that in the case of EDZ cut-off before seal construction, a few hundred years are sufficient for the equivalent permeability to decrease below 10^{-19} m^2, the permeability of the drift seal. For the case without EDZ cut-off before seal construction, the time required is considerably longer.

The most conservative relation overall is Olivella's microfracture model which predicts the highest permeability. Therefore, the permeability evolution based on Olivella's relation was chosen for implementation in the integrated TSPA code module LOPOS used by GRS.

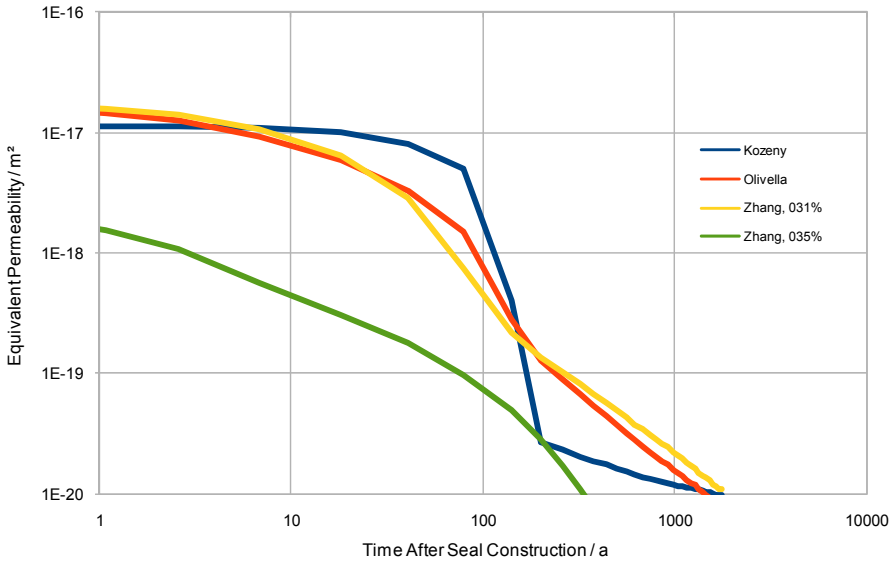

Fig. 6.8 Equivalent permeability versus time after seal construction for an equivalent cross section of 23 m^2, case with EDZ cut-off

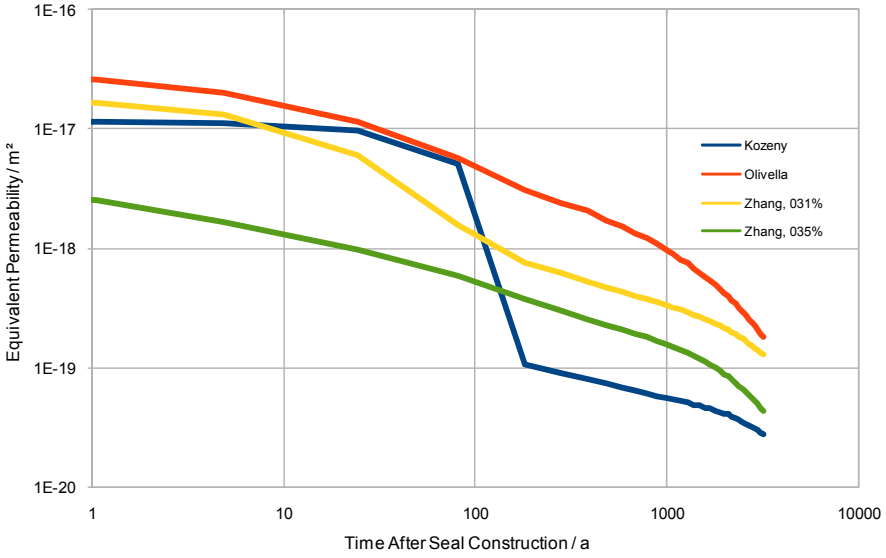

Fig. 6.9 Equivalent permeability versus time after seal construction for an equivalent cross section of 23 m^2, no EDZ cut-off

The permeability evolutions with and without EDZ cut-off were approximated by exponential functions. For the case with EDZ cut-off, the approximation has to be split in two regimes:

$$k = 1.8 \cdot 10^{-17}\,m^2 \cdot \exp(-0.0297/a \cdot t) \qquad \text{for } t < 140\ a$$

$$k = 5 \cdot 10^{-19}\,m^2 \cdot \exp(-0.37/a \cdot (t - 140a)^{0.33}) \qquad \text{for } t \geq 140\ a$$

For the case without EDZ cut-off, a closed approximation of the form

$$k = 3.05 \cdot 10^{-17}\,m^2 \cdot \exp(-0.35/a \cdot t^{0.33})$$

is sufficient. The equivalent porosities are given by

$$\phi = 0.033542 \cdot \exp(-0.012/a \cdot t) \qquad \text{with EDZ cut-off}$$

$$\phi = 0.033621 \cdot \exp(-0.012/a \cdot t) \qquad \text{without EDZ cut-off}$$

The calculated equivalent permeability for the two cases and their respective approximations is shown in figs. 6.10 and 6.11, respectively. An additional “best fit” but insufficient closed function for the case without EDZ cut-off is shown in fig. 6.10 for comparison.

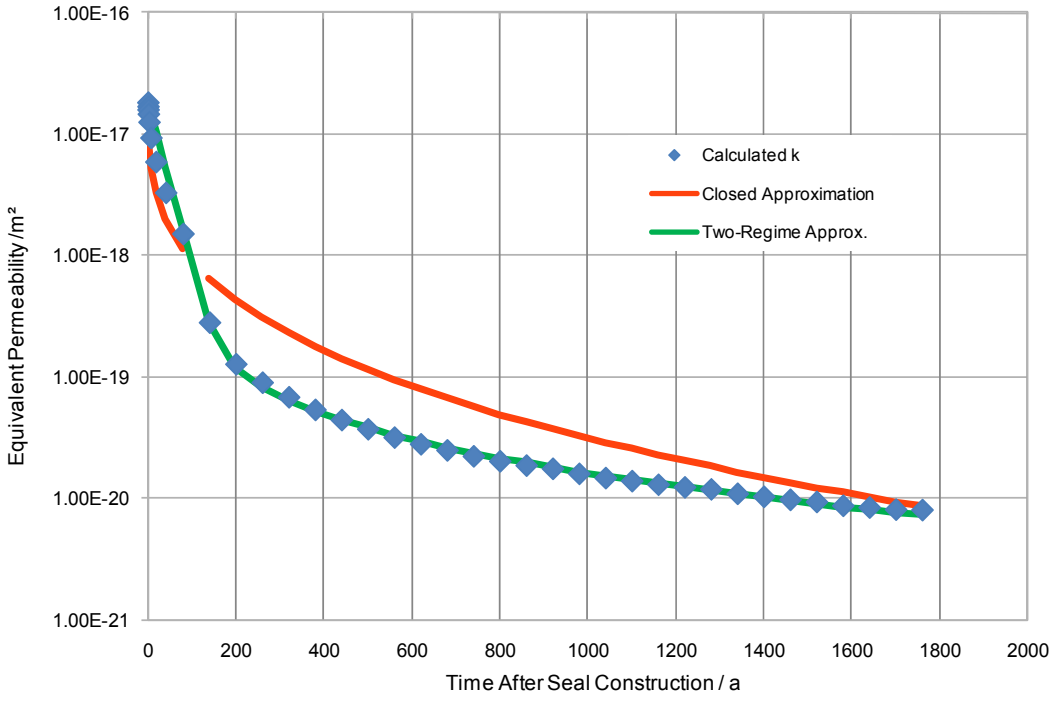

Fig. 6.10 Proposed equivalent permeability versus time after seal construction for an equivalent cross section of 23 m^2, EDZ cut-off

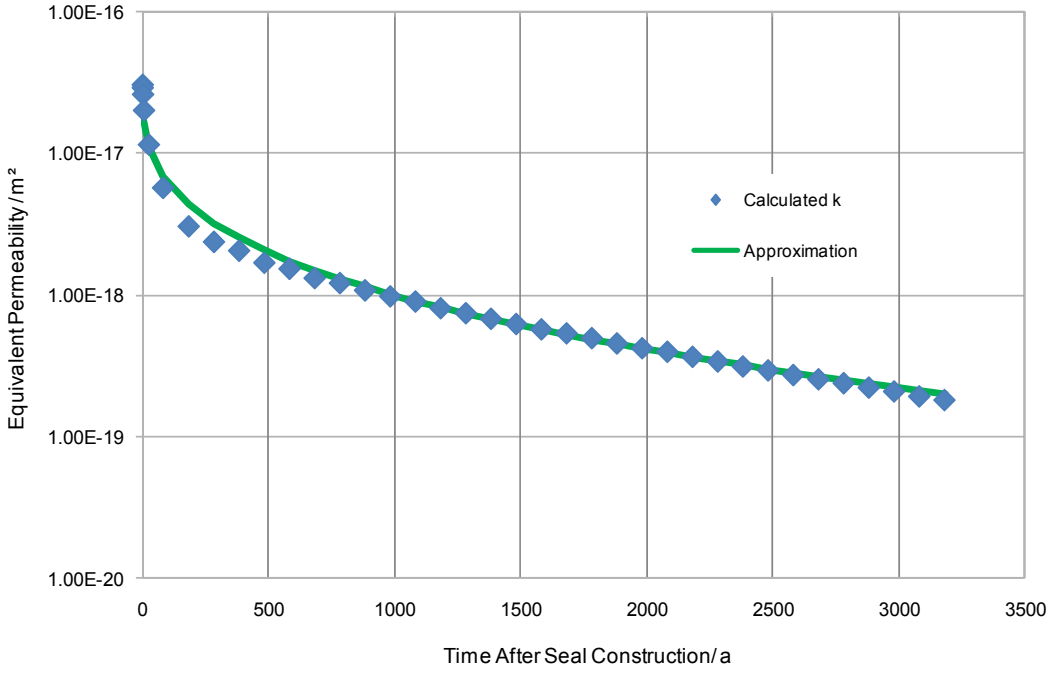

Fig. 6.11 Proposed equivalent permeability versus time after seal construction for an equivalent cross section of 23 m^2, no EDZ cut-off

6.4 Results of the drift model calculation with LOPOS

The time-dependent permeability and porosity functions for the evolution of the EDZ derived from the process-level modelling were implemented in the TSPA code module LOPOS. The simplified schematic model for the drift system comprises the seal – a technical hydraulic barrier ("dam") –, the EDZ around the seal and the undisturbed rock salt. The compartments of the EDZ and the dam are connected with compartments of the shaft and the disposal field, see fig. 6.1. The disposal field is considered as a sink of infinite volume (without convergence). The shaft is the potential path for brine inflow. The approximations for the evolution of equivalent permeability and porosity were used for the TSPA calculations.

The time intervals for the TSPA calculations are limited by the relevance of the brine flow into the EDZ. In contrast to the flow resistance of the dam, which is assumed to be constant over time, the flow resistance of the EDZ will rise by convergence and healing. With the model parameters described above, the EDZ flow resistance will be

higher than the dam flow resistance after about 200 years (with EDZ cut-off before seal construction) or after about 4500 years (without EDZ cut-off), see fig. 6.12.

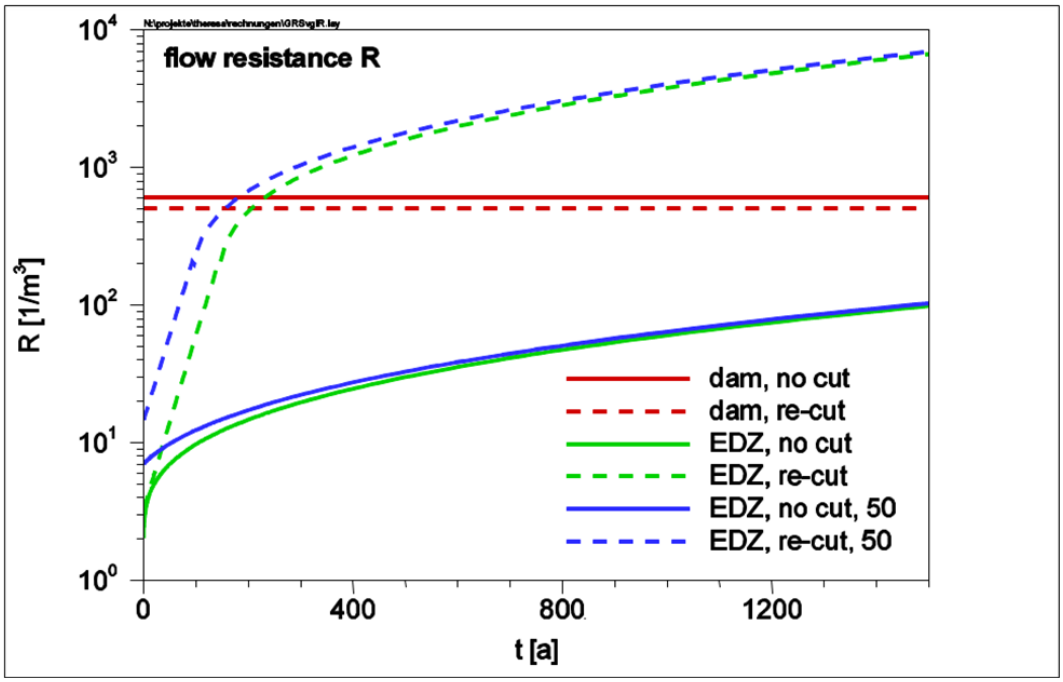

Fig. 6.12 Flow resistance of the EDZ and the dam for the different cases

(no cut = no EDZ cut-off, re-cut = EDZ cut-off before seal construction, 50 = brine at seal front 50 years after construction)

Looking at the equivalent permeability instead of the flow resistance (fig. 6.13), the same conclusion can be drawn. EDZ permeability decreases below the dam permeability of 10^{-19} m^2 only 200 years after seal construction (with EDZ cut-off) or after about 4500 years (without EDZ cut-off). After this time, the brine flow into the EDZ will be less significant. Therefore, calculations for cases with EDZ cut-off were finished at about thousand years after seal construction, while calculations for cases without EDZ cut-off were performed for about 4500 years.

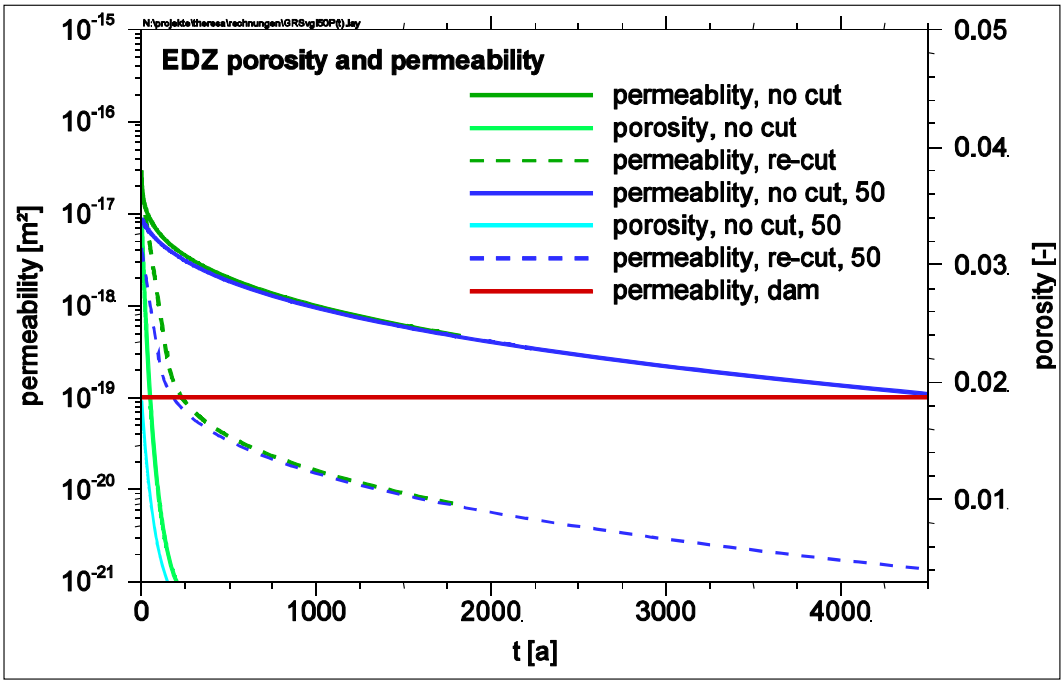

Fig. 6.13 Permeability and porosity evolution of the EDZ and the dam for the different cases

(no cut = no EDZ cut-off, re-cut = EDZ cut-off before seal construction, 50 = brine at seal front 50 years after construction)

The time point of an early brine inflow by shaft seal failure seems to be of little significance for the evolution of the EDZ permeability and porosity. In figs. 6.12 and 6.13, the flow resistance and permeability curves are shown for the cases “brine inflow directly after seal construction” and “brine inflow 50 years after seal construction”. The calculations show that the time point of brine contact (under hydrostatic pressure) at the drift seal front has only a very small influence on the long-term evolutions of EDZ equivalent permeability and porosity – whether without EDZ cut-off or with EDZ cut-off. This, however, cannot be finally discussed based on these results, because EDZ permeability and porosity will depend on the fluid pressure in the pore space, which could not be modelled here.

In the case of brine inflow into the EDZ the pore volume will be filled by brine and gas. The influence of the gas phase had to be neglected in the TSPA calculation. Instead, it was assumed that when the brine arrives at the seal front, the EDZ pore volume is instantaneously filled with brine under hydrostatic pressure. In consequence, the EDZ pore volume and brine volume are equal, see fig. 6.14. With regard to the brine volume inflow into the EDZ this assumption is conservative.

In contrast to this, the pore volume and brine volume of the dam are not equal. The pore volume of the dam will not be completely filled by brine within several thousand years – neither without EDZ cut-off nor with EDZ cut-off – because of higher flow resistance and pore volume in comparison to the EDZ, see fig. 6.14. In cases with EDZ cut-off (“re-cut”) the total pore volume of the dam is slightly higher and the flow resistance of the dam slightly lower because of the enlarged cross section of the dam.

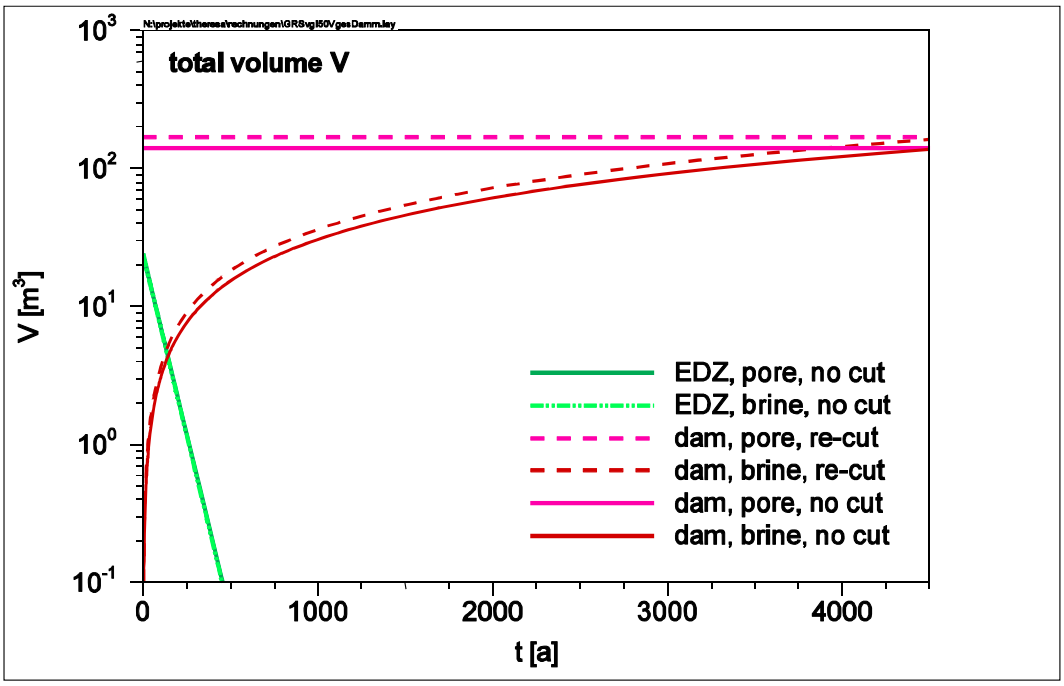

Fig. 6.14 Total pore volume and brine volume evolution of the EDZ and the dam for the different cases using GRS’ approximations

With the assumptions and parameters used for the calculations, brine flow via the drift seal is very slow. As a consequence, the EDZ will be the relevant flow path for several hundred years. Figure 6.15 shows that the flow rates of the EDZ depend on the EDZ cut-off and time of brine inflow. The flow rates of brine inflow and outflow are very similar, but slightly shifted in time. In the case without EDZ cut-off before seal construction (“no cut”) the flow rates and the brine volumes flow through the EDZ are at all times higher compared to the case with EDZ cut-off (“re-cut”). In case of later brine inflow (e. g., “re-cut, 50”) the flow rates and brine volumes are lower compared to an earlier brine inflow (e. g., “re-cut”).

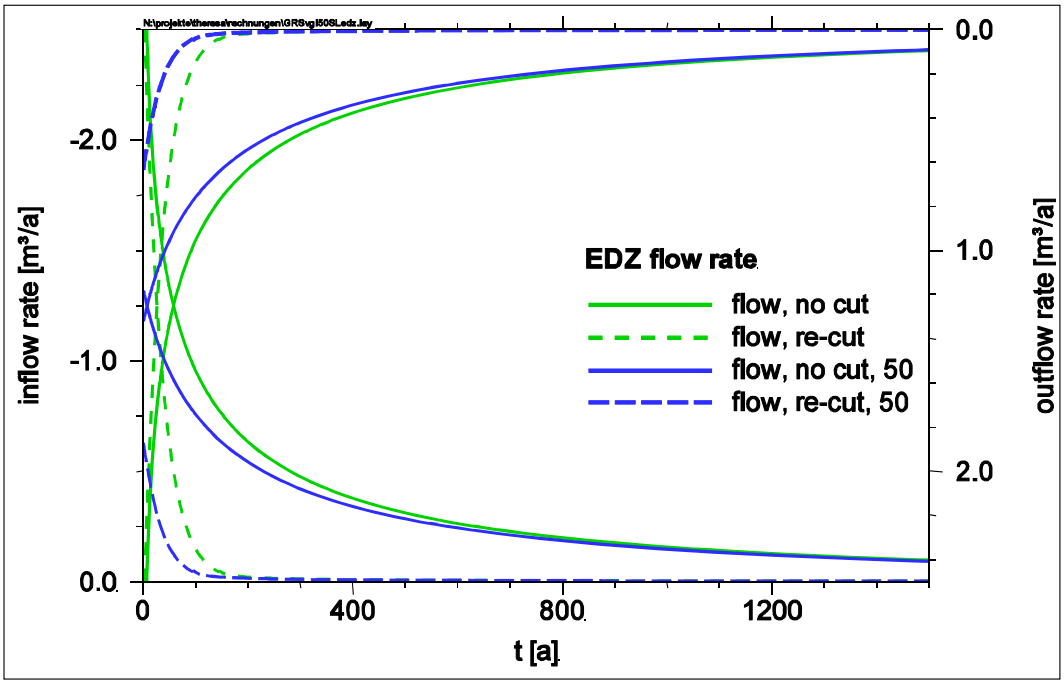

Fig. 6.15 Brine flow into the EDZ and the dam for the different cases

(no cut = no EDZ cut-off, re-cut = EDZ cut-off before seal construction, 50 = brine at seal front 50 years after construction)

6.5 Discussion of Reference Case calculation results

The results of the first TSPA calculations using time-dependent functions for EDZ permeability and porosity using the code LOPOS are plausible and consistent. They are also conservative with regard to the assumptions made:

- For the process-level modelling that provided the porosity evolution, parameters that produced a maximum dilatancy were used.
- Conservative permeability-porosity relations were used.
- After brine inflow via the shaft, instantaneous full saturation of the EDZ was assumed.

It is possible to model different permeability-porosity relations with different long-term evolutions if the respective input parameters are available. Under the given assumptions, the calculations which were performed show that in most cases the EDZ will be the important flow path for brines. The relevance of the EDZ as a flow path for brines will increase

- without cut-off of the EDZ,
- with earlier brine inflow, and
- with higher flow resistance of the seal (dam).

It seems that the importance of the EDZ as brine flow path will decrease significantly after a few hundreds of years at the latest with EDZ cut-off before seal construction. Without EDZ cut-off before seal construction a few thousands of years may be necessary, because of the different time required for convergence to reseal the dilatant zones of rock salt. Thus, if no EDZ cut-off was performed before seal construction, the EDZ could be active throughout all the time while there is an open porosity in the backfilled emplacement drift (see fig. 6.2).

The permeability functions are based on a single mechanical model, the CIMNE approach, for the EDZ evolution. While this model was able to describe the laboratory benchmark test quite well, it had to be modified to obtain a significant dilatancy in the drift model. A conservative approach that neglected hardening was chosen, leading to a maximum dilatancy for this model formulation. Other mechanical models of some of the other project partners had comparably good results. It would have been desirable to have simulations using these models for the reference case as well, in order to reduce the uncertainty in the prediction of the porosity evolution. This could not be performed within the financial scope of the THERESA project.

Another source of uncertainty is the fact that all models for EDZ evolution were calibrated on few tests and checked against a single laboratory benchmark test. In order to decide which model with which parameters describes the reality best (or even sufficiently), more experimental data, both existing and specially obtained for this objective, both from lab tests and in-situ experiments, have to be considered. This was also not possible in the scope of THERESA.

7 Summary and conclusions

7.1 Background and objectives

The objective of the THERESA project was to develop, verify and improve the modelling capabilities of constitutive models and computer codes for analysis of coupled THMC processes in geological and engineered barriers for use in Performance Assessment (PA) of the long-term safety of nuclear waste repositories. Work package 3 of the project addressed the evaluation and improvement of numerical modelling capabilities for assessing the performance and safety of nuclear waste repositories in rock salt, with particular regard to the long-term evolution of the Excavation Damaged Zone (EDZ), considering thermal-hydraulic-mechanical (THM) processes.

The development needs were based on an issue evaluation table which had been drafted in the first months of the project and was regularly updated. An important issue derived from this table is the model simulation of the evolution and especially the self-sealing of the EDZ which evolves as a result of the mechanical response of the rock to excavation of underground openings. The dilatancy threshold will be exceeded in the region close to the opening, leading to micro-fracturing and an associated increase of porosity and permeability of the salt rock. Consequently, the focus of the work in WP3 was on modelling of rock salt dilatancy and on re-compaction or healing effects.

The project partners involved in WP3 were the Gesellschaft für Anlagen- und Reaktorsicherheit (GRS) mbH as WP coordinator, the Federal Institute for Geosciences and Natural Resources (BGR), the Centre Internacional de Mètodes Numèrics en Enginyeria (CIMNE), the DBE TECHNOLOGY GmbH (DBE TEC), the Forschungszentrum Karlsruhe (FZK) GmbH, the Institut für Gebirgsmechanik (IfG) GmbH, the Nuclear Research and Consultancy Group (NRG), and the Technische Universität Clausthal (TUC). The University Utrecht (UU) acted as contractor of NRG.

This report summarizes the results of GRS, CIMNE, DBE TEC, and IfG. The conclusions follow those of the THERESA Deliverable D9 which represents the WP3 final report /WIE 09b/.

7.2 Work plan and achievements

The overall objective of WP3 of the THERESA project was the evaluation and improvement of numerical modelling capabilities for assessing the performance and safety of nuclear waste repositories in rock salt, with particular regard to the long-term evolution of the excavation damaged zone, considering thermal-hydraulic-mechanical (THM) processes. The work plan for achieving this objective was structured as follows.

- Evaluation of the capabilities and/or development needs of the numerical modelling codes used by the participating teams and compilation of data relevant for model calibration/improvement.
- Model implementation in the computer codes and testing of the calibrated models.
- Definition and benchmark simulation of one test case (TC), with measured data from a large-scale laboratory test involving coupled THM processes, focusing on code capacities for realistic system representation, reliable conceptualisation, quantification of uncertainties in models and results, and capacities for long-term performance assessment predictions.
- Expression of the applied process models in terms of a so-called compartment model and implementation in integrated TSPA codes to perform long-term performance assessment predictions for a repository Reference Case (RC).

Model description and calibration

For the validation and calibration of the constitutive models and computer codes for the analysis of THM processes in the EDZ in rock salt, GRS performed a number of laboratory experiments on the reference salt (*Asse Speisesalz*). The combined damage and sealing tests were carried out on salt samples with measurements of deformation and permeability under various stress conditions, serving to calibrate the parameters associated to the models.

Most of the process-level models used by the different project partners for numerical modelling are based on consideration of a continuous medium and the dilatancy concept, which relates damage and self-sealing to pore space increase or decrease, respectively. Although not all problems were solved in detail during the calibration phase, all these models reached an advanced calibration state which allowed using them for the prediction of the laboratory benchmark test.

DBE TEC additionally used the discrete element code PFC^{3D}. Within the time schedule of this project, however, the derivation of particle assemblies that can be used as a model for rock salt was not possible. A reason is the vast number of degrees of freedom within such a system. While the DEM is already being applied to industrial granular systems, methods for its application to continuous systems are much less developed. Nevertheless, DEM-models could help to qualitatively understand the processes leading to failure of rock.

Laboratory test case

Due to apparative problems and restrictions several tests instead of the one originally envisaged were performed at the GRS laboratory. The “official” benchmark test involved a sample of 100 mm diameter and 190 mm length which was subjected to several deviatoric load steps, a re-compaction phase and a phase of elevated temperature. The data of a large hollow cylinder test, which had originally been planned for the benchmark case, were also provided for an optional simulation exercise.

Benchmark simulation of test case

Model simulation of the tests took place in two steps: In the first step, only the loading history of the tests was provided, and the modelling teams were expected to perform a blind prediction. In the second step, the measured sample responses in terms of strains and permeability were distributed and an interpretation modelling phase with improvement of the calibration followed.

CIMNE modelled both the benchmark test case and the hollow cylinder with satisfying results for the volumetric strain. Permeability could be modelled well with a cubic law, but the necessary assumptions for fracture spacing and aperture make it difficult to provide a reliable permeability prediction. It is, however, a promising approach because it can be combined with anisotropy and can be applied to unsaturated conditions and gas flow.

IfG was able to simulate all the effects encountered in the benchmark test case with their constitutive laws in a satisfying way. The validity of the calculated dilatancy and of the used porosity-permeability relation for an EDZ was demonstrated by back analyses of in-situ tests in an underground drift in the Asse mine.

DBE TEC used two constitutive laws for dilatant behaviour. Both describe dilatancy as an inverse behaviour of crushed salt compaction. The first is a non-associated flow rule derived from CIMNE's model, the second is based on an associated flow rule adopted from a model introduced by FZK. A major concern of DBE TEC was to derive an overall permeability of the tested sample from the permeability distribution obtained in the purely mechanical simulation.

Reference case simulation

Based on CIMNE's model for the mechanical behaviour of the salt and the permeability-porosity coupling, the evolution of porosity and permeability around a sealed drift in a repository was simulated for two cases, with or without cut-off of the drift contour with a major part of the EDZ prior to seal construction. The porosity and permeability distributions were transferred into respective equivalent time-dependent values of EDZ porosity and permeability that could be used as input to the TSPA code module LOPOS, which was extended by the implementation of time-dependent permeability.

With several conservative assumptions, it was possible to perform calculations simulating a brine inflow via the shaft at different time points after drift seal construction. The results show that in most cases the EDZ will be the important flow path for brines. The relevance of the EDZ as a flow path for brines will increase

- without cut-off of the EDZ around the drift seal,
- with earlier brine inflow, and
- with higher flow resistance of the seal.

It seems that the importance of the EDZ as brine flow path will decrease significantly after a few hundreds of years at the latest with EDZ cut-off before seal construction. Without EDZ cut-off before seal construction a few thousands of years may be necessary.

7.3 Conclusions and lessons learned

Most of the partners taking part in the THERESA WP3 were able to successfully simulate the laboratory benchmark test.

While the models of eight different project partners were tested in the benchmark simulation of the laboratory test case, the permeability functions for the reference case were only based on one single mechanical model for the EDZ evolution. The mechanical models of some of the other project partners had comparably good results. It would have been desirable to have simulations using these models for the reference case as well, in order to reduce the uncertainty in the prediction of the porosity evolution. This could not be performed within the financial scope of the THERESA project.

In fact, whether the models used in the benchmark simulation are really suitable for calculating in-situ configurations still has to be validated in most cases. In order to decide which model with which parameters describes the reality best (or even sufficiently), more experimental data, both existing and specially obtained for this objective, both from lab tests and in-situ experiments, will have to be considered. This was also not possible within the scope of THERESA.

The experiences during the laboratory experiments to provide the data for the benchmark simulation showed that lab testing itself still holds major problems and obstacles, if non-standard test configurations are envisaged.

In this sense, THERESA has not solved all the problems of EDZ characterisation and modelling. This could, in fact, not reasonably be expected considering the size of the project. On the other hand, important progress was made:

- Several approaches for modelling the THM behaviour of rock salt were documented, improved, calibrated and tested successfully.
- The database for the THM behaviour of rock salt was broadened, as far as possible within the financial scope of the project.
- Time-dependent EDZ permeability was implemented in a TSPA code module for the first time.
- First calculations concerning the significance of the EDZ around a drift seal in case of a brine intrusion via the shaft were performed, even though the results may suffer from insufficient confirmation of models.

A special benefit was that practically all European institutions that work in the field of radioactive waste disposal in rock salt were joined in the THERESA project.

The shortcomings of characterization and modelling of the EDZ in rock salt, as they present themselves after THERESA, can be summarized as follows:

- The database for calibration of the models, i. e., the number of available well-defined and documented experiments, was not sufficient. Additional experiments will be indispensable for sound model calibration.
- As a consequence, the calibration had to be carried out on a weak database and is therefore incomplete.
- Some of the models showed weaknesses during test case simulation and need further improvement.
- TSPA modelling was based on only one process-level model, which itself is not sufficiently calibrated and validated.

On the whole, THERESA was a success, as it provides a sound and complete basis for further investigations, especially with regard to the EDZ in rock salt. This future work, which is considered indispensable for completion of the EDZ complex, should comprise

- Further experimental investigation with well-defined objectives and boundary conditions to complete the database on dilatancy and re-compaction, including investigation of the influence of brine and increased pore pressures on EDZ re-compaction,
- Further development of some and extended calibration of all of the process-level models, including validation of their suitability for in-situ application,
- Implementation of time-dependent EDZ permeability functions derived from comprehensively calibrated models in the TSPA codes, and
- Performing reliable predictions of the impact of brine inflow into a repository with realistic assumptions.

8 References

/ALK 07/ Alkan, H., Cinar, Y., Pusch, G. (2007): Rock salt dilatancy boundary from combined acoustic emission and triaxial compression tests. Int. J. Rock Mech. Min. Sci. Vol. 44, No. 1, 108-120, Jan 2007.

/ALK 08/ Alkan, H. & Müller, W. (2008): Numerical Modelling of Dilatancy Induced Percolative Permeation in Rock Salt. Bericht ISTec-A-1319, März 2008.

/BEC 99/ Bechthold, W., Rothfuchs, T., Poley, A., Ghoreychi, M., Heusermann, S., Gens, A., Olivella, S., (1999): Backfilling and Sealing of Underground Repositories for Radioactive Waste in Salt (BAMBUS Project), EUR 19124, Commission of the European Communities.

/BEC 04/ Bechthold, W., Smailos, E., Heusermann, S., Bollingerfehr, W., Bazargan Sabet, B., Rothfuchs, T., Kamlot, P., Grupa, J., Olivella, S., Hansen, F.D. (2004): Backfilling and Sealing of Underground Repositories for Radioactive Waste in Salt (BAMBUS-II Project), EUR 20621, Commission of the European Communities.

/BRE 94/ Breidenich, G. (1994): Gekoppelte Berechnung der thermomechanischen Feldgrößen in einer Steinsalzformation infolge der Einlagerung radioaktiver wärmefreisetzender Abfälle, PhD-Thesis, RWTH Aachen.

/CRI 98/ Cristescu, N. & U. Hunsche (1998): Time Effects in Rock Mechanics. Series: Materials, Modelling and Computation, John Wiley & Sons, Chichester (UK).

/CRI 02/ Cristescu, N. D. New trends in rock mechanics, To the beginning of the third Millenium, International Applied Mechanics, Vol. 38, No. 1, 2002.

/DOW 06/ Theresa project: “Description of Work”, Annex 1 to the project contract FP6-036458.

/GUE 09/ Günther, R.-M. (2009): Erweiterter Dehnungs-Verfestigungs-Ansatz, Phänomenologisches Stoffmodell für duktile Salzgesteine zur Beschreibung primären, sekundären und tertiären Kriechens, PhD-Thesis, Mining Academy Freiberg, Institute for Geotechnics, Issue 2009-4, ISSN 1611-1605.

/HEI 91/ Hein, H. (1991): Ein Stoffgesetz zur Beschreibung des Thermomechanischen Verhaltens von Salzgranulat : Ein Beitrag zur Endlagerung wärmefreisetzender radioaktiver Abfälle, PdD-Thesis, RWTH Aachen.

/HEE 04/ Heemann, U., Heusermann, S. (2004). Theoretical and Experimental Investigation on Stresses and Permeability in the BAMBUS Project. DisTec 2004, Int. Conf. on Radioactive Waste Disposal, April 26-28, Berlin.

/ITA 04/ ITASCA (2004): PFC3D – Particle Flow Code in 3 Dimensions – Manuals for PFC^{3D} Version 3.1, Itasca Consulting Group, Inc.

/ITA 06/ ITASCA (2006): FLAC3D – Fast Lagrangian Analysis of Continua in 3 Dimensions – Manuals for FLAC^{3D} Version 3.1, Itasca Consulting Group, Inc.

/JIN 07/ Jing, L. and Stephansson, O. (2007): Fundamentals of discrete element methods for rock engineering - Theory and applications, Elsevier, Amsterdam.

/JOB 10/ Jobmann, M. and Billaux, D. (2010): Fractal model for permeability from porosity and pore radius information and application to excavation damaged zones surrounding waste emplacement boreholes in opalinus clay. Int. J. Rock Mech Min Sci. Vol 47, No. 4, 583-589, June 2010.

/MIN 04/ Minkley, W. (2004): Gebirgsmechanische Beschreibung von Entfestigung und Sprödbrucherscheinungen im Carnallitit, Habilitation Treatise, Shaker Verlag Aachen, 2004, ISSN 1860-0123.

/OLI 02/ Olivella, S. & A. Gens, (2002): A constitutive model for crushed salt, Int. J. Numer. Anal. Meth. Geomech., 26:719-746.

/OLI 08/ Olivella, S. and E. E. Alonso (2008): Gas flow through clay barriers, Geotechnique,58, No 3, 157-176.

/POP 02/ Popp, T. (2002). Transporteigenschaften von Steinsalz – Modellierung der Permeabilitäts-Porositäts-Beziehung. Meyniana 54, Seite 113-129, Kiel.

/PUD 04/ Pudewills, A. (2004): Numerical modelling of the long-term evolution of EDZ - Development of material models, implementation in finite-element codes, and validation, Forschungszentrum Karlsruhe.

/PUD 07/ Pudewills, A. (2007): BMBF-Verbundvorhaben Modellierung des mechanischen Verhaltens von Steinsalz - Vergleich aktueller Stoffgesetze und Vorgehensweisen, Abschlussbericht zu Teilvorhaben 6 (02C1054), Karlsruhe, FZKA, 2007.

/PUS 02/ Pusch, G., Alkan, H., Cinar, Y. (2002): Mechanische und hydraulische eigenschaften von Auflockerungszonen des Gebirges in Verbindung mit der Planung von Verschlussbauwerken im Salinar, Teil B: Hydraulische Modellbildung. Abschlussbericht zum BMBF-Forschungsvorhaben 02 C 0598.

/SCH 01/ Schulze, O., Popp, T., Kern, H. (2001): Development of damage and permeability in deforming rock salt. In: Ch. Talbot & M. Langer (eds.), Special Issue on Geosciences and Nuclear Waste Disposal Engineering Geology 61: 163 – 180, Elsevier, Amsterdam.

/SCH 07/ Schulze, O. (2007): Investigations on damage and healing of rock salt. In: M. Wallner., K.-H. Lux, W. Minkley & H.R. Hardy, Jr. (eds.), Proc. of the Sixth Conf. on the Mech. Behaviour of Salt. Hannover 2007: 33 – 44, Francis & Taylor, London.

/WIE 07/ Wieczorek, K., T. Rothfuchs, C.-L. Zhang, Th. Spies, U. Heemann, Chr. Lerch, S. Keesmann, A. Pudewills, P. Kamlot, J. Grupa, K. Herchen, S. Olivella and Chr. Spiers (2007): Compilation of existing constitutive models and experimental field or laboratory data for the thermal-hydraulic-mechanical (THM) modelling of the excavation disturbed zone (EDZ) in rock salt, European Commission, THERESA project, Deliverable D5, Coordinated by Gesellschaft für Anlagen- und Reaktorsicherheit (GRS) mbH, Braunschweig, Germany, 28 August 2007.

/WIE 08/ Wieczorek, K., U. Heemann, S. Keesmann, A. Pudewills, S. Olivella, P. Kamlot, C. Spiers and K. Herchen (2008), THERESA project, Work Package 3, Deliverable D6 - calibration of thermal-hydraulic-mechanical (THM) models of the excavation disturbed zone (EDZ) in rock salt, Coordinated by Gesellschaft für Anlagen- und Reaktorsicherheit (GRS) mbH, Braunschweig, Germany, 14 April 2008.

/WIE 09a/ Wieczorek, K., Grupa, J., Kamlot, P., Keesmann, S., Herchen, K., Heemann, U., Olivella, S., Pudewills, A. (2009): Theresa project, Deliverable D8: Model Application on Laboratory Benchmark Test, Coordinated by Gesellschaft für Anlagen- und Reaktorsicherheit (GRS) mbH, Braunschweig, Germany, 31 August 2009.

/WIE 09b/ Wieczorek, K. T. Rothfuchs, B. Förster, U. Heemann, S. Olivella, Chr. Lerch, A. Pudewills, P. Kamlot, J. Grupa, K. Herchen (2009): THERESA Deliverable D9, Coupled Processes in Salt Host-Rock Repositories - Final Report of Work Package 3, Coordinated by Gesellschaft für Anlagen- und Reaktorsicherheit (GRS) mbH, Braunschweig, 30 November 2009.

/ZHA 09/ Zhang, C.-L, Wieczorek, K., Rothfuchs, T. (2009), Theresa Project, Work Package 3, Deliverable D7, Laboratory Benchmark Tests on rock salt, Coordinated by Gesellschaft für Anlagen- und Reaktorsicherheit (GRS) mbH, Braunschweig, Germany, 30 March 2009.

9 List of figures

Fig. 3.1 Salt samples with attached strain gauges before testing 8

Fig. 3.2 Principle of triaxial compression tests with permeability measurement 9

Fig. 3.3 Volume and permeability changes of a salt sample under isostatic compaction 11

Fig. 3.4 Isostatic pre-compaction behaviour of a salt sample 11

Fig. 3.5 Stress-strain-permeability behaviour of a salt sample deformed by deviatoric loading at confining stress of 2 MPa 13

Fig. 3.6 Stress-strain-permeability behaviour of two salt samples deformed by deviatoric loading at confining stress of 1 MPa 14

Fig. 3.7 Determination of dilatancy point by detecting the minimum of volumetric strain 16

Fig. 3.8 Permeability–porosity relation obtained by re-compaction of damaged salt 17

Fig. 3.9 Porosity and permeability changes by re-compaction of damaged salt 18

Fig. 3.10 Large salt cores of 300 mm diameter and ~ 0.7 m length from the Asse mine 19

Fig. 3.11 Principle of the large-scale THM-test on a hollow salt cylinder 20

Fig. 3.12 Photos of a large hollow salt sample 1, inner packer and filter plate 23

Fig. 3.13 Results of the first part of the first large-scale test 24

Fig. 3.14 Results of the second part of the first large-scale test 25

Fig. 3.15 Photos of the large hollow salt sample 1 after dismantling 26

Fig. 3.16 Layout of the large-scale test 2 on a hollow salt cylinder (D = 280 mm / d = 102 mm / L = 460 mm) 27

Fig. 3.17 Loading history applied to a large hollow salt cylinder in the BMT test 28

Fig. 3.18 Responses of borehole deformation and gas permeability to the loading 28

Fig. 3.19 Details of fracturing by increasing the inner pressure in the borehole 30

Fig. 3.20 Dependence of fracture permeability on confining pressure 31

Fig. 3.21 Comparison of the large hollow salt cylinder before and after testing 32

Fig. 3.22 Schematic assembly of a salt sample in triaxial cell 34

Fig. 3.23 Determination of volumetric strain of a “drum shape” sample 34

Fig. 3.24 Responses of deformation and wave velocity to isostatic compression on sample TC1 35

Fig. 3.25 Evolution of strains measured on sample TC1 under deviatoric stresses 36

Fig. 3.26 Correlation between volumetric strain and wave velocity (TC1) 37

Fig. 3.27 Evolution of strains measured on sample TC2 under deviatoric stresses (TC test 2, first part; TC2A) 38

Fig. 3.28 Correlation between volumetric strain and wave velocity (TC2A) 38

Fig. 3.29 Load conditions applied to the previously deformed sample in TC test 2 (TC2B) 39

Fig. 3.30 Responses of deformation and wave velocity to loading and heating on the previously deformed sample (TC2B) 39

Fig. 3.31 Response of permeability to loading and heating on the previously deformed sample (TC2B) 40

Fig. 3.32 Correlation between permeability and wave velocity (TC2B) 40

Fig. 4.1 Representation of FADT (dissolution, diffusion and precipitation of salt) and DC creep (particle deformation through crystal dislocation processes) 44

Fig. 4.2 Stress function and flow rule F = G used for the viscoplastic generalization of the creep model (DC mechanism) 46

Fig. 4.3 Auxiliary functions gvFADT , gdFADT , gvDC and gdDC that appear in the viscosities 47

Fig. 4.4 Different deformation types depending on the stress state /CRI 02/ 48

Fig. 4.5 Simulation of a triaxial test at confining stress of 1 MPa, strain rate 10^{-7} s^{-1}, T = 30 °C, pore pressure of 0.5 MPa on a sample from 800 m level at Asse (sample 2) 50

Fig. 4.6 Stress path corresponding to the test simulated in fig. 4.5 (sample 2) 51

Fig. 4.7 Simulation of a triaxial test at salt sample deformed by deviatoric loading at confining stress of 2 MPa (decreased to 0.6), strain rate of 10^{-7} s^{-1} (increased to 10^{-6} s^{-1}), pore pressure of 0.9 MPa (decreased to 0.2) on a sample from 551 m level at Asse (sample 1) 52

Fig. 4.8 Stress path corresponding to the test simulated in fig. 4.7..... 53

Fig. 4.9 Stress-strain curves for the simulation of triaxial tests under different confinement stresses and strain rate of 10^{-7} s^{-1} 53

Fig. 4.10 Stress paths for for the simulation of triaxial tests under different confinement stresses and strain rate of 10^{-7} s^{-1} 54

Fig. 4.11 Modelling of different creep phases in material law Günther-Salzer..... 56

Fig. 4.12 Visco-elasto-plastic model concept in material law Minkley..... 57

Fig. 4.13 At left hand side, principle of a triaxial test and at right hand side, numerical model of a cylindrical specimen in a deformed state 58

Fig. 4.14 Evolution of differential stress (σ_1 - σ_3) versus axial strain, hardening until peak strength and softening in the dilatant domain, measured and calculated on Na3 from Asse mine, confining pressure 0.2 MPa..... 59

Fig. 4.15 Evolution of volumetric deformation versus axial strain, strong dilatancy increase while fracturing and slight increase after generation of shear bands in the dilatant domain, measured and calculated on Na3 from Asse mine, confining pressure 0.2 MPa..... 59

Fig. 4.16 Evolution of differential stress (σ_1 - σ_3) versus axial strain, hardening until peak strength and softening in the dilatant domain, measured and calculated on Na3 from Asse mine, confining pressure 1 MPa..... 60

Fig. 4.17 Evolution of volumetric deformation versus axial strain, strong dilatancy increase while fracturing and slight increase after generation of shear bands in the dilatant domain, measured and calculated on Na3 from Asse mine, confining pressure 1 MPa..... 60

Fig. 4.18 Evolution of differential stress (σ_1 - σ_3) versus axial strain, hardening until peak strength and softening in the dilatant domain, measured and calculated on Na3 from Asse mine, confining pressure 2 MPa..... 61

Fig. 4.19 Evolution of volumetric deformation versus axial strain, strong dilatancy increase while fracturing and slight increase after generation of shear bands in the dilatant domain, measured and calculated on Na3 from Asse mine, confining pressure 2 MPa..... 61

Fig. 4.20 Relevance of the laboratory test at 0.2 MPa for EDZ in-situ, relevance is mostly given for the domain of volumetric deformation < 1 % (axial deformation < 3 %) 62

Fig. 4.21 Hydraulical consequences of mechanically induced dilatancy at minimal stresses 0 – 0.6 MPa 63

Fig. 4.22 Cross section of single drift in halite mine, situation before reworking of contour zone, depth 775 m, A ≈ 15 m^2 64

Fig. 4.23 Cross section of single drift in halite mine, 4 months after reworking of contour zone, results of borehole permeability tests, depth 775 m, A ≈ 20 m^2 64

Fig. 4.24 Comparison of measured and calculated axial strain (a) and axial strain rate (b), data set BGR-94097 70

Fig. 4.25 Comparison of measured and calculated axial strain rate on logarithmic time scale, (a) data set BGR-94097, (b) data set BGR-95015 70

Fig. 4.26 Comparison of measured and calculated axial strain (a) and axial strain rate (b), data set BGR-95015 71

Fig. 4.27 Experimental and calculated stress-strain-behaviour, 3 MPa confining pressure, data set BGR-99088 72

Fig. 4.28 Numerical experiments with the modified Hein law, axial stress (dotted) and volumetric strain (solid) 72

Fig. 4.29 Assembly of particles in PFC3D being confined by walls (3269 balls) 74

Fig. 4.30 Two particles in contact, see /JIN 07/ /ITA04/ 75

Fig. 4.31 Calculation cycle in PFC3D 77

Fig. 4.32 Balls in contact 78

Fig. 4.33 Sketch of a strain-controlled tri-axial test 80

Fig. 4.34 Influence of bond parameters on mechanical behaviour (3269 balls) 81

Fig. 4.35 Variation of contact-stiffness (5664 balls) 82

Fig. 5.1 Simulated and measured results for TC2A 84

Fig. 5.2 Stress variation and temperature variation in the experiment TC2B (the variation used in the model is also shown) 84

Fig. 5.3 Comparison of measured and calculated deformations during TC2B 85

Fig. 5.4 Evolution of calculated deformations and calculated permeability (with Model I and Model II) during TC2B 86

Fig. 5.5 Evolution of calculated deformations and calculated permeability (with Model I and Model II) during Test B. Modified parameter (a_5 = 0.04) 87

Fig. 5.6 Comparison of measured and calculated permeability 88

Fig. 5.7 Stress history applied in the hollow test to perform the large scale test 89

Fig. 5.8 Measured and calculated evolution of permeability (s = 0.01 m) 89

Fig. 5.9 Scheme of set-up for the laboratory test and the calculation model for the large hollow cylinder 91

Fig. 5.10 Part 1: Axial stress and confining pressure 15 MPa, no interior pressure, 7 days creep 93

Fig. 5.11 Part 2: Increase of axial stress and confining pressure to 20 MPa, no interior pressure, 7 days creep (total 14 days creep) 93

Fig. 5.12 Scheme of set-up for the laboratory test and the calculation model 94

Fig. 5.13 Stress and temperature conditions at TC2A with measured strains versus time 95

Fig. 5.14 Location of stress states for test TC2A in octahedral stress space 96

Fig. 5.15 Blind prediction of TC2A: Applied differential stresses (black colour) 97

Fig. 5.16 Blind prediction of TC2A: Calculated (bold lines) strains in comparison with later provided test results (thin lines) 98

Fig. 5.17 Interpretation modelling of TC2A: Applied differential stresses (black colour) 98

Fig. 5.18 Interpretation modelling of TC2A: Calculated (bold lines) strains in comparison with later provided test results (thin lines) 99

Fig. 5.19 Stress and temperature conditions at TC2B (previously deformed salt sample) 100

Fig. 5.20 Location of stress states for TC2B in octahedral stress space 100

Fig. 5.21 Test course of TC2B, applied axial stress in magenta colour 101

Fig. 5.22 Comparison of measured axial and volume strain with calculation results in TC2B 102

Fig. 5.23 Porosity-permeability-relation: Dependence on dilatancy and confining pressure 103

Fig. 5.24 Comparison of in TC2B measured permeability with in dependence on dilatancy calculated magnitudes 104

Fig. 5.25 Loading scheme of TC2, phase TC2A (a) and phase TC2B (b) 105

Fig. 5.26 (a) Discretization of pistons (red) and sample (blue) on calculation grid
(b) axial and radial loading on the top and the lateral surface (coarse grid)
(c) grid points fixed in normal direction to corresponding planes (coarse grid) 106

Fig. 5.27 (a) Observation points for the determination of axial and strain
(b) quantities to be determined 107

Fig. 5.28 Simulation results with the linear dilatant model for TC2A 109

Fig. 5.29 Simulation results with the quadratic dilatant model for TC2A 110

Fig. 5.30 Simulation results with the quadratic dilatant model for TC2B
(a) evolution of strains over time
(b) development of secondary porosity 111

Fig. 5.31 Results at the end of simulation process TC2B, quadratic dilatant model case Q1
(a) distribution of porosity
(b) distribution of logarithmic permeability 113

Fig. 5.32 Measured and calculated permeability over time for TC2B (case Q1) 114

Fig. 6.1 Principle of the configuration considered for the reference case simulation 117

Fig. 6.2 Predicted disposal drift convergence for different cases of thermal behaviour 118

Fig. 6.3 Finite element model of the drift 120

Fig. 6.4 Porosity around the drift before EDZ cut-off (left) and at the time of seal construction, six months after EDZ cut-off (right) 121

Fig. 6.5 Porosity profile below the drift floor at different times for the case with EDZ cut-off 121

Fig. 6.6 Porosity profile below the drift floor without EDZ cut-off at different times 122

Fig. 6.7 Permeability-porosity relations considered for the determination of equivalent permeability 123

Fig. 6.8 Equivalent permeability versus time after seal construction for an equivalent cross section of 23 m^2, case with EDZ cut-off 125

Fig. 6.9 Equivalent permeability versus time after seal construction for an equivalent cross section of 23 m^2, no EDZ cut-off 125

Fig. 6.10 Proposed equivalent permeability versus time after seal construction for an equivalent cross section of 23 m^2, EDZ cut-off 126

Fig. 6.11 Proposed equivalent permeability versus time after seal construction for an equivalent cross section of 23 m^2, no EDZ cut-off 127

Fig. 6.12 Flow resistance of the EDZ and the dam for the different cases..... 128

Fig. 6.13 Permeability and porosity evolution of the EDZ and the dam for the different cases..... 129

Fig. 6.14 Total pore volume and brine volume evolution of the EDZ and the dam for the different cases using GRS' approximations 130

Fig. 6.15 Brine flow into the EDZ and the dam for the different cases..... 131

10 List of tables

Tab. 4.1 Parameters for simulation of the test on sample 2 51

Tab. 4.2 Parameters for simulation of the test on sample 2 52

Tab. 4.3 Mechanical parameters for *Asse Speisesalz* 69

Tab. 4.4 Variation of bond properties for 3269 balls 80

Tab. 5.1 Material properties 108

Tab. 6.1 Simulation schedule 120

THERESA

Coupled thermal-hydrological-mechanical-chemical (THMC) processes for application in repository safety assessment
(Contract Number: 036 458)

Issue Evaluation Table for Work Package 3

Deliverable 2

Appendix

#	Process Issue	Relevance for Input to PA	Availability of Data	Project	Need of Improvement	Need of Experiments	Remarks
Issue No.	Definition of key issues which need to be addressed in PA. List of issues related to theoretical concepts, physical processes, or parameters	Assessment of whether the issue is relevant to PA or not	Assessment of whether reliable data exist or it is feasible to derive defensible values for parameters for the issue in question	List of experiments addressing the issue and responsible organization	Assessment of whether further improvements are necessary for a more meaningful PA and the aim of improvements	Assessment of whether experiments are necessary to detect the site specific characterisation or to improve the knowledge about the issue in principal	Brief statement of status of issue
1	**DESIGN**						
1.1	**Repository Location and Geometry**						
1.1.1	Repository depth	Yes	Yes	BfS SR 2487	-	No	Level of disposal drifts between 700 and 1000m
1.1.2	In-situ stress conditions	Yes	Yes	Site specific	No	No	
1.1.3	Bedding-plane orientations	Yes	Yes	Site specific	-	-	On stratigraphical level. If relevant, consequences to barrier integrity.
1.1.4	Fracture-network orientations	No	-	-	-	-	Repository areas completely in homogeneous rock salt
1.1.5	Connected anhydrite layer with overburden	No	Yes	ISIBEL [18]	No	No	No relevance in case of complete containment concept, AkEnd [2], [18]
1.2	**Seal**						
1.2.1	Sealing method	Yes	Yes	1 m seal tests at WIPP, Asse dam [21], Salzdetfurth shaft seal [6], Sondershausen plug [33], Teutschenthal seal [17]	Optimization of sealing methods, in situ testing in realistic conditions	Yes	No long-term experience, especially with water/brine pressure acting on the seals, depending of the repository concepts
1.2.2	Sealing strategy	Yes	Yes	ISIBEL [18], Dammbau im Salzgebirge	Optimization of sealing concepts (arrangement and geometry of seals)	No	Depending of the repository concepts

#	Process Issue	Relevance for Input to PA	Availability of Data	Project	Need of Improvement	Need of Experiments	Remarks
2	**OPERATION PHASE**						
2.1	**Excavation**						
2.1.1	Excavation method	Yes	Yes	experiences and observations in salt mining	-	No	No blasting, preferentially continuous mining
2.2	**Elastic Mechanical Response (short term)**						
2.2.1	State of stress level	No	Yes		No	No	Minor relevance to salt
2.2.2	Elastic behaviour	Yes	Yes		No	Yes, on site	Material properties
2.3	**Visco-plastic Behaviour (long-term)**						
2.3.1	State of stress	Yes	Yes	Asse [14], Gorleben, Morsleben [15], WIPP [10]	-	No	
2.3.2	Rock creep	Yes	Yes	Asse [14], Gorleben, Morsleben [15], WIPP [10], VerbundProjekt Stoffgesetzvergleich [9], [32], [12]	Yes, transient creep, steady state creep at low stresses, and possible long-term effects of water [47]	Yes, on site	Different creep laws
2.3.3	Strain-dependent damaging and dilatancy	Yes	Yes	Verbund-Projekt Stoffgesetzvergleich [32]	Yes	Yes	Strain-dependent hardening and softening, dilatancy
2.4	**EDZ Evolution**						
2.4.1	Dilatancy, damage (fracturing), and permeability increase	Yes	Yes	EDZ-Workshop in Luxembourg [13], [27], [30], [40], Verbund-Projekt Stoffgesetzvergleich [17], BAMBUS I + II [3], [4], ALOHA [39], [41], Utrecht Uni. Programme, THERESA [46]	Yes, characterization of the fracturing and process, constitutive model to relate dilatancy to permeability	Yes	With opening of microcracks due to deviatoric stress and tensile stress, short term, long-term
2.4.2	Permeability-porosity relation	Yes	Yes	BAMBUS II [4], Müller-Lyda [24], Schulze [31], Utrecht Uni. Programme, NF-PRO [36], THERESA [42]	Yes, Evaluation of existing data and improvement of models	Yes	

#	Process Issue	Relevance for Input to PA	Availability of Data	Project	Need of Improvement	Need of Experiments	Remarks
2.5	**Support**						
2.5.1	Method	No	-	-	-	-	Not considered in the design

#	Process Issue	Relevance for Input to PA	Availability of Data	Project	Need of Improvement	Need of Experiments	Remarks
3	**CLOSURE PHASE**						
3.1	**EDZ Cutoff**						
3.1.1	Effectiveness of EDZ cutoff and evolution	Yes	Yes	ADDIGAS [16], Sonders-hausen [33]	Numerical back analy-ses for model validation	Yes, on site	Avoid continuous flow paths
3.1.2	Design optimization	No	-	-	Need of design studies	No	Avoid continuous flow paths and stress concentration
3.2	**Backfill / Seal**						
3.2.1	Backfill / sealing material	Yes	Yes	BAMBUS II [4], [25], [45], Salzdetfurth [6], SVV [11], Asse dam [21]	Qualification of materi-als and material models	Yes	Thermo-mechanical properties of new backfill materials, geochemical properties
3.2.2	Technically improved sealing	Yes		WIPP [1]		Yes	In the case of insufficient sealing capabilities on the interface between dam and host rock additional techniques are needed, e.g. injections [18], [22]
3.2.3	Seal effectiveness	Yes	Yes	BAMBUS I + II [3], [4], Salzdetfurth [6], SVV [11], Asse dam [21]	Processes at the seal-rock interface, modelling with respect to time	Yes	

#	Process Issue	Relevance for Input to PA	Availability of Data	Project	Need of Improvement	Need of Experiments	Remarks
4	**POST-CLOSURE PHASE**						
4.1	**Heating**						
4.1.1	Temperature field	Yes	Yes	BAMBUS I + II [3], [4]	-	No	
4.1.2	Material properties of host rock and backfill	Yes	Yes	BAMBUS I + II [3], [4]	Yes	Yes, on site	BAMBUS project yields insufficient approximation of stress-strain field at the same time in hot and cold area
4.2	**Self-sealing**						
4.2.1	Thermally enhanced backfill compaction and back pressure	Yes	Yes	BAMBUS I + II [3], [4], Salz-detfurth [6], SVV [11], Asse dam [21], RepoPerm [20]	Material model for (very) low porosity and permeability range	Yes	
4.2.2	EDZ self-sealing / healing (reduction of permeability)	Yes	Yes	BAMBUS II [4], Asse dam [21], Eberth [8], THERESA [43]	Process and achievable degree of self-sealing / healing, hydraulic conductivity versus time of seal construction	Yes	In addition to THERESA Project more experimental data are needed to clarify sealing/healing phenol-mena [26], [38]
4.2.3	Recrystallization	No	Yes	BAMBUS II [4], Utrecht Uni. experiments and models [26], [38]	Effect on pore discon-nection	Yes	In the presence of brine
4.3	**Gas Generation**						
4.3.1	Corrosion	Yes	Yes	Smailos [35]	Yes	No	THMRC calculations not yet tested due to lack of suitable codes / models
4.3.2	Pressure build-up	Yes	Yes		Gas storage capability of host rock and backfill	Yes	Workshops on gases in a repository [23], [29], aspects on gases in a repository [28], [34], [7]
4.3.3	Migration	Yes	Yes	ADDIGAS [16], NFPRO [20], BAMBUS II [2]	Gas transport	Yes	EDZ and intact rock

#	Process Issue	Relevance for Input to PA	Availability of Data	Project	Need of Improvement	Need of Experiments	Remarks
5	**ALTERED REPOSITORY CONDITIONS**						
	Of relevance for long-term performance assessment, but not considered in THERESA						
5.1	**Brine Intrusion (in the early post-closure phase)**						
5.1.1	Flow paths	Yes	No	-	Effect of effective porosity at low values, piping	Yes	Solid rock salt and crushed salt backfill
5.1.2	Brine migration	Yes	Yes	Experiments by GRS and Stoller [5]	Interaction between brine intrusion and gas generation, two phase flow	Yes	
5.1.3	Impact on rock salt, backfill, and seal properties (deformation, strength, permeability)	Yes	Yes	BGR experiments [44], Utrecht Uni. programme	Material laws for wet backfill and rock salt	Yes	
5.1.4	Dissolution and recrystallisation of the materials	Yes	Yes	Experiments by GRS and Stoller [5]	Yes	Yes	

References

[1] Ahrens, E. H.; Dale, T. F. (1996): Data report on the waste isolation pilot plant small-scale seal performance test, Series F grouting experiment. Sandia National Laboratories, Sandia Report SAND93-1000, Albuquerque, US.

[2] AkEnd (2002): Auswahlverfahren für Endlagerstandorte - Empfehlungen des AkEnd. Köln, 2002.

[3] Bechthold, W., Rothfuchs, T., Poley, A., Ghoreychi, M., Heusermann, S., Gens, A., and Olivella, S. (1999): Backfilling and Sealing of Underground Repositories for Radioactive Waste in Salt (BAMBUS-Project). Commission of the European Communities, EUR 19124 EN.

[4] Bechthold, W., Smailos, E., Heusermann, S., Bollingerfehr, W., Bazargan Sabet, B., Rothfuchs, T., Kamlot, P., Grupa, J., Olivella, S., and Hansen, F. D. (2003): Backfilling and Sealing of Underground Repositories for Radioactive Waste in Salt (BAMBUS-II Project), Commission of the European Communities, EUR 20621 EN.

[5] Becker, D.-A.; Bremer, N.-M.; Richter, K.-J.; Schneider, L.; Storck, R. (2000): Experimentelle und theoretische Untersuchung physikalisch-chemischer Vorgänge beim Laugenzutritt in Einlagerungsstrecken. Gesellschaft für Anlagen- und Reaktorsicherheit (GRS) mbH, GRS-164, Braunschweig.

[6] Breidung, K. P. (2002): Forschungsprojekt Schachtverschluss Salzdetfurth Schacht II. K+S AG, Bad Salzdetfurth, August 2002.

[7] Brewitz, W.; Kleemann, U. (2007): Radioactive Waste Disposal in Geological Formations. Proceedings of International Conference. November 6th - 9th 2007, Braunschweig Gesellschaft für Anlagen und Reaktorsicherheit (GRS) mbH, GRS - S - 49, Braunschweig.

[8] Eberth, S. (2007): Modellansätze zum Verheilungsverhalten von Steinsalz und ihre Anwendung auf Querschnittsabdichtungen im Salinargebirge. PhD-Thesis, TU Clausthal, 2007.

[9] Hampel, A.; Schulze, O.; Heemann, U.; Zetsche, F.; Günther, R.-M.; Salzer, K.; Minkley, W.; Hou, Z.; Wolters, R.; Düsterloh, U.; Zapf, D.; Rokahr, R.; Pudewills, A. (2007): BMBF-Verbundvorhaben: Die Modellierung des mechanischen Verhaltens von Steinsalz: Vergleich aktueller Stoffgesetze und Vorgehensweisen - Synthesebericht. FZK-PTKA, Karlsruhe

[10] Hansen, F. D. (2003): The Disturbed Rock Zone at the Waste Isolation Pilot Plant. SAND2003-3407, Sandia National Laboratories, Albuquerque / New Mexico, USA.

[11] Herbert, H.-J. (2007): Self Sealing Backfill (SVV) – A salt based material for constructing seals in salt mines. 6th Conf. on the Mechanical Behaviour of Salt, May 22-25, 2007, Hannover.

[12] Hou, Z.; Wolters, R.; Rokahr, R. Zapf, D.; Salzer, K.; Günther, R.-M.; Minkley, W.; Pudewills, A.; Heemann, U.; Schulze, O.; Zetsche, F.; Hampel, A. (2007): Comparison of advanced constitutive models for the mechanical behaviour of rock salt - results from a joint research project 2. Numerical modelling of two in situ case studies and comparison. 6th Conf. on the Mechanical Behaviour of Salt, May 22-25, 2007, Hannover.

[13] Hou, Z., Lux, K.-H. (2003): Mechanical degradation and self-healing of the excavation damaged zone around a drift dam in rock salt. Proceedings of European commission CLUSTER Conference and workshop "Impact of the excavation disturbed or damaged zone (EDZ) on the performance of radioactive waste geological repositories", Luxembourg, 3-5 November 2003.

[14] Hunsche, U., Hampel, A. (1999): Rock salt - the mechanical properties of the host rock material for a radioactive waste repository. Engineering Geology, Vol. 52, p. 271-291, Amsterdam (Elsevier). (Special Issue on Nuclear Waste Management in Earth Sciences. Eds.: Talbot, C., Langer, M.).

[15] Hunsche, U., Plischke, I., and Schulze, O. (1998): ERA Morsleben – Gebirgsmechanische und geotechnische Untersuchungen im Labor und in situ. BGR-Bericht, Hannover (unpublished).

[16] Jockwer, N.; Wieczorek, K. (2008): ADDIGAS Advective and diffusive gas transport in rock salt formations – Final Report. Gesellschaft für Anlagen- und Reaktorsicherheit (GRS) mbH, GRS-234, Braunschweig.

[17] Knoll, P. (2006): Entwicklung eines Grundkonzeptes für langzeitstabile Streckendämme im leichtlöslichen Salzgestein (Carnallitit) für UTD/UTV (Projekt "CARLA"), Teil 2: Erprobung von Funktionselementen. Bericht zum 1. Meilenstein, 31.07.2006, Teutschenthal.

[18] Krone, J., Weber, J. R., and Mönig, J., (2008): Überprüfung und Bewertung des Instrumentariums für eine sicherheitliche Bewertung von Endlagern für HAW – ISIBEL. Abschlussbericht. DBE TEC, Peine.

[19] Krone, J., Müller-Hoeppe, N., Brewitz, W., Mönig, J., Wallner, M., and Weber, J. R. (2007): Developing an advanced safety concept for an HLW repository in salt rock. Symp. Safety Cases for the Deep Disposal of Radioactive Waste: Where do we stand? OECD/NEA, 23-25 January 2007, Paris.

[20] Kröhn, K.-P.; Stührenberg, D.; Herklotz, M.; Heemann, U.; Lerch, C.; Xie, M. (2009): Restporosität und -permeabilität von kompaktierendem Salzgrus-Versatz in einem HAW-Endlager - Phase 1. Gesellschaft für Anlagen- und Reaktorsicherheit (GRS) mbH, in print, Braunschweig.

[21] Mauke, R., Schmidt, H. (2003): Untersuchung der Kontaktzone am Asse-Vordamm - Darstellung und Bewertung der Ergebnisse. Proc. 32. Geomechanik Kolloquium, Institut für Gebirgsmechanik GmbH und TU Bergakademie Freiberg, Institut für Geotechnik, Leipzig.

[22] Müller-Hoeppe, N.; Jobmann, M.; Polster, M.; Schmidt, H. (2007): The Role of Structural Reliability of Geotechnical Barriers of an HLW/SF Repository in Salt Rock within the Safety Case. OECD/NEA Syposium on "Safety Cases for the Deep Disposal of Radioaktive Waste - Where do we stand?", Paris, January 23.-25. 2007.

[23] Müller-Lyda, I. (1997): Erzeugung und Verbleib von Gasen in einem Endlager für radioaktive Abfälle – Bericht über den GRS-Workshop vom 29. und 30. Mai 1996 in Braunschweig. Gesellschaft für Anlagen- und Reaktorsicherheit (GRS) mbH, GRS-129, Braunschweig.

[24] Müller-Lyda, I., Birthler, H., Fein, E. (1999): Ableitung von Permeabilitäts-Porositätsrelationen für Salgrus. GRS-148, 74 S., GRS Braunschweig.

[25] Olivella, S., Gens, A. (2002): A constitutive model for crushed salt. Int. J. Numer. Anal. Meth. Geomech., 26, p. 719-746 (Wiley & Sons).

[26] Pennock, G.M., Zhang, X., Peach, C.J. and Spiers, C.J. (2007): Microstructural study of reconsolidated salt. 6th Conf. on the Mechanical Behaviour of Salt, May 22-25, 2007, Hannover.

[27] Rothfuchs, T., Wieczorek, K., Olivella, S., and Gens, A. (2003): Lessons Learned in Salt. European Commission CLUSTER Conference on the Impact of EDZ on the Performance of Radioactive Waste Geological Repositories, Luxembourg, 3-5 November 2003.

[28] Rübel, A.; Nosek, U.; Müller-Lyda, I.; Kröhn, K.-P.; Storck, R. (2004): Konzeptioneller Umgang mit Gasen im Endlager. Gesellschaft für Anlagen- und Reaktorsicherheit (GRS) mbH, GRS-205, Braunschweig.

[29] Rübel, A.; Mönig, J. (2008): Gase im Endlager im Salz Workshop der GRS in Zusammenarbeit mit dem PTKA-WTE, April 17th -18th, 2007, Berlin. Gesellschaft für Anlagen- und Reaktorsicherheit (GRS) mbH, GRS-242, Braunschweig.

[30] Schulze, O., Popp, T. (2002): Untersuchungen zum Dilalanzkriterium und zum Laugendruck-kriterium für die Beurteilung der Integrität eines Endlagerbergwerks in einer Steinsalzformation (The dilatancy criterion and fluid pressure criterion for the assessment of integrity of a permanent repository for radioactive waste in a rock salt formation). Z. Angew. Geol. 2/2002, p. 16 - 22.

[31] Schulze, O., Popp, T., and Kern, H. (2001): Development of damage and permeability in deforming rock salt. Engineering Geology, Vol. 61, p. 163-180, Amsterdam (Elsevier). (Special Issue on Geosciences and Nuclear Waste Disposal. Eds.: Talbot, C., Langer, M.).

[32] Schulze, O.; Heemann, U.; Zetsche, F.; Hampel, A.; Pudewills, A.; Günther, R.-M.; Minkley, W.; Salzer, K.; Hou, Z.; Wolters, R.; Rokahr, R.; Zapf, D. (2007): Comparison of advanced constitutive models for the mechanical behaviour of rock salt - results from a joint research project 1. Modelling of deformation processes and benchmark calculations. 6th Conf. on the Mechanical Behaviour of Salt, May 22-25, 2007, Hannover.

[33] Sitz, P.; Koch, G.; Gruner, M. (2002): Results from the large scale in situ drift sealing experiment in the salt mine Sondershausen. International Meeting "Clays in natural and engineered barriers for radioactive waste confinement", Reims, December 9-12, 2002.

[34] Skrzyppek, J., Mayer, G., Wilhelm, S., Niemeyer, M., Folle, S., Rolfs, O., and Suter, D. (2005): Untersuchung der Gasbildungsmechanismen in einem Endlager für radioaktive Abfälle und der damit verbundenen Auswirkungen auf die Führung des Nachweises der Endlagersicherheit. Colenco Power Engineering AG, Abschlussbericht (erstellt im Auftrag des BfS, Stand 31.05.2005), Colenco Bericht 3161/28, Baden, Schweiz.

[35] Smailos, E., Fiehn, B., Gago, J. A., and Azkarate, I. (1996): Corrosion studies on selected packaging materials for disposal of heat-generating radioactive wastes in rock salt formations. Final report, European Commission, Nuclear Science and TECHNOLOGY, EUR 17108 EN, Brüssel.

[36] Sneyers, A.; et al. (2008): Understanding and Physical and Numerical Modelling of the Key Processes in the Near Field and their Coupling for Different Host Rocks and Repository Strategies (NF-PRO). Commission of the European Communities, EUR 23730 EN.

[37] Spiers, C. J., Grupa, J., Salzer, K., Topp, T., and Stührenberg, D. (2005): Buffer / backfill in salt. Presentation in NFPRO second training course and workshop, 19-20 October 2005, Cardiff, Wales, UK.

[38] Urai, J. L.; Spiers, C. J. (2007): The effect of grain boundary water on deformation mechanisms and rheology of rocksalt during long-term deformation. 6th Conf. on the Mechanical Behaviour of Salt, May 22-25, 2007, Hannover.

[39] Wieczorek, K., Zimmer, U. (1998): Untersuchungen zur Auflockerungszone um Hohlräume im Steinsalzgebirge. Final Report, Gesellschaft für Anlagen- und Reaktorsicherheit (GRS) mbH, GRS-A-2651, Braunschweig.

[40] Wieczorek, K. (2003): EDZ in Rock Salt: Testing Methods and Interpretation. European Commission CLUSTER Conference on the Impact of EDZ on the Performance of Radioactive Waste Geological Repositories, Luxembourg, 3-5 November 2003.

[41] Wieczorek, K., Schwarzianeck, P. (2004): Untersuchung zur Auflockerungszone im Salinar (ALOHA2), Abschlussbericht. GRS-198, Gesellschaft für Anlagen- und Reaktorsicherheit (GRS) mbH, Braunschweig.

[42] Wieczorek, K.; Olivella, S., Keesmann, S., Herchen, K., Pudewills, A., Grupa, J., Heemann, U. (2009), Work Package 3, Deliverable D8: Model Application on Laboratory Benchmark Test, Gesellschaft für Anlagen- und Reaktorsicherheit (GRS) mbH, Germany.

[43] Work Package 3, Deliverable D9, Final report of WP3, Gesellschaft für Anlagen- und Reaktorsicherheit (GRS) mbH, Germany.

[44] Zhang, C.-L., Stührenberg, D. (1997): Compaction and its Effect on the Permeability of Crushed Salt with added Brine or Bentonite. 6th Int. Conf. on Radioactive Waste Management and Environmental Remediation, October 1997, Singapore.

[45] Zhang, C.-L., Rothfuchs, T., Droste, J. (2007): Post-Tests on Thermo-Mechanically Compacted Salt Backfill. 6th Conf. on the Mechanical Behaviour of Salt, May 22-25, 2007, Hannover.

[46] Zhang, C.-L., Wieczorek, K., and Rothfuchs, T. (2009), Work Package 3, Deliverable D7: Laboratory Benchmark Tests on Rock Salt. Gesellschaft für Anlagen- und Reaktorsicherheit (GRS) mbH, Germany.

[47] Zhang, X.; Peach, C. J.; Grupa, J.; Spiers, C. J. (2007): Stress relaxation experiments on compacted granular salt: effects of water. 6th Conf. on the Mechanical Behaviour of Salt, May 22-25, 2007, Hannover.

Gesellschaft für Anlagen- und Reaktorsicherheit (GRS) mbH

Schwertnergasse 1
50667 Köln
Telefon +49 221 2068-0
Telefax +49 221 2068-888

Forschungszentrum
85748 Garching b. München
Telefon +49 89 32004-0
Telefax +49 89 32004-300

Kurfürstendamm 200
10719 Berlin
Telefon +49 30 88589-0
Telefax +49 30 88589-111

Theodor-Heuss-Straße 4
38122 Braunschweig
Telefon +49 531 8012-0
Telefax +49 531 8012-200

www.grs.de

DBE TECHNOLOGY GmbH (DBE TEC)

Eschenstraße 55
31224 Peine

Institut für Gebirgsmechanik (IfG)

Friederikenstraße 60
04279 Leibzig

ISBN 978-3-939355-37-3